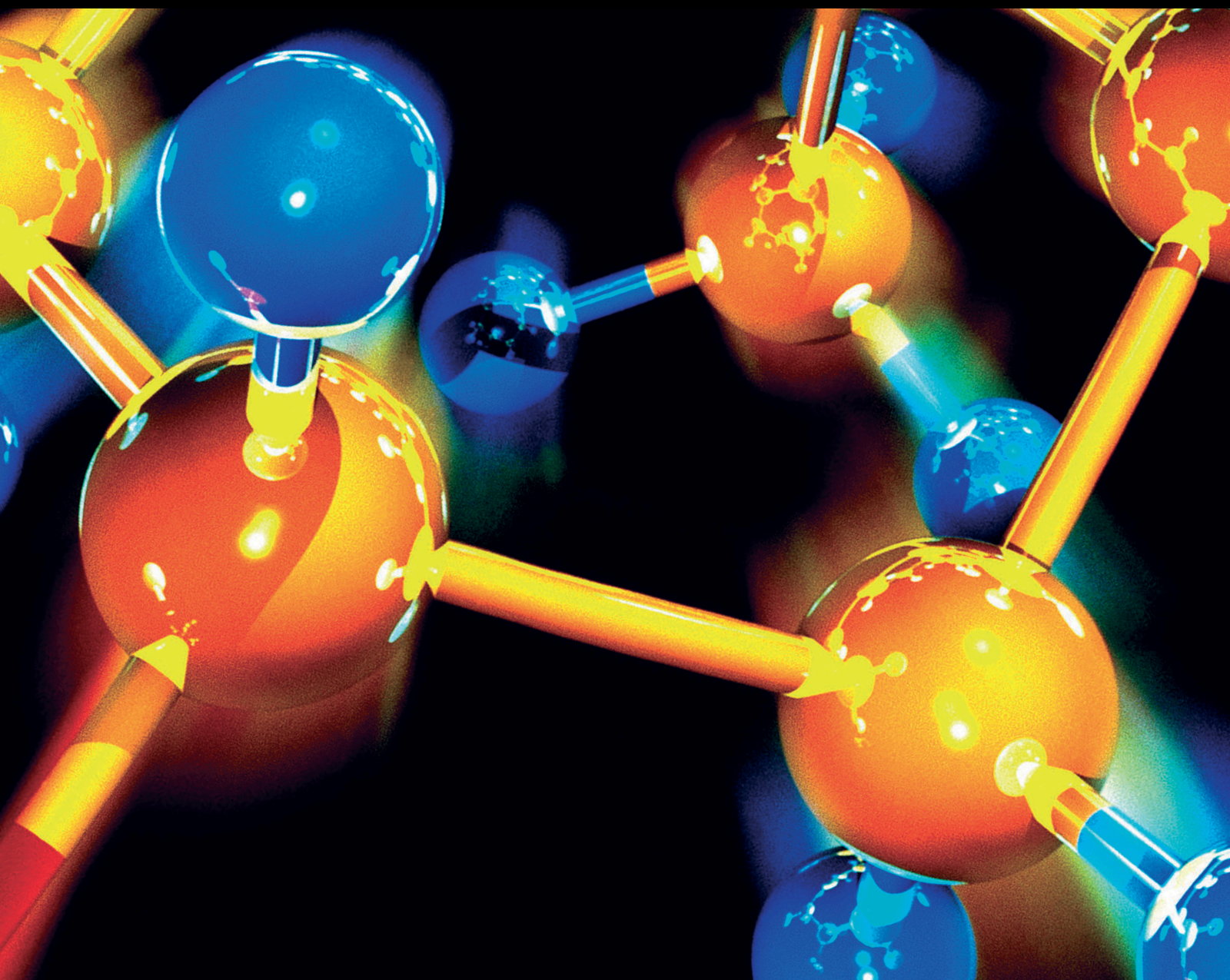


Pollutant Formation and Control during Fuel Thermochemical Conversion

Lead Guest Editor: Yanqing Niu

Guest Editors: Kuihua Han, Ningbo Gao, Liang Wang, and Norbert Miskolczi





Pollutant Formation and Control during Fuel Thermochemical Conversion

**Pollutant Formation and Control during
Fuel Thermochemical Conversion**

Lead Guest Editor: Yanqing Niu

Guest Editors: Kuihua Han, Ningbo Gao, Liang
Wang, and Norbert Miskolczi



Copyright © 2020 Hindawi Limited. All rights reserved.

This is a special issue published in "Journal of Chemistry." All articles are open access articles distributed under the Creative Commons Attribution License, which permits unrestricted use, distribution, and reproduction in any medium, provided the original work is properly cited.

Editorial Board

Stefania Abbruzzetti, Italy
Luqman C. Abdullah, Malaysia
Amitava Adhikary, USA
Daryoush Afzali, Iran
María D. Alba, Spain
Juan D. Alché, Spain
Mohammad A. Al-Ghouthi, Qatar
Shafaqat Ali, Pakistan
Patricia E. Allegratti, Argentina
Mohammednoor Altarawneh, Australia
Marco Anni, Italy
Alessandro Arcovito, Italy
José L. Arias Mediano, Spain
Hassan Arida, Saudi Arabia
Umair Ashraf, Pakistan
Iciar Astiasaran, Spain
Narcis Avarvari, France
Davut Avci, Turkey
Mohamed Azaroual, France
Hassan Azzazy, Egypt
Renal Backov, France
Suresh Kannan Balasingam, Norway
Florent Barbault, France
Maurizio Barbieri, Italy
James Barker, United Kingdom
Davide Barreca, Italy
Jorge Barros-Velázquez, Spain
Michele Benedetti, Italy
Laurent Billon, France
Marek Biziuk, Poland
Jean-Luc Blin, France
Tomislav Bolanca, Croatia
Ankur Bordoloi, India
Cato Brede, Norway
Leonid Breydo, USA
Wybren J. Buma, The Netherlands
J. O. Caceres, Spain
Claudio Cameselle, Spain
Joaquin Campos, Spain
Dapeng Cao, China
Stefano Caporali, Italy
Zenilda Cardeal, Brazil

Angela Cardinali, Italy
Stefano Carli, Italy
Maria F. Carvalho, Portugal
Susana Casal, Portugal
Thomas R. Caulfield, USA
David E. Chavez, USA
Riccardo Chelli, Italy
Zhongfang Chen, Puerto Rico
Zhen Cheng, USA
Ester Chiessi, Italy
Ann M. Chippindale, United Kingdom
Vladislav Chrastny, Czech Republic
Clara Cilindre, France
Roberto Comparelli, Italy
Filomena Conforti, Italy
Christophe Coquelet, France
Filomena Corbo, Italy
Jose Corchado, Spain
Maria N. D.S. Cordeiro, Portugal
Claudia Crestini, Italy
Gerald Culioli, France
Manuela Curcio, Italy
Shayessteh Dadfarnia, Iran
Samuel B. Dampare, Ghana
Umashankar Das, Canada
Victor David, Romania
Annalisa De Girolamo, Italy
Antonio De Lucas-Consuegra, Spain
Marcone A. L. de Oliveira, Brazil
Paula G. De Pinho, Portugal
Damião Pergentino de Sousa, Brazil
Francisco Javier Deive, Spain
Albert Demonceau, Belgium
Tianlong Deng, China
Fatih Deniz, Turkey
Stefano D'Errico, Italy
Matthias D'hooghe, Belgium
Claudio Di Iaconi, Italy
Irene Dini, Italy
Daniele Dondi, Italy
Yingchao Dong, China
Dennis Douroumis, United Kingdom

John Drexler, USA
Qizhen Du, China
Yuanyuan Duan, China
Philippe Dugourd, France
Frederic Dumur, France
Grégory Durand, France
Mehmet E. Duru, Turkey
Takayuki Ebata, Japan
Hani El-Nezami, Hong Kong
Arturo Espinosa Ferao, Spain
Carola Esposito Corcione, Italy
Valdemar Esteves, Portugal
Cristina Femoni, Italy
Gang Feng, China
Dieter Fenske, Germany
Jorge F. Fernandez-Sanchez, Spain
Alberto Figoli, Italy
Elena Forte, Italy
Sylvain Franger, France
Emiliano Fratini, Italy
Franco Frau, Italy
Bartolo Gabriele, Italy
Guillaume Galliero, France
Andrea Gambaro, Italy
Fernando Garay, Argentina
Gonzalo Garcia, Spain
James W. Gauld, Canada
Barbara Gawdzik, Poland
Pier Luigi Gentili, Italy
Dimosthenis L. Giokas, Greece
Alejandro Giorgetti, Italy
Alexandre Giuliani, France
Elena Gomez, Spain
Yves Grohens, France
Katharina Grupp, Germany
Tingyue Gu, USA
Luis F. Guido, Portugal
Maolin Guo, USA
Wenshan Guo, Australia
Leena Gupta, India
Muhammad J. Habib, USA
Jae Ryang Hahn, Republic of Korea
Christopher G. Hamaker, USA
Yusuke Hara, Japan
Naoki Haraguchi, Japan
Serkos A. Haroutounian, Greece
Hongshan He, USA

Nélio Henderson, Brazil
Javier Hernandez-Borges, Spain
Miguel Herrero, Spain
Mark Hoffmann, USA
Hanmin Huang, China
Doina Humelnicu, Romania
Charlotte Hurel, France
Shahid Hussain, China
Nenad Ignjatović, Serbia
Ales Imramovsky, Czech Republic
Muhammad Jahangir, Pakistan
Philippe Jeandet, France
Sławomir M. Kaczmarek, Poland
Ewa Kaczorek, Poland
Hossein Kazemian, Canada
Mostafa Khajeh, Iran
Alexander M. Kirillov, Portugal
Srećko I. Kirin, Croatia
Anton Kokalj, Slovenia
Sevgi Kolaylı, Turkey
Takeshi Kondo, Japan
Christos Kordulis, Greece
Ioannis D. Kostas, Greece
Yiannis Kourkoutas, Greece
Henryk Kozłowski, Poland
Yoshihiro Kudo, Japan
Isabel Lara, Spain
Bachir Latli, USA
Jolanta N. Latosinska, Poland
João Paulo Leal, Portugal
Yuan-Pern Lee, Taiwan
Woojin Lee, Kazakhstan
Matthias Lein, New Zealand
Landong Li, China
Huabing Li, China
Kokhwa Lim, Singapore
Teik-Cheng Lim, Singapore
Xinyong Liu, China
Jianqiang Liu, China
Xi Liu, China
Zhong-Wen Liu, China
Eulogio J. Llorent-Martínez, Spain
Pasquale Longo, Italy
Pablo Lorenzo-Luis, Spain
Devanand Luthria, USA
Konstantin V. Luzyanin, United Kingdom
Mari Maeda-Yamamoto, Japan

Isabel Mafra, Portugal
Dimitris P. Makris, Greece
Pedro M. Mancini, Argentina
Marcelino Maneiro, Spain
Giuseppe F. Mangiatordi, Italy
Casimiro Mantell, Spain
Ana B. Martin-Diana, Ireland
Carlos A Martínez-Huitle, Brazil
José M. G. Martinho, Portugal
Andrea Mastinu, Italy
Cesar Mateo, Spain
Georgios Matthaiolampakis, USA
Mehrab Mehrvar, Canada
Saurabh Mehta, India
Saima Q. Memon, Pakistan
Maurice Millet, France
Angelo Minucci, Italy
Liviu Mitu, Romania
Hideto Miyabe, Japan
Kaustubha Mohanty, India
Ana Moldes, Spain
Subrata Mondal, India
José Morillo, Spain
Giovanni Morrone, Italy
Marta E. G. Mosquera, Spain
Khaled Mostafa, Egypt
Ahmed Mourran, Germany
Markus Muschen, USA
Benjamin Mwashote, USA
Mallikarjuna N. Nadagouda, USA
Lutfun Nahar, United Kingdom
Mu. Naushad, Saudi Arabia
Gabriel Navarrete-Vazquez, Mexico
Jean-Marie Nedelec, France
Orazio Nicolotti, Italy
Nagatoshi Nishiwaki, Japan
Tzortzis Nomikos, Greece
Marjana Novic, Slovenia
Beatriz P. P. Oliveira, Portugal
Leonardo Palmisano, Italy
Mohamed Afzal Pasha, India
Dario Pasini, Italy
Angela Patti, Italy
Massimiliano F. Peana, Italy
Andrea Penoni, Italy
Franc Perdih, Slovenia
Jose A. Pereira, Portugal
Pedro Avila Pérez, Mexico
Maria Grazia Perrone, Italy
Silvia Persichilli, Italy
Thijs A. Peters, Norway
Christophe Petit, France
Marinos Pitsikalis, Greece
Rita Rosa Plá, Argentina
Fabio Polticelli, Italy
Josefina Pons, Spain
V. Prakash Reddy, USA
María Quesada-Moreno, Germany
Maurizio Quinto, Italy
Franck Rabilloud, France
Jamal Rafique, Brazil
C.R. Raj, India
Teodorico C. Ramalho, Brazil
Fateme Razeai, USA
Julia Revuelta, Spain
Alberto Ritieni, Italy
Muhammad Rizwan, Pakistan
Manfredi Rizzo, Italy
Maria P. Robalo, Portugal
Maria Roca, Spain
Nicolas Roche, France
Roberto Romeo, Italy
Antonio M. Romerosa-Nievas, Spain
Ioannis G. Roussis, Greece
Diego Sampedro, Spain
Shengmin Sang, USA
Eloy S. Sanz-Pérez, Spain
Stéphanie Sayen, France
Ewa Schab-Balcerzak, Poland
Hartwig Schulz, Germany
Gulaim A. Seisenbaeva, Sweden
Serkan Selli, Turkey
Murat Senturk, Turkey
Beatrice Severino, Italy
Hideaki Shirota, Japan
Cláudia G. Silva, Portugal
Artur M. S. Silva, Portugal
Ajaya Kumar Singh, India
Ponnurengam Malliappan Sivakumar, Japan
Tomás Sobrino, Spain
Raquel G. Soengas, Spain
Yujiang Song, China
Olivier Soppera, France
Ana Catarina Sousa, Portugal

Vivek Srivastava, India
Radhey Srivastava, USA
Theocharis C. Stamatatos, Greece
Athanasios Stavrakoudis, Greece
Darren Sun, Singapore
Kamal Swami, USA
Elad Tako, USA
Franco Tassi, Italy
Alexander Tatarinov, Russia
Lorena Tavano, Italy
Tullia Tedeschi, Italy
Vinod Kumar Tiwari, India
Augusto C. Tome, Portugal
Naoki Toyooka, Japan
Andrea Trabocchi, Italy
Philippe Trens, France
Ekaterina Tsipis, Russia
Andreas G. Tzakos, Greece
Esteban P. Urriolabeitia, Spain
Toyonobu Usuki, Japan
Giuseppe Valacchi, Italy
Patricia Valentao, Portugal
Marco Viccaro, Italy
Jaime Villaverde, Spain
Marc Visseaux, France
Alessandro Volonterio, Italy
Zoran Vujcic, Serbia
Carmen Wängler, Germany
Yun Wei, China
Wieslaw Wiczkowski, Poland
Bryan M. Wong, USA
Honghong Wu, China
Frank Wuest, Canada
Yang Xu, USA
Yuangen Yang, USA
Maria C. Yebra-Biurrún, Spain
Mina Yoon, USA
Tomokazu Yoshimura, Japan
Sedat Yurdakal, Turkey
Shin-ichi Yusa, Japan
Claudio Zaccone, Italy
Robert Zaleśny, Poland
Ronen Zangi, Spain
John CG Zhao, USA
Zhen Zhao, China
Minghua Zhou, China
Antonio Zizzi, Italy

Mire Zloh, United Kingdom
Grigoris Zoidis, Greece

Contents

Pollutant Formation and Control during Fuel Thermochemical Conversion

Yanqing Niu , Kuihua Han, Ningbo Gao , Liang Wang, and Norbert Miskolczi
Editorial (2 pages), Article ID 6073439, Volume 2020 (2020)

Nano-Azo Ligand and Its Superhydrophobic Complexes: Synthesis, Characterization, DFT, Contact Angle, Molecular Docking, and Antimicrobial Studies

Gehad G. Mohamed , Walaa H. Mahmoud, and Ahmed M. Refaat
Research Article (19 pages), Article ID 6382037, Volume 2020 (2020)

A Comprehensive Review on Thermal Coconversion of Biomass, Sludge, Coal, and Their Blends Using Thermogravimetric Analysis

Zeeshan Hameed, Salman Raza Naqvi, Muhammad Naqvi , Imtiaz Ali, Syed Ali Ammar Taqvi, Ningbo Gao , Syed Azfar Hussain, and Sadiq Hussain
Review Article (23 pages), Article ID 5024369, Volume 2020 (2020)

Influence of the Inner and Outer Secondary Air Ratios on the Combustion Characteristic and Flame Shape of a Swirl Burner with a Prechamber

Pengzhong Liu, Fang Niu , Xuewen Wang, Fei Guo, Wei Luo, and Naiji Wang
Research Article (9 pages), Article ID 4363016, Volume 2020 (2020)

Numerical Study on the Denitrification Efficiency of Selective Noncatalytic Reduction Technology in Decomposing Furnace

Shunsheng Xu, Jiazhen He , Fei Pei, Kun Li, Lele Liu, and Zhiyong Dai
Research Article (11 pages), Article ID 9484683, Volume 2020 (2020)

Kinetic Modeling Study of the Industrial Sulfur Recovery Process for Operating Condition Optimization

Shan Huang , Zhaohui Teng, Lisheng Zhang, Qulan Zhou , and Na Li
Research Article (12 pages), Article ID 4156216, Volume 2020 (2020)

Research on the Impact of Carbon Tax on CO₂ Emissions of China's Power Industry

Yue Yu , Zhi-xin Jin, Ji-zu Li , and Li Jia
Research Article (12 pages), Article ID 3182928, Volume 2020 (2020)

Reaction Kinetics of Chlorine Corrosion to Heating Surfaces during Coal and Biomass Cofiring

Yongzheng Wang , Yu Sun, Maozhen Yue, and Yungang Li
Research Article (10 pages), Article ID 2175795, Volume 2020 (2020)

Characteristics of Corrosion Related to Ash Deposition on Boiler Heating Surface during Cofiring of Coal and Biomass

Yongzheng Wang , Yu Sun, Lei Jiang, Lu Liu, and Yungang Li
Research Article (9 pages), Article ID 1692598, Volume 2020 (2020)

A Review of Urea Pyrolysis to Produce NH₃ Used for NO_x Removal

Denghui Wang , Ning Dong , Yanqing Niu , and Shien Hui 
Review Article (11 pages), Article ID 6853638, Volume 2019 (2019)

The Online Research of B₂O₃ on Crystal Behavior of High Ti-Bearing Blast Furnace Slag

Yin-he Lin , Bin Zheng, Lin-gen Luo , Yu-long Jia , and Li-qiang Zhang 

Research Article (8 pages), Article ID 5498325, Volume 2019 (2019)

Editorial

Pollutant Formation and Control during Fuel Thermochemical Conversion

Yanqing Niu ¹, Kuihua Han,² Ningbo Gao ¹, Liang Wang,³ and Norbert Miskolczi⁴

¹State Key Laboratory of Multiphase Flow in Power Engineering, School of Energy and Power Engineering, Xi'an Jiaotong University, 710049 Xi'an, Shaanxi, China

²Shandong Engineering Laboratory for High-efficiency Energy Conservation and Energy Storage Technology & Equipment, School of Energy and Power Engineering, Shandong University, 250061 Jinan, Shandong, China

³SINTEF Energy Research, Sem Saelands vei 11, 7034 Trondheim, Norway

⁴University of Pannonia, Faculty of Engineering, Institute of Chemical Engineering and Process Engineering, MOL Department of Hydrocarbon & Coal Processing, Egyetem u. 10, H-8200 Veszprém, Hungary

Correspondence should be addressed to Yanqing Niu; yqniu85@mail.xjtu.edu.cn

Received 3 August 2020; Accepted 4 August 2020; Published 26 November 2020

Copyright © 2020 Yanqing Niu et al. This is an open access article distributed under the Creative Commons Attribution License, which permits unrestricted use, distribution, and reproduction in any medium, provided the original work is properly cited.

The pollution emissions from the utilization of fuels have become a troublesome global problem due to its severe hazard to both human health and the environment. The pollutants emissions, such as SO₂, nitric oxides (NO_x), CO₂, heavy metals, and particulate matters (PM), have limited the utilization of environmental-friendly fuels and require to be reduced [1–4]. These pollutants come from the combustion, gasification, and pyrolysis process of coal, biomass, waste-derived fuels, and other solid fuels [1, 5]. Regulations and legislations are being updated for limiting emissions from thermal conversion of fuels and negative effects to human health and environment. There are ongoing research activities and technology development aiming at understanding, controlling, and preventing formation and emission of these pollutants. Thus, the aim of this special issue was to publish research papers addressing recent advances on the fuel thermochemistry and the following pollution issues.

After the evaluation of manuscripts submitted to the special issue, we have accepted ten for publication in the special issue. Liu and coworkers investigated the influence of inner and secondary air ratios (ISA/OSA) on the coal combustion characteristic and flame shape. In particular, the study was carried out in a swirl burner with a prechamber in a 14 MW pilot scale pulverized-coal combustion system. They found that the flame shape size exhibited an inflection

point with increasing ISA/OSA and the ratio of 1 : 2 was the optimized case under experiment conditions.

Xu and coworkers studied the denitrification of decomposing furnace for NO_x reduction. They modeled the 2500 t/d new dry-process cement kiln decomposing furnace and verified the simulation methods by the field test. They concluded that the NO concentration, NH₃ escape, and denitrification efficiency could be limited to 187.60 mg/m³, 32.40 mg/m³, and 74.75%, respectively.

Huang and coworkers built a reactor network analysis model with a detailed mechanism to describe and calculate the process in the sulfur recovery unit. Then, they used the verified model to find the optimum condition parameters for a real device in the Puguang gas field. The results were able to correlate to the best sulfur recovery to reduce pollution emissions and improve economic performance.

Yu and coworkers simulated the CO₂ emissions of China's power industry with different carbon tax levels based on the TIMES model. They quantitatively studied the power consumption demand, primary energy consumption structure, CO₂ emission characteristics, emission reduction potential, and cost of different carbon tax levels. The authors predicted the peak value of CO₂ emissions during 2030–2040; the medium carbon tax level was recommended for the most elastic impact on the national economy and the smallest GDP loss.

Wang and coworkers concerned the mechanism of chlorine corrosion to heating surface in the boiler for corrosion prevention and the safety of boiler operation. They studied the reaction kinetics of chlorine corrosion by the weight gain method and simulated the temperature, atmosphere, and fouling in the boiler. The authors reported a fast corrosion rate in the early stage of ash deposits but a slower rate after the formation of the protective layer on heat transfer tube surfaces. Low temperature and concentration of HCl in the gas phase were suggested. Another work by the authors is the investigation on the corrosion mechanism related to ash deposition on the boiler heating surface. They concluded that the addition of biomass aggravated the corrosion of metal tubes, and T91 was the ideal material for the biomass-fired boiler against metal corrosion.

Lin and coworkers investigated the effect of B_2O_3 additives on the crystal behavior of high Ti-bearing blast furnace slag. The authors concluded that the B_2O_3 additives can restrain the appearance of the perovskite phase, decrease the apparent viscosity, and promote the metallurgical properties of Ti-bearing blast furnace slag. Their findings provided a feasible and convenient method to prevent the slagging problem for Ti-bearing blast furnaces.

Mohamed and coworkers aim to synthesize Cr (III), Mn (II), Fe (III), Co (II), Ni (II), Cu (II), Zn (II), and Cd (II) complexes with the new diazo ligand (H_2L) and to examine their physical properties involving spectral behaviors and the electrical conductance values. They determined the efficiency of the synthesized complexes against pathogenic bacteria and obtained the contact angle, molecular structure, and molecular docking. The results showed that the Cd (II) complex can be considered as a super hydrophobic material and has significant biological activities with different sensitivity levels. The binding between H_2L and its Cd (II) complex with receptors of crystal structure of *S. aureus* (PDB ID: 3Q8U), crystal structure of protein phosphatase (PPZ1) of *Candida albicans* (PDB ID: 5JPE), receptors of breast cancer mutant oxidoreductase (PDB ID: 3HB5), and crystal structure of *Escherichia coli* (PDB ID: 3T88) was predicted and given in details.

Finally, this special issue includes two comprehensive reviews. Wang and coworkers reviewed the urea pyrolysis in three parts: urea pyrolysis pathway, catalytic hydrolysis of H₂NCO, and catalytic pyrolysis of aqueous urea solution. They proposed that the current research focused on the analysis of urea pyrolysis products and exploration of catalysts used to improve ammonia yields, but the mechanism study and development of a kinetic model with high accuracy need further exploration. Hameed and coworkers presented the state-of-the-art review on utilizing biomass and sewage sludge in combination with coal for improvement in energy conversion processes. They concluded the blending impact on tar release, alkali and ash, char characteristics, and thermal co-conversion behaviors. This study will provide recent development and future prospects for co-thermal conversion of these blends.

In conclusion, the current special issue offers updated information to the readers on the recent advancements regarding Pollutant Formation and Control during Fuel Thermochemical Conversion and gives a deeper insight into their formation mechanisms and control strategy. It is clearly evidenced that the thermochemical conversion of fossil fuel is a current topic and needs further investigation towards their clean and efficient utilization.

Conflicts of Interest

The editors declare that they have no conflicts of interest regarding the publication of this special issue.

Acknowledgments

The editors would like to thank all the authors, reviewers, and the editorial team of the Journal of Chemistry for their great support and contribution in making this special issue possible.

Yanqing Niu
Kuihua Han
Ningbo Gao
Liang Wang
Norbert Miskolczi

References

- [1] A. Williams, J. M. Jones, L. Ma, and M. Pourkashanian, "Pollutants from the combustion of solid biomass fuels," *Progress in Energy and Combustion Science*, vol. 38, no. 2, pp. 113–137, 2012.
- [2] P. Glarborg, J. A. Miller, B. Ruscic, and S. J. Klippenstein, "Modeling nitrogen chemistry in combustion," *Progress in Energy and Combustion Science*, vol. 67, pp. 31–68, 2018.
- [3] Y. Niu, H. Tan, and S. E. Hui, "Ash-related issues during biomass combustion: alkali-induced slagging, silicate melt-induced slagging (ash fusion), agglomeration, corrosion, ash utilization, and related countermeasures," *Progress in Energy and Combustion Science*, vol. 52, pp. 1–61, 2016.
- [4] L. Liu, K. Wang, S. Wang, R. Zhang, and X. Tang, "Assessing energy consumption, CO₂ and pollutant emissions and health benefits from China's transport sector through 2050," *Energy Policy*, vol. 116, pp. 382–396, 2018.
- [5] N. Gao, K. Kamran, C. Quan, and P. T. Williams, "Thermochemical conversion of sewage sludge: a critical review," *Progress in Energy and Combustion Science*, vol. 79, Article ID 100843, 2020.

Research Article

Nano-Azo Ligand and Its Superhydrophobic Complexes: Synthesis, Characterization, DFT, Contact Angle, Molecular Docking, and Antimicrobial Studies

Gehad G. Mohamed , Walaa H. Mahmoud, and Ahmed M. Refaat

Chemistry Department, Faculty of Science, Cairo University, Giza 12613, Egypt

Correspondence should be addressed to Gehad G. Mohamed; ggenidymohamed@sci.cu.edu.eg

Received 28 April 2020; Revised 17 June 2020; Accepted 26 June 2020; Published 23 October 2020

Guest Editor: Ningbo Gao

Copyright © 2020 Gehad G. Mohamed et al. This is an open access article distributed under the Creative Commons Attribution License, which permits unrestricted use, distribution, and reproduction in any medium, provided the original work is properly cited.

Metal complexes of the 2,2'-(1,3-phenylenebis(diazene-2,1-diyl))bis(4-aminobenzoic acid) diazo ligand (H_2L) derived from *m*-phenylenediamine and *p*-aminobenzoic acid were synthesized and characterized by different spectral, thermal, and analytical tools. The H_2L ligand reacted with the metal ions Cr(III), Mn(II), Fe(III), Co(II), Ni(II), Cu(II), Zn(II), and Cd(II) as 1:1 stoichiometry. All complexes displayed an octahedral geometry according to the electronic and magnetic moment measurements. The IR spectra revealed the binding of the azo ligand to the metal ions via two azo nitrogen atoms and protonated carboxylate O in a neutral tetradentate manner. Both IR and 1H NMR spectra documented the involvement of the carboxylate group without proton displacement. The thermal studies pointed out that the complexes had higher thermal stability comparable with that of the free ligand. SEM images revealed the presence of the diazo ligand and its Cd(II) complex in a nanostructure form. The contact angle measurements proved that the Cd(II) complex can be considered as a superhydrophobic material. The molecular and electronic structure of H_2L and $[Cd(H_2L)Cl_2] \cdot H_2O$ were optimized theoretically, and the quantum chemical parameters were calculated. The biological activities of the ligand, as well as its metal complexes, have been tested in vitro against some bacteria and fungi species. The results showed that all the tested compounds have significant biological activities with different sensitivity levels. The binding between H_2L and its Cd(II) complex with receptors of the crystal structure of *S. aureus* (PDB ID: 3Q8U), crystal structure of protein phosphatase (PPZ1) of *Candida albicans* (PDB ID: 5JPE), receptors of breast cancer mutant oxidoreductase (PDB ID: 3HB5), and crystal structure of *Escherichia coli* (PDB ID: 3T88) was predicted and given in detail using molecular docking.

1. Introduction

Azo compounds were highly colored compounds. They had widespread use as dyes and pigments in a variety of applications including fibers, coloring a large variety of leather, clothing, food, toys, medical devices, plastics, cosmetics, and dyeing of textile, as well as nonlinear and photo electronics, especially in optical information storage, biological medical studies, and advanced applications in organic synthesis [1–3]. In the development of metal complexes, the design and synthesis of a ligand was the most important step. They exhibited unique properties and novel reactivity due to electron-donor, electron-acceptor properties, structural,

functional groups, and the position of the ligand in the coordination sphere [4, 5]. Azo dyes with hydrophobic characters have wide applications especially when these dyes exhibit superhydrophobic characters. Some applications of water repellency include clothing that will be both breathable and water repellent, umbrellas that stayed completely dry, building materials, paints, epoxies, and silicones. Superhydrophobic paints and epoxies could greatly reduce the cost of transporting goods, also eliminate many of the effects of ice storms and aircraft icing. Low-permeability paint, used as a water and vapor barrier, is the standard way of protecting metal surfaces from corrosion. Superhydrophobic biomaterials are also being evaluated in more

demanding biological applications, such as the prevention of blood coagulation and drug delivery [6, 7].

New diazo ligand (H_2L) has the IUPAC name 2,2'-(1,3-phenylenebis(diazene-2,1-diyl))bis(4-aminobenzoic acid) (Scheme 1). This piece of work had devoted with the aim to synthesize Cr(III), Mn(II), Fe(III), Co(II), Ni(II), Cu(II), Zn(II), and Cd(II) complexes with the new diazo ligand and to examine their physical properties involving spectral behaviors and the electrical conductance values, and to determine the efficiency of the synthesized complexes against pathogenic bacteria. The molecular structure and molecular docking were also carried out in order to illustrate the way of bonding of the azo ligand and its complexes with receptors of the crystal structure of *S. aureus* (PDB ID: 3Q8U), crystal structure of protein phosphatase (PPZ1) of *Candida albicans* (PDB ID: 5JPE), receptors of breast cancer mutant oxidoreductase (PDB ID: 3HB5), and crystal structure of *Escherichia coli* (PDB ID: 3T88). In view of these findings, the contact angle measurements were performed to study the hydrophobic characters of the prepared compounds.

2. Experimental

2.1. Materials and Measurements

2.1.1. Materials and Reagents. The chemicals used were of highest purity available and pure grade. Most of them were used without further purification. *m*-Phenylenediamine (Sigma), *p*-aminobenzoic acid (VEB Berlin-Chemie), $CrCl_3 \cdot 6H_2O$ (Sigma), $MnCl_2 \cdot 2H_2O$ (Sigma), $NiCl_2 \cdot 6H_2O$ (BDH), $FeCl_3 \cdot 6H_2O$ (Sigma), $CoCl_2 \cdot 6H_2O$ (Aldrich), $CuCl_2 \cdot 2H_2O$ (Merck), $ZnCl_2$ (Strem Chemicals), and $CdCl_2$ (Aldrich) were used. Organic solvents were spectroscopic pure from BDH and included ethanol and *N,N*-dimethylformamide. Hydrochloric acid, sodium nitrite, and sodium acetate (AR) were used.

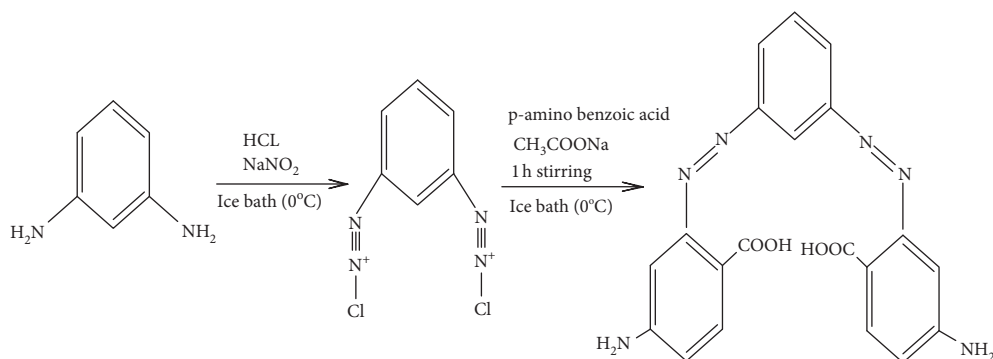
2.1.2. Solutions. 1×10^{-3} M stock solutions of complexes were prepared by dissolving the appropriate amount of the complexes in DMF. It was used for conductivity measurement. For UV-Vis spectra measurement, 1×10^{-4} or 1×10^{-5} M solutions of the diazo ligand and metal complexes were prepared by accurate dilution from the previously prepared stock solutions.

2.1.3. Measurements. Electronic and 1H NMR spectra were carried out at room temperature using Shimadzu 3101PC spectrophotometer and 300 MHz Varian-Oxford Mercury, respectively. For 1H NMR spectra, solution of $DMSO-d_6$ was used, and TMS was used as an internal standard. FT-IR spectra were recorded on a PerkinElmer 1650 spectrometer ($4000-400\text{ cm}^{-1}$) in KBr pellets. Electron spin resonance spectra were also recorded on the JES-FE2XG ESR spectrophotometer at Microanalytical Center, Tanta University. Microanalyses of carbon, hydrogen, and nitrogen were carried out at Microanalytical Center, Cairo University, Egypt, using CHNS-932 (LECO) Vario Elemental Analyzer. Analyses of the metals were conducted by dissolving the

solid complexes in concentrated HNO_3 and dissolving the residue in deionized water. The metal content was carried out using inductively coupled plasma atomic absorption spectrometry (ICP-AES), Egyptian Petroleum Research Institute. Mass spectra were recorded by the EI technique at 70 eV using the MS-5988 GS-MS Hewlett-Packard instrument at Microanalytical Center, National Center for Research, Egypt. The molar magnetic susceptibility was measured on powdered samples using the Faraday method. The diamagnetic corrections were made by Pascal's constant, and $Hg[Co(SCN)_4]$ was used as a calibrant. Molar conductivities of 10^{-3} M solutions of the solid complexes in DMF were measured using the Jenway 4010 conductivity meter. The thermogravimetric analyses (TG and DTG) of the solid complexes were carried out from room temperature to $800^\circ C$ using a Shimadzu TG-50H thermal analyzer. The X-ray powder diffraction analyses were carried out by using Philips Analytical X-ray BV, diffractometer-type PW 1840. Radiation was provided by the copper target (Cu anode 2000 W) high-intensity X-ray tube operated at 40 KV and 25 mA, and SEM (scanning electron microscopy) for these samples was performed at the Egyptian Mineral Resources Authority, using SEM Model Quanta 250 FEG (field emission gun) attached with an EDX unit (energy-dispersive X-ray analyses), with accelerating voltage 30 KV, magnification 14x up to 1,000,000 and resolution for Gun.1n. Contact angle was measured by the contact-angle Attension Theta model (version 2.7), Biolin Scientific company, Finland, Egyptian Nanotechnology Center (EGNC). The heavy phase was water, where the volume of drop was 4 mL, and the light phase was air. Divergence and the receiving slits were 1 and 0.2, respectively. The antimicrobial activities were carried out at Microanalytical Center, Cairo University, Egypt.

2.2. Synthesis of 2,2'-(1,3-Phenylenebis(diazene-2,1-diyl))bis(4-aminobenzoic Acid) (H_2L). *m*-Phenylenediamine (2 g/0.01 mol) was dissolved in 50 ml of ethanol, while 10 ml concentrated hydrochloric acid was diluted with about 60 g of crushed ice; then, dropwise addition of *m*-phenylenediamine solution to the crushed ice was carried out. To this cold solution, sodium nitrite (5 g/20 mL water) was added and stirred for about 1 h till dark reddish colored solution was obtained. The coupling agent *p*-aminobenzoic acid (5.6 g/0.02 mol) was dissolved in 50 ml of ethanol and then was added to the cold mixture. The resulting solution was stirred well, and sodium acetate (3 g) was added to neutralization. The solid product was removed by filtration, washed with hot ethanol followed by diethyl ether, and dried in a vacuum desiccator over anhydrous calcium chloride. Preparation of the (H_2L) ligand pathway is shown in Scheme 1.

Yield 90%; m.p. $> 300^\circ C$; reddish brown solid. Anal. Calcd for $C_{20}H_{16}N_6O_4$ (%): C, 59.20; H, 3.96; N, 20.70. Found (%): C, 58.74; H, 3.58; N, 20.17. IR (ν , cm^{-1}): 3433br (OH), 1603m (N=N), 1660m (C=O carboxylic), 1543s (COO_{asym}), 1384m (COO_{sym}). 1H NMR (300 MHz, $DMSO-d_6$, δ , ppm): 7.25–7.91 (m, 10H, Ar-H), 4.78 ppm (s, 4H,

SCHEME 1: Pathway of formation of the H₂L diazo ligand.

NH₂) and 10.12 ppm (s, 2H, COOH). UV-visible (λ_{\max} , nm): 375 ($\pi-\pi^*$), 271 ($n-\pi^*$).

2.3. Synthesis of Metal Complexes. H₂L ligand (0.45 g/1.11 mmol) was dissolved in the mixture of 30 ml DMF. Then, the metal chloride salts (1.11 mmol) were dissolved in 10 ml ethanol, and their hot solutions were added to the clear hot solution of the diazo ligand. The precipitated complexes were filtered and collected. They were washed with a little amount of ethanol and dried over vacuum. The route of synthesis is shown in Scheme 2.

2.3.1. [CrH₂LCl₂].2H₂O. Yield 92%; dark red; m.p. > 300°C. Anal. Calcd for Cr (C₂₀H₂₀Cl₃CrN₆O₆) (%): C, 40.61; H, 3.34; N, 14.03; Cl, 17.79; Cr, 8.23. Found (%): C, 40.85; H, 3.05; N, 14.23; Cl, 17.46; Cr, 8.68. IR (ν , cm⁻¹): 3423br (OH), 1610sh (N=N), 1655sh (C=O carboxylic), 1534m (COO_{asym}), 1402w (COO_{sym}), 537w (M-O), 426w (M-N). UV-visible (λ_{\max} , nm): 286 ($\pi-\pi^*$), 388 ($n-\pi^*$). Diffuse reflectance: 28,489, 24,780, and 13,449 cm⁻¹ for ⁴A_{2g}(F) → ⁴T_{2g}(F), ⁴A_{2g}(F) → ⁴T_{1g}(F), and ⁴A_{2g}(F) → ⁴T_{2g}(P).

2.3.2. [MnH₂LCl₂]. Yield 85%; pale green solid; m.p. > 300°C. Anal. Calcd for Mn (C₂₀H₁₆Cl₂MnN₆O₄) (%): C, 44.20; H, 3.00; N, 15.80; Cl, 13.30; Mn, 10.49. Found (%): C, 44.54; H, 3.20; N, 15.34; Cl, 12.86; Mn, 10.37. IR (ν , cm⁻¹): 3423br (OH), 1599m (N=N), 1655s (C=O carboxylic), 1553m (COO_{asym}), 1389s (COO_{sym}), 556w (M-O), 439w (M-N). UV-visible (λ_{\max} , nm): 269 ($\pi-\pi^*$), 374 ($n-\pi^*$). Diffuse reflectance: 26,645, 19,648, and 15,660 cm⁻¹ for ⁴T_{1g} → ⁶A_{1g}, ⁴T_{2g}(G) → ⁶A_{1g}, and ⁴T_{1g}(D) → ⁶A_{1g} transitions.

2.3.3. [FeH₂LCl₂].Cl.H₂O. Yield 93%; black solid; m.p. > 300°C. Anal. Calcd for Fe (C₂₀H₁₈Cl₃FeN₆O₅) (%): C, 41.02; H, 3.07; N, 14.63; Cl, 18.41; Fe, 9.32. Found (%): C, 41.27; H, 3.29; N, 14.35; Cl, 18.27; Fe, 9.57. IR (ν , cm⁻¹): 3442br (OH), 1600sh (N=N), 1563s (C=O carboxylic), 1555m (COO_{asym}), 1401s (COO_{sym}), 578w (M-O), 442w (M-N). UV-visible (λ_{\max} , nm): 271 ($\pi-\pi^*$), 363 ($n-\pi^*$).

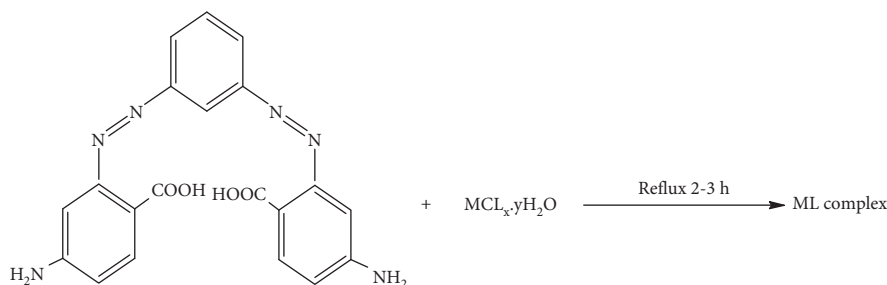
Diffuse reflectance: 21,490 and 20,890 cm⁻¹ for ⁶A_{1g} → T_{2g}(G), ⁶A_{1g} → ⁵T_{1g} and charge transfer, respectively.

2.3.4. [CoH₂LCl₂]. Yield 91%; brown solid; m.p. > 300°C. Anal. Calcd for Co (C₂₀H₁₆Cl₂CoN₆O₄) (%): C, 42.90; H, 2.99; N, 15.60; Cl, 13.20; Co, 11.53. Found (%): C, 43.12; H, 2.86; N, 15.11; Cl, 12.86; Co, 11.04. IR (ν , cm⁻¹): 3425br (OH), 1612sh (N=N), 1652s (C=O carboxylic), 1537m (COO_{asym}), 1384m (COO_{sym}), 553w (M-O), 431w (M-N). UV-visible (λ_{\max} , nm): 260 ($\pi-\pi^*$), 343 ($n-\pi^*$). Diffuse reflectance: 23,110, 15,240, and 12,845 cm⁻¹ for ⁴T_{1g}(F) → ⁴T_{2g}(F), ⁴T_{1g}(F) → ⁴A_{2g}(F), and ⁴T_{1g}(F) → ⁴T_{1g}(P) transitions.

2.3.5. [NiH₂LCl₂]. Yield 93%; dark brown solid; m.p. > 300°C. Anal. Calcd for Ni (C₂₀H₁₆Cl₂N₆NiO₄) (%): C, 43.90; H, 3.00; N, 15.71; Cl, 13.20; Ni, 11.45. Found (%): C, 43.51; H, 2.87; N, 15.22; Cl, 13.05; Ni, 11.04. IR (ν , cm⁻¹): 3420br (OH), 1611m (N=N), 1654s (C=O carboxylic), 1537m (COO_{asym}), 1391s (COO_{sym}), 541w (M-O), 432w (M-N). UV-visible (λ_{\max} , nm): 287 ($\pi-\pi^*$), 365 ($n-\pi^*$). Diffuse reflectance: 26,680, 14,757, and 13,122 cm⁻¹ for ligand-metal charge transfer (LMCT), ³A_{2g}(F) → ³T_{2g}(F), ³A_{2g}(F) → ³T_{1g}(F), and ³A_{2g}(F) → ³T_{1g} transitions.

2.3.6. [CuH₂LCl₂].3/2H₂O. Yield 91%; reddish brown solid; m.p. > 300°C. Anal. Calcd for Cu (C₂₀H₁₉Cl₂CuN₆O_{5.5}) (%): C, 42.56; H, 3.76; N, 14.36; Cl, 12.91; Cu, 11.56. Found (%): C, 42.47; H, 3.35; N, 14.85; Cl, 12.55; Cu, 11.31. IR (ν , cm⁻¹): 3450br (OH), 1614m (N=N), 1650s (C=O carboxylic), 1554w (COO_{asym}), 1392m (COO_{sym}), 561w (M-O), 445w (M-N). UV-visible (λ_{\max} , nm): 270 ($\pi-\pi^*$), 346 ($n-\pi^*$). Diffuse reflectance: 24 729 and 13 290 cm⁻¹ for ²B_{1g} → ²B_{2g}, ²B_{1g} → ²Eg and ²B_{1g} → ²A_{1g} transitions for LMCT.

2.3.7. [Zn(H₂L)Cl₂].H₂O. Yield 95%; reddish yellow solid; m.p. > 300°C. Anal. Calcd for Zn (C₂₀H₁₈Cl₂N₆O₅Zn) (%): C, 42.97; H, 3.22; N, 15.04; Cl, 12.71; Cu, 11.96. Found (%): C, 42.81; H, 3.07; N, 14.88; Cl, 12.54; Zn, 11.54. IR (ν , cm⁻¹): 3433br (OH), 1628m (N=N), 1656s (C=O carboxylic), 1551m (COO_{asym}), 1389s (COO_{sym}), 573w (M-O), 429w (M-N). ¹H NMR (300 MHz, DMSO-d₆, δ , ppm): 7.20–7.89



SCHEME 2: Synthesis of metal complexes of the diazo ligand (H_2L).

(m, 10H, Ar-H), 4.78 ppm (s, 4H, NH_2) and 10.40 ppm (s, 2H, COOH); UV-visible (λ_{max} , nm): 280 ($\pi-\pi^*$), 395 ($n-\pi^*$).

2.3.8. $[Cd(H_2L)Cl_2] \cdot H_2O$. Yield 94%; orange solid; m.p. $> 300^\circ C$. Anal. Calcd for $Cd(C_{20}H_{18}CdCl_2N_6O_5)$ (%): C, 39.67; H, 2.97; N, 13.88; Cl, 11.73; Cu, 18.57. Found (%): C, 39.56; H, 2.71; N, 13.68; Cl, 11.64; Cd, 18.13. IR (ν , cm^{-1}): 3450br (OH), 1618 m (N=N), 1656s (C=O carboxylic), 1538s (COO_{asym}), 1390m (COO_{sym}), 546w (M-O), 435w (M-N). 1H NMR (300 MHz, DMSO- d_6 , δ , ppm): 7.25–7.93 (m, 10H, Ar-H), 4.78 ppm (s, 4H, NH_2) and 10.38 ppm (s, 2H, COOH); UV-visible (λ_{max} , nm): 275($\pi-\pi^*$), 350 ($n-\pi^*$).

2.4. *Spectrophotometric Studies*. The absorption spectra were recorded for 1×10^{-4} M solutions of the free diazo ligand and its metal complexes dissolved in DMF. The spectra were scanned within the wavelength range from 200 to 700 nm.

2.5. Pharmacology

2.5.1. *Antimicrobial Activity*. The antimicrobial activity was carried out using the diffusion agar technique [7, 8]. LB agar media surfaces were inoculated with four investigated bacteria (Gram-positive bacteria: *Bacillus subtilis* and *Staphylococcus aureus*; Gram-negative bacteria: *Neisseria gonorrhoeae* and *Escherichia coli*) and one strain of fungi (*Candida albicans*) and then transferred to a saturated disk with a tested solution in the center of Petri dishes (agar plates). DMSO served as a control. All Petri dishes were incubated at $25^\circ C$ for 48 h where clear or inhibition zones were detected around each disk. Antibacterial activity was calculated [9, 10] by subtracting the diameter of the inhibition zone resulting with dimethylformamide from that obtained in each case. Amikacin and ketokonazole were used as reference compounds for antibacterial and antifungal activities, respectively. All experiments were performed as triplicate, and data plotted were the mean value.

2.6. *Computational Methodology*. The electronic structure calculations of H_2L and Zn(II) complex were carried out using the Gaussian09 suite of program [11]. They were fully optimized employing DFT-based B3LYP method along with the LANL2DZ basis set. In order to incorporate the effect of the solvent around the molecule, the TD-DFT method

(along with the LANL2DZ basis set) was used to calculate the electronic absorption spectra of the ligand and its Zn(II) complex. The contribution of the molecular orbital to HOMO and LUMO was also calculated.

2.7. *Molecular Docking*. Crystal structure of *S. aureus* (PDB ID: 3Q8U), crystal structure of protein phosphatase (PPZ1) of *Candida albicans* (PDB ID: 5JPE), receptors of breast cancer mutant oxidoreductase (PDB ID: 3HB5), and crystal structure of *Escherichia coli* (PDB ID: 3T88) were used in this study. Molecular docking studies were performed using MOE 2008 software [12] in order to find out the possible binding modes of the most active compounds against the above receptors. It is an interactive molecular graphics program for calculating and displaying feasible docking modes of a receptor and ligand and complex molecules. It necessitates the ligand and the receptor as the input in the PDB format. The amino acid chain was kept, and the water molecules and cocrystallized ligands were removed. The structure of complexes in the PDB file format was created by Gaussian03 software. Crystal structure of HSA (human serum albumin) (PDB ID: 5FUO), crystal structure of protein phosphatase (PPZ1) of *Candida albicans* (PDB ID: 5JPE), receptors of breast cancer mutant oxidoreductase (PDB ID: 3HB5), and crystal structure of *Escherichia coli* (PDB ID: 3T88) were downloaded from the Protein Data Bank (<http://www.rcsb.org/pdb>).

3. Results and Discussion

3.1. *Characterization of the Free Diazo Ligand (H_2L)*. The synthesized diazo ligand (H_2L) was soluble in DMF and DMSO solvents and of high melting point which indicated its stability. From the elemental analysis data of the ligand (Supplementary Table 1), it was found that the theoretical values were in agreement with the found values. The IR spectrum of the free diazo ligand was carried out in the range of $4000-400\text{ cm}^{-1}$, and the most effective bands are listed in Supplementary Table 2. The broad band observed at 3433 cm^{-1} can be attributed to the $\nu(O-H)$ stretching vibration. Also, band observed at 1660 cm^{-1} and sharp band at 1603 cm^{-1} can be attributed to C=O stretching vibration [13] and N=N [14], respectively. Also, the $\nu(COO)_{asym}$ and $\nu(COO)_{sym}$ stretching vibration bands were observed at 1543 and 1384 cm^{-1} , respectively.

^1H NMR spectrum of the free diazo ligand (H_2L) in $\text{DMSO-}d_6$ exhibited the following signals: 7.25–7.91 ppm (m, 10H, Ar-H) [13], 4.78 ppm (s, 4H, NH_2) [15–17], and 10.12 ppm (s, 2H, COOH). These signals indicated that three different types of protons were present in the diazo ligand. The position of NH_2 was confirmed from carrying out the spectra in the deuterated solvent.

The mass spectrum of the ligand (H_2L) showed an accurate parent molecular ion peak at m/z 404 amu, matched with the theoretical molecular weight. Also, the mass spectrum displayed multiple peaks corresponding to successive degradation of the ligand. The base peak appeared at m/z = 134 due to the $[\text{C}_7\text{H}_6\text{NO}_2]^+$ ion. The other fragments gave the peaks at 104, 132, 136, 164, 240, and 268 amu with various intensities.

3.2. Characterization of Metal Complexes

3.2.1. Elemental Analyses. The stoichiometry and formulation of the free diazo ligand (H_2L) and its metal complexes were confirmed by their elemental analysis (Supplementary Table 1). The metal:ligand ratio was found to be 1:1 in all complexes, which has been arrived by estimating the carbon, hydrogen, nitrogen, chloride, and metal contents of the complexes. The elemental analyses of the ligand and its complexes revealed good agreement with the proposed structures. The ligand and its metal complexes have high melting points, and they were found to be air-stable. The diazo ligand was soluble in common organic solvents, and all the complexes were freely soluble in DMF and DMSO but insoluble in methanol, ethanol, and water. The results of elemental analyses suggested formulae $[\text{M}(\text{H}_2\text{L})\text{Cl}_2] \cdot n\text{H}_2\text{O}$ ($\text{M} = \text{Co}(\text{II}), \text{Ni}(\text{II}), \text{Cu}(\text{II}), \text{Mn}(\text{II}), \text{Zn}(\text{II})$ and $\text{Cd}(\text{II})$) and $[\text{M}(\text{H}_2\text{L})\text{Cl}_2]\text{Cl} \cdot n\text{H}_2\text{O}$ ($\text{M} = \text{Cr}(\text{III})$ and $\text{Fe}(\text{III})$).

3.2.2. Molar Conductance. The results given in Supplementary Table 1 showed that the $\text{Cr}(\text{III})$ and $\text{Fe}(\text{III})$ complexes had molar conductivity values of 59 and $77 \Omega^{-1} \text{mol}^{-1} \text{cm}^2$, respectively. It is obvious from these data that these chelates were ionic in nature, and they were electrolytes [18], but the molar conductivity values of $\text{Mn}(\text{II}), \text{Co}(\text{II}), \text{Ni}(\text{II}), \text{Cu}(\text{II}), \text{Zn}(\text{II}),$ and $\text{Cd}(\text{II})$ chelates fall in the range of $11\text{--}31 \Omega^{-1} \text{mol}^{-1} \text{cm}^2$ indicative of their nonelectrolytic nature [14].

3.2.3. IR Spectral Studies. The infrared spectra of the H_2L ligand and its metal complexes taken in the region $4000\text{--}400 \text{ cm}^{-1}$ are listed in Supplementary Table 2 which gave the most useful assignments for bands diagnostic to the mode of coordination of the ligand. The band observed at 1603 cm^{-1} in the free diazo ligand (H_2L) was assigned to the $\nu(\text{N}=\text{N})$ stretching vibration. This band was found in the spectra of the complexes at $1610\text{--}1628 \text{ cm}^{-1}$. Also, another band observed at 1660 cm^{-1} assigned to carbonyl of carboxylate $\nu(\text{C}=\text{O})$ at the free diazo ligand (H_2L) was found in the spectra of the complexes at $1649\text{--}1656 \text{ cm}^{-1}$ (Supplementary Table 2). The shift in the azo groups of the diazo

ligand confirmed the participation of the azo group in chelation.

The broad band at 3433 cm^{-1} observed in the diazo ligand was shifted to $3423\text{--}3450 \text{ cm}^{-1}$, which was attributed to the $\nu(\text{O-H})$ stretching vibration. This shift can be attributed to the bond formation with metal ions and also the presence of hydrated water molecules. The broadening of this band may be attributed to the presence of the intramolecular hydrogen bond [19].

The $\nu_{\text{asym}}(\text{COO}^-)$ and $\nu_{\text{sym}}(\text{COO}^-)$ stretching vibrations were observed at 1543 and 1384 cm^{-1} , respectively, for the free diazo ligand (H_2L) [19–26]. Coordination with metal ions via the carboxylate O atom and nitrogen atom was indicated by the shift in the position of the $\nu_{\text{asym}}(\text{COO}^-)$ and $\nu_{\text{sym}}(\text{COO}^-)$ stretching vibration bands to $1534\text{--}1555$ and $1384\text{--}1402 \text{ cm}^{-1}$, respectively, for ligand-metal complexes.

New bands of low intensity were observed in the far-IR region in the range of $530\text{--}578$ and $427\text{--}445 \text{ cm}^{-1}$ which can be assigned to $\nu(\text{M-O})$ and $\nu(\text{M-N})$ stretching vibrations, respectively [20–28]. Therefore, from the IR spectral studies, it was concluded that the H_2L ligand behaved as a neutral tetradentate ligand with N coordination sites and protonated carboxylate oxygen upon coordinated to the metal ions [20–27].

3.2.4. ^1H NMR Spectral Studies. The ^1H NMR spectra of the diazo ligand and its $\text{Zn}(\text{II})$ complex were recorded in $\text{DMSO-}d_6$ solution using tetramethylsilane (TMS) as the internal standard. ^1H NMR spectrum of the ligand revealed the following signals at $\delta = 4.78$ (m, 4H, NH_2), $7.05\text{--}7.94$ (m, 10H, Ar-H), and 10.18 ppm (s, 2H, COOH). The shift in the carboxylic acid protons (10.40 ppm) indicated that oxygen of (COOH) groups was coordinated to the $\text{Zn}(\text{II})$ ion. However, the singlet signal of the amino group that appeared at $\delta 4.78$ ppm (s, 4H, NH_2) means that the two singlet signals assigned to the two NH_2 protons remained in their position as in the free diazo ligand (H_2L), confirming the remaining of these groups inert towards coordination. The upfield shift in the spectrum of the complex relative to the free ligand can be attributed to the effect of metal ions in chelation.

3.2.5. Mass Spectroscopy. The electronic mass spectrum of the $[\text{Zn}(\text{H}_2\text{L})\text{Cl}_2] \cdot \text{H}_2\text{O}$ complex confirmed formation of this complex by showing a molecular ion peak at $m/z = 540.81 \text{ g/mol}$ corresponding to $(\text{M-H}_2\text{O})$, which was very close to the expected molecular weight which was 540.50 g/mol , and it also showed a peak at $m/z = 403$ amu, respectively, corresponding to the ligand moiety. The intensities of these peaks showed the stability of the complex.

3.2.6. Spectrophotometric Studies. UV-visible spectral data of the ligand and its chelate (10^{-4} M) solutions in DMF were recorded from 200 to 700 nm at room temperature using the same solvent as blank. The free ligand (H_2L) exhibited broad bands in the UV-visible region at 375 and 271 nm . The first band was assigned to the intraligand $n \rightarrow \pi^*$ electronic

transition. The second broad band around 271 nm was assigned to the $\pi \rightarrow \pi^*$ electronic transition. The $n \rightarrow \pi^*$ and $\pi \rightarrow \pi^*$ transition bands were shifted to 339–395 and 261–285 nm, respectively, indicating that the ligand coordinated to metal ions [29, 30].

3.2.7. Magnetic Susceptibility and Electronic Spectral Studies.

A comparison of the electronic spectra of the free diazo ligand (H_2L) coordinated with those of the corresponding metal complexes was discussed. This can be considered as evidence for the complex formation. Additionally, the diffused reflectance spectra of metal complexes showed different bands at different wavelengths; each one was corresponding to a certain transition which suggested the geometry of the complexes. The diffused reflectance spectra of the complexes were dominated by intense intraligand charge-transfer bands.

The diffused reflectance spectrum of the Cr(III) complex exhibited three bands at 28,489, 24,780, and $13,449\text{ cm}^{-1}$ which may be assigned to the ${}^4A_{2g}(F) \rightarrow {}^4T_{2g}(F)$, ${}^4A_{2g}(F) \rightarrow {}^4T_{1g}(F)$, and ${}^4A_{2g}(F) \rightarrow {}^4T_{2g}(P)$ spin-allowed d–d transitions, respectively. The magnetic moment value was found to be 4.81 BM which indicated the presence of the Cr(III) complex in the octahedral geometry [31, 32].

The diffused reflectance spectrum of the Mn(II) complex showed three bands at 26,645, 19,490, and $15,660\text{ cm}^{-1}$ assignable to ${}^4T_{1g} \rightarrow {}^6A_{1g}$, ${}^4T_{2g}(G) \rightarrow {}^6A_{1g}$, and ${}^4T_{1g}(D) \rightarrow {}^6A_{1g}$ transitions, respectively [31]. The magnetic moment value was found to be 5.54 BM which indicated the presence of the Mn(II) complex in the octahedral structure.

From the diffused reflectance spectrum, it is observed that the Fe(III) chelate exhibited bands at 21,490 and $20,890\text{ cm}^{-1}$, which may be assigned to the ${}^6A_{1g} \rightarrow T_{2g}(G)$ and ${}^6A_{1g} \rightarrow {}^5T_{1g}$ transitions in the octahedral geometry of the complex [33]. The observed magnetic moment value of the Fe(III) complex was found to be 5.30 BM. The reflectance spectrum of the Co(II) complex displayed bands near 23,110, 15,240, and $12,845\text{ cm}^{-1}$, assigned to ${}^4T_{1g}(F) \rightarrow {}^4T_{2g}(F)$, ${}^4T_{1g}(F) \rightarrow {}^4A_{2g}(F)$, and ${}^4T_{1g}(F) \rightarrow {}^4T_{1g}(P)$ transitions, respectively. These bands suggested an octahedral geometry for the Co(II) complex. The magnetic moment value of the Co(II) complex was 5.16 BM which was consistent with the high-spin octahedral geometry.

The diffused reflectance spectrum of the Ni(II) complex showed absorption bands at 20,680, 14,757, and $13,120\text{ cm}^{-1}$ which are attributed to ${}^3A_{2g}(F) \rightarrow {}^3T_{2g}(F)$, ${}^3A_{2g}(F) \rightarrow {}^3T_{1g}(F)$, and ${}^3A_{2g}(F) \rightarrow {}^3T_{1g}$ transitions, respectively, and assignable to the octahedral geometry for the Ni(II) complex [34]. The magnetic moment value of the Ni(II) complex was 3.80 BM corresponding to the octahedral complex. The diffused reflectance spectrum of the Cu(II) complex exhibited broad bands in ranges 24,729 and $13,290\text{ cm}^{-1}$ assigned to ${}^2B_{1g} \rightarrow {}^2B_{2g}$, ${}^2B_{1g} \rightarrow {}^2E_g$ and ${}^2B_{1g} \rightarrow {}^2A_{1g}$ transitions, respectively. These bands suggested distorted octahedral geometry for the Cu(II) complex. The magnetic moment value was found to be 1.78 BM indicating octahedral geometry [35].

The Zn(II) and Cd(II) complexes were diamagnetic. According to the empirical formulae, an octahedral geometry was proposed for these chelates.

3.2.8. ESR Studies of the Cu(II)- H_2L Complex. The ESR spectrum of the Cu(II) complex was recorded in DMSO at 300 and 77 K (Figure 1). The observed order for the Cu(II) complex ($A_{\parallel} (197) > A_{\perp} (98.88)$; $g_{\parallel} (2.445) > g_{\perp} (2.333)$) indicated that the complex exerted an octahedral geometry [35–37]. The observed value of G for the Cu(II) complex ($G=1.421$) implied that the exchange coupling was not present, and misalignment was appreciable. The trend $g_{\parallel} > g_{\perp} > g_e (2.0023)$ showed that the unpaired electron was localized in the $d_{x^2-y^2}$ orbital of the Cu(II) ion in the complex [35–38]. The $g_{\text{iso}} (2.0023)$ value was less than 2.3 which indicated the covalent character of the metal-ligand bond, and the α^2 value (0.76) suggested the presence of in-plane covalency. The calculated value ($g_{\parallel}/A_{\parallel}$) 124 cm for the complex was consistent with the slightly distorted structure. The orbital reduction factors K_{\parallel} and K_{\perp} were estimated from the following expressions: $K_{\parallel} = (g_{\parallel} - 2.0023) \Delta E/8\lambda$ and $K_{\perp} = (g_{\perp} - 2.0023) \Delta E/2\lambda$, $\lambda = -828\text{ cm}^{-1}$ (spin-orbit coupling constant for the free ion), and $K_{\parallel} (0.718) > K_{\perp} (0.45)$ showed poor in-plane π bonding.

3.2.9. Powder X-Ray Diffraction and SEM. The XRD patterns indicated crystalline nature for the H_2L diazo ligand and the Cd(II) complex only. It can be easily seen that the pattern of the H_2L diazo ligand differed from its metal complexes, which may be attributed to the formation of a well-defined distorted crystalline structure. Probably, this behavior was due to the incorporation of water molecules into the coordination sphere. On comparing the XRD spectra of the chelates with the XRD spectra of the free ligand, it was concluded that all chelates under study can be considered to have amorphous structures as they lack sharp peaks except the Cd(II) complex where it had a crystalline structure. Therefore, the nonsimilarity of the XRD pattern between the metal ions and chelates suggested that these chelates had different phase structures than the free diazo ligand (H_2L). Such facts suggested that H_2L and the Cd(II) complex were crystalline, while its Cr(III), Mn(II), Fe(III), Co(II), Ni(II), Cu(II), and Zn(II) complexes were amorphous.

The average crystallite size (ξ) can be calculated from the XRD pattern according to the Debye–Scherrer equation [39, 40]:

$$\xi = \frac{K\lambda}{\beta_{1/2} \cos \theta} \quad (1)$$

The equation uses the reference peak width at angle θ , where λ is the wavelength of the X-ray radiation (1.541874 \AA), K is a constant taken as 0.95 for organic compounds [37], and $\beta_{1/2}$ is the width at half maximum of the reference diffraction peak measured in radians. The dislocation density, δ , is the number of dislocation lines per

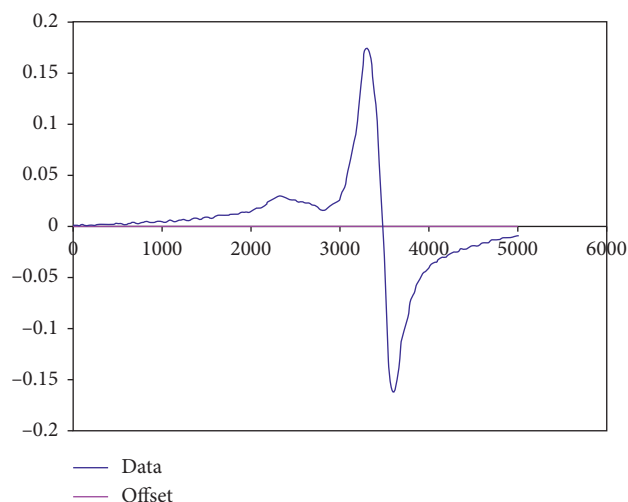


FIGURE 1: ESR spectrum of the $[\text{Cu}(\text{H}_2\text{L})\text{Cl}_2] \cdot 3/2\text{H}_2\text{O}$ complex

unit area of the crystal. The value of δ is related to the average particle diameter (ξ) by the following relation [41, 42]:

$$\delta = \frac{1}{\xi^2}. \quad (2)$$

The value of δ was calculated and found to be 33.78 and 26.77 nm, and the value of δ was 8.76×10^{-4} and $1.39 \times 10^{-3} \text{ nm}^{-2}$ for H_2L and $\text{Cd}(\text{II})$ complex, respectively, giving evidence for the formation of the free azo ligand and its cadmium(II) complex in a nanosize.

The SEM micrographs of H_2L and its $\text{Cd}(\text{II})$ are given in Figure 2. There is a significant difference in the morphological structures, and the particle size is in the nanometer range. The particle size of the ligand was 64–67 nm, while the $\text{Cd}(\text{II})$ complex was 20–32 nm.

3.2.10. Contact Angle. For two centuries or more of research, wetting phenomena still remain popular topics of investigations. Young's static and dynamic contact angle equations [6, 7] are the most common and relevant parameters describing the wetting property of a surface with respect to liquid water:

$$\cos \theta_Y = \left(\frac{\sigma_{sv} - \sigma_{sl}}{\sigma_{lv}} \right), \quad (3)$$

where θ_Y = Young's contact angle, σ_{sv} = surface tension (energy per unit surface) of the solid-vapor interface, σ_{sl} = surface tension of the solid-liquid interface, and σ_{lv} = surface tension of the liquid-vapor interface.

The mean contact angles were measured for H_2L and its metal complexes (Supplementary Figure 3). The data listed in Table 1 proved that the diazo ligand and all the complexes are hydrophobic, and the $\text{Cd}(\text{II})$ complex can be considered as a superhydrophobic material. Superhydrophobic surfaces are actively studied across a wide range of applications and industries and are now finding increased use in the biomedical areas. A partial list includes clothing that will be both breathable and water repellant, umbrellas that stayed

completely dry, building materials, paints, epoxies, goods transport, and anticorrosion. Superhydrophobic materials such as this promising nano- $\text{Cd}(\text{II})$ complex exhibit a number of unique properties that arise from the high roughness of a low surface energy material that stabilizes a nonwetted state [6, 7].

3.2.11. Thermal Analyses. Thermogravimetric analyses of the metal complexes under investigation were used to get information about the thermal stability of these new complexes, to decide whether the water molecules (if present) were inside or outside the inner coordination sphere of the central metal ion, and to suggest a general scheme for thermal decomposition of these chelates. In the present investigation, heating rates were suitably controlled at $10^\circ\text{C min}^{-1}$ under nitrogen atmosphere, and the weight loss was measured from the ambient temperature up to $\sim 1000^\circ\text{C}$. The TG curves of the complexes are listed in Table 2. The weight losses for each chelate were calculated within the corresponding temperature ranges.

The thermal decomposition process of H_2L involved three decomposition steps. Decomposition of H_2L started at 30°C and finished at 100°C with three stages. The first stage of decomposition involved the removal of four molecules of NH_3 and two molecules of carbon dioxide gas in the 30 – 355°C temperature range and was accompanied by a weight loss of 36.53% (calcd. = 36.41%). The second and third stages of decomposition occurred in the 355 – 1000°C temperature range, corresponding to the loss of the $\text{C}_{18}\text{H}_4\text{N}_2$ molecule and were accompanied by a weight loss of 62.76% (calcd. = 62.59%).

Decomposition of the $[\text{Cr}(\text{H}_2\text{L})\text{Cl}_2]\text{Cl} \cdot 2\text{H}_2\text{O}$ complex started at 45°C and finished at 1000°C with four stages at four maxima at 79, 210, 377, and 865°C and was accompanied by a weight loss of 80.29%, corresponding to the loss of $2\text{H}_2\text{O}$, $3/2\text{Cl}_2$, 2N_2 , CH_4 , and $\text{C}_{17}\text{H}_{12}\text{NO}_{2.5}$ molecules which was very close to the calculated value of 81.53%.

Thermogravimetric curve for the $[\text{Mn}(\text{H}_2\text{L})\text{Cl}_2]$ complex showed two weight loss events. The first step of decomposition occurred within the range of 30 – 435°C , with a maximum temperature at 234°C , and it corresponds to the loss of Cl_2 , 2N_2 gases and $\text{C}_9\text{H}_5\text{N}_2$ molecules. The second step of decomposition occurred in the range of 435 – 1000°C with the maximum temperature at 595°C . There were significant mass loss events due to the decomposition of the $\text{C}_4\text{H}_{11}\text{O}_3$ molecule (Table 2).

The thermal decomposition of the $[\text{Fe}(\text{H}_2\text{L})\text{Cl}_2]\text{Cl} \cdot \text{H}_2\text{O}$ complex proceeded via five degradation steps. The first step of decomposition occurred within the temperature range from 45 to 100°C , with a maximum temperature at 75°C , and it corresponds to the loss of one water molecule of hydration. The second step of decomposition occurred in the range of 100 – 355°C , with one maxima at 244°C , and corresponds to the elimination of $3/2\text{Cl}_2$, 3N_2 , 3CH_4 , and CO_2 with a mass loss of 47.89% (calcd. = 48.33%). The last three steps of decomposition occurred within the temperature range of 355 – 1000°C with three maxima at 485, 565, and 803°C and were simultaneously decomposed to ferric oxide

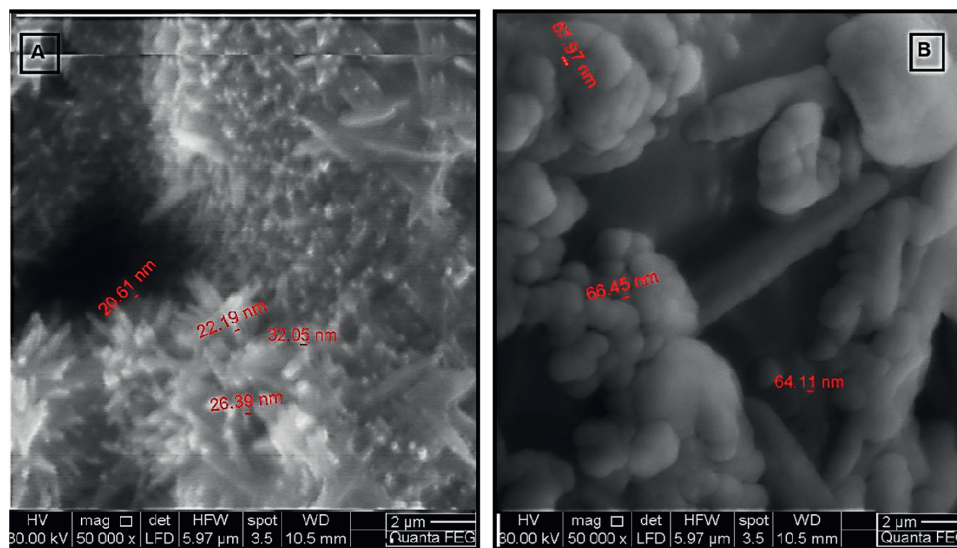


FIGURE 2: The SEM micrographs of (a) Cd(II)-H₂L and (b) H₂L.

TABLE 1: The mean contact angle of H₂L and its complexes.

Compound	Mean contact angle (°)	Wettability classification	Surface morphology
[Cr(H ₂ L)Cl ₂].Cl.2H ₂ O	137	Hydrophobic	Rough and porous
[Mn(H ₂ L)Cl ₂]	128	Hydrophobic	Rough and porous
[Fe(H ₂ L)Cl ₂].Cl.H ₂ O	142	Hydrophobic	Rough and porous
[Co(H ₂ L)Cl ₂]	123	Hydrophobic	Rough and porous
[Ni(H ₂ L)Cl ₂]	132	Hydrophobic	Rough and porous
[Cu(H ₂ L)Cl ₂].3/2H ₂ O	133	Hydrophobic	Rough and porous
[Zn(H ₂ L)Cl ₂].H ₂ O	128	Hydrophobic	Rough and porous
[Cd(H ₂ L)Cl ₂].H ₂ O	153	Superhydrophobic	Very rough and very porous
H ₂ L azo dye ligand	103	Hydrophobic	Rough and porous

TABLE 2: Thermoanalytical results (TG and DTG) of the H₂L ligand and its metal complexes.

Complex	TG range (°C)	DTG max	n*	Mass loss estim (calcd)% (total mass loss)	Assignment	Residues
Diazo ligand (H ₂ L)	30–355	216	1	36.53 (38.61)	Loss of 4NH ₃ and 2CO ₂	—
	355–1000	476,602	2	61.76 (61.38) 100.0 (99.90)	Loss of C ₁₈ H ₁₄ N ₂	—
[Cr(H ₂ L)Cl ₂].Cl.2H ₂ O	45–115	79	1	8.88 (8.53)	Loss of 2H ₂ O and NH ₃	1/2 Cr ₂ O ₃
	115–310	210	1	30.00 (29.90)	Loss of 3/2Cl ₂ , 2N ₂ , and CH ₄	
[Mn(H ₂ L)Cl ₂]	310–990	377,865	2	41.30 (43.10) 80.18 (81.53)	Loss of C ₁₇ H ₁₂ NO _{2.5}	7C + MnO
	30–435	234	1	58.98 (58.86)	Loss of 2N ₂ , Cl ₂ , and C ₉ H ₅ N ₂	
[Fe(H ₂ L)Cl ₂].Cl.H ₂ O	435–1000	592	1	20.88 (20.18) 79.66 (79.04)	Loss of C ₄ H ₁₁ O ₃	5C + 1/2Fe ₂ O ₃
	45–100	75	1	3.29 (3.07)	Loss of H ₂ O	
[Co(H ₂ L)Cl ₂]	100–355	244	1	47.89 (48.33)	Loss of 3/2Cl ₂ , 3N ₂ , 3CH ₄ , and CO ₂	2C + CoO
	355–1000	485,565,803	3	25.37 (24.63) 76.62 (76.03)	Loss of C ₁₁ H ₄ O _{0.5}	
[Ni(H ₂ L)Cl ₂]	30–260	177	1	12.23 (12.45)	Loss of 2NH ₃ and 1/2Cl ₂	8C + NiO
	260–475	364	1	6.33 (6.64)	Loss of 1/2 Cl ₂	
[Cu(H ₂ L)Cl ₂].3/2H ₂ O	475–890	640	1	60.3 (60.03) 78.91 (79.09)	Loss of C ₁₈ H ₁₃ N ₅ O	2C + CuO
	40–290	199	1	31.24 (31.27)	Loss of 4NH ₃ , N ₂ , and Cl ₂	
[Zn(H ₂ L)Cl ₂].H ₂ O	290–970	395,883	2	35.57 (36.70) 67.85 (67.95)	Loss of C ₁₂ H ₄ O ₃	3C + ZnO
	45–145	88	1	4.71 (4.77)	Loss of 3/2H ₂ O	
[Cd(H ₂ L)Cl ₂].H ₂ O	145–990	287	1	77.67 (76.92) 82.38 (81.70)	Loss of C ₁₈ H ₁₆ Cl ₂ N ₆ O ₃	CdO
	45–130	86	1	5.42 (5.72)	Loss of H ₂ O and 1/2N ₂	
[Cr(H ₂ L)Cl ₂].Cl.2H ₂ O	130–270	205	1	10.36 (10.26)	Loss of 2N ₂	CdO
	270–1000	348,467	2	63.4 (63.20) 79.17 (79.18)	Loss of C ₁₇ H ₁₆ Cl ₂ NO ₃	
[Ni(H ₂ L)Cl ₂]	40–130	98	1	2.95 (2.90)	Loss of H ₂ O	CdO
	130–355	222	1	25.63 (25.62)	Loss of 3N ₂ and Cl ₂	
[Cd(H ₂ L)Cl ₂].H ₂ O	355–1000	414,591,833	3	50.15 (50.25) 78.73 (78.77)	Loss of C ₂₀ H ₁₆ O ₃	

n* = number of decomposition steps.

contaminated with carbon as a final product. They were accompanied by a weight loss of 25.37% (calcd. = 24.63%) and corresponded to the loss of the $C_{11}H_4O_{0.5}$ molecule. The actual weight loss from these five steps was 76.62% which was close to the calculated value of 76.03%.

The thermal degradation of the $[Co(H_2L)Cl_2]$ complex took place in three degradation stages within the temperature range from 30 to 990°C. The first stage of decomposition occurred at maximum 177°C and was accompanied by a weight loss of 12.23% (calcd. = 12.45%) corresponding to the loss of 2NH₃ and 1/2Cl₂ gases. The second and third steps of decomposition occurred at two maxima 364 and 640°C and were accompanied by a weight loss of 6.33% (calcd. = 6.64%) and 60.30% (calcd. = 60.03%), respectively, corresponding to the loss of 1/2Cl₂ gas and C₁₈H₃N₅O molecule giving CoO contaminated with carbon as a final product. Theoretically, the weight loss in these steps was 78.91% which agrees with the experimental value of 79.09%.

The $[Ni(H_2L)Cl_2]$ complex lost upon heating 4NH₃, Cl₂, and N₂ gases in the first step of decomposition within the temperature range of 40–290°C. The last two steps of decomposition occurred at two maxima at 395 and 880°C. These steps were associated with the loss of the C₁₂H₄O₃ molecule forming NiO contaminated with carbon as a final product. The actual total weight loss of 67.85% was in agreement with the calculated total weight loss value of 67.95%.

The complex $[Cu(H_2L)Cl_2] \cdot 3/2H_2O$ lost upon heating all water molecules at one maxima 90°C with an estimated weight loss of 4.70% (calcd. = 4.77%). The dehydrated Cu(II) complex was simultaneously decomposed to CuO and 2C at the 287°C maximum temperature. The total weight loss amounted to 82.38% (calcd. = 81.74%).

The $[Zn(H_2L)Cl_2] \cdot H_2O$ complex was thermally decomposed into four steps within the temperature range from 45 to 1000°C. The first decomposition step with an estimated mass loss of 5.42% (calcd. = 5.72%) occurred within the temperature range from 45 to 130°C. This step may be attributed to the liberation of the hydrated water molecules and NH₃ gas. The remaining three decomposition steps of the Zn(II) complex were observed within the temperature range from 130 to 1000°C. Estimated mass losses of 73.76% (calcd. = 74.42%) were reasonably accounted for the removal of two 2N₂ gases and a C₁₇H₁₆Cl₂NO₃ molecule in two steps.

TG curve of the $[Cd(H_2L)Cl_2] \cdot H_2O$ complex displayed a five-step decomposition. The first step of decomposition occurred within the temperature range from 40 to 130°C, with a maximum temperature at 98 °C, and corresponded to the loss of one water molecule of hydration. The second step of decomposition occurred in the range of 130–355 °C, with one maxima at 222°C, and corresponded to the elimination of Cl₂ and 3N₂ gases with a mass loss of 25.62% (calcd. = 25.63%). The last three steps of decomposition occurred within the temperature range of 355–1000°C with three maxima at 414, 591, and 833°C and were simultaneously decomposed to CdO as a final product. They were accompanied by a weight loss of 50.25% (calcd. = 50.15%) corresponding to the loss of the C₂₀H₁₆O₃ molecule. The weight loss from these five steps was 78.77% which was close to the calculated value of 78.73%.

3.3. Geometry Optimization. The geometric parameters (bond lengths and bond angles) of the optimized structures of the H₂L azo ligand and its Cd(II) complex (Figure 3) are listed in Supplementary Table 5. From the analysis of these data, the following remarks were found:

- (1) There was an elongation in the coordination bonds after complexation, and a large variation in N(11)-N(14), N(12)-N(13), O(35)-H(40), and O(38)-H(39) bond lengths of the ligand occurred upon complexation. It became slightly longer confirming that the coordination took place via azo N atoms and protonated O groups.
- (2) All the active groups taking part in coordination have bonds longer than those already existed in the ligands (for example, N=N).
- (3) The bond angles of the free ligand moiety were altered somewhat upon coordination; also, the bond angles surrounding the central cadmium atom in the complex lie in the range reported for octahedral geometry [43].
- (4) The decrease in the metal-chloride angles may be attributed to the intramolecular hydrogen bond [43].

3.4. Molecular Electrostatic Potential (MEP). The MEP is a plot of electrostatic potential mapped onto the constant electron density surface. It is also very useful in the research of the molecular structure with its physiochemical property relationship. It is also can be used to understand the molecular interactions and predict the reactive sites for electrophilic and nucleophilic attacks [43]. The MEP is directly related to chemical reactivity. Red color represented the regions of negative electrostatic potential. The negative regions are related to electrophilic reactivity. However, the electron-poor region has blue color (favor site for the nucleophilic attack) [43, 44], but the region with green color points to the neutral electrostatic potential region. Figure 4 represents 3D plots of the MEP for the parent ligand and its Cd(II) complex. It was found that oxygen and nitrogen atoms of free H₂L were surrounded by a greater negative charge surface, making these sites potentially more favorable for the electrophilic attack (Figure 4(a)), where a greater negative charge was surrounded to the metal center (Figure 4(b)) confirming the complexation process.

3.5. Mulliken Charges. Supplementary Table 6 and Supplementary Figure 6 clarify Mulliken atomic charges for some important atoms. The calculated charge value for N13 and N14 is -0.08 and -0.007 a.u., respectively, in contrast to the expected one (-1 a.u.), which indicated electron transfer from these atoms to the metal center. Furthermore, decrease of oxygen and chlorine formal charge from the expected values is a reason for migration of electrons to the cadmium center in order to forming the complex. Finally, this charge transfer from donor atoms to the metal center causes the calculated value to decrease to -0.756 a.u. against the formal charge of +2 for the cadmium atom [43, 44].

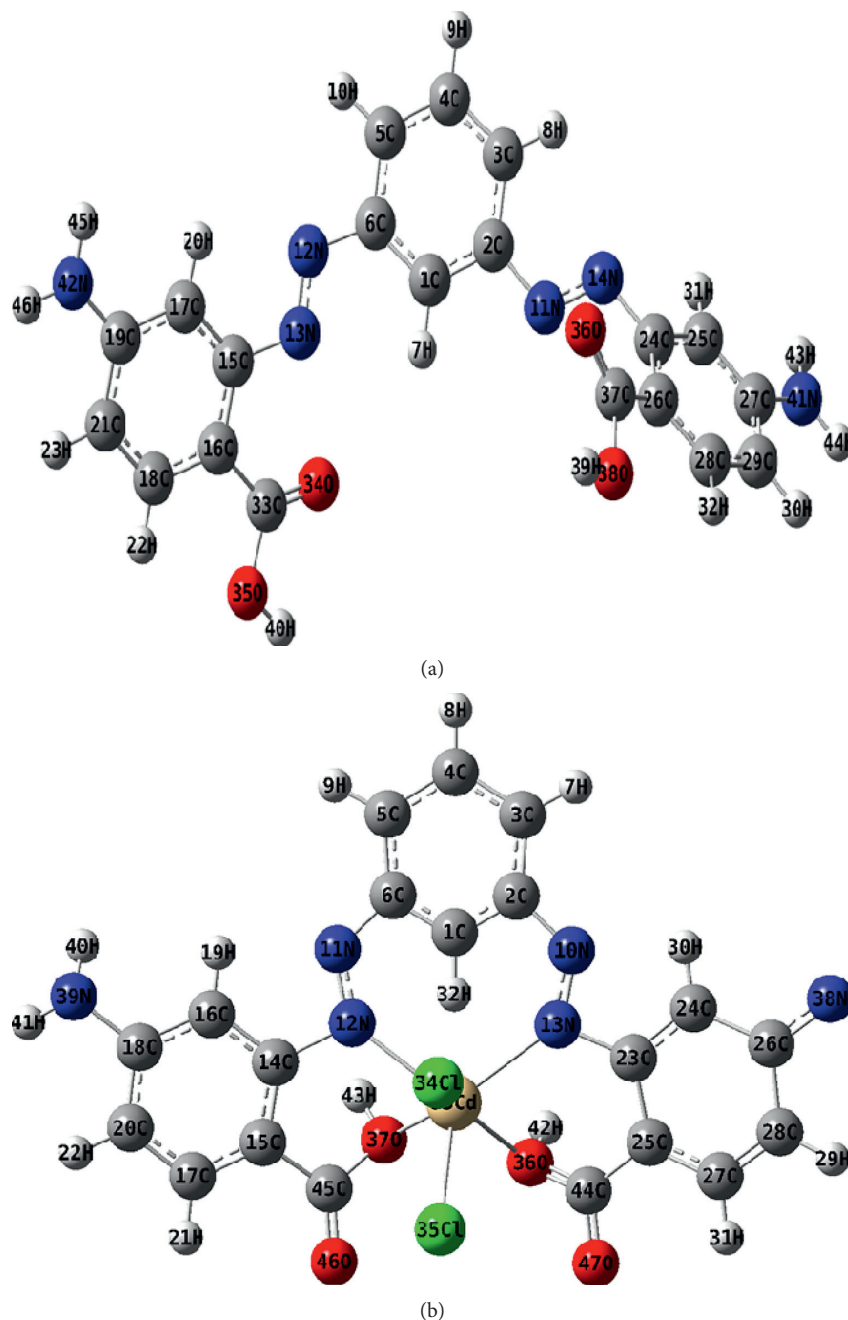


FIGURE 3: The optimized structure of (a) H_2L and (b) $[Cd(H_2L)Cl_2] \cdot H_2O$.

3.6. Molecular Parameters. Figure 5 shows the molecular orbital representation of the H_2L ligand and its Cd(II) complex along with their HOMO, LUMO energies and energy band gaps. Both the highest occupied molecular orbital (HOMO) and lowest unoccupied molecular orbital (LUMO) were the main orbitals that participate in chemical stability [11, 44, 45]. The HOMO represented the ability to donate an electron; LUMO as an electron acceptor represents the ability to obtain an electron. In other words, the energy of the HOMO is directly related to the ionization potential; LUMO energy is directly related to the electron affinity. Hence, these frontier energies play an important role

in the electric and optical properties. The energy gap between the HOMO and LUMO energies is a critical parameter in determining molecular electrical transport properties due to providing measurement of electron conductivity. In addition, this energy gap characterizes the molecular stability and spectroscopic properties of the molecular systems. The smaller energy gap describes a chemically soft molecule which can be easily polarizable. The HOMO-LUMO energy gap has proved to be an important tool in determining the kinetic stability and chemical reactivity of a molecule. The lower energy gap is a suitable condition where a molecule can be excited easily, whereas a

higher energy gap leads to higher kinetic stability but lower chemical reactivity of the molecule. The difference between the energy gap for the ligand reflects the presence of the complexation status. The increase in the global electrophilicity value attributed to the highest capacity of accepted electrons, so the ligand has a highly powerful donation ability. The calculation of both absolute hardness (η) and absolute softness (σ) parameters is useful to recognize the molecular stability and reactivity. The calculations of the binding energy indicated that the increase of the value of the calculated binding energy of the complex compared to that of the free ligand indicated that the stability of the formed Cd(II) complex was higher than that of the free diazo ligand.

Additional parameters such as chemical potentials P_i , global electrophilicity ω , global softness S , electrophilicity index (χ), and additional electronic charge ΔN_{\max} were calculated for the free H_2L ligand and the Cd- H_2L complex (Table 3). The high ω value of both free H_2L and Cd(II) complex suggested a great chance and priority for biological activity which is further confirmed by the experimental data.

The mentioned quantum chemical parameters were calculated with the help of the following equations [43, 44]:

$$\begin{aligned} \Delta E &= E_{\text{LUMO}} - E_{\text{HOMO}}, \\ \chi &= \frac{-(E_{\text{HOMO}} + E_{\text{LUMO}})}{2}, \\ \eta &= \frac{E_{\text{LUMO}} - E_{\text{HOMO}}}{2}, \\ \sigma &= \frac{1}{\eta}, \\ P_i &= -\chi, \\ S &= \frac{1}{2\eta}, \\ \omega &= \frac{P_i^2}{2\eta}, \\ \Delta N_{\max} &= \frac{P_i}{\eta}. \end{aligned} \quad (4)$$

3.7. Vibrational Properties. In order to acquire the spectroscopic signature of the diazo ligand and its complexes, a frequency calculation analysis was performed. Vibrational properties had been investigated to determine vibrational modes connected with the molecular structure of the cadmium (II) complex using FT-IR spectra based on the optimized geometry. It is well known that the vibrational frequencies computed at quantum chemical methods such as DFT levels contain well-known systematic errors. The scaling factor of 0.96 for the LanL2DZ level was used to correct the effects of anharmonicity and neglected part of electron correlation [11, 44, 45]. The theoretical and the experimental spectra are shown in Supplementary Figure 8.

It is also noteworthy that experimental results belong to the solid phase, while theoretical calculations belong to a gas phase.

The stretching vibration of a free or nonhydrogen-bonded OH group of H_2L appears at 3664 cm^{-1} [11, 45]. $\nu(\text{COO}^-)_{\text{asy}}$ and $\nu(\text{COO}^-)_{\text{sy}}$ stretching of the free ligand appeared at 1597 cm^{-1} and 1392 cm^{-1} , respectively. The theoretical spectrum of the free azo ligand showed νNH_2 and $\nu\text{N}=\text{N}$ modes at 3637 and 1694 cm^{-1} , respectively. In the Cd(II) complex, the chelating ring occurred by means of the ligand bonding to the cadmium (II) ion with a tetradentate N,O chelated mode. It was observed from Figures 6 that the wavenumber interval between the $\nu(\text{COO}^-)_{\text{asy}}$ and $\nu(\text{COO}^-)_{\text{sy}}$ stretching modes is an effective indicator of forming complexation. The wavenumber value of $\nu\text{N}=\text{N}$ for the complex was lower than free H_2L which was an indicator of the coordination through the nitrogen atom. The spectrum of the Cd(II) complex showed νNH_2 at a wave number very close to free H_2L at 3639 cm^{-1} confirming that this group did not participate in the complex formation process. $\nu\text{M}-\text{O}$, $\nu\text{M}-\text{N}$, and $\nu\text{M}-\text{Cl}$ modes of the Cd(II) complex were found at 564 , 487 , and 326 cm^{-1} , respectively. The calculated and experimental data were very close to each other (Supplementary Figure 8).

3.8. Structural Interpretation of Metal Complexes. The structures of the complexes of the H_2L diazo ligand with Cr(III), Mn(II), Fe(III), Co(II), Ni(II), Cu(II), Zn(II), and Cd(II) ions were confirmed by the elemental analyses, IR, molar conductance, magnetic, mass, solid reflectance, and thermal analysis data. Therefore, from the IR spectra, it was concluded that H_2L behaved as a neutral tetradentate ligand coordinated to the metal ions via two nitrogen atoms of azo groups (N=N) and two oxygen atoms of protonated carboxylate groups (COO). From the molar conductance data, it was found that the complexes were electrolytes. On the basis of the above observations and from the magnetic and solid reflectance measurements, octahedral geometry was suggested for the investigated complexes (Figure 6).

3.9. Antimicrobial Activity of Metal Complexes

3.9.1. Antifungal Activities. The preliminary fungi toxicity screening of the H_2L diazo ligand and complexes was performed against *Candida albicans* in vitro by the diffusion technique [46]. H_2L free ligand and Cr(III), Mn(II), and Fe(III) complexes showed no fungal growth inhibition, but Co(II), Ni(II), Cu(II), Zn(II), and Cd(II) complexes showed fungal growth inhibition at different rates (Figure 7). The Cd(II) and Ni(II) complexes in this study were nearly two times more active than the ketokonazole standard against the *Candida albicans* microorganism used (Table 4).

3.9.2. Antibacterial Activities. The antibacterial activities of the H_2L diazo ligand and its complexes against *Bacillus subtilis*, *Staphylococcus aureus*, *Neisseria gonorrhoeae*, and *Escherichia*

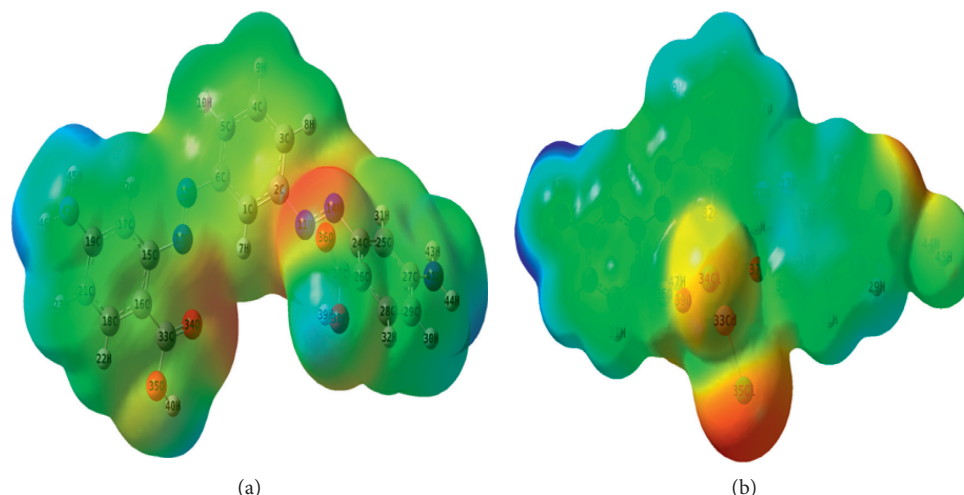


FIGURE 4: Molecular electrostatic potential map of (a) H_2L and (b) $[Cd(H_2L)Cl_2].H_2O$. The electron density isosurface is 0.004 a.u.

Compound	HOMO	LUMO	HOMO-LUMO energy gap (hartree)
H_2L			0.123116
$Cd-H_2L$			0.05565

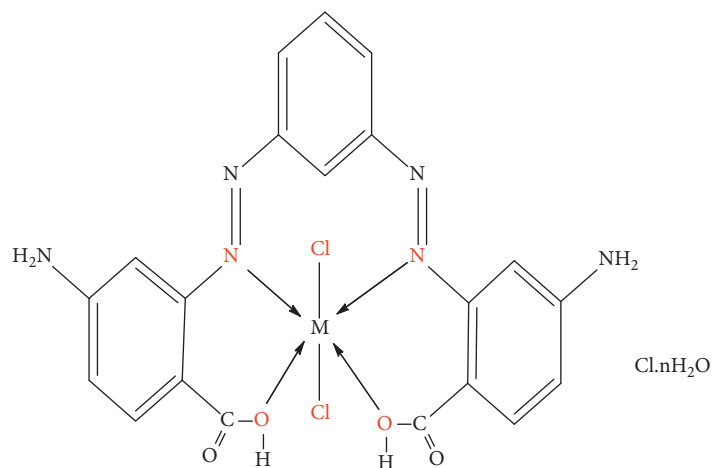
FIGURE 5: Surface phase of frontier orbitals of H_2L and $[Cd(H_2L)Cl_2].H_2O$.

coli are presented in Table 4. The H_2L ligand was found to have no activity at all towards both different types of bacteria (Gram-positive *Bacillus subtilis* and *Staphylococcus aureus* and Gram-negative *Neisseria gonorrhoeae* and *Escherichia coli*). This can be attributed to their very versatile nutritional capability, adaptability to various hydrocarbon rings, and the possession of the pump mechanism which ejects metal complexes as soon as they enter the cell [47]. In addition, *Bacillus subtilis*, *Staphylococcus aureus*, *Neisseria gonorrhoeae*, and *Escherichia coli* were sensitive to all the complexes, and an inhibitory zone was obtained in the range of 9.0–23.0 mm (Figure 7).

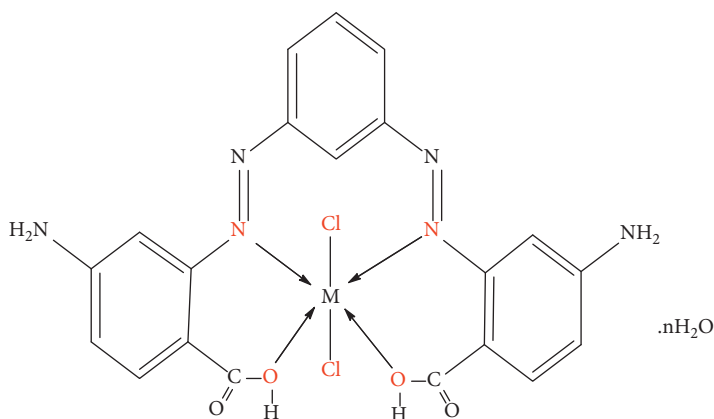
In all cases, the metal complexes were found to be more active than the H_2L ligand expectedly due to chelation, which reduced the polarity of the metal atom, mainly

TABLE 3: The calculated quantum chemical parameters of H_2L and its Cd(II) complex.

The quantum parameter	H_2L	$[Cd(H_2L)Cl_2].H_2O$
E (a.u.)	-1402.46	-140.88
Dipole moment (Debye)	1.37	18.022
E_{HOMO} (eV)	-6.095	-5.61
E_{LUMO} (eV)	-2.977	-4.096
ΔE (eV)	3.349	1.508
χ (eV)	4.534	4.853
η (eV)	1.559	0.757
σ (eV) ⁻¹	0.641	1.321
Pi (eV)	-4.534	-4.853
S (eV) ⁻¹	0.321	0.661
ω (eV)	6.593	15.559
ΔN_{max}	2.9	6.412



In case of Cr(III) and Fe(III) complexes (where $n = 2$ for Cr(III) complex and $n = 1$ for Fe(III) complex)



In case of Mn(II), Co(II), Ni(II), Cu(II), Zn(II) and Cd(II) complexes (where $n = 1$ for Cd(II) and Zn(II) complexes, $n = 1.5$ for Cu(II) complex and $n = 0$ for Mn(II), Co(II), and Ni(II))

FIGURE 6: The proposed structures of H_2L and its complexes.

because of partial sharing of its positive charge with donor groups of the ligand and possible π -electron delocalization on the aromatic rings. This increased the lipophilic character, favouring its permeation into the bacterial membrane, causing the death of the organisms [48].

Higher activity of the metal complex was probably due to greater lipophilic nature of the complex. It increased the activity of the metal complex and can be explained on the basis of Overton's concept and Tweedy's chelation theory [49–52]. According to Overton's concept of cell permeability, the lipid membrane that surrounds the cell favours the passage of only lipid-soluble materials due to which liposolubility was considered to be an important factor that controls the antimicrobial activity. On chelation, the polarity of the metal ion will be reduced to a greater extent due to the overlap of the ligand orbital and partial sharing of the positive charge of the metal ion with donor groups [53, 54]. Furthermore, it increased the delocalization of the π electrons over the whole chelate ring and enhanced the lipophilicity of the complex. This increased lipophilicity enhanced the penetration of the complexes into the lipid membrane and thus blocked the metal-binding sites on enzymes of microorganisms [55]. These metal complexes

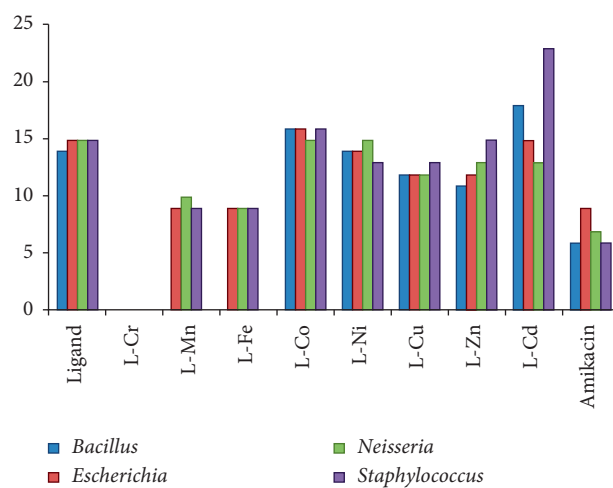


FIGURE 7: Biological activity of H_2L and its complexes.

also disturb the respiration process of the cell and thus block the synthesis of proteins, which restricts further growth of the organism [56].

TABLE 4: Biological activity of the H₂L ligand and its metal complexes.

Sample	Inhibition zone diameter (mm/mg sample)				
	<i>Bacillus subtilis</i>	<i>Escherichia coli</i>	<i>Neisseria gonorrhoeae</i>	<i>Staphylococcus aureus</i>	<i>Candida albicans</i>
Control: DMSO	0.0	0.0	0.0	0.0	0.0
Ligand (H ₂ L)	0.0	0.0	0.0	0.0	0.0
[Cr(H ₂ L)Cl ₂].Cl.2H ₂ O	14	15	15	15	0.0
[Mn(H ₂ L)Cl ₂]	9	10	9	0.0	0.0
[Fe(H ₂ L)Cl ₂].Cl.H ₂ O	9	9	9	0.0	0.0
[Co(H ₂ L)Cl ₂]	16	16	15	16	12
[Ni(H ₂ L)Cl ₂]	14	14	15	13	16
[Cu(H ₂ L)Cl ₂].3/2H ₂ O	12	12	12	13	10
[Zn(H ₂ L)Cl ₂].H ₂ O	11	12	13	15	9
[Cd(H ₂ L)Cl ₂].H ₂ O	18	15	13	23	17
Amikacin	6	9	7	6	0
Ketokonazole	—	—	—	—	9

TABLE 5: Energy values obtained in docking calculations of H₂L with receptors of the crystal structure of *S. aureus* (PDB ID: 3Q8U), crystal structure of protein phosphatase (PPZ1) of *Candida albicans* (PDB ID: 5JPE), receptors of breast cancer mutant oxidoreductase (PDB ID: 3HB5), and crystal structure of *Escherichia coli* (PDB ID: 3T88).

Receptor	Ligand moiety	Receptor	Interaction	Distance	E (kcal/mol)
5JPE	N 41	O HIS 413 (A)	H-donor	3.07	-2.5
	N 14	NE2 HIS 290 (A)	H-acceptor	3.33	-2.3
	O 34	NH2 ARG 386 (A)	H-acceptor	3.01	-2.8
	O 36	NH2 ARG 261 (A)	H-acceptor	2.93	-1.4
	O 36	NE2 HIS 290 (A)	H-acceptor	2.99	-1.1
3HB5	N 41	OD1 ASN 152(X)	H-donor	2.83	-3.1
	N 42	O GLY 9(X)	H-donor	3.44	-0.7
	O 36	OG SER 142(X)	H-acceptor	2.87	-1.5
	6-ring	CD2 PHE 192(X)	Pi-H	3.75	-0.6
3Q8U	O 38	OE1 GLU 95 (A)	H-donor	2.90	-6.0
	N 42	OE2 GLU 51 (A)	H-donor	3.00	-2.0
	N 14	N THR 91 (A)	H-acceptor	3.54	-1.6
	O 34	NZ LYS 9 (A)	H-acceptor	3.58	-0.6
	O 34	NH2 ARG 102 (A)	H-acceptor	3.04	-2.9
3T88	O 38	OE1 GLU 95 (A)	H-donor	2.90	-6.0
	O 38	O PHE 162 (A)	H-donor	3.33	-0.6
	N 41	OD2 ASP 163 (A)	H-donor	3.11	-2.2
	N 14	OH TYR 97 (A)	H-acceptor	3.18	-1.2
	O 36	OH TYR 97 (A)	H-acceptor	3.38	-0.6

TABLE 6: Energy values obtained in docking calculations of [Cd(H₂L)Cl₂].H₂O with receptors of the crystal structure of *S. aureus* (PDB ID: 3Q8U), crystal structure of protein phosphatase (PPZ1) of *Candida albicans* (PDB ID: 5JPE), receptors of breast cancer mutant oxidoreductase (PDB ID: 3HB5), and crystal structure of *Escherichia coli* (PDB ID: 3T88).

Receptor	Ligand moiety	Receptor	Interaction	Distance	E (kcal/mol)
5JPE	N 42	OD2 ASP 373 (A)	H-donor	2.89	-3.1
	O 48	O ARG 386 (A)	H-donor	3.07	-0.7
	O 38	NH2 ARG 386 (A)	H-acceptor	3.16	-2.4
	6-ring	CE2 TYR 437 (A)	Pi-H	4.62	-0.6
3HB5	O 48	O CYS 185 (X)	H-donor	2.53	-0.2
	O 48	OG SER 142 (X)	H-acceptor	2.68	-4.7
	6-ring	CG1 VAL 225 (X)	Pi-H	4.14	-0.7
3Q8U	N 10	OE1 GLU 51 (A)	H-donor	2.72	-18
	N 10	OE2 GLU 51 (A)	H-donor	3.38	-0.7
	CL 36	O HIS 48 (A)	H-donor	3.68	-0.7
	O 48	O GLY 116 (A)	H-donor	2.79	-2.2
	O 50	NH1 ARG 125 (A)	H-acceptor	2.85	-4.4
	N 10	OE1 GLU 51 (A)	Ionic	2.72	-6.7
	N 10	OE2 GLU 51 (A)	Ionic	3.38	-2.4
3T88	N 10	OD1 ASP 118 (A)	Ionic	2.69	-7.0
	O 38	OH TYR 97 (A)	H-acceptor	2.68	-2.0

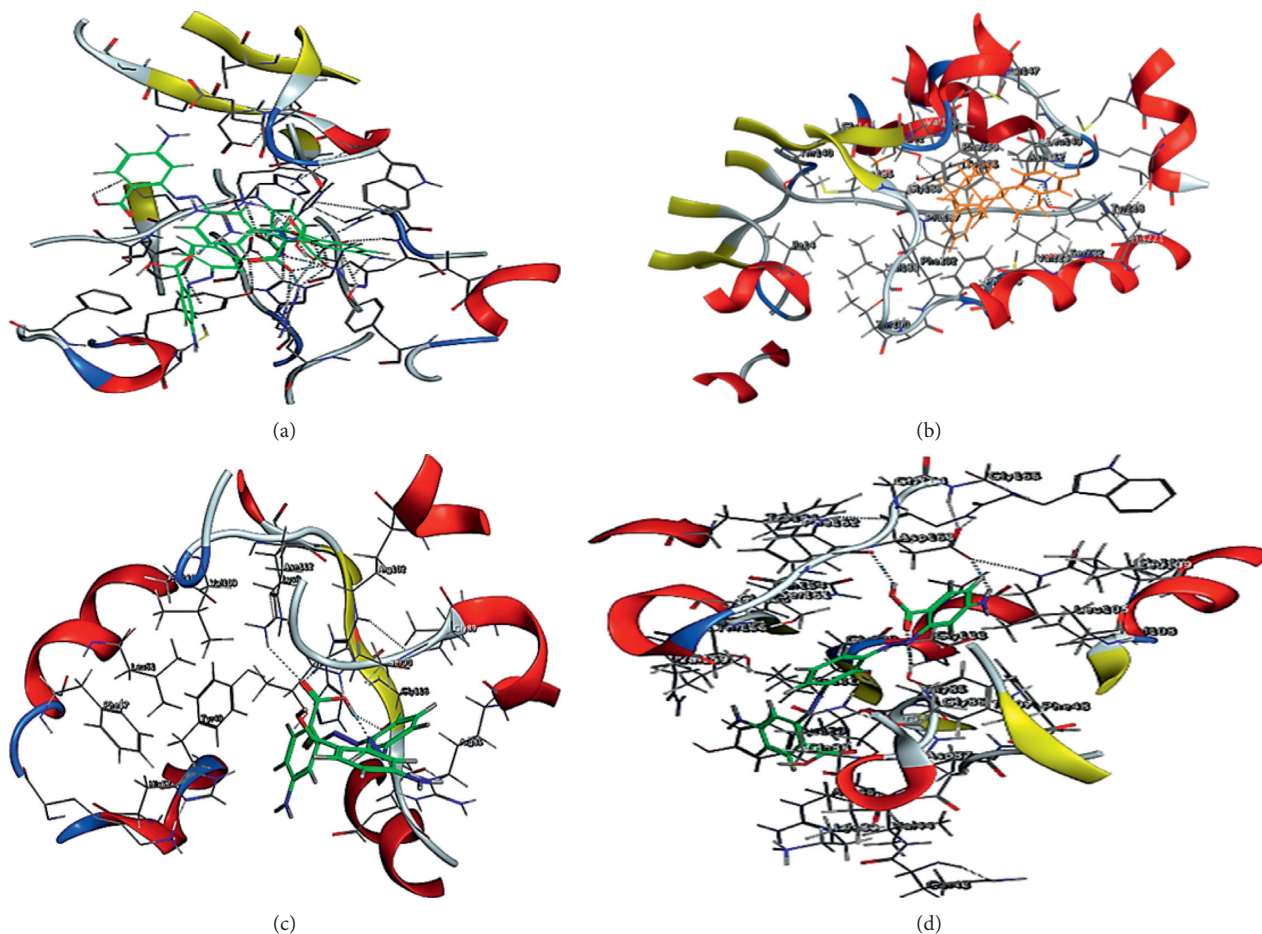


FIGURE 8: 3D plot of the interaction between the H_2L ligand with receptors of (a) 5JPE, (b) 3HB5, (c) 3Q8U, and (d) 3T88.

A look at the antibiotic, amikacin, activities (6.0–9.0 mm) against various bacterial isolates relative to the metal complexes (9.0–23.0 mm) showed that the activities of the former were much lower, with optimum activity being about half of metal complexes, against all the bacterial organisms.

When the antimicrobial activity of metal complexes is investigated, the following principal factors [57] should be considered: (i) the chelate effect of the ligands; (ii) the nature of the N-donor ligands; (iii) the total charge of the complex; (iv) the existence and the nature of the ion neutralizing the ionic complex; and (v) the nuclearity of the metal center in the complex. This is probably one of the reasons for the diverse antibacterial activity shown by the complexes, while the nature of the metal ion coordinated to the H_2L ligand may have a significant role to this diversity. In general, all the complexes exhibited better inhibition than free H_2L against *Bacillus subtilis*, *Staphylococcus aureus*, *Neisseria gonorrhoeae*, and *Escherichia coli* (Table 4). More specifically, Cd(II) and Co(II) complexes showed the best inhibition among all the complexes in this study, and they were one to twenty-three times more active than the H_2L diazo ligand against all the microorganisms used, indicating that the coordination of the H_2L ligand to Cd(II) and Co(II) ions

enhanced its antimicrobial activity (Figure 7). On the contrary, the rest complexes present higher antimicrobial activity to H_2L against the four microorganisms.

3.10. Molecular Docking. Targeting the minor groove of DNA through binding to a small molecule has long been considered an important tool in molecular recognition of a specific DNA sequence. DNA is considered a major biological target for metal complexes that have pharmacological activity. In this context, molecular docking between H_2L and $[Cd(H_2L)Cl_2] \cdot H_2O$ with four possible biological targets, receptors of the crystal structure of *S. aureus* (PDB ID: 3Q8U), crystal structure of protein phosphatase (PPZ1) of *Candida albicans* (PDB ID: 5JPE), receptors of breast cancer mutant oxidoreductase (PDB ID: 3HB5), and the crystal structure of *Escherichia coli* (PDB ID: 3T88), was performed. The structures of these macromolecules were obtained from the Protein Data Bank. The calculated binding energies for the interaction with these proteins are listed in Tables 5 and 6. The 3D plot curves of docking with free H_2L and $[Cd(H_2L)Cl_2] \cdot H_2O$ are shown in Figures 8 and 9.

From these data, the following can be concluded [58–60]:

- (1) First, H_2L and its Cd(II) complex showed strong binding affinities for all proteins

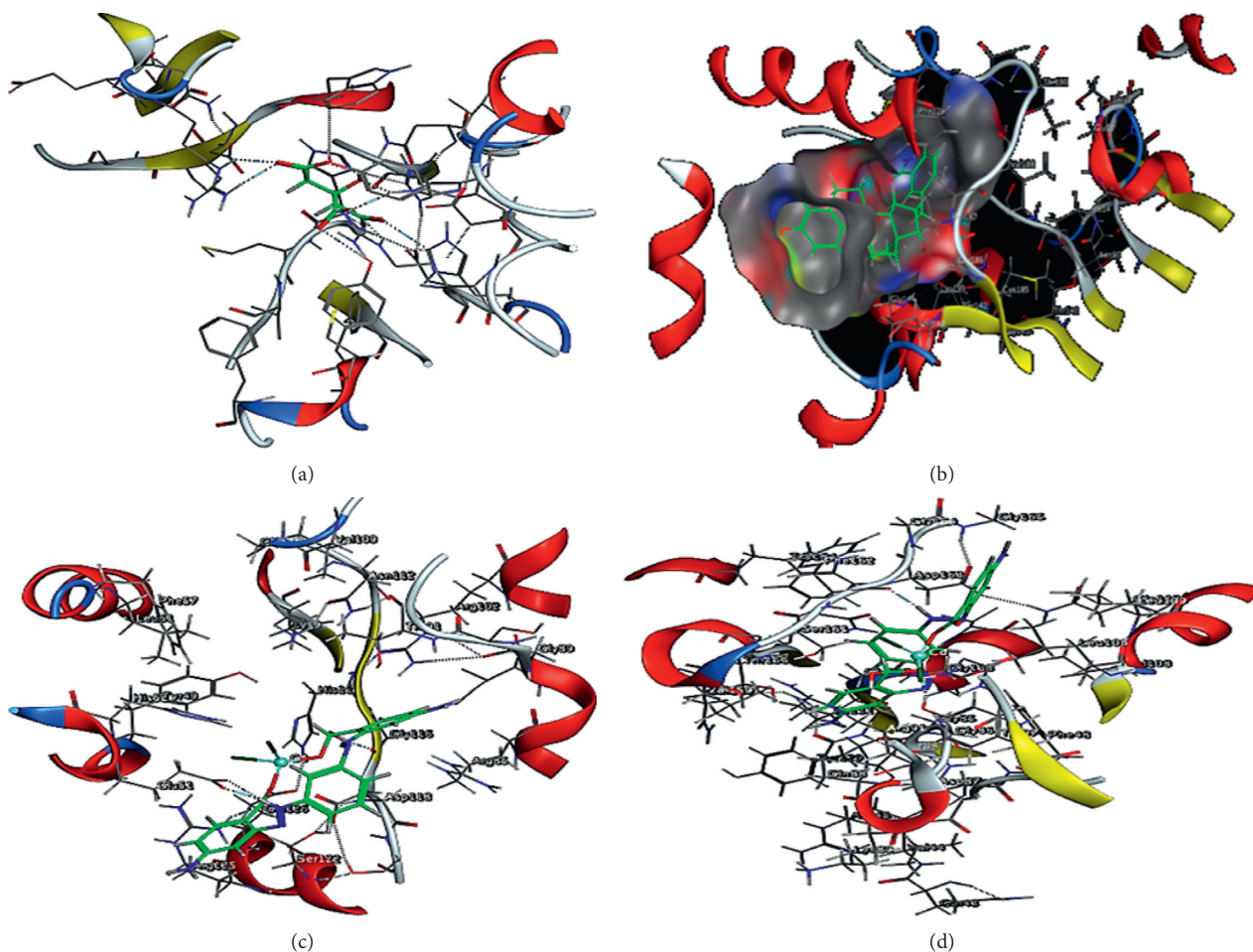


FIGURE 9: 3D plot of the interaction between Cd-H₂L with receptors of (a) 5JPE, (b) 3HB5, (c) 3Q8U, and (d) 3T88.

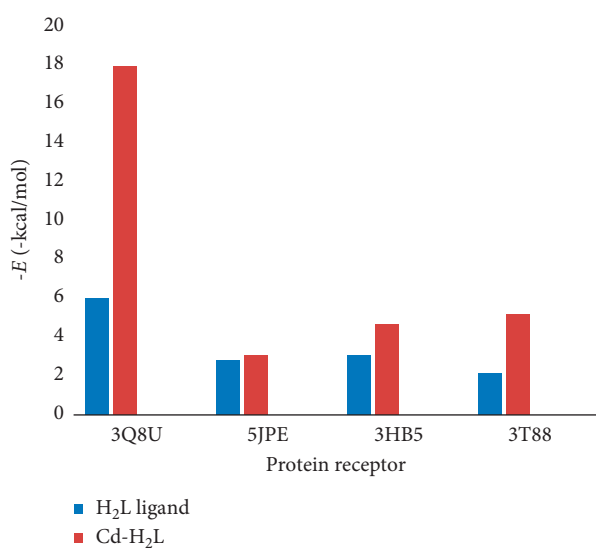


FIGURE 10: The binding energy of the interaction between H₂L and Cd-H₂L and receptors of 5JPE, 3HB5, 3Q8U, and 3T88.

- (2) The [Cd(H₂L)Cl₂].H₂O complex binds stronger than the free ligand to different proteins, see Figure 10
- (3) The binding energy for the interaction of the cadmium (II) complex with the receptor protein 3Q8U was three times less than the free diazo ligand confirming the high activity of this compound [58]
- (4) A closer look at the interactions indicated that the presence of heteroatoms such as oxygen and nitrogen was critical to how the compound binds [59]
- (5) Generally speaking, H-acceptor interaction dominates the binding of the synthesized complexes to different receptors besides the metal binding to the protein backbone

4. Conclusion

A new diazo ligand, 2,2'-(1,3-phenylenebis(diazene-2,1-diyl))bis(4-aminobenzoic acid), was synthesized and treated with different metal salts to give the corresponding metal complexes. The new ligand H₂L reacted with the metal ions

as 1 : 1 unit. The analytical data showed that reactions of the free diazo ligand (H_2L) with Mn(II), Co(II), Ni(II), Cu(II), Zn(II), and Cd(II) formed complexes with chemical formulae $[M(H_2L)Cl_2] \cdot nH_2O$ ($M = Co(II), Ni(II), Cu(II), Mn(II), Zn(II)$ and $Cd(II)$) and $[M(H_2L)Cl_2]Cl \cdot nH_2O$ ($M = Cr(III)$ and $Fe(III)$). The possible structures of the ligand and its metal-azo complexes were proposed based on elemental analyses, 1H NMR, ESR, MS, IR, and UV-Vis electronic absorption. It was concluded that the H_2L ligand behaved as a neutral tetradentate ligand with N coordination sites and protonated carboxylate oxygen upon coordination to the metal ions leading to the formation of octahedral geometries for all complexes. The thermal studies for the compounds showed a higher thermal stability for the complexes than that of the free ligand. This may be due to chelation, the type, and the number of solvents of crystallization in the metal complexes. Also, the ligand and its metal complexes were screened in vitro against microorganisms (bacteria or fungi). The results of biological activity showed that the Cd(II) complex had higher antibacterial activity against the (Gram-positive) bacteria and fungi, while Co(II) had higher antibacterial activity against the (Gram-negative) bacteria compared to the free ligand and other metal complexes. Molecular docking studies of the free ligand and the Cd(II) complex with four different receptors clarified that the Cd(II) complex showed the minimum binding ability with the binding energy of -18 kcal/mol with the crystal structure of *S. aureus* (3Q8U).

Data Availability

The data used to support the findings of this study are available from the corresponding author upon request.

Conflicts of Interest

The authors declare no conflicts of interest.

Supplementary Materials

Supplementary Table (1): analytical and physical data of H_2L and its metal complexes. Supplementary Table (2): IR spectra ($4000-400\text{ cm}^{-1}$) of H_2L and its metal complexes. Supplementary Table (5): different optimized parameters of H_2L and $[Cd(H_2L)Cl_2] \cdot H_2O$ complex. Supplementary Table (6): different Mulliken charges of H_2L and $[Cd(H_2L)Cl_2] \cdot H_2O$ complex. Supplementary Figure 3: contact angle images of (a) Cr(III), (b) Mn(II), (c) Fe(III), (d) Co(II), (e) Ni(II), (f) Cu(II), (g) Zn(II), and (h) Cd(II) complexes and (i) H_2L ligand. Supplementary Figure 6: comparison of Mulliken charges for (a) free H_2L and (b) cadmium complex. Supplementary Figure 8: the theoretical IR spectra of (a) H_2L and (b) $[Cd(H_2L)Cl_2] \cdot H_2O$ and the experimental IR spectra of (c) H_2L and (d) $[Cd(H_2L)Cl_2] \cdot H_2O$. (*Supplementary Materials*)

References

- [1] X. Li, Y. Wu, D. Gu, and F. Gan, "Spectral, thermal and optical properties of metal(II)-azo complexes for optical recording media," *Dyes and Pigments*, vol. 86, no. 2, pp. 182–189, 2010.
- [2] M. C. Garrigós, F. Reche, M. L. Mañín, and A. Jiménez, "Determination of aromatic amines formed from azo colorants in toy products," *Journal of Chromatography A*, vol. 976, no. 1-2, pp. 309–317, 2002.
- [3] Y. Karaman, N. Menek, F. A. Bicer, and H. Olmez, "Voltammetric investigations of 2,2'-azobispyridine zinc(II) and nickel(II) complexes," *International Journal of Electrochemical Science*, vol. 10, pp. 3106–3116, 2010.
- [4] A. Khalil, N. M. Aboamara, W. S. Nasser, W. H. Mahmoud, and G. G. Mohamed, "Photodegradation of organic dyes by PAN/SiO₂-TiO₂-NH₂ nanofiber membrane under visible light," *Separation and Purification Technology*, vol. 224, pp. 509–514, 2019.
- [5] J. Sima, "Mechanism of photoredox reactions of iron(III) complexes containing salen-type ligands," *Croatica Chemica Acta*, vol. 74, p. 593, 2001.
- [6] J. T. Simpson, S. R. Hunter, and T. Aytug, "Superhydrophobic materials and coatings, a review," *Reports on Progress in Physics*, vol. 78, Article ID 086501, 2015.
- [7] E. J. Falde, S. T. Yohe, Y. L. Colson, and M. W. Grinstaff, "Superhydrophobic Materials for Biomedical Applications," *Biomaterials*, vol. 104, pp. 87–103, 2016.
- [8] T. A. Halgren, "Merck molecular force field. I. Basis, form, scope, parameterization, and performance of MMFF94," *Journal of Computational Chemistry*, vol. 17, no. 5-6, pp. 490–519, 1998.
- [9] I. Sakiyan, E. Loğoğlu, S. Arslan, N. Sari, and N. Sakiyan, "Antimicrobial activities of N-(2-hydroxy-1-naphthalidene)-amino acid(glycine, alanine, phenylalanine, histidine, tryptophane) Schiff bases and their manganese(III) complexes," *Biometals: An International Journal on the Role of Metal Ions in Biology, Biochemistry, and Medicine*, vol. 17, no. 2, pp. 115–120, 2004.
- [10] P. Skehan, R. Storeng, D. Scudiero et al., "New colorimetric cytotoxicity assay for anticancer-drug screening," *JNCI Journal of the National Cancer Institute*, vol. 82, no. 13, pp. 1107–1112, 1990.
- [11] S. Sangilipandi, D. Sutradhar, K. Bhattacharjee et al., "Synthesis, structure, antibacterial studies and DFT calculations of arene ruthenium, Cp*Rh, Cp*Ir and tricarbonylrhenium metal complexes containing 2-chloro-3-(3-(2-pyridyl)pyrazolyl)quinoxaline ligand," *Inorganica Chimica Acta*, vol. 441, pp. 95–108, 2016.
- [12] Chemical Computing Group Inc., *Molecular Operating Environment (MOE 2008.10)*, Chemical Computing Group Inc., Montreal, QC, Canada, 2008.
- [13] A.-N. M. A. Alaghaz, H. A. Bayoumi, Y. A. Ammar, and S. A. Aldhlmani, "Synthesis, characterization, and antipathogenic studies of some transition metal complexes with N,O-chelating Schiff's base ligand incorporating azo and sulfonamide Moieties," *Journal of Molecular Structure*, vol. 1035, pp. 383–399, 2013.
- [14] M. M. Abo-Aly, A. M. Salem, M. A. Sayed, and A. A. Abdel Aziz, "Spectroscopic and structural studies of the Schiff base 3-methoxy-N-salicylidene-o-amino phenol complexes with some transition metal ions and their antibacterial, antifungal activities," *Spectrochimica Acta Part A: Molecular and Biomolecular Spectroscopy*, vol. 136, pp. 993–1000, 2015.
- [15] I. Babahan, S. Emirdağ-Öztürk, and E. Poyrazoğlu-Çoban, "Spectroscopic and biological studies of new mononuclear metal complexes of a bidentate NN and NO hydrazone-oxime ligand derived from egonol," *Spectrochimica Acta Part A: Molecular and Biomolecular Spectroscopy*, vol. 141, pp. 300–306, 2015.

- [16] G. G. Mohamed, H. F. Abd El-Halim, M. M. I. El-Dessouky, and W. H. Mahmoud, "Synthesis and characterization of mixed ligand complexes of lomefloxacin drug and glycine with transition metals. Antibacterial, antifungal and cytotoxicity studies," *Journal of Molecular Structure*, vol. 999, no. 1–3, pp. 29–38, 2011.
- [17] H. Naeimi, J. Safari, and A. Heidarneshad, "Synthesis of Schiff base ligands derived from condensation of salicylaldehyde derivatives and synthetic diamine," *Dyes and Pigments*, vol. 73, no. 2, pp. 251–253, 2007.
- [18] M. Hanif and Z. H. Chohan, "Design, spectral characterization and biological studies of transition metal(II) complexes with triazole Schiff bases," *Spectrochimica Acta Part A: Molecular and Biomolecular Spectroscopy*, vol. 104, pp. 468–476, 2013.
- [19] A. Maiti and S. Ghosh, "Synthesis and reactivity of the oxovanadium(IV) complexes of two NO donors and potentiation of the antituberculosis activity of one of them on chelation to metal ions: Part IV," *Journal of Inorganic Biochemistry*, vol. 36, no. 2, pp. 131–139, 1989.
- [20] R. G. Deghadi, W. H. Mahmoud, and G. G. Mohamed, "Metal complexes of tetradentate azo-dye ligand derived from 4,4'-oxydianiline; Preparation, structural investigation, biological evaluation and MOE studies," *Accepted Manuscript Applied Organometallic Chemistry*, vol. 34, no. 10, 2020.
- [21] V. L. Dorofeev, "Infrared spectra and the structure of drugs of the fluoroquinolone group," *Pharmaceutical Chemistry Journal*, vol. 38, pp. 45–49, 2004.
- [22] M. S. Refat, G. G. Mohamed, R. F. de Farias et al., "Spectroscopic, thermal and kinetic studies of coordination compounds of Zn(II), Cd(II) and Hg(II) with norfloxacin," *Journal of Thermal Analysis and Calorimetry*, vol. 102, no. 1, pp. 225–232, 2010.
- [23] N. G. Zaki, W. H. Mahmoud, A. M. El Kerdawy El Kerdawy, A. M. Abdallah, and G. G. Mohamed, "Heteroleptic complexes of cocaine/TMEDA with some f block metals: synthesis, DFT studies, spectral, thermal, cytotoxicity and antimetastatic properties," *Spectrochimica Acta Part A: Molecular and Biomolecular Spectroscopy*, vol. 229, Article ID 117938, 2020.
- [24] L. J. Bellamy, *The Infrared Spectra of Complex Molecules*, Chapman and Hall, London, UK, third edition, 1975.
- [25] K. Nakamoto, *Infrared Spectra of Inorganic and Coordination Compounds*, Wiley Interscience, New York, NY, USA, 1970.
- [26] W. H. Mahmoud, G. G. Mohamed, and M. M. I. El-Dessouky, "Coordination modes of bidentate lornoxicam drug with some transition metal ions. Synthesis, characterization and in vitro antimicrobial and antitumor activity studies," *Spectrochimica Acta Part A: Molecular and Biomolecular Spectroscopy*, vol. 122, pp. 598–608, 2014.
- [27] W. H. Mahmoud, F. N. Sayed, and G. G. Mohamed, "Azo dye with nitrogen donor sets of atoms and its metal complexes: synthesis, characterization, DFT, biological, anticancer and Molecular docking studies," *Applied Organometallic Chemistry*, vol. 32, pp. 1–19, Article ID e4347, 2018.
- [28] R. Cini, G. Giorgi, A. Cinquantini, C. Rossi, and M. Sabat, "Metal complexes of the antiinflammatory drug piroxicam," *Inorganic Chemistry*, vol. 29, no. 26, pp. 5197–5200, 1990.
- [29] Y.-T. Liu, G.-D. Lian, D.-W. Yin, and B.-J. Su, "Synthesis, characterization and biological activity of ferrocene-based Schiff base ligands and their metal (II) complexes," *Spectrochimica Acta Part A: Molecular and Biomolecular Spectroscopy*, vol. 100, pp. 131–137, 2013.
- [30] H. Irving and R. J. P. Williams, "637. The stability of transition-metal complexes," *Journal of the Chemical Society (Resumed)*, vol. 75, pp. 3192–3210, 1953.
- [31] W. H. Mahmoud, N. F. Mahmoud, G. G. Mohamed, A. Z. El-Sonbati, and A. A. El-Bindary, "Ternary metal complexes of guaifenesin drug: synthesis, spectroscopic characterization and in vitro anticancer activity of the metal complexes," *Spectrochimica Acta Part A: Molecular and Biomolecular Spectroscopy*, vol. 150, no. 1, pp. 451–460, 2015.
- [32] G. G. Mohamed, E. M. Zayed, and A. M. M. Hindy, "Coordination behavior of new bis Schiff base ligand derived from 2-furan carboxaldehyde and propane-1,3-diamine. Spectroscopic, thermal, anticancer and antibacterial activity studies," *Spectrochimica Acta Part A: Molecular and Biomolecular Spectroscopy*, vol. 145, pp. 76–84, 2015.
- [33] W. Chen, Y. Wu, D. Gu, and F. Gan, "Synthesis, optical and thermal characterization of novel thiazolyl heterocyclic azo dye," *Materials Letters*, vol. 61, no. 19–20, pp. 4181–4184, 2007.
- [34] M. R. Mahmoud, A. M. Hamman, and S. A. Ibrahim, "Chromium complexes of O,O-dihydroxyazo dye," *Zeitschrift für Physikalische Chemie*, vol. 265, pp. 203–211, 1994.
- [35] P. Subbaraj, A. Ramu, N. Raman, and J. Dharmaraja, "Synthesis, characterization, DNA interaction and pharmacological studies of substituted benzophenone derived Schiff base metal(II) complexes," *Journal of Saudi Chemical Society*, vol. 19, no. 2, pp. 207–216, 2015.
- [36] N. Kavitha and P. V. Anantha Lakshmi, "Synthesis, characterization and thermogravimetric analysis of Co(II), Ni(II), Cu(II) and Zn(II) complexes supported by ONNO tetradentate Schiff base ligand derived from hydrazino benzoxazine," *Journal of Saudi Chemical Society*, vol. 21, pp. S457–S466, 2017.
- [37] W. H. Mahmoud, T. A. Awed, and G. G. Mohamed, "Construction and characterization of nano iron complex ionophore for electrochemical determination of Fe(III) in pure and different real water samples," *Applied Organometallic Chemistry*, vol. 33, pp. 1–17, Article ID e5206, 2019.
- [38] A. M. F. Benial, V. Ramakrishnan, and R. Murugesan, "Single crystal EPR of Cu(C₅H₅NO)₆(BF₄)₂: an example of admixed ground state," *Spectrochimica Acta Part A: Molecular and Biomolecular Spectroscopy*, vol. 56, no. 14, pp. 2775–2781, 2000.
- [39] K. B. Gudasi, S. A. Patil, R. S. Vadavi, R. V. Shenoy, and M. Nethaji, "Crystal structure of 2-[2-hydroxy-3-methoxyphenyl]-3-[2-hydroxy-3-methoxybenzylamino]-1,2-dihydroquinazolin-4(3H)-one and the synthesis, spectral and thermal investigation of its transition metal complexes," *Transition Metal Chemistry*, vol. 31, no. 5, pp. 586–592, 2006.
- [40] A. Z. El-Sonbati, M. A. Diab, A. A. El-Bindary, G. G. Mohamed, and S. M. Morgan, "Thermal, spectroscopic studies and hydrogen bonding in supramolecular assembly of azo rhodanine complexes," *Inorganica Chimica Acta*, vol. 430, pp. 96–107, 2015.
- [41] N. A. El-Ghamaz, M. A. Diab, A. A. El-Bindary, A. Z. El-Sonbati, and S. G. Nozha, "Thermal, dielectric characteristics and conduction mechanism of azo dyes derived from quinoline and their copper complexes," *Spectrochimica Acta Part A: Molecular and Biomolecular Spectroscopy*, vol. 143, pp. 200–212, 2015.
- [42] S. Velumani, X. Mathew, P. J. Sebastian, S. K. Narayandass, and D. Mangalaraj, "Structural and optical properties of hot wall deposited CdSe thin films," *Solar Energy Materials and Solar Cells*, vol. 76, no. 3, pp. 347–358, 2003.

- [43] S. Basavaraja, D. S. Balaji, M. D. Bedre, D. Raghunandan, P. M. Prithviraj Swamy, and A. Venkataraman, "Solvothetical synthesis and characterization of acicular α -Fe₂O₃ nanoparticles," *Bulletin of Materials Science*, vol. 34, no. 7, pp. 1313–1317, 2011.
- [44] T. A. Yousef, O. K. Alduaij, S. F. Ahmed, G. M. Abu El-Reash, and O. A. El-Gammal, "Structural, DFT and biological studies on Cr(III) complexes of semi and thiosemicarbazide ligands derived from diketo hydrazide," *Journal of Molecular Structure*, vol. 1125, pp. 788–799, 2016.
- [45] W. A. Zordok and S. A. Sadeek, "Synthesis, thermal analyses, characterization and biological evaluation of new enrofloxacin vanadium(V) solvates(L) (L = An, DMF, Py, Et₃N and o-Tol)," *Journal of Molecular Structure*, vol. 1120, pp. 50–61, 2016.
- [46] R. Takjoo, S. S. Hayatolghaibi, and H. Amiri Rudbari, "Preparation, X-ray structure, spectral analysis, DFT calculation and thermal study on palladium(II) coordination compound with Schiff base derived from S-allyldithiocarbamate," *Inorganica Chimica Acta*, vol. 447, pp. 52–58, 2016.
- [47] S. Altürk, D. Avcı, Ö. Tamer, Y. Atalay, and O. Şahin, "A cobalt (II) complex with 6-methylpicolinate: synthesis, characterization, second- and third-order nonlinear optical properties, and DFT calculations," *Journal of Physics and Chemistry of Solids*, vol. 98, pp. 71–80, 2016.
- [48] W. H. Mahmoud, M. M. Omar, and F. N. Sayed, "Synthesis, spectral characterization, thermal, anticancer and antimicrobial studies of bidentate azo dye metal complexes," *Journal of Thermal Analysis and Calorimetry*, vol. 124, no. 2, pp. 1071–1089, 2016.
- [49] M. J. Pelczar, E. C. S. Chan, and N. R. Krieg, "Host-parasite interaction; nonspecific host resistance," in *Microbiology Concepts and Applications*, pp. 478–479, McGraw-Hill Inc., New York, NY, USA., 6th edition, 1999.
- [50] W. H. Mahmoud, F. N. Sayed, and G. G. Mohamed, "Synthesis, characterization and in vitro antimicrobial and anti-breast cancer activity studies of metal complexes of novel pentadentate azo dye ligand," *Applied Organometallic Chemistry*, vol. 30, no. 11, pp. 959–973, 2016.
- [51] A. T. Çolak, F. Çolak, O. Z. Yeşilel, D. Akduman, F. Yılmaz, and M. Tümer, "Supramolecular cobalt(II)-pyridine-2,5-dicarboxylate complexes with isonicotinamide, 2-amino-3-methylpyridine and 2-amino-6-methylpyridine: syntheses, crystal structures, spectroscopic, thermal and antimicrobial activity studies," *Inorganica Chimica Acta*, vol. 363, no. 10, pp. 2149–2162, 2010.
- [52] S. Belaid, A. Landreau, S. Djebbar, O. Benali-Baitich, G. Bouet, and J.-P. Bouchara, "Synthesis, characterization and antifungal activity of a series of manganese(II) and copper(II) complexes with ligands derived from reduced N,N'-O-phenylenebis(salicylideneimine)," *Journal of Inorganic Biochemistry*, vol. 102, no. 1, pp. 63–69, 2008.
- [53] K. Kralova, K. Kwassova, O. Svajlenova, and J. Vanco, "Chem. Biological activity of copper(II) N-salicylideneaminoacidato complexes. Reduction of chlorophyll content in freshwater alga *Chlorella vulgaris* and inhibition of photosynthetic electron transport in Spinach chloroplasts," *Chemical Papers*, vol. 58, pp. 357–361, 2004.
- [54] R. Nair, A. Shah, S. Baluja, and S. Chanda, "Synthesis and antibacterial activity of some Schiff base complexes," *Journal of the Serbian Chemical Society*, vol. 71, no. 7, pp. 733–744, 2006.
- [55] Y. Vaghasia, R. Nair, M. Soni, S. Baluja, and S. Chanda, "Synthesis, structural determination and antibacterial activity of compounds derived from vanillin and 4-aminoantipyrine," *J. Serb. Chem. Soc.* vol. 69, pp. 991–998, 2004.
- [56] N. Mahalakshmi and R. Rajavel, "Synthesis, spectroscopic, DNA cleavage and antibacterial activity of binuclear schiff base complexes," *Arabian Journal of Chemistry*, vol. 7, no. 4, pp. 509–517, 2014.
- [57] E. K. Efthimiadou, A. Karaliota, and G. Psomas, "Mononuclear metal complexes of the second-generation quinolone antibacterial agent enrofloxacin: synthesis, structure, antibacterial activity and interaction with DNA," *Polyhedron*, vol. 27, no. 6, pp. 1729–1738, 2008.
- [58] F. A. Beckford, A. Brock, A. Gonzalez-Sarrias, and N. P. Seeram, "Cytotoxic gallium complexes containing thiosemicarbazones derived from 9-anthraldehyde: molecular docking with biomolecules," *Journal of Molecular Structure*, vol. 1121, pp. 156–166, 2016.
- [59] K. Zheng, M.-X. Yan, Y.-T. Li, Z.-Y. Wu, and C.-W. Yan, "Synthesis and structure of new dicopper(II) complexes bridged by N-(2-hydroxy-5-methylphenyl)-N'-[3-(dimethylamino)propyl]oxamide with in vitro anticancer activity: a comparative study of reactivities towards DNA/protein by molecular docking and experimental assays," *European Journal of Medicinal Chemistry*, vol. 109, pp. 47–58, 2016.
- [60] G. M. Morris, D. S. Goodsell, R. S. Halliday et al., "Automated docking using a Lamarckian genetic algorithm and an empirical binding free energy function," *Journal of Computational Chemistry*, vol. 19, no. 14, pp. 1639–1662, 1998.

Review Article

A Comprehensive Review on Thermal Coconversion of Biomass, Sludge, Coal, and Their Blends Using Thermogravimetric Analysis

Zeeshan Hameed,¹ Salman Raza Naqvi,¹ Muhammad Naqvi ,² Imtiaz Ali,³ Syed Ali Ammar Taqvi,⁴ Ningbo Gao ,⁵ Syed Azfar Hussain,⁶ and Sadiq Hussain⁷

¹School of Chemical & Materials Engineering, National University of Sciences & Technology, Islamabad, Pakistan

²Department of Engineering and Chemical Sciences, Karlstad University, Karlstad, Sweden

³Department of Chemical and Materials Engineering, King Abdulaziz University, Rabigh, Saudi Arabia

⁴Department of Chemical Engineering, NED University of Engineering & Technology, Karachi, Pakistan

⁵School of Energy and Power Engineering, Xi'an Jiaotong University, Xi'an 710049, China

⁶Department of Chemical Engineering, Ecole Polytechnique de Montréal, Montréal, Canada

⁷Department of Chemical Engineering, NFC-Institute of Engineering & Technology, Khanewal Road, Multan, Pakistan

Correspondence should be addressed to Muhammad Naqvi; raza.naqvi@kau.se

Received 28 February 2020; Revised 16 May 2020; Accepted 22 June 2020; Published 4 August 2020

Academic Editor: Hassan Arida

Copyright © 2020 Zeeshan Hameed et al. This is an open access article distributed under the Creative Commons Attribution License, which permits unrestricted use, distribution, and reproduction in any medium, provided the original work is properly cited.

Lignocellulosic biomass is a vital resource for providing clean future energy with a sustainable environment. Besides lignocellulosic residues, nonlignocellulosic residues such as sewage sludge from industrial and municipal wastes are gained much attention due to its large quantities and ability to produce cheap and clean energy to potentially replace fossil fuels. These cheap and abundantly resources can reduce global warming owing to their less polluting nature. The low-quality biomass and high ash content of sewage sludge-based thermal conversion processes face several disadvantages towards its commercialization. Therefore, it is necessary to utilize these residues in combination with coal for improvement in energy conversion processes. As per author information, no concrete study is available to discuss the synergy and decomposition mechanism of residues blending. The objective of this study is to present the state-of-the-art review based on the thermal coconversion of biomass/sewage sludge, coal/biomass, and coal/sewage sludge blends through thermogravimetric analysis (TGA) to explore the synergistic effects of the composition, thermal conversion, and blending for bioenergy production. This paper will also contribute to detailing the operating conditions (heating rate, temperature, and residence time) of copyrolysis and cocombustion processes, properties, and chemical composition that may affect these processes and will provide a basis to improve the yield of biofuels from biomass/sewage sludge, coal/sewage sludge, and coal/biomass blends in thermal coconversion through thermogravimetric technique. Furthermore, the influencing factors and the possible decomposition mechanism are elaborated and discussed in detail. This study will provide recent development and future prospects for cothermal conversion of biomass, sewage, coal, and their blends.

1. Introduction

Fossil fuels have been extensively used for the last two centuries to meet the energy demand of the growing population for global development [1–3]. The increase in the environmental and sustainability summons due to the greenhouse emissions that are related to fossil fuel usage and the unceremonious distribution of fossil fuel resources has

increased the global energy [4, 5]. It is the need of the time to introduce an alternate energy approach to meet current and future energy demands [6]. The replacement of conventional fossil fuels with sewage sludge, coal, and lignocellulosic biomass fuels as renewable energy resources is considered promising as these have already contributed to around 10% of the global energy supply [7–12]. Soncini et al. stated that from the past thirty years, lignocellulosic biomass was a focal

point of research for renewable energy because 56% of energy is provided by biomass, 26% by solar, 11% by wind power, 5% by geothermal energy, and 2% by hydropower [13]. In the future, utilization of renewable sources and biofuels will increase from 2 to 27% [14]. The abundance of biomass and sewage sludge coupled with lower environmental concern and technical ease is the main reason for intensive research and utilization of these sources as feedstocks [15].

Coal is the largest source of energy in the United States (filling to about 42% of net energy demand) [16]. Global coal demand dropped during 2014–2016 despite the economic growth during these two years. The growth in the energy demand in China, the US, and Europe has been met partly by renewables and natural gas switch in power generation from coal. However, coal demand grew in India and South East Asia Region due to the increased power demand for their social development and growing economies. Still, in the 21st century, coal is a major source of world energy due to lower cost and a higher energy density [17]. It is expected that coal will contribute to future energy demands in many fast-developing countries, such as China and India [18]. The conversion of biomass to fuels and chemicals by thermal conversion has a substantial value in the petrochemical industry (Figure 1). The major downside of coal is that it is responsible for the emission of ecologically damaging compounds such as sulfur (S), nitrogen (N), and heavy metals, so its utilization with biomass and sewage sludge can mitigate the impact [21].

Lignocellulosic biomass, a clean and alternative energy source, has been the point of focus for its abundance and the lower tendency of greenhouse gas emissions [22]. CO_2 exhausted from the burning of biomass is absorbed through photosynthesis, thereby controlling global warming [23, 24]. Sewage sludge is another important energy source to produce biofuels through thermochemical conversion, which also solves the disposal problem of waste sludge. The dried sewage sludge is reasonably rich in volatile matters and high in calorific value [25]. Cellulose, hemicellulose, lignin, and extractives are the main constituents of lignocellulosic biomass. Lignocellulosic biomass can be crudely categorized as woody, nonwoody, and wastes. These can be converted into bio-oils, gases, and chemicals through different thermochemical processes such as pyrolysis, gasification, liquefaction, and high-pressure supercritical extraction [26, 27]. Lignocellulosic biomass is considered as the largest sustainable energy source and approximately 220 billion tons of dry biomass is produced annually. It is also called the sole source of obtaining energy because it provides around 14% of the world's energy supply. According to the UN Food and Agriculture Organization, the world biomass production has increased from 19 million tons to 25 million tons in between 2012 and 2017 [28]. The coconversion of lignocellulosic biomass and sludge by using copyrolysis process can improve the quality of bio-oils and other gaseous products. The use of copyrolysis processes is gaining attention due to its simple and efficient operation to produce liquid [29]. Copyrolysis of lignocellulosic biomass and coal blends can offer several advantages such as reduction in

CO_2 , SO_x , and NO_x emissions and improve economy and efficiency [30]. A thermogravimetric analyser (TGA) can study the behavior and characteristics of coconversion through copyrolysis. TGA is an important tool to study thermal degradation behavior and synergic effect of many copyrolysis samples [31, 32]. TGA measures the percentage of mass loss of a sample with respect to temperature and time from these data; thermal decomposition behavior during pyrolysis is examined [33]. Moreover, kinetics of degradation of organic material during the pyrolysis process can also be investigated. Thermal degradation is an important factor in designing pyrolysis and copyrolysis processes. TGA is also useful in studying the synergy of different feedstock such as coal, lignocellulosic biomass, and sludge. The synergetic effects depend on the different types of feedstock mix, the intensity of sample contact, type of reactor, experimental conditions, and characteristics of the sample [34]. The effect of mixing ratio and temperature on the product distribution can also be studied by TGA. The most important advantage of thermal coconversion of coal, lignocellulosic biomass, and sewage sludge blends is the reduction in the harmful emissions. Thermal coconversion of biomass and sludge with coal is a relatively profound, cost-effective, and efficient process [35]. Thermal conversion of lignocellulosic biomass can reduce the landfill methane emission and coconversion can reduce the N_2O emission as compared to the conversion of coal alone [36]. Thermal coconversion of coal and lignocellulosic biomass offers a better way to utilize coal and wastes/biomass in an inexpensive, harmless, and environmentally acceptable manner [37].

Previously published work on the thermal conversion of the different types of lignocellulosic biomass, sewage sludge, and coal is summarized in many review articles (Figure 2). Some review articles have focused on the advancement of conversion techniques to improve the oil quality (Figure 3). However, blending ratio is an important factor in thermal coconversion biomass and sludge/coal, and to the best of authors' knowledge, there is no comprehensive review on the thermal coconversion of different blends using TGA. The compiled data and related discussions in this review will be beneficial in designing and developing efficient cothermal processes.

Thermal coconversion is getting much attention recently from the researcher due to its economic as well as environmental benefits. Especially during the past ten years, an exponential increase has been seen in the published literature at Web of Science related to thermal coconversion of coal/sludge or coal/biomass.

The work has been mostly published by the authors from the developing and developed nations. China is by far leading the rest of the world. Compared to sludge, the copyrolysis of coal/biomass is found in more instances. Most of the related literature appeared in *Bioresource Technology*, *Energy and Fuels*, *Fuel*, and *Journal of Analytical and Applied Pyrolysis* (Figure 4). From 2010 onwards, a sharp increase in the number of published papers is quite evident.

The aim of this paper is to comprehensively review the thermal coconversion of the different types of lignocellulosic biomass, sewage sludge, and coal to reveal the synergistic

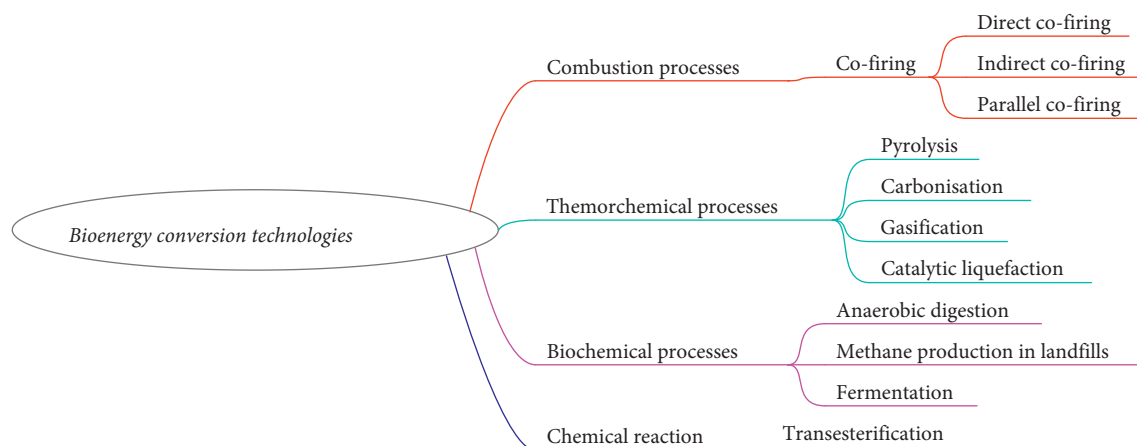


FIGURE 1: Biomass conversion processes [19, 20].

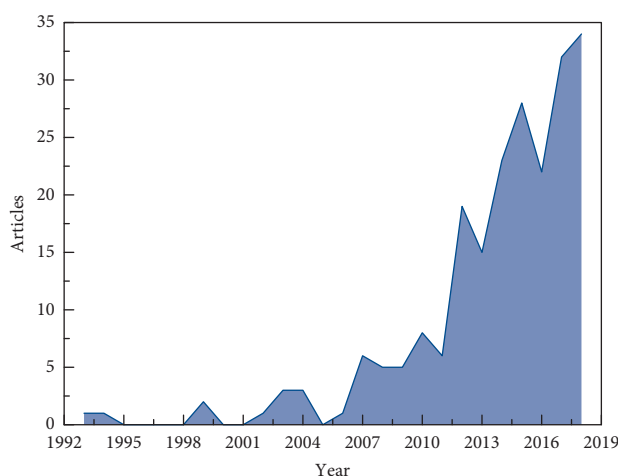


FIGURE 2: Annual scientific publication on the cothermal conversion of coal/sludge or coal/biomass appeared in the Web of Science database.

effect of their composition, conversion processes, and blending impact. Previously, there are no concrete and unique studies coupled with thermal coconversion (pyrolysis or combustion) of biomass, sludge, coal, and their blends and discussed their challenges. In addition, some comprehensive discussion is provided emphasizing the behavior of lignocellulosic biomass and blending ratio with coal and sewage sludge focusing on the relevant properties and technical issues that may influence the yield of bio-oils during thermal coconversion. In result, the effect of the properties and chemical composition of blending mixtures of sewage sludge, coal, and lignocellulosic biomass blends on the behavior of these processes will provide pinpoints to increase the efficiency and yield of biofuels obtained from biomass/sewage sludge, coal/sewage sludge, and coal/biomass blends by improving the operating conditions of TGA technique.

2. Feedstock and Thermal Coconversion

The selection of feedstock mainly depends on two factors: availability and the property of the material. The feedstock

is divided into three main categories. One is lignocellulosic biomass other is coal, and the third is municipal waste.

2.1. Lignocellulosic Biomass. The most abundant feedstock is lignocellulosic biomass. Any organic material that can be burned and used as a fuel is called lignocellulosic biomass. Lignocellulosic biomass is the most convenient energy asset that can be used to obtain different liquid fuels and bio-oils. All types of lignocellulosic biomass are classified into primary, secondary, and tertiary biomass based on their resource. Primary biomass can be formed directly by using solar energy and is grown from the land such as woody crops, oilseeds, rice husk, corn comb, rice straw, and bark from trees [38]. An energy research indicated that biomass has the capability to fulfil 10% of the energy supply globally [39]. Secondary biomass can be generated from chemical, physical, and biological processing of primary biomass resources. The bulging substitute as a raw material for bio-oil production for industrial corporations is usually plant-derived biomass, such as corn, sweet sorghum, sugarcane

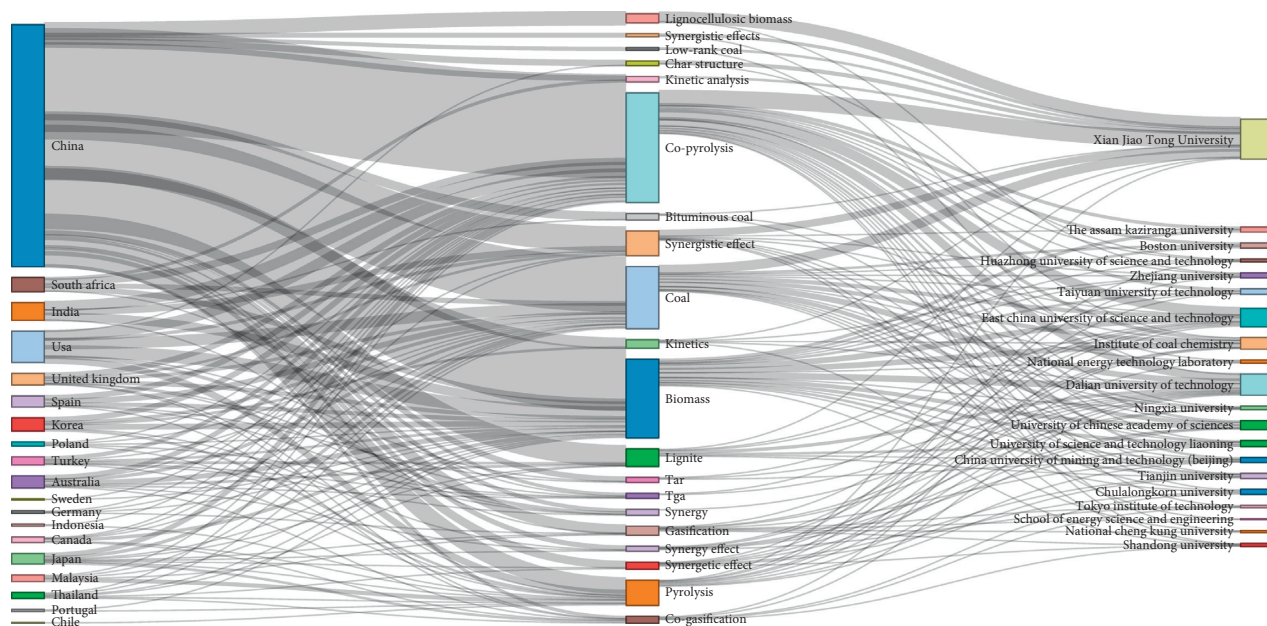


FIGURE 3: Sankey three-field plot of countries/keywords/affiliations.

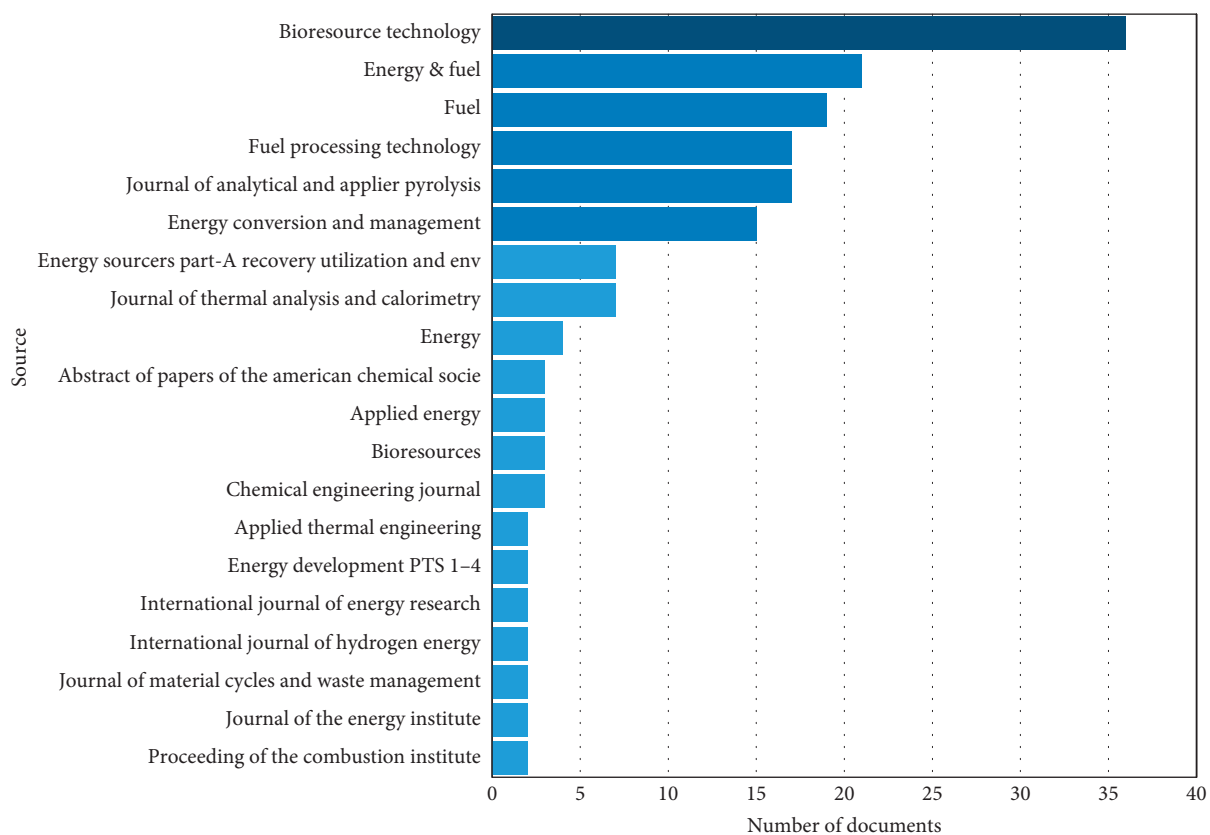
bagasse, wheat, and crop residue, and the feedstock prices are very practical, for example, 7.40 US\$/ton in which transportation cost is also included. Accordingly, commercialization of this second-generation biomass turned is being considered as very auspicious and valuable [40]. Tertiary biomass consists of animal fats, used vegetable oil, packaging wastes, and construction wastes. Hossain et al. indicated that microalgae wedged the awareness of presence as third-generation source of biofuel, raw material, nutrient, and collections of extremely treasured products in medicinal and agricultural industries [41]. She also suggested microalgae fuel could be applied for electricity generation by using static diesel engines. They all are composed of cellulose, hemicellulose, lignin, and extractives. Lignocellulosic biomass has the tendency to be transformed into bio-oils, gases, and chemicals [42, 43].

2.2. Coal. The other feedstock is coal, which is the second largest source used for energy and can be classified into bituminous, subbituminous, and lignite according to property and origin. Coal is a natural and abundant source to be used. The United States has approximately 260 billion short tons of recoverable reserves, that is, 27% of total reserves around the world. There are many studies which prove the potential of different types of coal in the usage of thermochemical conversion process under different operating conditions.

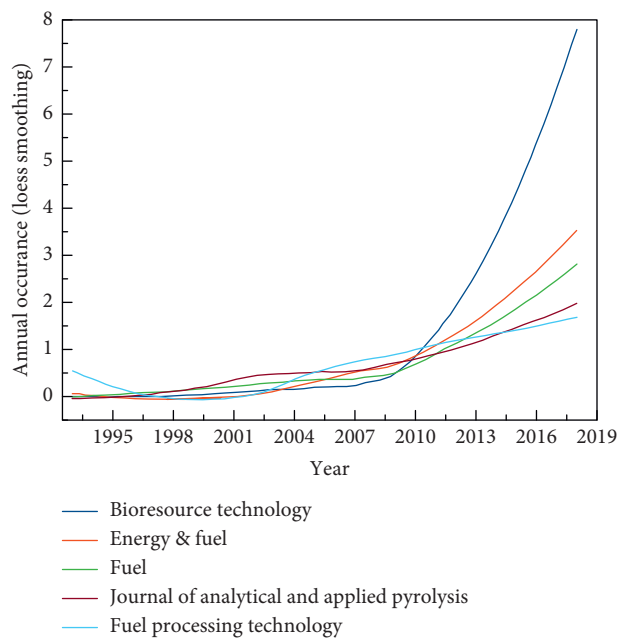
2.3. Sewage Sludge. The next important feedstock is sewage sludge, which is obtained from the municipal and industrial wastewater treatment plants. Sludge is collected as lumps, so it is necessary to reduce particle size and remove the excess moisture content (<10%) to upgrade the quality of the feedstock. To improve the quality of the products, the

feedstocks of different properties are mixed in desired blending ratios. Sewage sludge can provide energy and fuel by thermochemical conversion, so this is considered as the most promising alternate technology to reduce the amount of waste and harmful environmental impact. The amount of sewage sludge production is largely depending upon the level and method of treatment applied to wastewater, population growth, and volume of wastewater stream [44]. As indicated by Fytily et al., dried sewage has unpredictable substance of 30–88% and calorific esteem normally 11–25.5 MJ/kg [45]. The utilization of sewage sludge as sustainable power source assets is taken as a healthier choice since this source can give around 10% of worldwide vitality stock [30].

2.4. Thermal Coconversion. The conversion of individual coal through thermochemical conversion has environmental challenges in terms of harmful emission which can be minimized by using thermal coconversion of different raw materials, biomass, coal, and sewage sludge bends in different ratios [46]. The thermal coconversion depends upon how feedstock interacts under a specific condition with the specified ratio. Zhang et al. studied the synergy effect of lignite coal and biomass by grinding and sieving at a particle size range of 0.3–0.45 mm with 1 : 1 and dried it in an oven at 105°C for 24 h to improve the yield of the products [47]. Biomass and sewage sludge fuels usually contain a lower amount of fixed carbon and a higher percentage of volatile matter as compared to coal. Usually, thermal coconversion of coal and biomass or sewage sludge produces less carbon-containing compounds such as CO₂, CO, CH₄, and other light hydrocarbons as compared to the conversion of coal alone [48, 49]. Increasing biomass content in the blend can increase carbon-containing compounds like CO₂, CO, and light hydrocarbon gases while hydrogen content decreases. Kumabe et al. used



(a)



(b)

FIGURE 4: (a) Most relevant sources and (b) source growth rate.

biomass with the higher hydrogen content to increase the proportion of the hydrogen in the product, but the contrary resulted in the product [50].

3. Factors for Synergistic Effects on Thermal Coconversion

3.1. Ultimate, Proximate, and Chemical Composition Analysis of Coal. Coal is the combustible material containing 50% by weight of carbon. It is a carbonaceous material with some percentage of hydrogen, oxygen, nitrogen, sulfur, and ash. Based on the fractions of hydrogen, oxygen, and carbon present in the sample, coal is ranked into four main categories such as bituminous coal, lignite, anthracite, and subbituminous coal [51]. Coal is usually dried at 105°C for 24 h in a muffle furnace or electric furnace to improve the high heating value (HHV). The raw hydrothermally treated moisture-free coal has some oxygenated functional group such as carboxyl, phenolic, hydroxyl, and all acidic groups. Table 1 shows the elemental composition, proximate analysis, and calorific value of the different coals. The ultimate analysis shows that coals contain higher carbon (60–90%). The proximate analysis shows volatiles between 38% and 40% which is less than that present in sewage sludge and bagasse. The calorific value of coal not only depends on the moisture, ash, and oxygen contents, but it also varies with the drying process. The raw coal has a high HHV than residual coal, biomass, and sewage sludge. It has ranged from 8 to 38 MJ/kg. Ash is the leftover residue after combustion at 900°C. The elemental analysis of char obtained from a sample of coal showed trace amounts of Li, B, Na, Mg, Al, P, K, Ca, Fe, and Ba [62]. Bhatt et al. reported the order of relative elemental abundance in coal as Si > Al > Fe > Ca > Mg > K > Na > Sr > V > Zn > Mn > Cr > Cu > Pb > Ni > Co > As > Cd [63]. According to the literature review, to obtain the maximum yield of liquid fuel through efficient pyrolysis operation, it is important to understand the properties, chemical composition, and behavior of different samples of coal. Bituminous coal has been used more often as it contains a higher amount of volatile matter, indicating its higher hydrocarbon potential. Depending on the region from where the coal was extracted, the amount of sulfur may vary between 1% and 4%. Sulfur is an undesirable constituent of coal; it requires a pretreatment step to eliminate to avoid SO_x formation during combustion.

3.2. Ultimate, Proximate, and Chemical Composition Analysis of Lignocellulosic Biomass. Any organic material that can be burned and used as a fuel is called lignocellulosic biomass. It is the most convenient energy resource that can obtain different liquid fuels and bio-oils. Lignocellulosic biomass is a nonfossil and complex biogenic solid composed of many organic and inorganic constituents that originate from natural and technical resources. Natural resources are obtained from land- and water-based vegetation or generated by animal and human food digestion. Technical resources are obtained from the processing of the above natural resources [64]. Some of which are trees, shrubs, bamboos, grass, and plant leaves and waste such as food, rubbish, and industrial and municipal waste. Agriculture and forest

residues are also called lignocellulosic biomass because they are composed of cellulose, hemicellulose, and lignin. Some lignocellulosic biomass may contain extractives up to 10% [65]. Lignocellulosic biomass shows high reactivity during conversion as they contain lower ash, carbon, sulfur, and nitrogen and usually contain a higher amount of volatile matters, hydrogen, oxygen, phosphorous, calcium, and magnesium. Ash obtained from lignocellulosic biomass can capture hazardous material. Using biomass in copyrolysis has many benefits, as these are widely available cheapest sustainable energy resource and neutralize CO₂ in the atmosphere [66]. The chemical composition of lignocellulosic biomass affects thermal copyrolysis behavior. Lignocellulosic biomass containing a higher amount of hemicellulose and cellulose favors a high conversion rate during pyrolysis. The hemicellulose and cellulose degrade at a lower temperature range of 220–400°C while lignin degrades at a higher temperature of 500–900°C [67, 68]. The study of lignocellulosic constituents is relevant in copyrolysis as various constituents behave differently when subjected to thermal degradation. According to Naqvi and Naqvi, lignocellulosic biomass contains 35–50 wt.% cellulose, 20–40 wt.% hemicellulose, 20–27 wt.% lignin, and 1–10 wt.% extractives [26]. Properties differ among the biomass; their mixture or blends can be used to increase or reduce the required content at a certain level. Table 2 summarizes the proximate, ultimate, and chemical composition of different biomass samples. It can be observed that bagasse contains more volatiles than rice husk, showing that bagasse has higher thermal conversion ability than rice husk. Yu et al. find out that by increasing the pyrolysis temperature from 350–600°C, higher heating value (HHV) and volatile matter content of char were also increased [74]. Rice husk and corn stalk released CO₂, CO, CH₄, H₂, and other light hydrocarbons after thermal conversion. Anil et al. investigated the physiochemical properties of various agricultural residues (cotton stalk, rice husk, rice straw, and bagasse) in copyrolysis process [72]. It was observed that biomass has a higher percentage of volatile matter than that of coals and has a higher percentage of hemicellulose 47% as compared to cellulose and lignin. Table 3 depicts the elemental and chemical composition of products obtained from coal, lignocellulosic biomass, sludge, and their blends.

3.3. Ultimate, Proximate, and Chemical Composition Analysis of Sewage Sludge. The major source of sewage sludge is municipal wastewater treatment plants. Sewage sludge is a complex mixture of organic and inorganic substances [86]. The organic constituents are mainly proteins, peptides, lipids, polysaccharides, and plant macromolecules with phenolic structures or aliphatic structures along with organic micropollutants such as polycyclic aromatic hydrocarbons. The inorganic materials come from soil and polymer waste [87]. Samolada and Zabaniotou find out that sewage sludge also contains some precarious materials such as heavy metals, organic pollutants, and pathogens [88]. In most of the studies, the sewage sludge was dried at a certain temperature (<110°C) to improve fuel quality. The dried

TABLE 1: Elemental and chemical composition of coal.

Year	Sample	Proximate analysis (wt.%)				Ultimate analysis (wt.%)					HHV MJ/kg	Ref.
		Moisture	Volatiles	Ash	Fixed carbon	C	H	N	S	O		
2017	Coal	8.59	68.55	6.62	16.14	64.49	7.22	2.09	—	26.20	—	[52]
2017	Bituminous coal	4.18	30.56	15.38	49.88	79.31	4.72	1.03	1.3	13.38	—	[53]
2016	Bituminous coal	4.18	30.56	15.38	49.88	79.31	4.72	1.03	1.3	13.38	25.44	[54]
2016	South African coal	2.1	29.4	13.9	70.6	70.58	3.99	1.77	0.63	7.93	33.2	[55]
2016	Bituminous coal	—	36.8	9.7	53.5	70.5	4.1	1.0	—	14.7	—	[56]
2015	Bituminous coal	—	34.39	11.43	56.91	76.04	4.99	0.86	0.62	8.42	—	[57]
2015	Bituminous coal	2.28	9.09	16.57	72.06	74.50	2.66	1.39	0.48	18.96	28.10	[58]
2015	Bituminous coal	11.22	8.01	30.33	61.66	62.07	2.30	1.16	2.21	1.93	24.38	[59]
2014	Bituminous coal	4.18	30.56	15.38	49.88	79.31	4.72	1.02	1.3	13.38	25.44	[60]
2014	Bituminous coal	3.34	34.25	6.70	55.72	73.16	5.21	4.40	1.53	5.66	—	[61]

TABLE 2: Elemental and chemical composition of lignocellulosic biomass.

Year	Biomass	Proximate analysis (%)				Ultimate analysis (%)					Chemical composition (%)			Ref.
		Moisture	Volatiles	Ash	Fixed carbon	C	H	N	S	O	Cellulose	Hemicellulose	Lignin	
2017	Sugarcane bagasse	6.21	82.38	2.94	8.47	45.3	7.92	0.15	—	46.6				[69]
2017	Sugarcane bagasse	8.5	84.00	5.86	1.64	45.0	5.78	1.75	—	47.4				[69]
2017	Rice husk	10.89	73.41	15.14	11.44	41.9	6.34	1.85	0.47	49.4				[70]
2017	Rice husk	9.5	67.6	16.6	6.3	49.2	2.2	0.40	0.06	48.1				[71]
2016	Sugarcane bagasse	5.4	80.2	3.1	11.3	44.8	5.87	0.24	0.06	48.9	47.6	39	11.2	[72]
2016	Sugarcane bagasse	8.64	73.28	1.71	16.37	41.6	6.21	0.37	0.07	41.3				[73]
2016	Rice husk	8.8	59.2	26.2	14.6	35.6	4.5	0.19	0.02	59.7	35	33	23	[74]
2015	Sugarcane bagasse	4.99	73.5	2.41	19.1	41.9	6.04	0.53	0.24	48.8	35–50	20–30	20–27	[75]
2015	Rice husk	4.7	69.3	15.8	10.2	39.8	5.10	1.09	—	53.8	40.2	24.3	18.1	[76]
2015	Rice husk	3.56	67.93	14.84	13.67	44.8	6.35	0.42	—	48.3				[77]
2014	Sugarcane bagasse	4.99	73.5	2.41	19.1	41.9	6.04	0.53	0.24	48.8	35–50	20–30	2–27	[76]
2014	Sugarcane bagasse	—	90.02	1.33	9.60	47.1	6.14	0.30	—	46.4				[78]
2013	Rice husk	8.43	68.25	14.83	16.92	39.4	5.71	0.67	0.99	54.1	41.52	14.04	33.67	[79]
2013	Rice husk	12.08	60.55	12.35	15.2	45.4	5.40	0.48	0.06	36.05				[80]

lumps of sewage sludge were disintegrated to fine powder. Inguanzo et al. suggested the size range of sewage sludge used for different pyrolysis experiments in fixed bed systems [89]. Table 4 reviews the elemental and chemical composition of sewage sludge obtained from wastewater treatment plants. The volatile matters range between 38% and 70% and ash contents between 1 and 12%. As shown from the ultimate analysis, sewage sludge contains a higher percentage of carbon between 23% and 46% and a lower percentage of nitrogen and hydrogen contents. The extractives are slightly higher, about 7 wt.% dry ash free, than that present in biomasses. These extractives are composed of fatty acids, steroids, and aliphatic compounds and these extractives can improve the liquid fuel properties such as viscosity and

heating value and can provide ease in phase separation of liquid fuels. Sewage sludge contains a relatively higher nitrogen content than lignocellulosic biomass [96]. This comes from the protein fragments of samples and can favor its usage in fertilizer [97]. The proximate analysis reveals that the sewage sludge has a high ash content than lignocellulosic biomass, and this study shows that ash removal system should be installed with reactor while using this type of material. The ash obtained as a result of sewage sludge pyrolysis contains minerals such as quartz and calcite. The elemental analysis gives information regarding the mineral composition in terms of Fe, Ca, Mg, and K which helps catalyze the pyrolysis reaction. Some heavy metals such as Cr, Ni, Co, Hg, Cd, Pb, and Zn are also present in sewage

TABLE 3: Elemental and chemical composition of product obtained from coal, lignocellulosic biomass, sludge, and their blends.

Sample name	Volatile matter (%)	Fixed carbon (%)	Ash (%)	Calorific value (MJ/kg)	C (%)	H (%)	O (%)	N (%)	Ref.
Apricot stone biochar	19.83	71.70	8.47	30.76					
Hazelnut shell biochar	30.26	63.16	6.58	29.08					
Grapeseed biochar	39.45	50.96	9.50	26.73					[81]
Chestnut shell biochar	34.32	60.32	5.36	25.86					
Microalgae + sewage sludge + coal mixtures					9.80–15.89		17.24–53.65		[82]
(Bituminous coal + peanut shell) biochar	45.12–8.46	41.81–71.23	9.53–12.03	23.99–28.79	61.72–79.99	4.64–1.83	21.38–2.07	0.28–0.20	[83]
(Bituminous coal + wheat straw) biochar	35.65–8.67	53.36–77.99	8.15–11.82	16.82–24.07	49.81–70.29	3.99–1.98	36.39–14.95	1.04–0.45	
Sewage sludge biochar	43.9–12.5	4.1–2.7	52–84.1		25.7–9.4	2.8–0.3	66.8–89.5	4.7–1.1	
(Sewage sludge + rice husk) biochar	63.2–31.6	0.4–2.9	36.4–65.5	—	35.8–26.3	3.9–0.6	57.8–71.3	2.8–1.8	[84]
(Sewage sludge + sawdust) biochar	75.1–44.8	2.1–5.7	22.8–52.5		42.5–39.5	5.0–1.5	50.9–56.6	1.6–2.4	
(Dewatered sewage sludge + pine sawdust) biochar	5.64	48.36	46.0		35.87	1.66	13.89	2.06	[85]

sludge [97]. Xu et al. found that sewage sludge contained 60.34% of volatile matters and a lower percentage of carbon content about 36.8% with a HHV of 14.90 MJ/kg [98]. According to the findings of Nadia et al., sewage sludge obtained from municipal wastewater treatment plant contained a higher percentage of carbon and oxygen and has a lower percentage of fixed carbon, ash, and nitrogen [84]. A higher amount of volatile matter makes sewage sludge a better candidate as a feedstock for thermal conversion. Sijiang et al. concluded that higher moisture content in the sewage sludge can lead to the hydrogen-rich fuel which can be compensated by the addition of volatile matters [85]. Xiong et al. described that sewage sludge contained a higher percentage of protein about 27% and a lower percentage of extractives about 9.9% [99].

3.4. Thermal Coconversion

3.4.1. Copyrolysis. Copyrolysis is a simple and effective technique to obtain ideal liquid fuel or bio-oil. It is a process by which two or more different materials are mixed and used as feedstock. Copyrolysis of biomass can change the properties, quantity, and quality of liquid oil with no improvement in the system process. Copyrolysis has better applications in the industry than thermal cracking because of its attractive production and promising features. The successful feature of this technique is the combined effect of different materials. High yield of oil by using different blends of biomass with sewage sludge and coal has originated from hydrocarbons like paraffin, isoparaffins, olefins, naphthenes, and aromatics and a noncondensable gas [100]. The other main advantage of copyrolysis method is that it can reduce many environmental problems by reducing the amount of waste and avoiding disposal as landfills [101].

The operating method and conditions of copyrolysis are the same as that of simple pyrolysis. The process is performed in a reactor system with optimum operating temperatures in the absence of an oxidizing environment to obtain liquid oils. There are three basic steps of the copyrolysis process: the preparation of feedstock, copyrolysis, and condensation [102]. Inert gas is optionally used to displace vapors from the pyrolysis zone. Residence time plays a vital role in minimizing secondary reactions and maximizing oil yield, and suitable residence time suggested by researchers is less than 2 seconds [103].

Table 4 shows a detailed description of the literature survey of the different types of biomass/coal and biomass/sewage sludge blends through copyrolysis, various types of reactors operated under different conditions and providing various products. Akhtar and Amin reviewed that oil yield obtained by the copyrolysis process of biomass, sewage sludge, and coal is also affected by many parameters including the type of biomass, temperature, heating rate, reaction time, and particle size of feed. 45 wt.% of the oil can be obtained by subjecting the biomass blend at the typical temperature range of 400–600°C, and the optimum temperature at which the maximum oil is obtained depends upon the type and characteristics of blends [104]. According to different reviews, the other very important parameter is the ratio of different blends which has a direct influence on the production of oil [105, 106]. The type of reactors can also influence the efficiency of copyrolysis process and can affect the quality and quantity of the product. The best conditions for obtaining a high yield of bio-oil are the high heating rate, moderate temperature, and short residence time. Each reactor has promising features to obtain a specific type of products. For example, for fast pyrolysis to obtain maximum liquid product, fluidized bed reactors are preferred over fixed bed reactors as their operation and scalability are

TABLE 4: Elemental and chemical composition of sewage sludge.

Year	Sewage sludge	Proximate analysis				Ultimate analysis					HV MJ/kg	Biochemical composition		Ref.
		M (%)	VM (%)	FC (%)	Ash (%)	C (%)	H (%)	N (%)	S (%)	O (%)		Protein	Extr.	
2017	Municipal	5.1	60.34	1.13	33.43	36.88	4.94	5.03	1.14	52.01	14.90	—	—	[90]
2017	Wastewater treatment plant	7	50	3	40	27.9	4.7	4.5	1.4	34.6	12.50	28	3.5	[84]
2016	Wastewater treatment plant	5.6	54.2	8.6	37.2	40.6	7.1	7.7	3.3	41.2	11.1	—	—	[91]
2016	Wastewater treatment plant	7.4	63.1	7.1	22.5	38.0	5.1	6.9	1.2	19.0	—	—	—	[92]
2016	Wastewater treatment plant	5.8	54.1	6.0	34.2	34.9	4.8	4.5	1.1	14.8	—	—	—	[93]
2015	Wastewater treatment plant	8.71	61.11	9.20	26.89	45.16	7.20	7.69	—	27.59	16.18	—	—	[94]
2014	Wastewater treatment plant	4.43	68.57	16.42	15.01	53.24	7.39	6.12	—	33.25	24.2	—	—	[95]

simpler. Guo et al. investigated the co-pyrolytic behavior of biomass and coal and low heating rates (10–50°C/min) and higher heating rates (10°C/min) in tubular reactor and furnace and concluded that under inert atmospheric condition, the two fuels experience autonomous thermal conversion, but lower heating rates are better than higher heating rates in terms of better conversion [107]. Wang et al. explored the effect of residence time (30–150 min) on copyrolysis product of sewage sludge and biomass and concluded that extended residence times elevate the pH and ash contents of the biochars, but these conditions decreased the C, N, and H contents [108].

3.4.2. Cocombustion. Cocombustion is a high-temperature thermochemical conversion technique in which sludge/coal, coal/biomass, and biomass/sludge blends undergo thermal degradation and release volatile matter such as CO, CO₂, H₂O, H₂, CH₄, and tar. Among all thermochemical conversion techniques, cocombustion is the only technique used to produce both heat and electricity. The advantages include low cost, high efficiency, and low emission of SO_x and NO_x. The main drawback of using cocombustion technique is its scale forming tendency in the boiler and limitation in using alkali metals. Due to unwanted changes in ash configurations, the proportion of biomass is usually kept limited to approximately 10% of the fuel intake. Cocombustion of biomass with coal is the most important technique with respect to the economic and environmental benefits to curb CO₂ at a certain level [109]. Economically lower capital investment and lower amount of raw material are required, and the risk factor is minimal while using cocombustion techniques. Cocombustion techniques are further classified into three types; one is a direct cocombustion in which biomass or waste is directly fed into the reactor with coal (Figure 5).

In this process, both feedstocks are milled directly and fed individually into the reactor. It has low flexibility; also, the possibility of producing slag and fouling is high. Other is the indirect cocombustion in which separate gasifier should be installed to convert solid feedstock into syngas. It is a more

flexible technique, and the chance of slag formation and fouling is lower. Parallel cocombustion includes the setting up of a separate boiler to produce steam, which is useful in producing electricity. The parallel technique allows a greater amount of biomass and deals with contamination issues. The synergetic effect during cocombustion is usually articulated in terms of the high amount of gases, the high reactivity of the char during cocombustion, and reduction in harmful emission during cocombustion. Cocombustion operating parameters have a large influence on product quality and emission control. Xiao et al. studied the performance of sewage sludge and straw blends in cocombustion environment at heating rate of 10, 20, and 40°K·min⁻¹ and concluded that better efficiency of cocombustion achieved at higher heating rates [111]. Munir et al. investigated the effect of the thermal ratio of different types of biomass in addition to municipal waste in cocombustion environment and found that the adding of biomass enlarged NO lessening under air stage conditions [112].

3.5. Blending Impact. Biomass, coal, and sewage sludge blends in feedstock greatly influence the amount and properties of products. The following are the key points.

3.5.1. Blending Impact on Tar Release. Tar is defined as a mixture of aromatic compounds and derivatives of aromatic compounds produced under the partial oxidation environment at ambient to lower temperatures. The tar content produced during copyrolysis of lignocellulosic biomass, coal, and sewage sludge blends is one of the key factors affecting the succeeding process stages. It is one of the most stimulating elements of the syngas. The main factors that affect the yield of tar during copyrolysis are the type of feedstock and temperature. The blending of coal, sewage sludge, and lignocellulosic biomass particles can lower the yield of tar compared to the pyrolysis of individual feedstocks [113, 114]. Kumabe et al. found that increasing biomass ratio in a blend of lignocellulosic biomass and coal slightly decreased the yield of tar in a downdraft fixed bed reactor at 900°C [50]. Pinto et al. used a blend of 80% coal and 20% pine wood

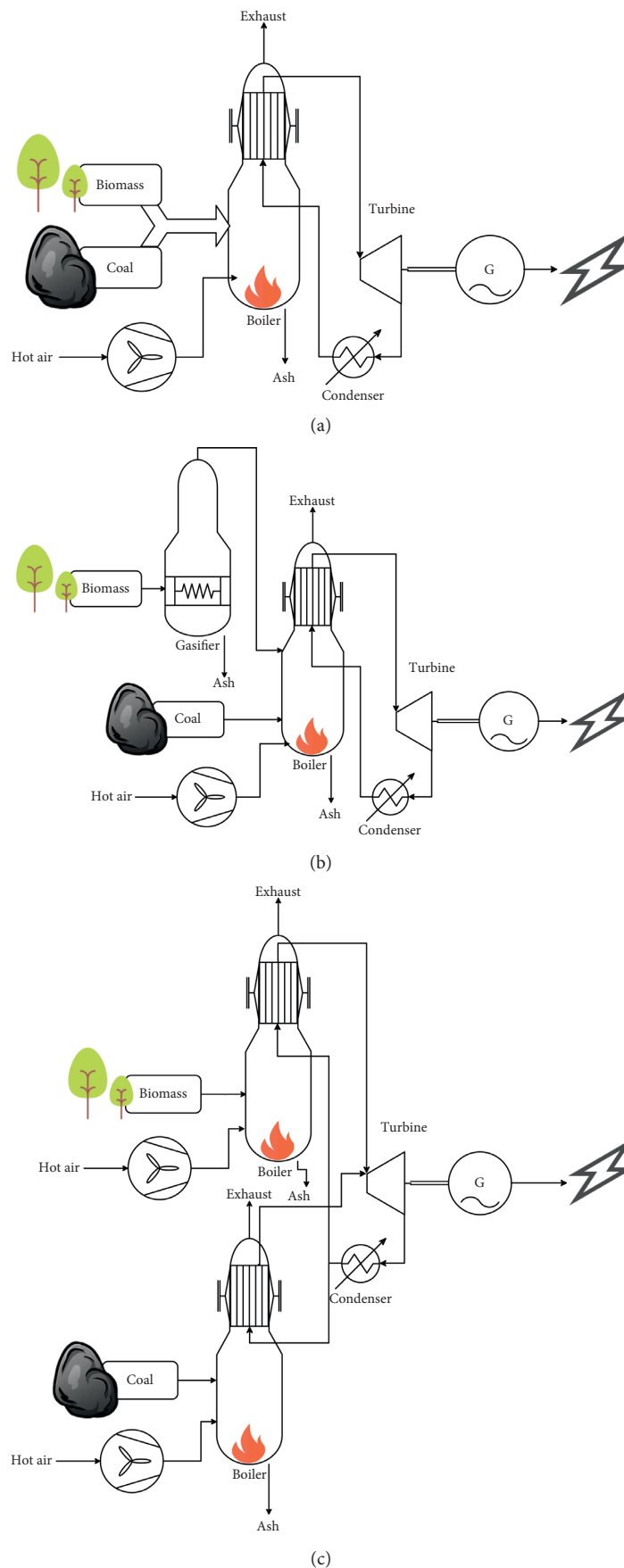


FIGURE 5: Cocombustion techniques: (a) direct cocombustion, (b) indirect cocombustion, and (c) parallel cocombustion [110].

waste in a fluidized bed reactor operating at atmospheric pressure and at a temperature of 850–900°C [115]. They found that an increase in the polyethylene waste into the blend can cause an increase in tar release which can be attributed to the breaking down of the feed element into smaller elements by thermal cracking. This can be avoided by blending three materials: coal, polyethylene waste, and pine that brings down tar release. This effect can also be reduced by using a dolomite catalyst during the cocombustion of coal and biomass/waste mixtures [116]. Collet et al. experimented on a blend of Polish coal and forest residue and found no effect on synergy [117]. Aznar et al. and Andre et al. also acknowledged higher tar yield with an increase in the ratio of biomass percentage of the coal/biomass blend and found a greater impact on synergetic effect during cocombustion at specified conditions [49, 118]. More investigation is still required to briefly explain the issue regarding tar release and its impact on the synergy effect during thermal coconversion of different coal, lignocellulosic biomass, and sewage sludge blends.

3.5.2. Blending Impact on Alkali and Ash. One of the major problems during thermal coconversion of blends is the deposition and formation of alkali and ash which can cause slagging, agglomeration, or fouling on the heat transfer surface of furnace and boiler because of the inorganic constituents of lignocellulosic biomass, waste, and coal mixture. The type of feedstock, operating condition, and flow dynamics have great influence on the characteristics of ash formation. Usually, ash obtained from lignocellulosic biomass has a low melting temperature as compared to ash obtained from coal, so it is necessary to pay attention to the behavior of ash produced from lignocellulosic biomass and coal mixture during copyrolysis or cocombustion. It is necessary to understand the different forms of alkali constituent present in blends and chemical reaction with a specific condition to investigate the ash produced from coal and biomass blends during thermal coconversion. Zheng et al. detected that the percentage of potassium in the fly ash is almost like the ash in the straw during combustion and the cocombustion process [119]. He determined that if the ash composition of the fuel and straw share are known, the total percentage of potassium in fly ash can be predicted. Condensation, vaporization, and agglomerations are the mechanisms used to produce ash during copyrolysis and cocombustion. Alkali metal and chloride present in biomass vaporize and KCl, NaCl, K₂SO₄, and Na₂SO₄ are formed. Strand et al. suggested two primary ways used to condense these vapors into particles: a homogeneous condensation in which vapor condenses into agglomerates and then into a particle, and the other is a heterogeneous condensation where the vapor on the surface of an existing particle entrains in the flue gas [120]. Wu et al. somewhat agree that the abrasive ash particles formed by mechanisms such as coalescence and shedding and fine particles are formed by vaporization and condensation mechanisms [121].

3.5.3. Blending Impact on Char Characteristics. Bernardo et al. investigated the physical and chemical properties of chars obtained in the copyrolysis of three waste plastic, tires, and pine mixtures [122]. He concluded that the yield of char increases with the addition of tire because the addition of plastic waste in copyrolysis of pine biomass had no effect on char yield. The quality of char obtained from copyrolysis has a greater influence on the calorific value. Paradelo et al. found that the char products obtained from the copyrolysis of a blend of biomass and plastic wastes have higher HHV than char obtained from pyrolysis of coal alone [116]. Brebu et al. concluded that char obtained from pyrolysis of pine cone contains higher oxygen content and lower calorific value than the char obtained from copyrolysis [123]. It was also found that the char contains less sulfur, so it can be easily used for the fuel in cocombustion of coal and lignocellulosic biomass. Another advantage of the char obtained from copyrolysis is its potential application as an absorbent to remove heavy metals.

4. Behavior of Thermal Coconversion through TGA

The behavior of thermal coconversion or synergetic effect of different types of coal, lignocellulosic biomass, and sewage sludge can be obtained by using thermal analysis tools such as thermogravimetric (TGA), derivative thermogravimetric (DTG), and differential scanning calorimetric (DSC) analyses (Table 5). TGA is an important tool to measure the percentage of mass loss with respect to temperature and time and to examine the thermal decomposition behavior during pyrolysis. A detailed review of TGA and kinetics of degradation of substances during pyrolysis can help in plan and develop the pyrolysis process [132]. According to different results obtained by TGA, pyrolysis of biomass is usually divided into three main stages; in the first stage, removal of moisture takes place at the temperature range of less than 200°C. In the second stage, from a temperature range of 200–600°C, the main decomposition of substance occurs due to devolatilization and oxidation.

Usually, during this stage cellulose, hemicellulose and lignin decompose and this stage is further subdivided into two parts; in the first part, at lower temperature range (200–450°C), cellulose and hemicellulose of any biomass sample decompose, and at a higher temperature (455°C to 1000°C), lignin is thermally degraded. In the third stage, at a temperature above 600°C, the reduction in the decomposition reaction occurs due to oxidation of char and remaining substance. The leftover material after complete burning is called ash. Ash contains different types of metallic substances that act as catalysts during the pyrolysis process. The weight of the sample in TGA can be varied from 1 to 150 mg, and sample weight greater than 10 mg is often reported with a sensitivity of 0.01 mg. However, lower sample weight of 1–2 mg is usually preferred, making sure the interior sample temperature remains close to the measured furnace

TABLE 5: Thermal coconversion of different samples by using copyrolysis and cocombustion techniques.

Year	Sample	Sample ratio (%)	Reactor type	Experimental conditions				Product	Observations	Ref.
				Temperature	Residence time	Heating rate	Feed			
2017	Sewage sludge + lignocellulosic biomass	SS : B 20 : 80 40 : 60 60 : 40 80 : 20	Moving bed reactor	25–1200°C	30 min	—	200 kg/h	Syngas (H ₂ + CO)	H ₂ content increased from 33% to 47% in blending of 60%SS + 40% biomass	[124]
2017	Coal + lignocellulosic biomass	Coal : B 100 : 0 50 : 50	Tubular furnace	25–900°C	40 min	10°C/min	25 g	Ash	Ash properties were performed for leaching test	[57]
2016	Rice husk + plastic waste	RH : PW 20 : 80 30 : 70 40 : 60 50 : 50	Batch reactor	25–800°C	35 min	5–6°C/min	—	Bio-oil	Around 66% of liquid compounds can be obtained by copyrolysis of 20% of RH blended with plastic waste. More than 20% RH is not favored for liquid oil production	[125]
2016	Coal + lignocellulosic biomass	Coal : B 0:100 25 : 75 50 : 50 75 : 25 100 : 0	Moving bed pyrolyzer	500–850°C	2 h	—	200 g/h	Gases and tar	Tar and gas yields showed an incremental trend with the increase in biomass ratio	[99]
2015	Sewage sludge + rice husk	SS : RH 50 : 50	Vacuum fixed bed reactor	900°C	2 h	10°C/min	10 g	Gas products	Higher amount of SS promoted CO ₂ -C and H ₂ O-C gasification reactions	[126]
2015	Bituminous coal + rice husk	B : coal 0:100 20 : 80 40 : 60 80 : 40 100 : 0	Fixed bed reactor	Up to 900°C	15 min	10–30°C/min	—	Biofuels	Experimental and calculated value observed differently for blended samples	[127]
2015	Sugarcane bagasse + sewage sludge	SS : SB 50 : 50 25 : 75	Pyrolyzer	25–600°C	—	10°C/min	10 mg	Biofuels	Cocombustion process showed lower activation energy	[128]
2014	Sewage sludge + lignocellulosic biomass	SS : B 0:100 30 : 70 50 : 50 70 : 30 100 : 0	TG-MS	40–800°C	—	10°C/min	10 mg	Gas products	CO ₂ , SO ₂ , NH ₃ , HCN, and NO were mainly gaseous species produced at temperature of 523–873°K	[60]

TABLE 5: Continued.

Year	Sample	Sample ratio (%)	Reactor type	Experimental conditions			Feed	Product	Observations	Ref.
				Temperature	Residence time	Heating rate				
2013	Sewage sludge + rice husk	SS:RH 0:100 10:90 20:80 30:70 50:50 70:30 100:0	Fixed bed reactor	25–900°C	1–2 s	10°C/min	2 g	Bio-oil, biogas	Without external heat source, copyrolysis could be the technology to dispose excessive sludge	[129]
2013	Sewage sludge + biomass	SS:B 0:100 100:0 90:10 80:20 70:30 60:40	Fixed bed tubular reactor	25–800°C	—	40°C/min	10 mg	Bio-oil, biogas	Presence of petroleum sludge promotes NH ₃ and HCN formation with biomass coconversion	[130]
2012	Biomass + waste materials	B:WM 30:70 50:50	Autoclave	450°C	15 min	5°C/min	—	Bio-oil, char, gases	A recovery of 63–81% of the pyrolysis oils was observed	[94]
2011	Sewage sludge + rice husk	SS:RH 70:30 50:50 30:70	Fluidized bed reactor	500–650°C	2 s	30°C/min	—	Bio-oil	Combination of feedstock helps in maximizing the volume of feedstock for energy conversion via pyrolysis	[131]

temperature. The sample can be loaded in TGA as a fine powder or small pieces. DTG is a simple analytical tool to determine the amount of mass loss rate as a function of temperature. By examining the DTG curves, the temperature at which maximum rate mass loss appears can be determined by the position of the peaks in the curve. It is also used to find out the kinetic parameters (activation energy, preexponential factor, and order of reaction) of different organic materials during isothermal and nonisothermal conditions.

4.1. Thermogravimetric Analysis of Coal/Biomass Blends.

The thermal coconversion of lignocellulosic biomass and coal blends has the advantage of reducing greenhouse gas emissions, such as sulfur oxides (SO_x) and nitrogen oxides (NO_x) [5]. The conversion of different types of lignocellulosic biomass such as sugarcane bagasse and rice husk blended with coal can be easily realized cheaply with minor modifications in the current coal operating plants to adopt the use of blend. Coconversion of coal and lignocellulosic biomass gives the advantage of using cleaner feedstock to dispose of wastes/biomass safely and economically [133]. Cothermal characteristics of coal and lignocellulosic biomass blends can be examined widely by thermal analytical techniques such as

TG, DTG, and DTA. TGA can rapidly assess the fuel value, the initial temperature at which degradation of component starts, and the final temperature at which degradation of component ends, and other characteristics such as maximum reactivity temperature, the rate of maximum reactivity, and amount of final residue. Thermal methods such as TG, DTG, and DTA have been used extensively to study a variety of thermal characteristics and parameters for the thermal conversion of different materials with coal. Thermal analysis can be used also to estimate kinetic parameters of different thermal processes. The main concern of the thermogravimetric study is to show that the decrease in particle size can cause a decline in ignition temperature. Thermal analysis of different coal and lignocellulosic biomass samples showed different stages in terms of temperature ranges during pyrolysis, combustion, and gasification processes. In coal-biomass blends, three different stages can be commonly observed. During the first stage, removal of moisture is carried out, and during the second stage, decomposition of cellulose and hemicellulose components occurs, and in the third stage, lignin degradation can be observed. By using the blends of biomass and coal, the decomposition of biomass is more dominant in the second stage than the decomposition of coal and the third stage is decomposition of coal with

TABLE 6: A list of literature about the thermal coconversion of coal and lignocellulosic biomass using thermogravimetric analysis.

Year	Sample	Experimental facility	Blends coal: biomass	Thermal behavior	Medium	Initial mass (mg)	Heating rate (°C/min)	Temperature range (°C)	T _v ^a	T _f ^b	-DTG _{max} ^c	TDTG _{max} ^d (°C)	Ref.
2017	Coal and bagasse	TGA-DTG	80:20	Combustion	CO ₂	12	5	25–900	460 380	604 570	1.8%/°C 0.8%/°C	300, 470	[124]
2017	Coal and hazelnut shell	TGA-DTG with MS	25:75 50:50 75:25	Combustion	Air	10	20	25–950	376 363 349	602 633 635	12%/min 10%/min 7%/min	415 416 425	[57]
2016	Coal and rice husk	TG-DTA	80:20 60:40 40:60 20:80	Combustion	Air	5	2.5 5 10 20	25–900	574 545 534 524	772 770 760 749	2.4%/°C 1.5%/°C 1.0%/°C 1.3%/°C	738 737 722 598	[125]
2015	Bituminous coal and rice straw	TG-DTG	80:20 60:40 40:60 20:80	Pyrolysis	Nitrogen	—	10 15 20 25 30	25–900	220–240	346–740	0.08–0.5%/°C	330–350	[127]
2015	Coal and sugarcane bagasse	TG-DTG	80:20 60:40 40:60 20:80	Pyrolysis	Nitrogen	25	10	25–1100	160	900	0.16%/°C 0.31%/°C 0.49%/°C 0.63%/°C	308, 353, 440	[134]
2014	Bituminous coal and bagasse	TG-DTG	75:25 4:1 3:2	Pyrolysis	Nitrogen	10	10 20 40	25–950	318, 208, 271	346, 293, 461	5.8%/min 1.2%/min	346, 293, 349	[60]
2014	Coal and bagasse	TG-DTA	1:1 2:3 1:4 90:10 80:20 70:30 60:40 50:50	Gasification	CO ₂	20	5	25–1300	295 294 296 290 291	416 390 384 376 374	0.99%/°C 1.77%/°C 2.11%/°C 2.50%/°C 3.28%/°C	346 345 344 344 343	[135]
2013	Coal and sugarcane bagasse	TG-DTG	0.2 0.4 0.6 0.8	Pyrolysis	Nitrogen	5–25	20	25–900	210–390	390–450	9–10.8%/min	210, 365	[136]
2013	Lignite and rice husk	TG-DTA	2.5 5 10 20 25 30	Pyrolysis	Nitrogen	5	10	25–800	200	400	—	330, 490	[137]
2013	Bituminous coal and sugarcane bagasse	TG-DTA	75:25	Combustion	Air	7	10 20 25 30	25–750	200	600	0.05%/min	330	[138]

a = T_v; b = T_f; c = -DTG_{max}; d = TDTG_{max}.

residual biomass. The major gaseous pollutants released from the thermal processes CO, CO₂, CH₄, NO, and SO₂ were studied previously by TG-DTA. The thermal behavior of the material during thermal analysis techniques depend on heating rates (5, 10, 20, 30, 40, 50, and 100°C/min), reacting medium or environment (inert and oxidative by using N₂, argon, O₂, and CO₂), mass and size of the sample used, and temperature ranges to be operated. These parameters can affect the product distribution and percentage of solid-liquid and gaseous fuels. Knowledge of these parameters can help to optimize the process. Table 6 gives a detailed description of a literature survey on the thermal behavior of various biomass and coal blends using different thermal analysis techniques. The commonly used blend ratios are 1 : 1, 2 : 3, 3 : 4, 4 : 3, and 3 : 2. Recently, Kandasamy Jayaraman et al. studied coal and biomass blends and they concluded that by increasing the ratio of biomass in the blends, the mass loss percentage increases, indicating the high reactivity of samples, and the activation energies were also increased by increasing biomass ratio in the blends [57]. Betancur et al. studied that coal and biomass blends increased combustion efficiency [124]. Blends showed lower ignition temperatures, and activation energies were decreased in the CO₂ environment as compared to N₂. Guangwei Wang et al. stated the synergistic effect of the combustion process of coal and biomass blends was prevalent as they increased the ignition performance by increasing the ratio of biomass [125]. Li et al. studied the copyrolysis of the coal and biomass blends and indicated the deviations in weight fractions [127].

4.2. Thermogravimetric Analysis of Sewage Sludge/Biomass Blends. Cothermal processes such as copyrolysis and cocombustion of sewage sludge with different types of lignocellulosic biomass can be applied for converting sewage sludge into useful energy and construction materials [139]. The other advantage of copyrolysis and cocombustion can help in reducing hazardous emissions to the atmosphere. Sludge has a low HHV, so burning of sewage sludge alone is neither cost-effective nor environmentally friendly. The blending of sewage sludge with lignocellulosic biomass material can make burning easier. The physical and chemical properties of the different materials used can affect the characteristics of the thermal process and residue obtained [140]. TGA is effective in studying the thermal behavior and characteristics of combustion of sewage sludge, biomass, coal, and other materials [141, 142]. It is an important technique to measure the percentage of mass loss of a sample with respect to temperature and time and to examine the thermal decomposition behavior during copyrolysis and cocombustion. It is also helpful in studying the kinetics of degradation of organic material during copyrolysis and cocombustion processes. Thermal degradation is a key element in designing sustainable copyrolysis and cocombustion processes. The thermal degradation of lignocellulosic biomass and sewage sludge is a very complicated process because of a variety of reactions. Conversion of different solid biomass and sewage sludge blends to gaseous and liquid products is difficult and complicated, so TG-DTA

can be helpful by interpreting the kinetics to better understand the cocombustion and copyrolysis processes. The advantage of TGA is that it can easily assess the fuel value and the temperature at which combustion, pyrolysis, and gasification start and end. It can provide information about the highest reactivity temperature, the total amount of ash remaining, and complete burning time, and these techniques are important to study the thermal behavior of the pyrolysis process. The other advantage of TG-DTA is that it can determine the purity of mineral, organic, and inorganic compounds [75]. Ergudenler et al. describe that the weight of the sample can be varied from range 1–150 mg; usually, the weight of sample greater than 10 mg is preferred with a sensitivity of 0.01 mg. But if the excellent results are required, weight must be 1–2 mg [143].

Table 7 describes the detailed description of the literature about the TG-DTA analysis of a different type of sample to study the pyrolysis and copyrolysis behavior under certain conditions. Mian Hu et al. stated that by blending sewage sludge with biomass (pine sawdust), the devolatilization properties of sewage sludge increased whereas the initial decomposition temperatures increased by increasing biomass ratio [144]. Jiang et al. stated that by increasing the ratio of biomass with sewage sludge, the reactivity of blends increases [145]. Yang et al. studied the synergistic effect of copyrolysis of sewage sludge and wheat straw. The synergistic effect resulted in speeding up the pyrolysis process, the increase in the volatiles, and reduction in char yield. The synergistic effect was maximum at a biomass proportion of 60% [146].

4.3. Thermogravimetric Analysis of Coal/Sewage Sludge Blends. TGA is a useful tool to examine the copyrolysis and cocombustion behavior of sewage sludge, coal, and their mixture. Different atmospheric conditions (inert condition for copyrolysis and oxidizing condition for cocombustion) can be used.

Table 8 describes the detailed description of thermal coconversion of coal and sewage sludge obtained from different sources through thermogravimetric analysis to examine the copyrolysis or cocombustion characteristics. Previous studies on the TGA of thermal coconversion of coal and dewatered sewage sludge blends show that the addition of 10% of sewage sludge in the coal-sludge blend has hardly brought any change in heat release and weight loss during thermal coconversion processes [147, 148]. Barbosa et al. worked on the sewage sludge and coal blend impregnated with molasses to study the cocombustion characteristics and found that fuel quality obtained from this type of blend was improved [149]. But the char characteristics remained the same as that of bituminous coal. Zhuo et al. experimented on 80% coal and 20% sludge blends to study the cocombustion behavior under N₂/O₂ and CO₂/O₂ atmosphere and find out that blend gives distinctive combustion peaks as compared to combustion of sludge [150]. Jin et al. studied the influence of the blend ratio of 60% coal and 40% dewatered sewage sludge on flammability index, combustion characteristic index, and release of harmful emission and heavy metals

TABLE 7: A list of literature about the thermal coconversion of sewage sludge and lignocellulosic biomass using thermogravimetric analysis.

Year	Sample	Experimental facility	Blending SS: Biomass	Thermal behavior	Medium	Initial Mass mg	Temp range (°C)	Heating rate (°C/min)	T _v ^a	T _f ^b	-DTG _{max} ^c (%/min)	TDTG _{max} ^c (°C)	Ref.
2017	Rice husk and sewage sludge	TG-DTG	70:30	Combustion	Air	10	25-1000	25	272.1	532.5	9.75	333.8	[77]
			50:50						269.1	559.6	10.90	295.1	
			30:70						264.8	547.5	10.05	338.5	
2016	Sewage sludge and rice straw	TG-DTA	25:75	Combustion	Air	5	25-800	20	263	765	9	299.2	[78]
			50:2:50 75:25						258	745	12.5	299.3	
2016	Sewage sludge and biomass	TG-DTA	80:20	Pyrolysis	Nitrogen	—	30-1000	20	179	727	343	6.54	[79]
			60:40						180	719	344	8.54	
			40:60						181	603	344	10.59	
2015	Sludge + lingo-cellulosic biomass	TG-DTA	20:80	Pyrolysis	Nitrogen	—	25-900	15	182	602	344	12.68	
			50:50						200	575	—	370	
2015	Sewage sludge and rice straw	TG-DTA	50:50	Pyrolysis	Nitrogen	—	150-500	20	200	500	16	330	
			25:75										
2015	Sewage sludge and sawdust	TG-DTA	50:50	Pyrolysis	Nitrogen	10	25-1000	10	315	900	—	650	
			75:25										
			10:90										
2013	Sewage sludge and rice husk	TG-DTG	20:80	Pyrolysis	Nitrogen	10	25-900	20	200	500	6.05	310	
			30:70										
			50:50										
			70:30										

a = T_v; b = T_f; c = -DTG_{max}; d = TDTG_{max}.

TABLE 8: A list of literature pertaining to the thermal coconversion of coal and sludge using thermogravimetric analysis.

Year	Sample	Experimental facility	Blends coal: sludge	Thermal behavior	Medium	Initial mass (mg)	Temperature range (°C)	Heating rate (C/min)	T _v ^a	T _f ^b	DTG _{max} ^c (%/min)	TDTG _{max} ^c (°C)	Reference
2017	Coal and sewage sludge	TGA-DTG	50:50	Cocombustion	Air	15	25–800	20	200	600	0.80	450	[82]
2017	Coal and textile dying sludge	TGA-DSC	80:20	Cocombustion	Air	10.5	20–1000	20	536.6	682.7	11.4	605.7	[83]
2016	Coal and sewage sludge	TGA-DTG	40:20	Cocombustion	Air	10	20–1000	25	428	800	1.5	550	[90]
2016	Bituminous coal and sludge	TG-DTG	90:10	Copyrolysis	N ₂	25	25–1200	5	475	1200	0.0114	605	[91]
2016	Bituminous coal and sludge	TG-DTG	90:10	Cocombustion	O ₂	25	25–1200	5	505	1105	0.1128	900	[91]
2015	Coal and sewage sludge	TG-DTG	1:1, 2:1, 3:1	Cocombustion	Air	5	30–900	20	200	650	10	450	[92]
2014	Coal and sewage sludge	TG-DTG	10:90, 20:80, 30:70, 50:50	Copyrolysis	N ₂	10	25–1200	30	200	850	0.16	420	[93]
2013	Coal and sewage sludge	TG-DTG	90:10	Cocombustion	Air	15	25–1000	10, 40, 100	200	800	0.03	450	

a = T_v; b = T_f; c = -DTG_{max}; d = TDTG_{max}.

[151]. This effect is ignorable if the dewatered sewage sludge ratio is kept at less than 20%. Coimbra et al. studied the copyrolysis and cocombustion behavior of bituminous coal and pulp mill sludge blend of ratio 90 : 10 and concluded that cocombustion behavior of blend is similar to that of conversion behavior of coal alone, but the copyrolysis of blends occurs at lower devolatilization temperature than that of pyrolysis of coal [52]. Zhang et al. also studied the combustion characteristics of blends of different ratios of sewage sludge and coal [53]. Xia and Li concluded from their result that the TG and DTG profiles of sewage sludge should be the same as the profile of coal but different from coal under different blending ratios [152].

5. Future Perspectives

This review provides a detailed description on the thermal coconversion of different biomass, sewage sludge, and coal blends through TGA to obtain optimum energy recovery entrained from a different type of sewage sludge, biomass, and coal; however, there are still many challenges to solve the problem related to the copyrolysis and cocombustion of blends. To overcome these challenges, some steps should be taken to improve the process in order to obtain maximum conversion. The production of biofuels through thermal coconversion processes is not fully established on a commercial scale, so work should be done to make it better energy recovery option commercially. The different kinetic models should be developed to find out the optimum operating condition to design the copyrolysis or cocombustion process to obtain the highest yield with lower investment. More research is required in the field of thermal coconversion of coal, biomass, and sewage sludge blends in which focus should be on scaling up and cost reduction. A computational model should be developed to optimize the physical, chemical, and reaction parameters that will help to design the process.

6. Conclusions

This review investigates the thermal coconversion of biomass/sewage sludge, coal/sewage sludge, and coal/biomass by using thermogravimetric analysis (TGA). Different elemental, chemical composition, and experimental conditions like the type of sample, type of reactors, different temperature ranges, heating rates, and residence time were reviewed to observe synergetic effects during copyrolysis of sewage sludge, lignocellulosic biomass, and coal blends. Many researchers have acknowledged that the copyrolysis process can expressively improve the yield and eminence of pyrolysis oil without helping aid such as catalysts, solvents, and pressure.

This technique can be considered as a simple, cheap, and effective to obtain the optimum yield. This study will provide a better understanding to reduce the failure points in obtaining and applying the copyrolysis process to obtain the maximum yield of the product. A detailed review of TGA of copyrolysis of different substances like sewage sludge, lignocellulosic biomass, and coal blends, therefore, can help

plan and develop efficient industrial copyrolysis process. Based on the critical analysis, the following recommendations are suggested for future perspective:

- (i) Low energy intensive operation with high-quality products techniques should be explored
- (ii) Feedstock advance pretreatment processes could be adopted to enhance the devolatilization
- (iii) Synergistic effect of biomass types with other residues and their interactions should be comprehensively investigated
- (iv) Strict dewatering and drying steps are required before thermal coconversion processes proceeding for higher energy consumption
- (v) Researcher should investigate the economic and environmental concern related to thermal coconversion processes to reduce greenhouse gases

Conflicts of Interest

The authors declare that they have no conflicts of interest.

Acknowledgments

This study was supported by Karlstad University, Sweden, and the National University of Sciences and Technology, Pakistan.

References

- [1] S. R. Naqvi, I. Ali, S. Nasir et al., "Assessment of agro-industrial residues for bioenergy potential by investigating thermo-kinetic behavior in a slow pyrolysis process," *Fuel*, vol. 278, Article ID 118259, 2020.
- [2] M. H. Tahir, Z. Zhao, J. Ren, T. Rasool, and S. R. Naqvi, "Thermo-kinetics and gaseous product analysis of banana peel pyrolysis for its bioenergy potential," *Biomass and Bioenergy*, vol. 122, pp. 193–201, 2019.
- [3] U. Jamil, A. H. Khoja, R. Liaquat, S. R. Naqvi, W. N. N. Wan Omar, and N. A. S. Amin, "Copper and calcium-based metal organic framework (MOF) catalyst for biodiesel production from waste cooking oil: A process optimization study," *Energy Conversion and Management*, vol. 215, Article ID 112934, 2020.
- [4] M. Shahbaz, T. Al-Ansari, M. Aslam et al., "A state of the art review on biomass processing and conversion technologies to produce hydrogen and its recovery via membrane separation," *International Journal of Hydrogen Energy*, vol. 45, no. 30, pp. 15166–15195, 2020.
- [5] Z. Khan, S. Yusup, M. Aslam et al., "NO and SO₂ emissions in palm kernel shell catalytic steam gasification with in-situ CO₂ adsorption for hydrogen production in a pilot-scale fluidized bed gasification system," *Journal of Cleaner Production*, vol. 236, Article ID 117636, 2019.
- [6] Y. Uemura, N. T. T. Tran, S. R. Naqvi, and N. Nishiyama, "Nano-catalysts for upgrading bio-oil: catalytic decarboxylation and hydrodeoxygenation," in *Proceedings of the AIP Conference*, AIP Publishing LLC, Bydgoszcz, Poland, 2017.
- [7] Z. Hameed, Z. Aman, S. R. Naqvi, R. Tariq, I. Ali, and A. A. Makki, "Kinetic and thermodynamic analyses of sugar cane bagasse and sewage sludge co-pyrolysis process," *Energy & Fuels*, vol. 32, no. 9, pp. 9551–9558, 2018.

- [8] S. R. Naqvi, Z. Hameed, R. Tariq et al., "Synergistic effect on co-pyrolysis of rice husk and sewage sludge by thermal behavior, kinetics, thermodynamic parameters and artificial neural network," *Waste Management*, vol. 85, pp. 131–140, 2019.
- [9] S. R. Naqvi, R. Tariq, Z. Hameed et al., "Pyrolysis of high-ash sewage sludge: thermo-kinetic study using TGA and artificial neural networks," *Fuel*, vol. 233, pp. 529–538, 2018.
- [10] M. Khan, M. T. Mehran, S. R. Naqvi et al., "Role of perovskites as a bi-functional catalyst for electrochemical water splitting: a review," *International Journal of Energy Research*, 2020, In press.
- [11] M. Ayoub, W. J. Wei, M. Ahmad et al., "Glycerol conversion to diglycerol via etherification under microwave irradiation," In *Triglycerides and Cholesterol*, IntechOpen, London, UK, 2020.
- [12] N. Gao, X. Jia, G. Gao, Z. Ma, C. Quan, and S. R. Naqvi, "Modeling and simulation of coupled pyrolysis and gasification of oily sludge in a rotary kiln," *Fuel*, vol. 279, Article ID 118152, 2020.
- [13] R. M. Soncini, N. C. Means, and N. T. Weiland, "Co-pyrolysis of low rank coals and biomass: product distributions," *Fuel*, vol. 112, pp. 74–82, 2013.
- [14] M. Rehan, A.-S. Nizami, U. Rashid, and M. R. Naqvi, "Waste biorefineries: future energy, green products and waste treatment," *Frontiers in Energy Research*, vol. 7, p. 55, 2019.
- [15] S. R. Naqvi, R. Tariq, Z. Hameed et al., "Pyrolysis of high ash sewage sludge: kinetics and thermodynamic analysis using coats-redfern method," *Renewable Energy*, vol. 131, pp. 854–860, 2019.
- [16] M. Balat, "Influence of coal as an energy source on environmental pollution," *Energy Sources, Part A: Recovery, Utilization, and Environmental Effects*, vol. 29, no. 7, pp. 581–589, 2007.
- [17] I. C. I. A. J. I. e. a. Board, *Insights Series, 21st Century Coal-Advanced Technology and Global Energy Solution*, 2013.
- [18] I. E. Agency and F. Birol, *World Energy Outlook 2013*, International Energy Agency, Paris, France, 2013.
- [19] S. R. Naqvi, S. Jamshaid, M. Naqvi et al., "Potential of biomass for bioenergy in Pakistan based on present case and future perspectives," *Renewable and Sustainable Energy Reviews*, vol. 81, pp. 1247–1258, 2018.
- [20] J. Yan, M. Raza Naqvi, and E. Dahlquist, "Bioenergy poly-generation, carbon capture and storage related to the pulp and paper industry and power plants," *Biomass as Energy Source*, pp. 163–176, CRC Press, Boca Raton, FL, USA, 2013.
- [21] A. T. Ubando, W.-H. Chen, R. R. Tan, and S. R. Naqvi, "Optimal integration of a biomass-based polygeneration system in an iron production plant for negative carbon emissions," *International Journal of Energy Research*, 2019.
- [22] M. Naqvi, J. Yan, E. Dahlquist, and S. R. Naqvi, "Waste biomass gasification based off-grid electricity generation: a case study in Pakistan," *Energy Procedia*, vol. 103, no. 103, pp. 406–412, 2016.
- [23] M. Naqvi, J. Yan, E. Dahlquist, and S. R. Naqvi, "Off-grid electricity generation using mixed biomass compost: a scenario-based study with sensitivity analysis," *Applied Energy*, vol. 201, pp. 363–370, 2017.
- [24] C. A. Salman, M. Naqvi, E. Thorin, and J. Yan, "Gasification process integration with existing combined heat and power plants for polygeneration of dimethyl ether or methanol: a detailed profitability analysis," *Applied Energy*, vol. 226, pp. 116–128, 2018.
- [25] S. Niu, M. Chen, Y. Li, and T. Lu, "Combustion characteristics of municipal sewage sludge with different initial moisture contents," *Journal of Thermal Analysis and Calorimetry*, vol. 129, no. 2, pp. 1189–1199, 2017.
- [26] S. R. Naqvi and M. Naqvi, "Catalytic fast pyrolysis of rice husk: influence of commercial and synthesized microporous zeolites on deoxygenation of biomass pyrolysis vapors," *International Journal of Energy Research*, vol. 42, no. 3, pp. 1352–1362, 2018.
- [27] U. Sikander, M. F. Samsudin, S. Sufian et al., "Tailored hydroxalite-based Mg-Ni-Al catalyst for hydrogen production via methane decomposition: effect of nickel concentration and spinel-like structures," *International Journal of Hydrogen Energy*, vol. 44, no. 28, pp. 14424–14433, 2019.
- [28] F. Abnisa, W. M. A. Wan Daud, and Management, "A review on co-pyrolysis of biomass: an optional technique to obtain a high-grade pyrolysis oil," *Energy Conversion and Management*, vol. 87, pp. 71–85, 2014.
- [29] J. Alvarez, M. Amutio, G. Lopez, J. Bilbao, and M. Olazar, "Fast co-pyrolysis of sewage sludge and lignocellulosic biomass in a conical spouted bed reactor," *Fuel*, vol. 159, pp. 810–818, 2015.
- [30] S. Malik, F. Fatima, A. Imran et al., "Improved project control for sustainable development of construction sector to reduce environment risks," *Journal of Cleaner Production*, vol. 240, Article ID 118214, 2019.
- [31] M. Bassyouni, I. Ali, and S. M. S. Abdel-hamid, "Study of thermo-kinetic properties of graphite micro-platelet-enriched vinyl ester composites," *Journal of Thermal Analysis and Calorimetry*, vol. 131, no. 2, pp. 1055–1065, 2018.
- [32] K.-M. Lu, W.-J. Lee, W.-H. Chen, and T.-C. Lin, "Thermogravimetric analysis and kinetics of co-pyrolysis of raw/torrefied wood and coal blends," *Applied Energy*, vol. 105, pp. 57–65, 2013.
- [33] I. Ali, "Misuse of pre-exponential factor in the kinetic and thermodynamic studies using thermogravimetric analysis and its implications," *Bioresource Technology Reports*, vol. 2, pp. 88–91, 2018.
- [34] M. H. Tahir, G. Çakman, J. L. Goldfarb, Y. Topcu, S. R. Naqvi, and S. Ceylan, "Demonstrating the suitability of canola residue biomass to biofuel conversion via pyrolysis through reaction kinetics, thermodynamics and evolved gas analyses," *Bioresource Technology*, vol. 279, pp. 67–73, 2019.
- [35] A. Magdziarz and M. Wilk, "Thermogravimetric study of biomass, sewage sludge and coal combustion," *Energy Conversion and Management*, vol. 75, pp. 425–430, 2013.
- [36] A. Inayat, M. Ayoub, A. Z. Abdullah, S. Ullah, and S. R. Naqvi, "Decomposition of N₂O at low temperature over CO₃O₄ prepared by different methods," *Environmental Progress & Sustainable Energy*, vol. 38, no. 4, p. 13129, 2019.
- [37] Z. Gogebakan, Y. Gogebakan, and N. Selçuk, "Co-firing of olive residue with lignite in bubbling FBC," *Combustion Science and Technology*, vol. 180, no. 5, pp. 854–868, 2008.
- [38] A. Bokhari, L. F. Chuah, L. Z. Y. Michelle et al., "Microwave enhanced catalytic conversion of canola-based methyl ester: optimization and parametric study," in *Advanced Biofuels*, pp. 153–166, Elsevier, Amsterdam, Netherlands, 2019.
- [39] M. Naqvi, E. Dahlquist, A.-S. Nizami et al., "Gasification integrated with small chemical pulp mills for fuel and energy production," *Energy Procedia*, vol. 142, pp. 977–983, 2017.
- [40] N. Hossain, J. H. Zaini, and T. J. I. J. o. T. Mahlia, "A review of bioethanol production from plant-based waste biomass by yeast fermentation," *International Journal of Technology*, vol. 8, no. 1, p. 5, 2017.

- [41] N. Hossain, J. Zaini, and T. M. I. Mahlia, "Experimental investigation of energy properties for *Stigonematales* sp. microalgae as potential biofuel feedstock," *International Journal of Sustainable Engineering*, vol. 12, no. 2, pp. 123–130, 2019.
- [42] N. Hossain and T. M. I. Mahlia, "Progress in physicochemical parameters of microalgae cultivation for biofuel production," *Critical Reviews in Biotechnology*, vol. 39, no. 6, pp. 835–859, 2019.
- [43] S. R. Naqvi, Y. Uemura, N. B. Osman, S. Yusup, and M. F. Nuruddin, "Physicochemical properties of pyrolysis oil derived from fast pyrolysis of wet and dried rice husk in a free fall reactor," in *Applied Mechanics and Materials*, Trans Tech Publications, Stafa-Zurich, Switzerland, 2014.
- [44] A. Christodoulou and K. Stamatelatu, "Overview of legislation on sewage sludge management in developed countries worldwide," *Water Science and Technology*, vol. 73, no. 3, pp. 453–462, 2015.
- [45] D. Fytli and A. Zabaniotou, "Utilization of sewage sludge in EU application of old and new methods-a review," *Renewable and Sustainable Energy Reviews*, vol. 12, no. 1, pp. 116–140, 2008.
- [46] M. Buyukada, "Uncertainty estimation by Bayesian approach in thermochemical conversion of walnut hull and lignite coal blends," *Bioresource Technology*, vol. 232, pp. 87–92, 2017.
- [47] L. Zhang, S. Xu, W. Zhao, and S. Liu, "Co-pyrolysis of biomass and coal in a free fall reactor," *Fuel*, vol. 86, no. 3, pp. 353–359, 2007.
- [48] Y. G. Pan, E. Velo, X. Roca, J. J. Manyà, and L. Puigjaner, "Fluidized-bed co-gasification of residual biomass/poor coal blends for fuel gas production," *Fuel*, vol. 79, no. 11, pp. 1317–1326, 2000.
- [49] M. P. Aznar, M. A. Caballero, J. A. Sancho, and E. Francés, "Plastic waste elimination by co-gasification with coal and biomass in fluidized bed with air in pilot plant," *Fuel Processing Technology*, vol. 87, no. 5, pp. 409–420, 2006.
- [50] K. Kumabe, T. Hanaoka, S. Fujimoto, T. Minowa, and K. Sakanishi, "Co-gasification of woody biomass and coal with air and steam," *Fuel*, vol. 86, no. 5–6, pp. 684–689, 2007.
- [51] H. N. S. Schafer, "Carboxyl groups and ion exchange in low-rank coals," *Fuel*, vol. 49, no. 2, pp. 197–213, 1970.
- [52] R. N. Coimbra, S. Paniagua, C. Escapa, L. F. Calvo, and M. Otero, "Thermal valorization of pulp mill sludge by co-processing with coal," *Waste and Biomass Valorization*, vol. 7, no. 4, pp. 995–1006, 2016.
- [53] L. Zhang, F. Duan, and Y. Huang, "Effect of organic calcium compounds on combustion characteristics of rice husk, sewage sludge, and bituminous coal: thermogravimetric investigation," *Bioresource Technology*, vol. 181, pp. 62–71, 2015.
- [54] G. K. Parshetti, A. Quek, R. Betha, and R. Balasubramanian, "TGA-FTIR investigation of co-combustion characteristics of blends of hydrothermally carbonized oil palm biomass (EFB) and coal," *Fuel Processing Technology*, vol. 118, pp. 228–234, 2014.
- [55] J. Q. Xia and H. P. Li, "Co-pyrolysis characteristics study of dianchi lake sludge and coal," *Advanced Materials Research*, vol. 860–863, pp. 518–521, 2014.
- [56] D.-X. Li, J.-B. Liu, M. R. Farahani, M. Imran, and M. K. Jamil, "Techno-economic study of coal pyrolysis for production of chemicals using a high-pressure fluidized bed," *Energy Sources, Part B: Economics, Planning, and Policy*, vol. 12, no. 7, pp. 654–658, 2017.
- [57] K. Jayaraman, M. V. Kok, and I. Gokalp, "Thermogravimetric and mass spectrometric (TG-MS) analysis and kinetics of coal-biomass blends," *Renewable Energy*, vol. 101, pp. 293–300, 2017.
- [58] Z. Wu, W. Yang, H. Meng et al., "Physicochemical structure and gasification reactivity of co-pyrolysis char from two kinds of coal blended with lignocellulosic biomass: effects of the carboxymethylcellulose sodium," *Applied Energy*, vol. 207, pp. 96–106, 2017.
- [59] S. Zellaoui, C. Schönnenbeck, N. Zouaoui-Mahzoul et al., "Pyrolysis of coal and woody biomass under N₂ and CO₂ atmospheres using a drop tube furnace—experimental study and kinetic modeling," *Fuel Processing Technology*, vol. 148, pp. 99–109, 2016.
- [60] Z. Wu, S. Wang, J. Zhao, L. Chen, and H. Meng, "Synergistic effect on thermal behavior during co-pyrolysis of lignocellulosic biomass model components blend with bituminous coal," *Bioresource Technology*, vol. 169, pp. 220–228, 2014.
- [61] Y. Zhang and Y. Zheng, "Co-gasification of coal and biomass in a fixed bed reactor with separate and mixed bed configurations," *Fuel*, vol. 183, pp. 132–138, 2016.
- [62] M. Rahman, A. Samanta, and R. Gupta, "Production and characterization of ash-free coal from low-rank Canadian coal by solvent extraction," *Fuel Processing Technology*, vol. 115, pp. 88–98, 2013.
- [63] M. S. Bhatt, "Effect of ash in coal on the performance of coal fired thermal power plants. Part I: primary energy effects," *Energy Sources, Part A: Recovery, Utilization, and Environmental Effects*, vol. 28, no. 1, pp. 25–41, 2006.
- [64] B.-J. Lin, W.-H. Chen, T.-H. Hsieh, H. C. Ong, P. L. Show, and S. R. Naqvi, "Oxidative reaction interaction and synergistic index of emulsified pyrolysis bio-oil/diesel fuels," *Renewable Energy*, vol. 136, pp. 223–234, 2019.
- [65] S. R. Naqvi, Y. Uemura, N. Osman, and S. Yusup, "Production and evaluation of physicochemical characteristics of paddy husk bio-char for its C sequestration applications," *BioEnergy Research*, vol. 8, no. 4, pp. 1800–1809, 2015.
- [66] Z. Wu, Y. Li, D. Xu, and H. Meng, "Co-pyrolysis of lignocellulosic biomass with low-quality coal: optimal design and synergistic effect from gaseous products distribution," *Fuel*, vol. 236, pp. 43–54, 2019.
- [67] M. Naqvi, E. Dahlquist, and J. Yan, "Complementing existing CHP plants using biomass for production of hydrogen and burning the residual gas in a CHP boiler," *Biofuels*, vol. 8, no. 6, pp. 675–683, 2017.
- [68] A. S. Qureshi, I. Khushk, S. R. Naqvi et al., "Fruit waste to energy through open fermentation," *Energy Procedia*, vol. 142, pp. 904–909, 2017.
- [69] Q. Sohaib, A. Muhammad, and M. Younas, "Fast pyrolysis of sugarcane bagasse: effect of pyrolysis conditions on final product distribution and properties," *Energy Sources, Part A: Recovery, Utilization, and Environmental Effects*, vol. 39, no. 2, pp. 184–190, 2017.
- [70] S. Al Arni, "Comparison of slow and fast pyrolysis for converting biomass into fuel," *Renewable Energy*, vol. 124, pp. 197–201, 2018.
- [71] F. Pinto, J. Gominho, R. N. André et al., "Effect of rice husk torrefaction on syngas production and quality," *Energy & Fuels*, vol. 31, no. 5, pp. 5183–5192, 2017.
- [72] A. K. Varma and P. Mondal, "Physicochemical characterization and pyrolysis kinetic study of sugarcane bagasse using thermogravimetric analysis," *Journal of Energy Resources Technology*, vol. 138, no. 5, 2016.

- [73] S. Yi, X.-m. He, H.-t. Lin, H. Zheng, C.-h. Li, and C. Li, "Synergistic effect in low temperature co-pyrolysis of sugarcane bagasse and lignite," *Korean Journal of Chemical Engineering*, vol. 33, no. 10, pp. 2923–2929, 2016.
- [74] Y. Yu, Y. Yang, Z. Cheng et al., "Pyrolysis of rice husk and corn stalk in auger reactor. 1. Characterization of char and gas at various temperatures," *Energy & Fuels*, vol. 30, no. 12, pp. 10568–10574, 2016.
- [75] J. I. Montoya, C. Valdés, F. Chejne et al., "Bio-oil production from Colombian bagasse by fast pyrolysis in a fluidized bed: an experimental study," *Journal of Analytical and Applied Pyrolysis*, vol. 112, pp. 379–387, 2015.
- [76] S. A. El-Sayed and M. E. Mostafa, "Pyrolysis characteristics and kinetic parameters determination of biomass fuel powders by differential thermal gravimetric analysis (TGA/DTG)," *Energy Conversion and Management*, vol. 85, pp. 165–172, 2014.
- [77] T. Kan and Q. Li, "Influence of temperature on properties of products from steam pyrolysis of rice husk in a fluidized bed," *Energy Sources, Part A: Recovery, Utilization, and Environmental Effects*, vol. 37, no. 17, pp. 1883–1889, 2015.
- [78] S. Vecino Mantilla, P. Gauthier-Maradei, P. Álvarez Gil, and S. Tarazona Cárdenas, "Comparative study of bio-oil production from sugarcane bagasse and palm empty fruit bunch: yield optimization and bio-oil characterization," *Journal of Analytical and Applied Pyrolysis*, vol. 108, pp. 284–294, 2014.
- [79] M. S. Abu Bakar and J. O. Titiloye, "Catalytic pyrolysis of rice husk for bio-oil production," *Journal of Analytical and Applied Pyrolysis*, vol. 103, pp. 362–368, 2013.
- [80] S. Gu, J. Zhou, Z. Luo, Q. Wang, and M. Ni, "A detailed study of the effects of pyrolysis temperature and feedstock particle size on the preparation of nanosilica from rice husk," *Industrial Crops and Products*, vol. 50, pp. 540–549, 2013.
- [81] D. Özçimen and A. Ersoy-Meriçboyu, "Characterization of biochar and bio-oil samples obtained from carbonization of various biomass materials," *Renewable Energy*, vol. 35, no. 6, pp. 1319–1324, 2010.
- [82] N. Hossain and N. A. H. Morni, "Co-pelletization of microalgae-sewage sludge blend with sub-bituminous coal as solid fuel feedstock," *BioEnergy Research*, vol. 13, no. 2, pp. 618–629, 2020.
- [83] B. Yousaf, G. Liu, Q. Abbas et al., "Systematic investigation on combustion characteristics and emission-reduction mechanism of potentially toxic elements in biomass- and biochar-coal co-combustion systems," *Applied Energy*, vol. 208, pp. 142–157, 2017.
- [84] N. Ruiz-Gómez, V. Quispe, J. Ábrego, M. Atienza-Martínez, M. B. Murillo, and G. Gea, "Co-pyrolysis of sewage sludge and manure," *Waste Management*, vol. 59, pp. 211–221, 2017.
- [85] H. Chen, Y. Zhai, B. Xu et al., "Characterization of bio-oil and biochar from high-temperature pyrolysis of sewage sludge," *Environmental Technology*, vol. 36, no. 4, pp. 470–478, 2015.
- [86] P. Manara and A. Zabaniotou, "Towards sewage sludge based biofuels via thermochemical conversion—a review," *Renewable and Sustainable Energy Reviews*, vol. 16, no. 5, pp. 2566–2582, 2012.
- [87] I. Fonts, G. Gea, M. Azuara, J. Ábrego, and J. Arauzo, "Sewage sludge pyrolysis for liquid production: a review," *Renewable and Sustainable Energy Reviews*, vol. 16, no. 5, pp. 2781–2805, 2012.
- [88] M. C. Samolada and A. A. Zabaniotou, "Comparative assessment of municipal sewage sludge incineration, gasification and pyrolysis for a sustainable sludge-to-energy management in Greece," *Waste Management*, vol. 34, no. 2, pp. 411–420, 2014.
- [89] M. Inguanzo, A. Domínguez, J. A. Menéndez, C. G. Blanco, and J. J. Pis, "On the pyrolysis of sewage sludge: the influence of pyrolysis conditions on solid, liquid and gas fractions," *Journal of Analytical and Applied Pyrolysis*, vol. 63, no. 1, pp. 209–222, 2002.
- [90] K. Wang, Y. Zheng, X. Zhu, C. E. Brewer, and R. C. Brown, "Ex-situ catalytic pyrolysis of wastewater sewage sludge—a micro-pyrolysis study," *Bioresource Technology*, vol. 232, pp. 229–234, 2017.
- [91] J. Alvarez, G. Lopez, M. Amutio et al., "Characterization of the bio-oil obtained by fast pyrolysis of sewage sludge in a conical spouted bed reactor," *Fuel Processing Technology*, vol. 149, pp. 169–175, 2016.
- [92] H. Fan and K. He, "Fast pyrolysis of sewage sludge in a curie-point pyrolyzer: the case of sludge in the city of Shanghai, China," *Energy & Fuels*, vol. 30, no. 2, pp. 1020–1026, 2016.
- [93] Y.-F. Huang, C.-H. Shih, P.-T. Chiueh, and S.-L. Lo, "Microwave co-pyrolysis of sewage sludge and rice straw," *Energy*, vol. 87, pp. 638–644, 2015.
- [94] J. Alvarez, M. Amutio, G. Lopez, I. Barbarias, J. Bilbao, and M. Olazar, "Sewage sludge valorization by flash pyrolysis in a conical spouted bed reactor," *Chemical Engineering Journal*, vol. 273, pp. 173–183, 2015.
- [95] Q. Xie, P. Peng, S. Liu et al., "Fast microwave-assisted catalytic pyrolysis of sewage sludge for bio-oil production," *Bioresource Technology*, vol. 172, pp. 162–168, 2014.
- [96] Q. Zhang, M. Luo, L. Yan, A. Yang, and X. Hui, "Kinetic analysis of low-rank coal pyrolysis by model-free and model-fitting methods," *Journal of Chemistry*, vol. 2019, Article ID 9075862, 7 pages, 2019.
- [97] X. Wen, Y. Bai, S. Zhang, A. Ding, L. Zheng, and J. Li, "Distributions and sources of sedimentary sterols as well as their indications of sewage contamination in the Guanting reservoir, Beijing," *Journal of Chemistry*, vol. 2020, Article ID 3050687, 11 pages, 2020.
- [98] X. Xu, B. Zhao, M. Sun et al., "Co-pyrolysis characteristics of municipal sewage sludge and hazelnut shell by TG-DTG-MS and residue analysis," *Waste Management*, vol. 62, pp. 91–100, 2017.
- [99] S. Xiong, J. Zhuo, B. Zhang, and Q. Yao, "Effect of moisture content on the characterization of products from the pyrolysis of sewage sludge," *Journal of Analytical and Applied Pyrolysis*, vol. 104, pp. 632–639, 2013.
- [100] J.-P. Cao, L.-Y. Li, K. Morishita et al., "Nitrogen transformations during fast pyrolysis of sewage sludge," *Fuel*, vol. 104, pp. 1–6, 2013.
- [101] S. Deng, H. Tan, X. Wang et al., "Investigation on the fast co-pyrolysis of sewage sludge with biomass and the combustion reactivity of residual char," *Bioresource Technology*, vol. 239, pp. 302–310, 2017.
- [102] B. Zhang, Z. Zhong, M. Min, K. Ding, Q. Xie, and R. Ruan, "Catalytic fast co-pyrolysis of biomass and food waste to produce aromatics: analytical Py-GC/MS study," *Bioresource Technology*, vol. 189, pp. 30–35, 2015.
- [103] A. V. Bridgwater, "Review of fast pyrolysis of biomass and product upgrading," *Biomass and Bioenergy*, vol. 38, pp. 68–94, 2012.
- [104] I. Velghe, R. Carleer, J. Yperman, and S. Schreurs, "Study of the pyrolysis of municipal solid waste for the production of valuable products," *Journal of Analytical and Applied Pyrolysis*, vol. 92, no. 2, pp. 366–375, 2011.

- [105] Y. G. Pan, E. Velo, and L. Puigjaner, "Pyrolysis of blends of biomass with poor coals," *Fuel*, vol. 75, no. 4, pp. 412–418, 1996.
- [106] S. R. Naqvi, Y. Uemura, and S. B. Yusup, "Catalytic pyrolysis of paddy husk in a drop type pyrolyzer for bio-oil production: the role of temperature and catalyst," *Journal of Analytical and Applied Pyrolysis*, vol. 106, pp. 57–62, 2014.
- [107] F. Guo, X. Li, Y. Wang, Y. Liu, T. Li, and C. Guo, "Characterization of Zhundong lignite and biomass co-pyrolysis in a thermogravimetric analyzer and a fixed bed reactor," *Energy*, vol. 141, pp. 2154–2163, 2017.
- [108] Z. Wang, K. Liu, L. Xie, H. Zhu, S. Ji, and X. Shu, "Effects of residence time on characteristics of biochars prepared via co-pyrolysis of sewage sludge and cotton stalks," *Journal of Analytical and Applied Pyrolysis*, vol. 142, Article ID 104659, 2019.
- [109] T. Nussbaumer, "Combustion and Co-combustion of biomass: fundamentals, technologies, and primary measures for emission reduction," *Energy & Fuels*, vol. 17, no. 6, pp. 1510–1521, 2003.
- [110] J. Zuwała and J. Lasek, "6-Co-combustion of low-rank coals with biomass," in *Low-Rank Coals for Power Generation, Fuel and Chemical Production*, Z. Luo and M. Agraniotis, Eds., pp. 125–158, Woodhead Publishing, Sawston, UK, 2017.
- [111] H.-m. Xiao, X.-q. Ma, and Z.-y. Lai, "Isoconversional kinetic analysis of co-combustion of sewage sludge with straw and coal," *Applied Energy*, vol. 86, no. 9, pp. 1741–1745, 2009.
- [112] S. Munir, W. Nimmo, and B. M. Gibbs, "The effect of air staged, co-combustion of pulverised coal and biomass blends on NO_x emissions and combustion efficiency," *Fuel*, vol. 90, no. 1, pp. 126–135, 2011.
- [113] C. Brage, Q. Yu, G. Chen, and K. Sjöström, "Tar evolution profiles obtained from gasification of biomass and coal," *Biomass and Bioenergy*, vol. 18, no. 1, pp. 87–91, 2000.
- [114] I. Narváez, J. Corella, and A. Orió, "Fresh tar (from a biomass gasifier) elimination over a commercial steam-reforming catalyst. Kinetics and effect of different variables of operation," *Industrial & Engineering Chemistry Research*, vol. 36, no. 2, pp. 317–327, 1997.
- [115] F. Pinto, H. Lopes, R. N. André, I. Gulyurtlu, and I. Cabrita, "Effect of catalysts in the quality of syngas and by-products obtained by co-gasification of coal and wastes. (1) Tars and nitrogen compounds abatement," *Fuel*, vol. 86, no. 14, pp. 2052–2063, 2007.
- [116] F. Paradelo, F. Pinto, I. Gulyurtlu, I. Cabrita, and N. Lapa, "Study of the co-pyrolysis of biomass and plastic wastes," *Clean Technologies and Environmental Policy*, vol. 11, no. 1, pp. 115–122, 2009.
- [117] A.-G. Collot, Y. Zhuo, D. R. Dugwell, and R. Kandiyoti, "Co-pyrolysis and co-gasification of coal and biomass in bench-scale fixed-bed and fluidised bed reactors," *Fuel*, vol. 78, no. 6, pp. 667–679, 1999.
- [118] R. N. André, "Fluidised bed co-gasification of coal and olive oil industry wastes," *Fuel*, vol. 84, no. 12, pp. 1635–1644, 2005.
- [119] Y. Zheng, P. A. Jensen, A. D. Jensen, B. Sander, and H. Junker, "Ash transformation during co-firing coal and straw," *Fuel*, vol. 86, no. 7–8, pp. 1008–1020, 2007.
- [120] M. Strand, M. Bohgard, E. Swietlicki, A. Gharibi, and M. Sanati, "Laboratory and field test of a sampling method for characterization of combustion aerosols at high temperatures," *Aerosol Science and Technology*, vol. 38, no. 8, pp. 757–765, 2004.
- [121] H. Wu, T. Wall, G. Liu, and G. Bryant, "Ash liberation from included minerals during combustion of pulverized coal: the relationship with char structure and burnout," *Energy & Fuels*, vol. 13, no. 6, pp. 1197–1202, 1999.
- [122] M. Bernardo, N. Lapa, M. Gonçalves et al., "Physico-chemical properties of chars obtained in the co-pyrolysis of waste mixtures," *Journal of Hazardous Materials*, vol. 219–220, pp. 196–202, 2012.
- [123] M. Brebu, S. Ucar, C. Vasile, and J. Yanik, "Co-pyrolysis of pine cone with synthetic polymers," *Fuel*, vol. 89, no. 8, pp. 1911–1918, 2010.
- [124] Y. Betancur, A. Sánchez, A. Bueno-López, and D. López, "Impact of biomass and main biomass components on coal reactivity under oxy-combustion conditions-A comparison of physicochemical char properties obtained under N₂ and CO₂ atmospheres," *Energy & Fuels*, vol. 31, no. 5, pp. 5603–5611, 2017.
- [125] G. Wang, J. Zhang, J. Shao et al., "Thermal behavior and kinetic analysis of co-combustion of waste biomass/low rank coal blends," *Energy Conversion and Management*, vol. 124, pp. 414–426, 2016.
- [126] J. Zhu, L. Wan, H. Chen, Y. Zhu, and L. Yang, "Pilot test of Co-pyrolysis characteristics of wet sewage sludge and sawdust in an external heating moving bed," *Energy Procedia*, vol. 105, pp. 570–575, 2017.
- [127] S. Li, X. Chen, A. Liu, L. Wang, and G. Yu, "Co-pyrolysis characteristic of biomass and bituminous coal," *Bioresource Technology*, vol. 179, pp. 414–420, 2015.
- [128] F. Pinto, M. Miranda, and P. Costa, "Production of liquid hydrocarbons from rice crop wastes mixtures by co-pyrolysis and co-hydrolysis," *Fuel*, vol. 174, pp. 153–163, 2016.
- [129] W. Zhang, C. Yuan, J. Xu, and X. Yang, "Beneficial synergetic effect on gas production during co-pyrolysis of sewage sludge and biomass in a vacuum reactor," *Bioresource Technology*, vol. 183, pp. 255–258, 2015.
- [130] L. M. Torquato, C. E. M. Braz, C. A. Ribeiro, J. M. V. Capela, and M. S. Crespi, "Kinetic study of the co-firing of bagasse-sludge blends," *Journal of Thermal Analysis and Calorimetry*, vol. 121, no. 1, pp. 499–507, 2015.
- [131] H.-S. Ding and H. Jiang, "Self-heating co-pyrolysis of excessive activated sludge with waste biomass: energy balance and sludge reduction," *Bioresource Technology*, vol. 133, pp. 16–22, 2013.
- [132] S. R. Naqvi, Y. Uemura, N. Osman, and S. Yusup, "Kinetic study of the catalytic pyrolysis of paddy husk by use of thermogravimetric data and the coats-redfern model," *Research on Chemical Intermediates*, vol. 41, no. 12, pp. 9743–9755, 2015.
- [133] M. Sami, K. Annamalai, and M. Wooldridge, "Co-firing of coal and biomass fuel blends," *Progress in Energy and Combustion Science*, vol. 27, no. 2, pp. 171–214, 2001.
- [134] C. A. Strydom, T. Z. Sehume, J. R. Bunt, and J. C. van Dyk, "The influence of selected biomass additions on the co-pyrolysis with an inertinite-rich medium rank C grade South African coal," *Journal of the Southern African Institute of Mining and Metallurgy*, vol. 115, no. 8, pp. 707–716, 2015.
- [135] C. Xu, S. Hu, J. Xiang et al., "Interaction and kinetic analysis for coal and biomass co-gasification by TG-FTIR," *Bioresource Technology*, vol. 154, pp. 313–321, 2014.
- [136] A. O. Abovade, J. F. Görgens, M. Carrier, E. L. Meyer, and J. H. Knoetze, "Thermogravimetric study of the pyrolysis characteristics and kinetics of coal blends with corn and sugarcane residues," *Fuel Processing Technology*, vol. 106, pp. 310–320, 2013.

- [137] D. K. Park, S. D. Kim, S. H. Lee, and J. G. Lee, "Co-pyrolysis characteristics of sawdust and coal blend in TGA and a fixed bed reactor," *Bioresource Technology*, vol. 101, no. 15, pp. 6151–6156, 2010.
- [138] D. A. Mortari, I. Ávila, and P. M. Crnkovic, "Co-firing study of sugar cane bagasse and coal applying thermogravimetric analysis and kinetic," in *Proceedings of the International Congress of Mechanical Engineering-COBEM*, Ribeirão Preto, Brazil, 2013.
- [139] S. Werle and R. K. Wilk, "A review of methods for the thermal utilization of sewage sludge: the polish perspective," *Renewable Energy*, vol. 35, no. 9, pp. 1914–1919, 2010.
- [140] J. Kalemkiewicz and U. Chmielarz, "Ashes from co-combustion of coal and biomass: new industrial wastes," *Resources, Conservation and Recycling*, vol. 69, pp. 109–121, 2012.
- [141] S. R. Naqvi, A. Bibi, M. Naqvi et al., "New trends in improving gasoline quality and octane through naphtha isomerization: a short review," *Applied Petrochemical Research*, vol. 8, no. 3, pp. 131–139, 2018.
- [142] S. R. Naqvi, Y. Uemura, S. Yusup, N. Nishiyama, and M. Naqvi, "Catalytic consequences of micropore topology on biomass pyrolysis vapors over shape selective zeolites," *Energy Procedia*, vol. 105, pp. 557–561, 2017.
- [143] A. Ergudenler and A. E. Ghaly, "Determination of reaction kinetics of wheat straw using thermogravimetric analysis," *Applied Biochemistry and Biotechnology*, vol. 34-35, no. 1, pp. 75–91, 1992.
- [144] H. Rong, T. Wang, M. Zhou, H. Wang, H. Hou, and Y. Xue, "Combustion characteristics and slagging during co-combustion of rice husk and sewage sludge blends," *Energies*, vol. 10, no. 4, 2017.
- [145] L.-b. Jiang, X.-z. Yuan, H. Li et al., "Co-pelletization of sewage sludge and biomass: thermogravimetric analysis and ash deposits," *Fuel Processing Technology*, vol. 145, pp. 109–115, 2016.
- [146] X. Wang, S. Deng, H. Tan et al., "Synergetic effect of sewage sludge and biomass co-pyrolysis: a combined study in thermogravimetric analyzer and a fixed bed reactor," *Energy Conversion and Management*, vol. 118, pp. 399–405, 2016.
- [147] M. Otero, L. Calvo, M. Gil, A. Garcia, and A. Moran, "Co-combustion of different sewage sludge and coal: a non-isothermal thermogravimetric kinetic analysis," *Bioresource Technology*, vol. 99, no. 14, pp. 6311–6319, 2008.
- [148] S.-W. Park and C.-H. Jang, "Characteristics of carbonized sludge for co-combustion in pulverized coal power plants," *Waste Management*, vol. 31, no. 3, pp. 523–529, 2011.
- [149] R. Barbosa, N. Lapa, D. Boavida, H. Lopes, I. Gulyurtlu, and B. Mendes, "Co-combustion of coal and sewage sludge: chemical and ecotoxicological properties of ashes," *Journal of Hazardous Materials*, vol. 170, no. 2-3, pp. 902–909, 2009.
- [150] Z. Zhuo, J. Liu, S. Sun et al., "Thermogravimetric characteristics of textile dyeing sludge, coal and their blend in N₂/O₂ and CO₂/O₂ atmospheres," *Applied Thermal Engineering*, vol. 111, pp. 87–94, 2017.
- [151] Y. Jin, Y. Li, and F. Liu, "Combustion effects and emission characteristics of SO₂, CO, NO_x and heavy metals during co-combustion of coal and dewatered sludge," *Frontiers of Environmental Science & Engineering*, vol. 10, no. 1, pp. 201–210, 2016.
- [152] J. Q. Xia and H. P. Li, "Co-pyrolysis characteristics study of Dianchi lake sludge and coal," in *Advanced Materials Research*, Trans Tech Publications, Stafa-Zurich, Switzerland, 2014.

Research Article

Influence of the Inner and Outer Secondary Air Ratios on the Combustion Characteristic and Flame Shape of a Swirl Burner with a Prechamber

Pengzhong Liu,^{1,2} Fang Niu ,² Xuewen Wang,^{1,2} Fei Guo,² Wei Luo,² and Naiji Wang²

¹China Coal Research Institute, Beijing 100013, China

²China Coal Research Institute Company of Energy Conservation, Beijing 100013, China

Correspondence should be addressed to Fang Niu; nf37@163.com

Received 22 February 2020; Revised 30 May 2020; Accepted 15 June 2020; Published 24 July 2020

Guest Editor: Yanqing Niu

Copyright © 2020 Pengzhong Liu et al. This is an open access article distributed under the Creative Commons Attribution License, which permits unrestricted use, distribution, and reproduction in any medium, provided the original work is properly cited.

The swirl burner with a prechamber was used in a 14 MW pulverized-coal combustion experiment to investigate the influence of inner and secondary air ratios (ISA/OSA) on the combustion characteristic and flame shape in this work. The temperatures and species concentrations in the prechamber were measured via the flue gas analyzer and thermocouples. The flame shape beyond the prechamber outlet was captured by using a high-speed camera. The results showed that the combustion efficiency was increased and low nitrogen combustion was achieved by adopting the swirl burner with a prechamber. The high temperature corrosion and slagging phenomenon did not occur in the prechamber. The influence of ISA/OSA on temperature and species concentration profiles at different areas in the prechamber was different. The flame shape size exhibited an inflection point with increasing ISA/OSA. Considering, comprehensively, the temperature peak, near wall temperature, oxygen-free zone, CO concentration, flame length, flame diameter, and divergence angle, the case of ISA/OSA = 1 : 2 had great processing on combustion efficiency and NO_x emission. Thus, ISA/OSA = 1 : 2 was selected as the optimized case under experiment conditions.

1. Introduction

Pulverized-coal (PC) combustion is one of the maximum coal application approaches. Combustion efficiency and pollutant emissions are the two key factors that restrict the development of PC combustion technology. In order to improve the economic efficiency and ease the pressure on environmental protection, large low nitrogen and high effective combustion technologies [1–5] are developed, such as air staging, fuel staging, flue gas recirculation, fuel rich/lean combustion, and preheating combustion. Achieving these technologies usually depended on the burner or furnace. For the swirl burner, the inner recirculation zone can be formed to keep combustion stable, which is generally applied to the PC boiler. Combining with the abovementioned technologies, the swirl burner has the ability of improving the combustion efficiency and achieving low nitrogen combustion. Flow characteristic analysis is a significant approach to understand and optimize the combustion characteristic of

a swirl burner. Li et al. [6] experimentally investigated the gas-particle flow characteristic of an axial swirl burner (LNASB). The air field, gas-particle flow and combustion characteristic of the swirl burner (CFR) were researched by Chen et al. [7, 8]. Also, Zhou et al. [9] numerically analyzed that flame stability and the NO_x formation mechanism depend on the flow and combustion characteristic of the swirl burner (HT-NR3). Thus, the influences of the swirl burner different variable (such as operating conditions and burner structure) on PC combustion were investigated by the flow and combustion characteristic. For all swirl burners without an adjustable structure, operating conditions [10–15] had significantly impacted on the flow and combustion characteristic. On the influence of the ISA or OSA ratio, Liu et al. [16] researched the position and size of the recirculation zone for LNASB, and the combustion characteristic was discussed in a 600 MW supercritical boiler; some dissertations [17–19] in china, respectively, studied the air flow and combustion characteristic for the CFR swirl

burner, and Jing et al. [13] discussed the gas-particle flow characteristic. Xue et al. [14] investigated carbon burnout and NO_x emission with different experimental coals for a radially biased swirl burner. Jiang et al. [20] experimentally researched how to avoid high temperature corrosion by ISA opening of a swirl burner in an opposed wall fired ultra-supercritical boiler. The abovementioned literatures indicated that the relationship between ISA and OSA of a swirl burner had a significant influence on PC combustion.

The swirl burner with a prechamber structure was used to solve the combustion difficult problem on inferior coal by enhancing the recirculation zone and particle concentration. With developing stable combustion technologies [21, 22] and high temperature corrosion and slagging occurring frequently, application of the prechamber structure gradually decreased. At present, a swirl burner with a prechamber appeared in an industrial boiler combining with low nitrogen combustion technologies. Jiang et al. [23] numerically investigated the combustion characteristic of the swirl burner with a double-cone prechamber in an industrial boiler; combining with deep air staging, Wang et al. [24] discussed the NO_x emission of an industrial boiler. Chi et al. [25] also studied the combustion characteristic of a swirl burner with a prechamber. However, the influence of the ratio of ISA and OSA (ISA/OSA) on the flow and combustion characteristic for a swirl burner with a prechamber was less researched. Gong et al. [26] researched the influence of ISA/OSA for a swirl burner with a prechamber, but ISA and OSA were not provided at the same burner outlet.

In our present work, the influence of ISA/OSA had been investigated on the air flow and combustion characteristic for a swirl burner with a prechamber, but the primary air and PC was reverse flow in the prechamber. Therefore, we decided to experimentally research the influence of ISA/OSA on the combustion and flame characteristic for a swirl burner with a prechamber, in which primary air and PC were normal flow.

2. Experiment and Methods

The 14 MW pilot scale PC combustion experiment system was built in our work. Combining with measurement devices and methods, the data of temperature and species concentration in the prechamber and flame shape beyond the prechamber outlet were obtained to analyse the influence of ISA/OSA.

2.1. Pulverized-Coal Combustion Experiment System.

Figure 1 shows the schematic diagram of the experiment system, which consisted of the coal feeding system, wind system, ignition system, control system, a swirl burner, temperature and gas species concentrations measurements system, and flame capture system. The coal feeding system included storage facilities and feeding devices, and the feeding speed was adjusted by frequency of feeding devices. During each experiment condition, three times of 10 min feeding speed calibration were carried out, and the error was maintained within $\pm 8\%$. A Roots fan and three blowers

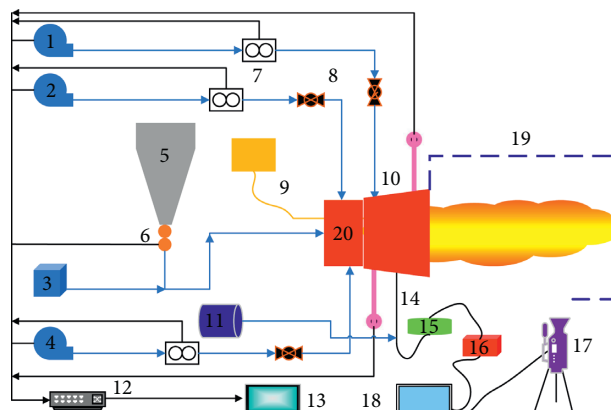


FIGURE 1: Schematic diagram of the experiment system. 1, 2, and 4- blower; 3- Roots fan; 5- storage facilities; 6- feeding device; 7- mass flowmeter; 8- valve; 9- ignition device; 10- thermocouple; 11- air compressor; 12- signal exchanger; 13- desktop computer; 14- sampling device; 15- filter unit; 16- flue gas analyzer 17- high-speed camera; 18- notebook computer; 19- protective wall; and 20- burner.

provide PA (primary air), ISA, OSA, and TA (tertiary air), respectively. Then, the valve was adjusted to control the flow rate displayed by the mass flowmeter. The fuel oil for the ignition system was ignited first, then the PC was fed to achieve stable combustion, and finally, the fuel oil stopped being supplied. The control system was responsible for the start and stop of the whole experiment system. The schematic diagram of the swirl burner is shown in Figure 2, which had 9 axial movable swirl vanes in ISA, an expanding cone-shaped prechamber, a combustion stabilizing device, and an isolated area of PA and OSA.

2.2. Experiment Methods and Conditions. The temperature and gas species concentrations measurements system and the flame capture system in Figure 1 were introduced as measurement methods. The 1.5 m long stainless steel K-type thermocouple with its own signal converter was adopted to realize the online display of temperature. The measurement range of the thermocouple was $0\text{--}1300^\circ\text{C}$ with an error of 0.5% . After the temperature was stable, the fluctuation range of $\pm 10^\circ\text{C}$ was recorded as the measurement value. Flue gas was sampled by using a water-cooled sucking probe, which consisted of a centrally-located sampling pipe surrounded by a double-deck stainless steel tube with high pressure water for probe cooling. After being quickly cooled by water, gas samples through the unit and were filtered and, then, analyzed online by using a MRU VARIO PLUS flue gas analyzer to obtain the gas species concentrations, with an accuracy consisting of $\pm 2\%$ for the measurement values of O_2 and CO . Sixty groups' data were measured at each measuring point for 120 s, and the mean value of 30 s stability data was selected as the flue gas species concentration value of this point. The flame capture system mainly meant the high-speed camera, which used its supporting application software (PCC 3.1) to select camera parameters such as a resolution of 1080×504 , exposure time of $200 \mu\text{s}$, and

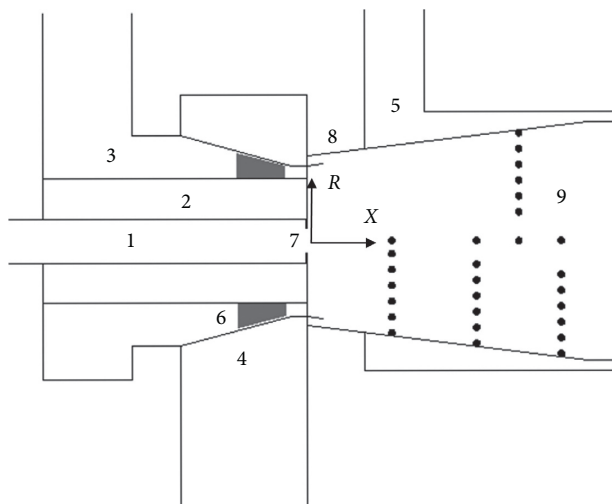


FIGURE 2: Schematic diagram of the swirl burner with the pre-chamber. 1-primary air duct; 2-isolate duct; 3-inner secondary air duct; 4-outer secondary air duct; 5-tertiary air duct; 6-axial movable swirl vanes; 7-combustion stabilizing device; 8-expanding cone-shaped prechamber; 9-location of measuring points.

sampling rate of 1700 fps etc. The scale was arranged at the same section with the burner axis, the high-speed camera took 8337 pictures of the flame, and the picture of the best flame stability and length was selected as the follow-up picture.

In this combustion experiment, Shenfu long flame coal in China was used as the experimental coal, and its basic characteristics are shown in Table 1. As a kind of high volatile coal, it could ensure the smooth ignition and stable combustion for the process of experiment. To avoid the problem of high temperature corrosion and slagging and the flame biasing of the swirl burner horizontal arrangement, wall and swirl wind should be controlled. Considering the flow type difference of ISA and OSA, three experimental cases (ISA/OSA = 2:1, 1:1, 1:2) were chosen, and the main flow gradually changed from ISA to OSA. The ISA swirl number (S) in Table 2 was calculated using following formula [10]:

$$S = \frac{2}{3} \times \left[\frac{1 - (d_i/d_o)^3}{1 - (d_i/d_o)^2} \right] \times \tan(\theta), \quad (1)$$

where d_i is the inner diameter of the ISA duct, d_o is the outer diameter of the ISA duct, and θ is the special swirl vane angle in experimental conditions. The other specific experiment parameters such as air mass flow and speed are shown in Table 2.

The axial distance of the burner outlet section and the radial distance of the central axis were defined as X and R , respectively. Four sections $X=268, 536, 670,$ and 804 mm from the measurement position of the burner outlet were selected. The measurement points of each section were, respectively, 10, 60, 110, 160, 210, and 260 mm from the wall surface of the prechamber, and the last point was the central axis. Finally, the temperature and flue gas species concentrations, respectively, were measured.

TABLE 1: The basic characteristics of experimental coal.

Proximate analysis (as received wt %, ad)	
Volatiles	33.60
Ash	7.02
Moisture	5.62
Fixed carbon	53.76
Net heating value (kJ/kg)	27200
Ultimate analysis (as received wt %, ad)	
Carbon	61.54
Hydrogen	4.16
Oxygen	11.64
Nitrogen	0.82
Sulfur	0.43

TABLE 2: Experimental conditions and parameters.

ISA/OSA	2:1	1:1	1:2
Feeding speed (kg/h)	1140	1140	1140
Primary air (kg/h)	900	900	900
Primary air speed (m/s)	26.3	26.3	26.3
Inner secondary air (kg/h)	3889	2917	1945
Inner secondary air speed (m/s)	22.3	16.7	11.1
ISA swirl number (S)	1.6	1.6	1.6
Outer secondary air (kg/h)	1945	2917	3889
Outer secondary air speed (m/s)	14.0	21.0	28.0
Tertiary air (kg/h)	1955	1955	1955
Tertiary air speed (m/s)	4.5	4.5	4.5
All air temperature ($^{\circ}\text{C}$)	20	20	20

3. Results and Discussion

The experimental results were obtained and divided into three parts to discuss the influence of ISA/OSA, and then, the specific process is as follows.

3.1. Effect of the ISA/OSA for Temperature in the Prechamber.

Figure 3 shows different temperature profiles in the pre-chamber with different ISA/OSA. (a), (b), (c), and (d) in Figure 3 are $X=268$ mm, 536 mm, 670 mm, and 804 mm, respectively. For all the cross sections of ISA/OSA in the radial direction, the high temperature zone could be seen in different areas of each temperature profile. This finding demonstrated that sufficient combustion of PC depended on ISA in the prechamber. OSA was used to decrease wall temperature and rich fuel combustion appeared on the central axis. T_p (peak temperature) = 933 $^{\circ}\text{C}$ appeared at $R=191$ mm for ISA/OSA = 2:1 was lower and farther away from the central axis than other cases in the high-temperature zone, Figure 3(a). The divergence ability of strong swirl was the main reason. Another T_p found was 1015 $^{\circ}\text{C}$ at $R=41$ mm, indicating that PC ignited and burned near the central axis. The temperature for ISA/OSA = 2:1 was higher than others in the area near the wall ($R > 191$ mm), indicating that the function of ISA was to ensure complete combustion. Figures 3(b) and 3(c) are same as 3(a). In Figure 3(d), T_p appeared at the same position, and the difference of vales was slight. The temperature for ISA/OSA = 1:1 was higher than that of others at the

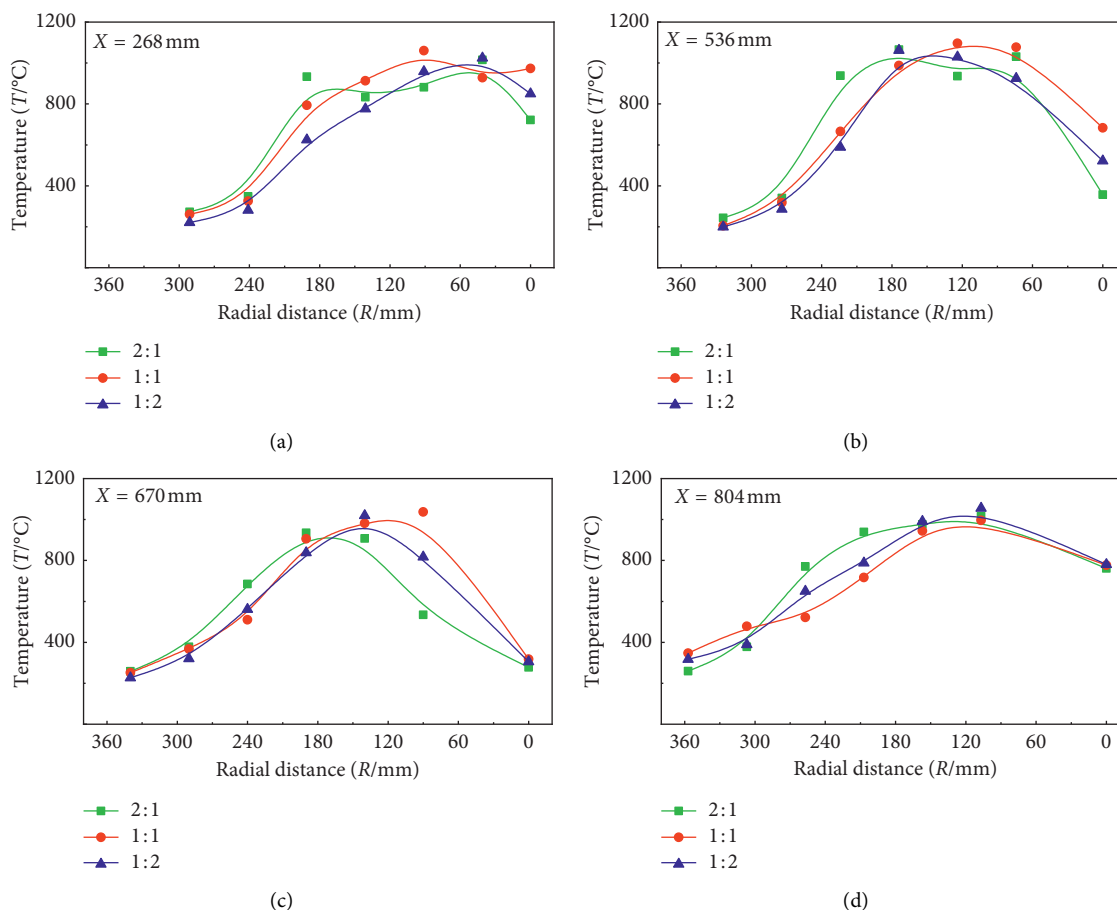


FIGURE 3: Temperature profiles along radial distance for different ISA/OSA. (a) $X = 268$ mm. (b) $X = 536$ mm. (c) $X = 670$ mm. (d) $X = 804$ mm.

$R = 307\text{--}357$ mm area, indicating that the ISA or OSA remaining mainstream position helped to reduce wall temperature of the prechamber downstream.

Figure 4 shows the temperature profiles of the central axis (Figure 4(a)) and the wall position in the prechamber (Figure 4(b)) with different ISA/OSA. Along axis distance, the low-temperature zone could be seen for all ISA/OSA in Figure 4(a). The reason was that the mixing of ISA decayed and the endothermic process of PC pyrolysis appeared. Comparing different ISA/OSA, the temperature for ISA/OSA = 2:1 was lower than that of others. It was indicated that T_p was lower and farther at the same PA and PC feeding speed. In Figure 4(b), the distance from the measurement point to the prechamber inner wall was 10 mm, and temperatures for all ISA/OSA were lower than 400°C . It was indicated that high temperature corrosion could be avoided, and the prechamber adopted general steel material. The results showed that OSA designed had a cooling effect in the prechamber. Besides the $X = 804$ mm point, temperature for ISA/OSA = 1:2 was lower than that of others, indicating that increasing OSA enhanced the cooling effect.

For the swirl burner with a prechamber, the function of PA, ISA, and OSA, respectively, was ignition, ensuring stable combustion and decreasing temperature in the prechamber. Also, the endothermic process of PC pyrolysis appeared, and

high-temperature corrosion was avoided. The influence of ISA/OSA on different position temperature in the prechamber was significant.

3.2. Effect of the ISA/OSA for Flue Gas Species Concentrations in the Prechamber. The O_2 and CO concentration profiles with different ISA/OSA are shown in Figures 5 and 6, respectively. The O_2 concentration increased from near 0% to near 21%, and the CO concentration decreased from high concentration to near 0 ppm along radial direction for different ISA/OSA at all cross sections. The oxygen-free and high CO concentration zone ($\text{O}_2 < 1\%$, $\text{CO} > 5 \times 10^4$ ppm) could be found in the prechamber. It could be attributed to PC incomplete combustion and species diffusion.

For the case of ISA/OSA = 2:1, the O_2 concentration ($R > 120$ mm) and oxygen-free zone, respectively, were higher and smaller than others, and the CO concentration was lower first and higher than others, as shown in Figures 5(a), 5(b), 6(a), and 6(b). The reason was that the divergence ability of strong swirl inhibited species diffusion. In Figures 5(c) and 6(c), the difference of O_2 concentration profiles for three ISA/OSA was not obvious besides $R = 90\text{--}140$ mm, and CO concentration for ISA/OSA = 1:2 was slightly higher than others besides the central axis point.

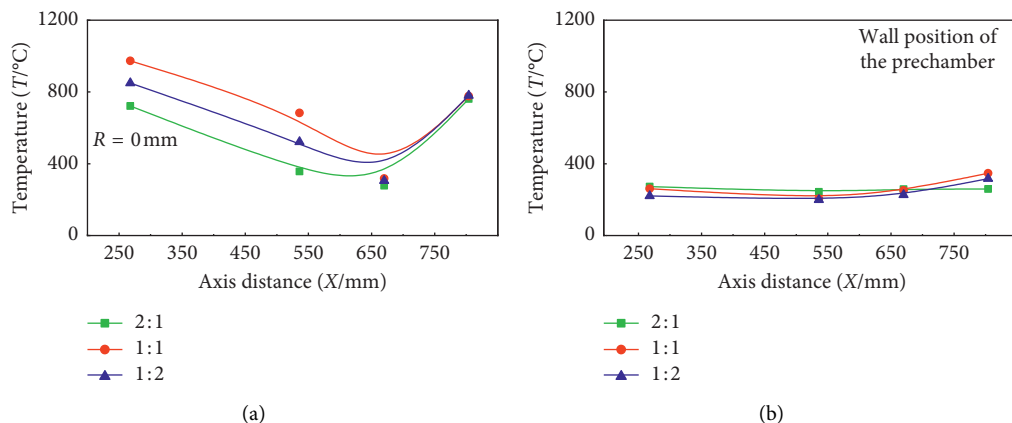
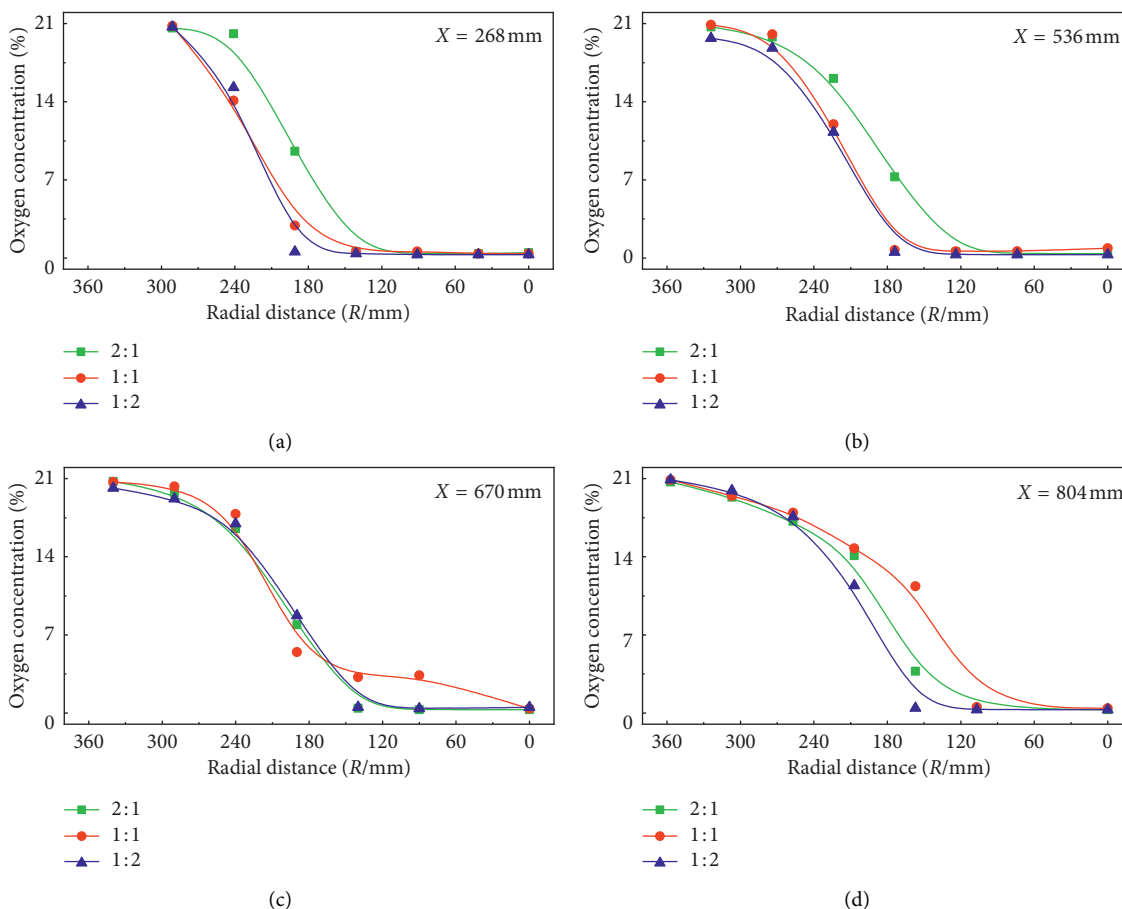


FIGURE 4: Temperature profiles along axis distance for different ISA/OSA.

FIGURE 5: O₂ concentration profiles along radial distance for different ISA/OSA. (a) X = 268 mm. (b) X = 536 mm. (c) X = 670 mm. (d) X = 804 mm.

It was indicated that ISA and OSA gradually mixed. In Figures 5(d) and 6(d), the oxygen-free zone and O₂ concentration ($R > 120$ mm), respectively, were bigger and lower than others, and the CO concentration was higher than others for ISA/OSA = 1 : 2. The reason was that the mixing of PA and SA was weak, under the diversity of ISA and OSA was larger condition.

Figures 7 and 8 showed the O₂ and CO concentration profiles of the central axis (Figures 7(a) and 8(a)) and the wall position of the prechamber (Figures 7(b) and 8(b)) for three ISA/OSA. There were oxygen-free and high CO concentration on the central axis with different ISA/OSA. The CO concentration for ISA/OSA = 2 : 1 was higher than that of others, indicating that pyrolysis processing was

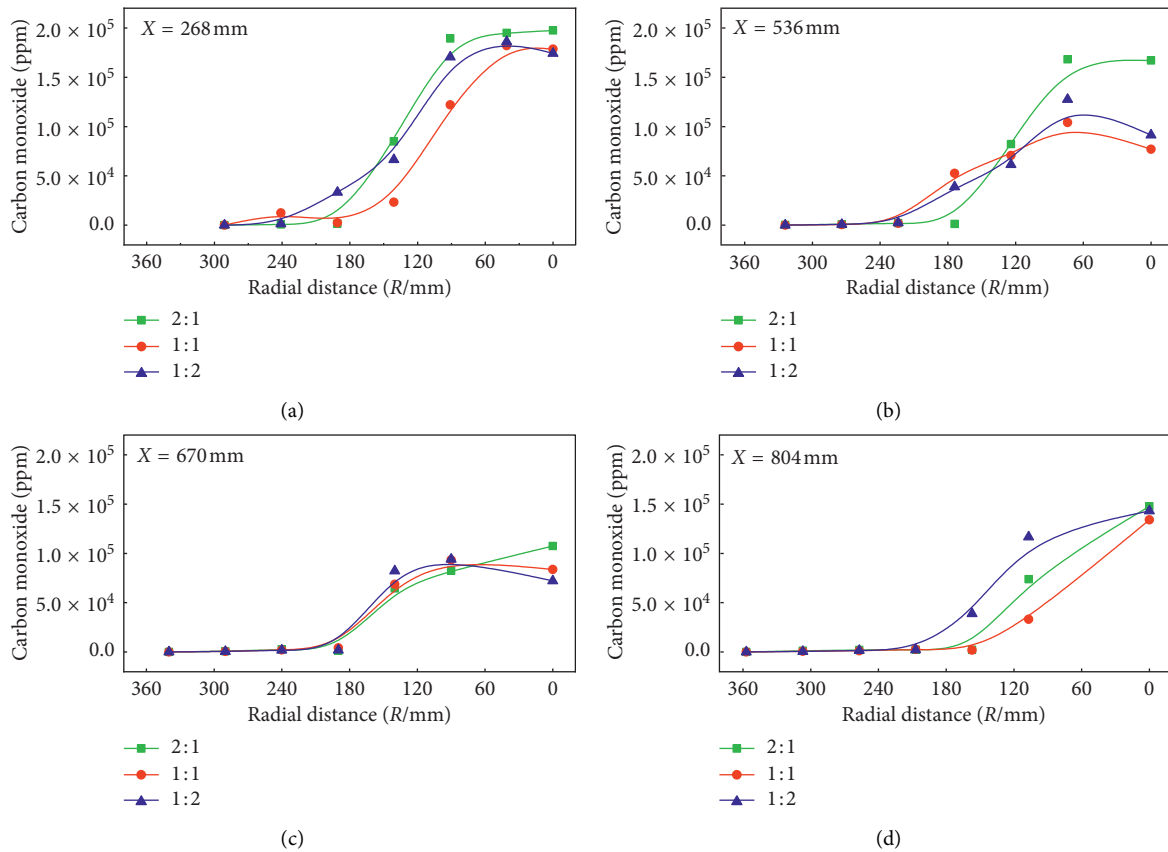


FIGURE 6: CO concentration profiles along radial distance for different ISA/OSA. (a) $X = 268$ mm. (b) $X = 536$ mm. (c) $X = 670$ mm. (d) $X = 804$ mm.

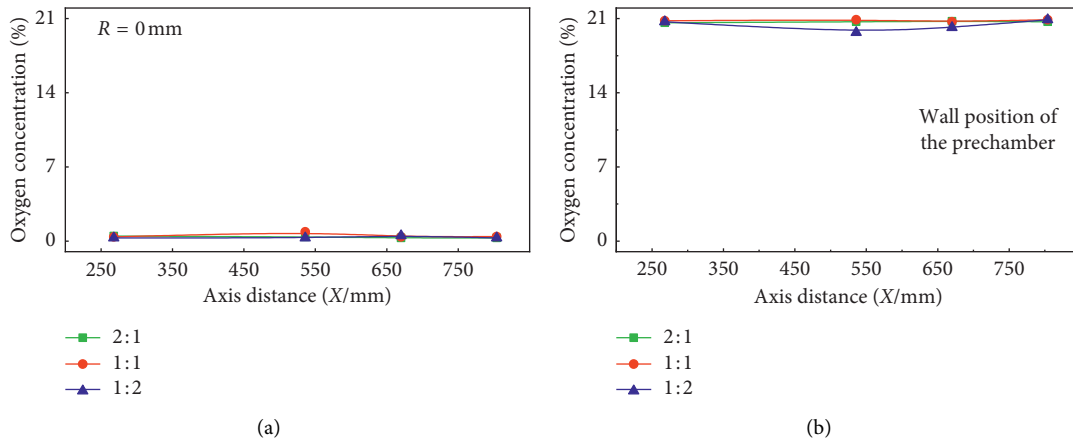


FIGURE 7: O_2 concentration profiles along axis distance for different ISA/OSA.

strong to decrease temperature. At the side wall of the prechamber, the O_2 concentration and CO concentration were close to 21% and 0 ppm with different ISA/OSA, indicating that the cooling effect of ISA was evidenced. Also, the high temperature corrosion and slagging could be avoided.

In the prechamber of the swirl burner, the zone of oxygen-free and high CO concentration was found on the centre. The results showed that strong reducing atmosphere

inhibited NO_x generation and decreased NO_x emission. ISA/OSA had impacted on no oxygen boundary and CO concentration of different regions. The high temperature corrosion and slagging phenomenon did not occur.

3.3. Effect of the ISA/OSA for a Flame Shape beyond the Prechamber Outlet. Figure 9 shows different flame shapes and profiles for different ISA/OSA. All images in Figure 9

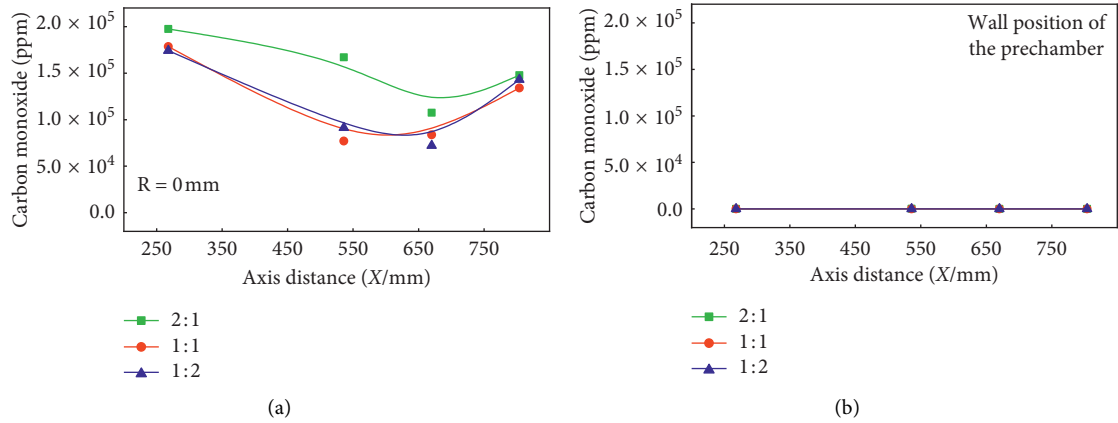
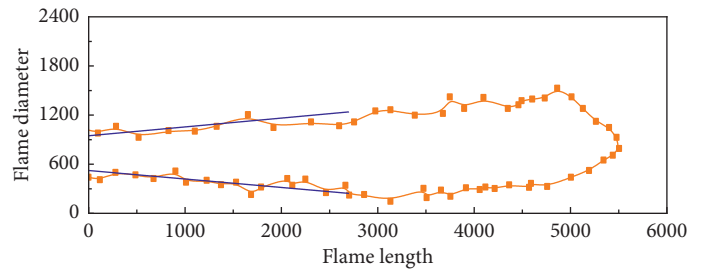
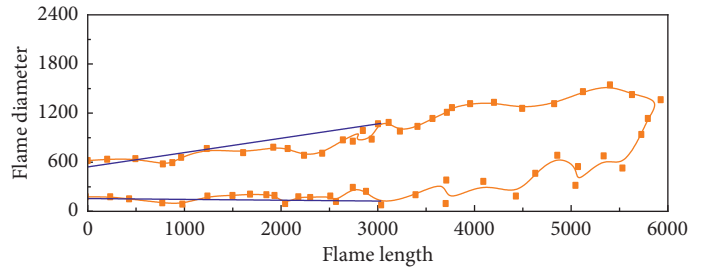
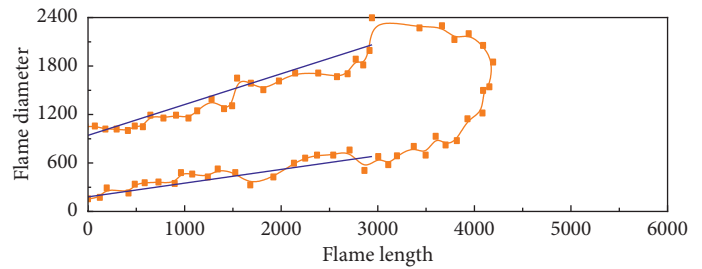


FIGURE 8: CO concentration profiles along axis distance for different ISA/OSA.



(a)

(b)

FIGURE 9: Flame shapes and profiles for different ISA/OSA.

showed that the flame surface had a typical turbulence structure, which was favorable for mass, heat diffusion, and flame propagation beyond the prechamber outlet. This

indicated that the prechamber had the advantages in enhancing flame stability when it was adopted in the swirl burner. Also, the interaction with external air flow indicates

TABLE 3: Flame shapes size for different ISA/OSA.

ISA/OSA	Upper flame surface		Downward flame surface		Flame diameter (mm)	Flame divergence angle (°)	Flame length (mm)
	Intercept (mm)	Slope	Intercept (mm)	Slope			
2:1	941.9	0.3813	179.1	0.1670	762.8	12.1	4194
1:1	542.4	0.1752	156.3	-0.0102	386.1	10.5	5926
1:2	947.3	0.1079	522.5	-0.1033	424.8	11.9	5504

that it was diffusion flame. Therefore, the flame was judged as a turbulent diffusion structure. A long low-speed flow region was formed to stabilize flame, because high-speed jets and the prechamber structure were used. According to the scale placed on the central axis section of the swirl burner, the flame profiles were drawn to obtain the flame length data beyond the prechamber outlet. At the same time, the slope and intercept of the fitting line were used to obtain the flame diameter and divergence angle data at the prechamber outlet. The specific data are shown in Table 3.

The divergence angle decreased from 12.1° to 10.5° at first and, later, rose to 11.9° with decreasing ISA/OSA. The finding indicated that the flame divergence angle for ISA/OSA = 1:1 was lower than that for others. Also, the flame length was longer than that of others, and the diameter was narrower than that of others. The length value varied from 4194 mm to 5926 mm at first and, later, to 5504 mm with decreasing ISA/OSA, and the diameter varied from 762.8 mm to 386.1 mm and to 424.8 mm. The rough and short flame for ISA/OSA = 2:1 were caused due to its rotational divergent ability. The flame length was shortened, and the diameter was widened due to the low-speed flow region slight shortening beyond the prechamber outlet.

The gradient of jet velocity along the radial direction was low for ISA/OSA = 1:1 which stretched the low-speed flow region of flame stability.

The swirl burner with the prechamber had stable PC combustion flame with different ISA/OSA. An inflection point of flame shape was found, indicating that reasonable ISA/OSA needed to be considered.

Temperatures and species concentrations in the prechamber reflected PC burning out, low nitrogen combustion, corrosion, and slagging. Flame shape beyond the prechamber outlet exhibited a jet characteristic and high temperature zone in the future boiler. Also, the flame shape was affected by the combustion characteristic in the prechamber. Thus, the combustion efficiency and NO_x emissions were predicted by temperatures, species concentrations, and flame shapes. Combining with the influence of ISA/OSA, reasonable ISA/OSA was selected to the optimize operation condition of the swirl burner with the prechamber.

4. Conclusions

The temperatures and flue gas species concentrations in the prechamber and flame shapes beyond the prechamber outlet of the burner were researched and analyzed with variable ISA/OSA, and conclusions were obtained as follows:

- (1) The high temperature, the oxygen-free zone, and high CO concentrations were found in the prechamber, and a long stable flame shape was observed

beyond the prechamber outlet. It was evidenced that the swirl burner with the prechamber had certain ability of increasing the combustion efficiency and low nitrogen combustion. The high-temperature corrosion and slagging phenomenon of the prechamber were avoided by designing OSA.

- (2) The influence of ISA/OSA was reflected on the temperature peak, near wall temperature, oxygen-free boundary, and CO concentrations in the prechamber. In the prechamber upstream, the temperature peak and oxygen-free zone decreased, with increasing ISA/OSA, near wall temperature, and CO concentrations. In the prechamber downstream, the oxygen-free zone increased, with decreasing ISA/OSA, and CO concentrations increased. The temperature peak had a slight difference.
- (3) The influence of ISA/OSA on the flame shape was analyzed by flame length, diameter, and divergence angle. Flame length had a maximum inflection point, with decreasing ISA/OSA, and flame diameter and divergence angle had a minimum inflection point. The relation between flame length and others was a contradiction and needed to consider comprehensively.
- (4) According to temperature profiles, species concentrations profiles, and flame shapes size, the ISA/OSA = 1:2 case had higher temperature peak and CO concentrations, larger oxygen-free zone, and lower near wall temperature. Also, flame length was longer, and flame diameter and divergence angle were larger. Therefore, the ISA/OSA = 1:2 experimental condition was selected as a reasonable operating condition, under the experimental coal, 63% load, and ISA swirl number $S = 1.6$ of the swirl burner with a prechamber.

Data Availability

No data were used to support this study. The burn of the experiment is available from the authors.

Conflicts of Interest

The authors declare that there are no conflicts of interest regarding the publication of this paper.

Acknowledgments

This research was financially supported by the Foundation of China Coal Technology Engineering Group (2018TDMS007) and China Coal Research Institute Company of Energy Conservation (2020JNCX01-04).

References

- [1] W. Fan, Z. Lin, Y. Li, J. Kuang, and M. Zhang, "Effect of air-staging on anthracite combustion and NO_x Formation," *Energy & Fuels*, vol. 23, no. 1, pp. 111–120, 2009.
- [2] J. Yang, R. Sun, S. Sun et al., "Experimental study on NO_x reduction from staging combustion of high volatile pulverized coals. Part 2. Fuel staging," *Fuel Processing Technology*, vol. 138, pp. 445–454, 2015.
- [3] H. K. Kim, Y. Kim, S. M. Lee, and K. Y. Ahn, "NO reduction in 0.03–0.2 MW oxy-fuel combustor using flue gas recirculation technology," *Proceedings of the Combustion Institute*, vol. 31, no. 2, pp. 3377–3384, 2007.
- [4] Z. Li, S. Li, Q. Zhu et al., "Effects of particle concentration variation in the primary air duct on combustion characteristics and NO_x emissions in a 0.5-MW test facility with pulverized coal swirl burners," *Applied Thermal Engineering*, vol. 73, no. 1, pp. 859–868, 2014.
- [5] Z. Ouyang, J. Zhu, and Q. Lu, "Experimental study on pre-heating and combustion characteristics of pulverized anthracite coal," *Fuel*, vol. 113, pp. 122–127, 2013.
- [6] Z. Li, L. Zeng, G. Zhao et al., "Cold experimental investigations into gas/particle flow characteristics of a low- NO_x axial swirl burner in a 600-MW wall-fired pulverized-coal utility boiler," *Experimental Thermal and Fluid Science*, vol. 37, pp. 104–112, 2012.
- [7] Z. Chen, Z. Li, J. Jing, L. Chen, S. Wu, and Y. Yao, "Study on flow fields of centrally fuel rich swirl burner and its applications," *Korean Journal of Chemical Engineering*, vol. 26, no. 5, pp. 1186–1193, 2009.
- [8] Z. Chen, Z. Li, Q. Zhu, and J. Jing, "Gas/particle flow and combustion characteristics and NO_x emissions of a new swirl coal burner," *Energy*, vol. 36, no. 2, pp. 709–723, 2011.
- [9] C. Zhou, Y. Wang, Q. Jin, Q. Chen, and Y. Zhou, "Mechanism analysis on the pulverized coal combustion flame stability and NO_x emission in a swirl burner with deep air staging," *Journal of the Energy Institute*, vol. 92, no. 2, pp. 298–310, 2019.
- [10] Y. Sung and G. Choi, "Effectiveness between swirl intensity and air staging on NO_x emissions and burnout characteristics in a pulverized coal fired furnace," *Fuel Processing Technology*, vol. 139, pp. 15–24, 2015.
- [11] J. Jing, Z. Li, Q. Zhu, Z. Chen, and F. Ren, "Influence of primary air ratio on flow and combustion characteristics and NO_x emissions of a new swirl coal burner," *Energy*, vol. 36, no. 2, pp. 1206–1213, 2011.
- [12] S. Li, Z. Li, B. Jiang, Z. Chen, and X. Zhang, "Effect of secondary air mass flow rate on the airflow and combustion characteristics and NO_x formation of the low-volatile coal-fired swirl burner," *Asia-Pacific Journal of Chemical Engineering*, vol. 10, no. 6, pp. 858–875, 2015.
- [13] J. Jing, C. Zhang, W. Sun, J. An, J. Bi, and Z. Li, "Influence of mass-flow ratio of inner to outer secondary air on gas-particle flow near a swirl burner," *Particuology*, vol. 11, no. 5, pp. 540–548, 2013.
- [14] S. Xue, S. Hui, T. Liu, Q. Zhou, T. Xu, and H. Hu, "Experimental investigation on NO_x emission and carbon burnout from a radially biased pulverized coal whirl burner," *Fuel Processing Technology*, vol. 90, no. 9, pp. 1142–1147, 2009.
- [15] R. Luo, N. Li, Y. Zhang et al., "Effect of the adjustable inner secondary air-flaring angle of swirl burner on coal-opposed combustion," *Journal of Energy Engineering*, vol. 142, no. 1, Article ID 04015081, 2016.
- [16] J. Liu, B. Sun, T. Bai et al., "Numerical simulation and optimization on temperature field of 600 MW supercritical swirl combustion boiler," *Proceedings of the CSEE*, vol. 31, no. 2, pp. 15–21, 2011.
- [17] S. Li, *Investigation of Central-Fuel-Richswirling Combustion Technology Withlow-Volatile Coal*, Harbin Institute of Technology, Harbin, China, 2016.
- [18] Y. Xie, *Influence of the Ratio of Inner Secondary Air and Outer Secondary Air on Combustion Characteristics of a Centrally Fuel Rich Swirl Burner*, Harbin Institute of Technology, Harbin, China, 2014.
- [19] Z. Wang, *Influence of the Ratio of Inner Secondary Air and Outer Secondary Air on Combustion Characteristics of a Swirl Burner under Sub-Stoichiometric Ratio*, Harbin Institute of Technology, Harbin, China, 2012.
- [20] B. Jiang, F. G. Liu, K. Liu, and H. J. Liu, "Experimental research on high temperature corrosion prevention technology for water wall of opposed wall fired ultra supercritical boiler," *Applied Mechanics and Materials*, vol. 654, pp. 69–73, 2014.
- [21] L. Zhao, Q. Zhou, and C. Zhao, "Fourth technology of combustion stability for swirl combustion," *Journal of Southeast University (Natural Science Edition)*, vol. 36, no. 4, pp. 551–555, 2006.
- [22] H. Zhou, D.-P. Sun, Q. Fang et al., "Development and prospect of combustion stabilizing technologies of pulverized coal," *Journal of Power Engineering*, vol. 28, no. 5, pp. 657–663, 2008.
- [23] S.-Y. Jiang, Y.-Y. Wang, J.-M. Zhou et al., "Numerical simulation on middle volatile coal combustion in reversed injection burner," *Journal of China Coal Society*, vol. 39, no. 6, pp. 1147–1153, 2014.
- [24] P. Wang, N. Wang, X. Chen et al., "Numerical simulation of deep air-staged technology in pulverized coal industrial boiler," *Clean Coal Technology*, vol. 24, no. 5, pp. 68–76, 2018.
- [25] J. Chi, Z. Chi, G. Sun et al., "Numerical simulation and experimental study of burner and furnace of pulverized coal-fired industrial boiler," *Power System Engineering*, vol. 29, no. 5, pp. 1–4, 2013.
- [26] Y. Gong, X. Xu, D. Wang et al., " NO_x emission characteristics of a novel low- NO_x swirl burner," *Clean Coal Technology*, vol. 25, no. 6, pp. 118–125, 2019.

Research Article

Numerical Study on the Denitrification Efficiency of Selective Noncatalytic Reduction Technology in Decomposing Furnace

Shunsheng Xu,^{1,2} Jiazhen He¹ ,¹ Fei Pei,¹ Kun Li,¹ Lele Liu,¹ and Zhiyong Dai¹

¹School of Mechanical Engineering, Xiangtan University, Xiangtan 411105, China

²School of Energy Science and Engineering, Central South University, Changsha 410083, China

Correspondence should be addressed to Jiazhen He; 1356088529@qq.com

Received 13 January 2020; Revised 27 May 2020; Accepted 8 June 2020; Published 9 July 2020

Guest Editor: Yanqing Niu

Copyright © 2020 Shunsheng Xu et al. This is an open access article distributed under the Creative Commons Attribution License, which permits unrestricted use, distribution, and reproduction in any medium, provided the original work is properly cited.

In order to reduce the nitrogen oxide emission of cement plant, the denitrification of decomposing furnace is studied in this paper. Based on Fluent software platform, the 2500 t/d new dry-process cement kiln decomposing furnace of a plant is modeled and simulated by using air fractional combustion technology combined with selective noncatalytic reduction technology. The model and simulation methods are verified by the field test. The effects of the urea injection position and ammonia-nitrogen molar ratio on NO, NH₃, and denitrification efficiency are studied by numerical simulation. The results show that the optimal injection position of the urea solution is 12 m, the optimal ammonia/nitrogen molar ratio is 1.8, and the optimal injection velocity of the urea solution is 40 m/s. The simulation results obtained under the optimal parameters are as follows: NO concentration is 187.60 mg/m³, NH₃ escape is 32.40 mg/m³, and denitrification efficiency is 74.75%.

1. Introduction

Cement industry is the third largest source of NO_x pollution in China [1], and the resulting NO_x can cause environmental problems such as acid rain and photochemical smog [2, 3], so it is urgent to carry out energy-saving and emission reduction technology transformation. At present, NO_x emission reduction technologies mainly include low NO_x burners, fractional combustion (fuel classification or air classification), selective catalytic reduction (SCR), and selective noncatalytic reduction (SNCR) [4]. SCR denitrification technology is highly efficient, but it is expensive and complicated, involving ammonia supply system, ammonia injection system, catalyst, and other systems [5, 6]. In contrast, SNCR denitrification technology has a low operating cost and can be applied in combination with various nitrogen oxide emission reduction technologies [7–10].

Han et al. [11] conducted SNCR denitrification tests on power station boilers. The results showed that the optimal reaction temperature for denitrification of ammonia and urea solutions is about 1000°C, and the maximum denitrification efficiency of SNCR is about 90% under typical test

conditions with an ammonia-nitrogen ratio of 1.5. Li and Wu [12] completed the simulation process of SNCR of the experimental device in CRF by numerical simulation. Li et al. [13] conducted a simulation study on the CFB boiler cyclone separator and analyzed the influence of temperature window and ammonia-nitrogen molar ratio (NSR) on denitrification efficiency. They found that the optimal temperature window is 850~1050°C, and the optimal NSR is 1~1.5. At present, SNCR technology research is mostly concentrated in the field of power station boilers. Due to the inhibitory effect of calcium compounds such as limestone on the reaction of SNCR in the decomposing furnace, there are relatively few research studies on SNCR in the field of cement decomposing furnace, which leads to the limitation of the development of this technology in the cement industry. However, because of its economy and convenience, SNCR technology has great potential in optimizing SNCR denitrification and improving SNCR denitrification efficiency of the decomposing furnace.

Based on previous studies, this paper, based on Fluent software platform, simulates the SNCR denitrification based on the new dry cement kiln decomposing furnace air

fractional combustion. The effects of the injection location of urea solution along the height of the decomposing furnace, the ammonia-nitrogen molar ratio, and the injection velocity of urea solution on the NO concentration, NH₃ escape amount, and denitrification efficiency are studied in this paper. The formulated SNCR denitrification process parameters with better denitrification efficiency are obtained.

2. Numerical Simulation of SNCR in Decomposing Furnace

2.1. The Geometric Model. The object of this simulation is a decomposing furnace with an output of 2500 t/d in a cement plant in Hunan. The model of the decomposing furnace is modeled according to the actual scale, as shown in Figures 1 and 2. The pulverized coal and primary air in the decomposing furnace are sprayed into the furnace through the coal injection pipes on both sides of the lower column. The high-temperature flue gas from the end of the decomposing kiln enters the furnace through the bottom of the cone and is mixed with the pulverized coal airflow and the tertiary air for ignition and combustion [14]. The burnout air is sprayed into the furnace from the middle of the lower column, so that the pulverized coal and raw materials escaping from the core combustion zone continue to burn and decompose [15].

This article uses the ICEM software for simulating structural mesh, for improving the quality of the mesh, on the whole decomposing furnace using O-mesh technology, and the decomposing furnace reducing part and each entrance area mesh refinement processing, the calculation mesh is shown in Figure 3. The total number of grids was determined to be about 850,000 through mesh independence verification.

2.2. Calculation Model. The decomposing furnace model is complex and contains multiple high-speed airflow and mixed flow. The RNG k - ϵ model can better deal with the strong turbulent flow with high strain velocity and large flow line bending degree [16, 17], which is adopted for the gas-phase turbulence model in this study. The calculation formula is shown in the following equations:

$$\frac{\partial(\rho k)}{\partial t} + \frac{\partial(\rho k \mu_i)}{\partial x_i} = \frac{\partial}{\partial x_j} \left[\alpha_k (\mu + \mu_t) \frac{\partial k}{\partial x_j} \right] + G_k + \rho \epsilon, \quad (1)$$

$$\frac{\partial(\rho \epsilon)}{\partial t} + \frac{\partial(\rho \epsilon \mu_i)}{\partial x_i} = \frac{\partial}{\partial x_j} \left[\alpha_\epsilon (\mu + \mu_t) \frac{\partial \epsilon}{\partial x_j} \right] + \frac{C_{1\epsilon}^* G_k}{k} - C_{2\epsilon} \rho \frac{\epsilon^2}{k}, \quad (2)$$

where ρ is the density of the gas, kg/m³; k is turbulent kinetic energy; J ; ϵ is the turbulent dissipation velocity; μ is the molecular viscosity coefficient; μ_t is the turbulent viscosity coefficient; and C is the constant term coefficient.

Based on the detailed chemical reaction process of turbulent combustion in the decomposing furnace, component transport model and eddy dissipation conceptual

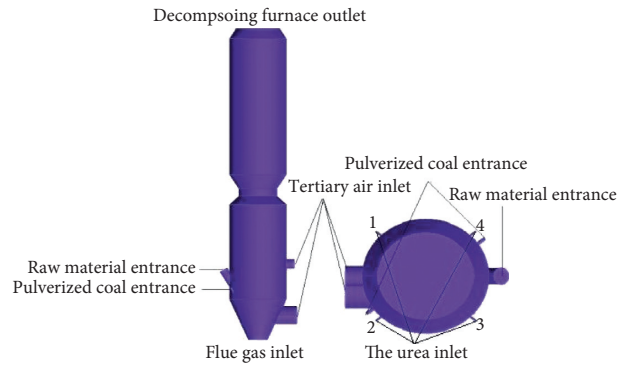


FIGURE 1: Geometry model of the decomposing furnace.

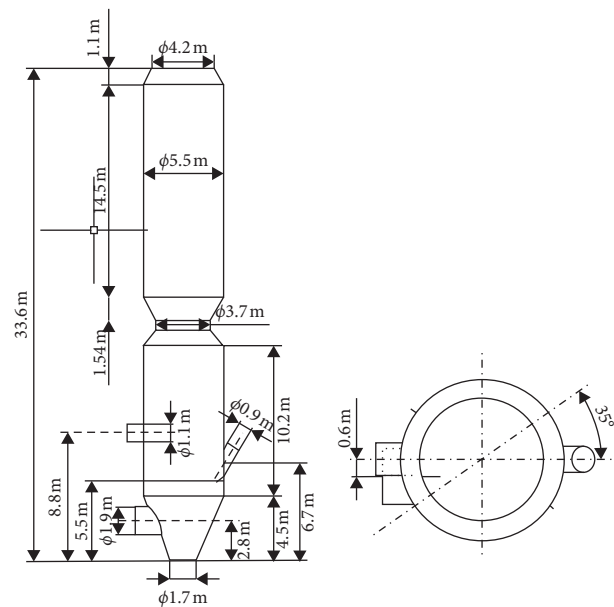


FIGURE 2: Dimensions of the decomposing furnace.

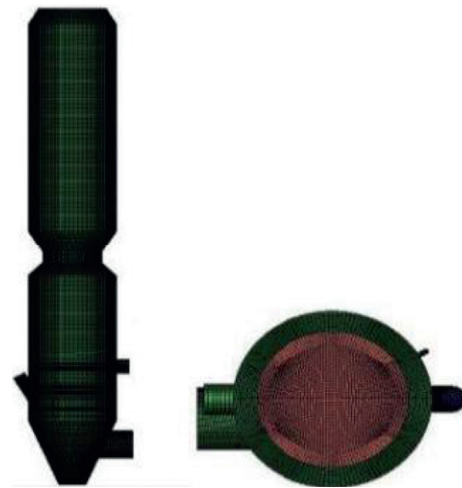


FIGURE 3: Decomposing furnace meshing diagram.

model (EDC) are selected in this paper, in which the diffusion/dynamic model is used for coke combustion and limestone decomposing. The moisture only considers evaporative heat absorption. The NO_x reaction model included in Fluent is selected for the pollutant model. Since under the condition of fractional air and furnace temperature (less than 1000°C) of the decomposing furnace, the rapid NO_x and thermal NO_x generated by the combustion of pulverized coal particles are few and negligible, only fuel NO_x is considered in the simulation, and the SCNR model is activated to use urea as the reducing agent of the reaction. According to the characteristics of pulverized coal particles and urea particles in the furnace, the discrete phase model (DPM) is used to calculate the particle phase flow, and the diameter of urea droplets is set at $50\text{--}200\ \mu\text{m}$. Since the proportion of particles in the mixed phase is less than 10%, the particles (assumed to be spherical) are regarded as the dilute phase, and the interactions between particles could be ignored, and only the resistance and gravity are taken into account [18, 19]. The temperature in the furnace is relatively high, and the temperature in the core combustion zone is about 1250 K. The main heat transfer mode is radiation heat transfer, so the radiation model adopts p1 model [20]. The chemical reaction mechanism of all NO_x involved in the decomposing furnace with limestone is shown in Table 1.

2.3. The Boundary Conditions. The boundary conditions of decomposing furnaces are summarized as shown in Tables 2 and 3 through the operating parameters, coal burning analysis data, and reasonable assumptions of running kilns.

2.4. SNCR Denitrification Design. In the process of SNCR denitrification, the main factors influencing the denitrification effect are reaction temperature, residence time of reducing agent, mixing degree of reducing agent, and flue gas and ammonia-nitrogen molar ratio. Combined with the actual situation of the cement manufacturing process, this paper mainly studied the effect of the injection location of urea solution, NSR, and injection speed of urea solution on denitrification. At the same time, in order to achieve the uniform mixing of the urea solution and the NO_x in the flue gas, this article will arrange four symmetrical nozzles along the different decomposing furnace height positions, and the specific layout position is shown as 1, 2, 3, and 4 in Figure 1.

The SNCR denitrification was studied using numerical simulation combined with experimental study, and the details are as follows:

- (1) Firstly, a combustion model of the 2500 t/d decomposing furnace was established. According to the established combustion model, the numerical simulation of the decomposing furnace was carried out by Fluent software. In order to validate the reliability of the combustion model, a series of experiments was performed on the 2500 t/d decomposing furnace. The temperature of the furnace outlet was measured by the gas pump thermocouple, and the flue gas composition was

measured by the KM940 flue gas analyzer. The simulation results were compared with the experimental results to obtain a more reliable decomposing furnace combustion model.

- (2) Secondly, the SNCR denitrification reaction is added to the obtained combustion model. The effects of the injection location of the urea solution, NSR, and the injection speed of the urea solution on SNCR denitrification were studied by numerical simulation. The urea solution is injected into the furnace at the heights of 6, 8, 10, 12, 14, 16, and 18 m, respectively. The NSR gradually increases from 1.0 to 2.0, whose increment is 0.2. The injection velocities of the urea solution are 20, 40, 60, and 80 m/s, respectively. The desulfurization efficiency and nitrogen oxide emissions under various parameters can be obtained by numerical simulation, and the process parameters with the best desulfurization effect can be concluded.
- (3) Finally, based on the simulation results, the operation parameters of the 2500 t/d decomposition furnace were adjusted, and the temperature and flue gas composition of the decomposition furnace outlet were measured again. Then the measured results are compared with the simulation results to provide a reliable basis for the simulated parameters.

3. Combustion Simulation and Experimental Verification

3.1. Simulation Analysis of Temperature Field and Concentration Field. The simulation results of combustion temperature and concentration of each component in the decomposing furnace are shown in Figure 4. The combustion temperature in the decomposing furnace is shown in Figure 4(a). The junction of the bottom cone and the lower column of the decomposing furnace is the core combustion zone. The highest combustion temperature is 1400 K and the average temperature is about 1250 K. The temperature distribution in the decomposing furnace is relatively uniform, which basically meets the requirements of the raw material decomposing process. After passing through the core combustion zone, the temperature gradually decreases along the Z-axis direction, and the temperature rises slightly when passing through the upper column, until the outlet temperature of the decomposing furnace drops to 1200 K. The distribution of O_2 , CO_2 , and CO is shown in Figures 4(b)–4(d). In the core combustion area, pulverized coal burns violently, and due to the large consumption of oxygen, the O_2 concentration drops sharply. Meanwhile, the CO_2 concentration increases rapidly and is accompanied by the generation of CO. The O_2 concentration at the outlet of the decomposing furnace drops to 1.26%, the CO_2 concentration increases to 31%, and the CO concentration value is 0.88%. The distribution cloud diagram of NO is shown in Figure 4(e). The concentration of NO in the cone of the decomposing furnace is relatively small, and in a local area, NO is generated in large amount with the pyrolysis of volatiles, and its peak value is $1648\ \text{mg}/\text{m}^3$. As the height of

TABLE 1: The equations of the conversion of NO_x and limestone.

No.	Reactions $k_f = AT^b \exp(-E/RT)$	A (s ⁻¹)	b	E (kJ/mol)
(R1)	$\text{NH}_3 + 1.25\text{O}_2 \rightarrow \text{NO} + 1.5\text{H}_2\text{O}$	3.10 E+08	0	8.31 E+07
(R2)	$\text{NH}_3 + 0.75\text{O}_2 \rightarrow 0.5\text{N}_2 + 1.5\text{H}_2\text{O}$	4.96 E+08	0	8.31 E+07
(R3)	$\text{HCN} + 0.75\text{O}_2 \rightarrow \text{CNO} + 0.5\text{H}_2\text{O}$	2.14 E+04	0	8.31 E+07
(R4)	$\text{CNO} + 0.5\text{O}_2 \rightarrow \text{NO} + \text{CO}$	1.02 E+12	0	2.12 E+08
(R5)	$\text{CNO} + \text{NO} \rightarrow \text{N}_2\text{O} + \text{CO}$	1.02 E+12	0	2.12 E+08
(R6)	$\text{NO} + \text{NH}_3 + 0.25\text{O}_2 \rightarrow \text{N}_2 + 1.5\text{H}_2\text{O}$	1.10 E+12	0	2.77 E+04
(R7)	$\text{NO} + \text{CO} \rightarrow 0.5\text{N}_2 + \text{CO}_2$	1.95 E+07	0	1.58 E+08
(R8)	$\text{N}_2\text{O} + 0.5\text{O}_2 \rightarrow \text{N}_2 + \text{O}_2$	1.50 E+11	0	1.68 E+08
(R9)	$\text{N}_2\text{O} + \text{CO} \rightarrow \text{N}_2 + \text{CO}_2$	1.24 E+09	0	4.92 E+07
(R10)	$\text{CO}(\text{NH}_2)_2 \rightarrow \text{NH}_3 + \text{HNCO}$	1.27 E+04	0	1.55 E+04
(R11)	$\text{CO}(\text{NH}_2)_2 + \text{H}_2\text{O} \rightarrow 2\text{NH}_3 + \text{CO}_2$	6.13 E+10	0	2.10 E+04
(R12)	$\text{CaCO}_3 \rightarrow \text{CaO} + \text{CO}_2$	6.08 E+04	0	2.05 E+08

TABLE 2: Boundary conditions.

The boundary conditions	Temperature (K)	Mass flow (kg/s)	Velocity (m/s)	Pressure (Pa)
Tertiary air (reducing air/burnout air)	1300	18.57 (15.83/2.74)	—	—
Decomposing furnace flue gas	1400	—	30	—
Pulverized coal	321	2.68	—	—
Primary air	321	—	45	—
CaCO ₃	1200	35.45	—	—
Decomposing furnace outlet	—	—	—	-1200

TABLE 3: Ultimate analysis of coal.

C _{ar}	H _{ar}	Ultimate analysis (wt. %)						Lower heating value Q _{net} (kJ/kg)
		O _{ar}	N _{ar}	S _{ar}	A _{ar}	M _{ar}	V _{daf}	
62.16	2.87	6.31	0.76	0.91	19.76	7.23	24.69	32789.3

the furnace increases, the tertiary air enters the furnace in stages, and a reducing atmosphere is generated due to fuel-rich combustion above the core combustion zone. Part of the NO is reduced along the height of the decomposing furnace, which gradually reduces the NO concentration. The unburned residual pulverized coal in the core area will be burned with the over-fire air as the smoke rises, and the secondary combustion will occur, which will increase the CO₂ concentration in the flue gas and gradually increase the NO concentration. The final NO concentration at the outlet of the decomposing furnace is 743 mg/m³.

3.2. Experimental Verification. In this paper, based on the feasibility of measurement, the flue gas temperature and component concentration at the outlet of the Chenzhou 2500 t/d decomposing furnace are measured and compared with the simulation results. Four measuring points are set at the outlet of the decomposing furnace, and the positions are 0, 0.5, 1.0, and 1.5 m away from the center of the measuring point. Exhaust thermocouple (s-type thermocouple, Siemens (China) Co., LTD.) was used to measure the temperature of flue gas. The KM940 flue gas analyzer made in Britain with high test accuracy and high temperature adaptability is used to measure the concentration of flue gas

components. In order to reduce the influence of zero drift of the instrument itself on the accuracy of the test, the instrument used before the test shall be strictly calibrated according to the regulations. Test values and simulation values of decomposing furnace outlet parameters are summarized in Table 4. It can be found from Table 4 that the error between the simulation results and the actual measured values is small, so the experimental results can be replaced by simulation. The simulation data used to support the findings of this study are included within the article, and the experimental data used to support the findings of this study are available from the corresponding author upon request.

4. Analysis of SNCR Simulation Results

4.1. Analysis of Results of Urea Solution Injection Position. The injection position of the urea solution determines the residence time of the urea in the furnace and the temperature conditions under which the urea reacts. When injected into the low position, the residence time is long, but the reaction temperature is too high, and the urea is easily oxidized; when injected into the high position, the reaction temperature is too low and the residence time is short, which easily leads to an increase in the amount of NH₃ escape. This article selects

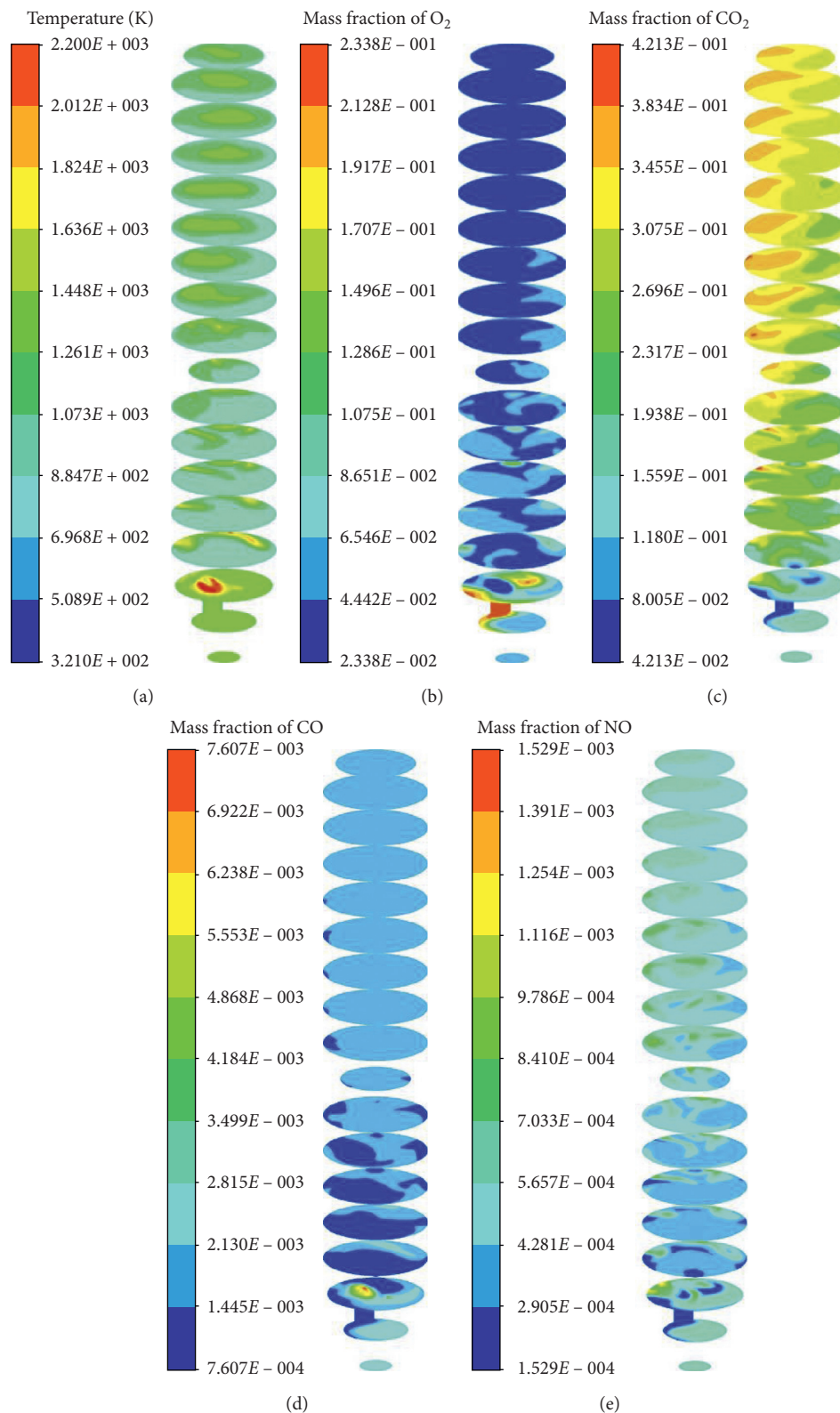


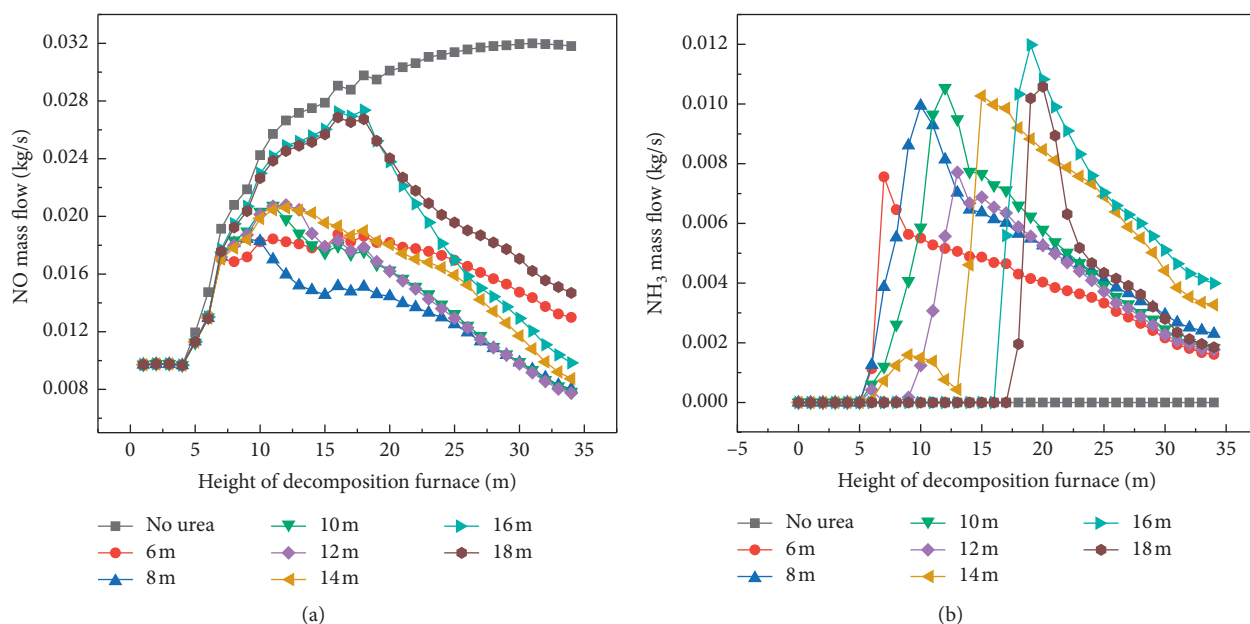
FIGURE 4: Numerical simulation of combustion in the decomposing furnace. (a) Temperature. (b) O_2 . (c) CO_2 . (d) CO. (e) NO.

the urea solution spray into the position, respectively, along the height direction (the Z-axis) of the decomposing furnace is 6, 8, 10, 12, 14, 16, and 18 m, and its temperature ranges from 950 to 1250 K.

The distribution of NO and NH_3 mass flow at different heights of the decomposing furnace under different injection positions of urea solution is shown in Figure 5. Under different incident positions of urea solution, the

TABLE 4: Comparison of the measured data and simulated data.

Data categories	Decomposing furnace outlet flue gas temperature (K)				Mass fraction (%)			Concentration (mg/m ³)
	a	b	c	d	O ₂	CO ₂	CO	NO
	Experimental data	1302.8	1310.4	1303.4	1283.2	3.10	73.1	0.18
Simulation data	1327.1	1337.7	1266.0	1240.0	2.90	69.3	0.19	743
Relative error	1.87	2.08	2.94	3.34	6.75	5.10	5.56	5.97

FIGURE 5: Flow curves of NO and NH₃ in the decomposing furnace under different injection positions. (a) NO and (b) NH₃.

concentration of NO and NH₃ in the decomposing furnace generally increases first and then decreases. The combustion of pulverized coal particles in the core combustion zone and the reducing tertiary air produces a large amount of NO, which causes a sharp increase in the NO concentration at the junction of the decomposing furnace cone and the lower half of the cylinder. Fuel-rich combustion in the core combustion zone consumes a large amount of oxygen due to the tertiary air classification. A reducing atmosphere is generated above the core combustion zone to reduce part of the NO, and the increase in NO concentration becomes slower. When the urea solution is injected into the decomposing furnace from a low height, the residence time of the urea solution is long and the reaction temperature is too high, which causes the urea to be easily oxidized. When the urea solution is injected into the decomposing furnace from a high height, the residence time of the urea solution is short and the reaction temperature is too low, which results in an increase in the concentration of NH₃ escape. The distribution curve of NO and NH₃ concentrations in the cross section of different injection heights of decomposing furnaces is shown in Figures 5(a) and 5(b). From Figures 5(a) and 5(b), when the injection height is 6 m, the peak concentrations of NO and NH₃ are lower. The reason is that the urea solution enters the furnace at a lower position, which is

close to the core combustion zone. And its average temperature is about 1300 K, which causes some of the NH₃ and H₂CO produced by the decomposing of urea to be oxidized to NO. Combined with the reducing ability of the urea decomposing product itself and the reason for being oxidized at high temperature, the two restrict each other and cause the lower peak concentration of NO and NH₃ in the furnace. When the injection heights are 16 and 18 m, the NO concentration is increasing under the height of the decomposing furnace below 15 m, and its peak value is 1491 mg/m³. And when the injection height is 16 m, the NH₃ escape amount is the largest, which is caused by the urea solution injection position being too high and the residence time shortened.

From the above analysis, it can be seen that the injection position of the urea solution has a significant influence on the ability to reduce nitrogen oxides. The variations of NO concentration and NH₃ escape concentration with injection height of urea solution are shown in Figure 6, and the variation of denitrification efficiency with injection height of urea solution is shown in Figure 7. The NO concentration and NH₃ escape concentration curves are “U” and “M,” respectively. When the injection height of the urea solution increases, the NO concentration at the outlet of the decomposing furnace decreases first and then increases.

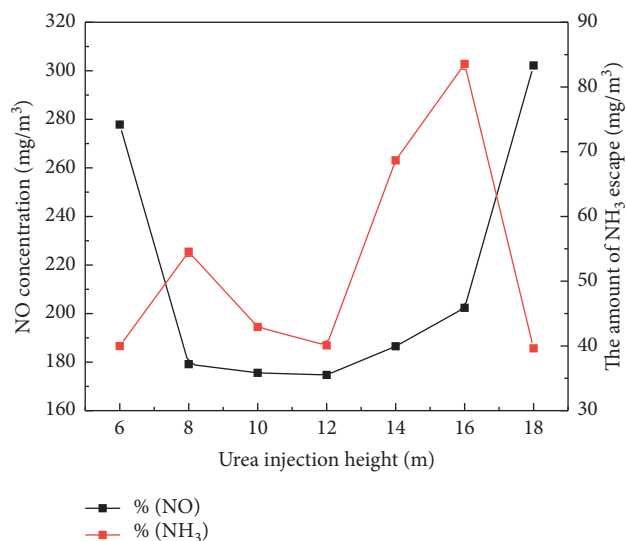


FIGURE 6: NO concentration and NH₃ of outlet under different injection positions.

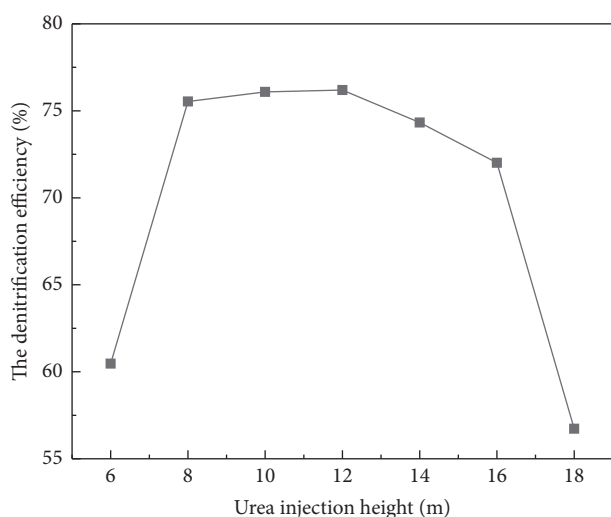


FIGURE 7: Denitrification efficiency under different injection positions.

Especially when the injection position is more than 16 m, the NO concentration rapidly increases from 207 mg/m³ to 320 mg/m³, and the amount of NH₃ escaping decreased significantly from 83.46 mg/m³ to 39.65 mg/m³. The reason is that the wind is divided into three winds (burnout wind) into the furnace and mixes with the flue gas, and the combustion of residual coal powder increases the temperature of the upper half of the column in the decomposing furnace, so that part of NH₃ is oxidized to NO. When the injection height is 12 m, the NO concentration and the escape amount of NH₃ are at a low level. It can be seen from Figure 7 that the SNCR denitrification efficiency curves at different heights are “inverted U,” and the denitrification nitration efficiency increases first and then decreases as the injection position increases. A comprehensive analysis of the

simulation results of SNCR at different injection heights of urea solution shows that the optimized injection height is 12 m. At this time, the NO concentration is 176 mg/m³, the amount of NH₃ escape is 39.98 mg/m³, and the denitrification efficiency is 76.26%.

4.2. Analysis of Ammonia-Nitrogen Molar Ratio (NSR) Results. According to the above SNCR chemical reaction principle, it is known that theoretically reducing 1 mol of NO requires 1 mol of NH₃, which is NSR is equal to 1. However, in practical engineering applications, it cannot guarantee that all decomposed NH₃ completely reacts with NO in the flue gas due to the complicated chemical reaction of urea and the complicated mixing process of the gas flow in the decomposing furnace. When NSR is greater than 2, excessive consumption of reducing agent will increase the running cost and increase the amount of NH₃ escape. The research scheme of the effect of different ammonia-nitrogen ratios (NSR) on denitrification is as follows: keep other parameter settings unchanged (from the above analysis results, the injection height of the urea solution is maintained at 12 m, and the NSR gradually increased from 1.0 to 2.0 (successive increments are 0.2)), and carry out simulation research on five sets of NSR schemes.

The variations of concentrations of NO and NH₃ in the decomposing furnace with NSR are shown in Figure 8. From the analysis in Figure 8, with different NSR, changes in the NO_x and NH₃ concentration in the decomposing furnace are more obvious. When the decomposing furnace height is below 11 m, the changes of NO and NH₃ concentrations in the furnace are basically synchronized. Between 11 m and 13 m, as the NSR increases, the peak value of NO concentration in the furnace decreases, and the peak value of NH₃ concentration increases. When the height of the decomposing furnace is more than 15 m, the NO concentration in the decomposing furnace generally decreases, and the slope of the NO curve increases with the increase of NSR. The reason is that when NSR is 1, the reduction reaction velocity increases with the increase of NSR, so more NO will be reduced. However, when NSR reached 1.8, NO in the decomposer had reached a low concentration and could not be reduced easily. If NH₃ continues to be increased, it will not only improve the denitrification efficiency, but also increase the NH₃ escapement.

The variations of NO concentration and NH₃ escape amount at the outlet of the decomposing furnace with NSR are shown in Figure 9. It can be seen from Figure 9 that the change trend of the NO concentration and the NH₃ escape amount line is just the opposite. With the increase of NSR, the NO concentration gradually decreases and the NH₃ escape amount gradually increases. When the NSR is 1.0, the NO concentration and NH₃ escape concentration are 373.94 mg/m³ and 16.42 mg/m³, respectively. At this time, the NO concentration of the decomposing furnace is the highest. When the NSR is greater than 1.8, the NH₃ escape concentration rises linearly, and the NO concentration decreases slowly at this time, indicating that the urea's ability to reduce NO tends to be saturated. The denitrification

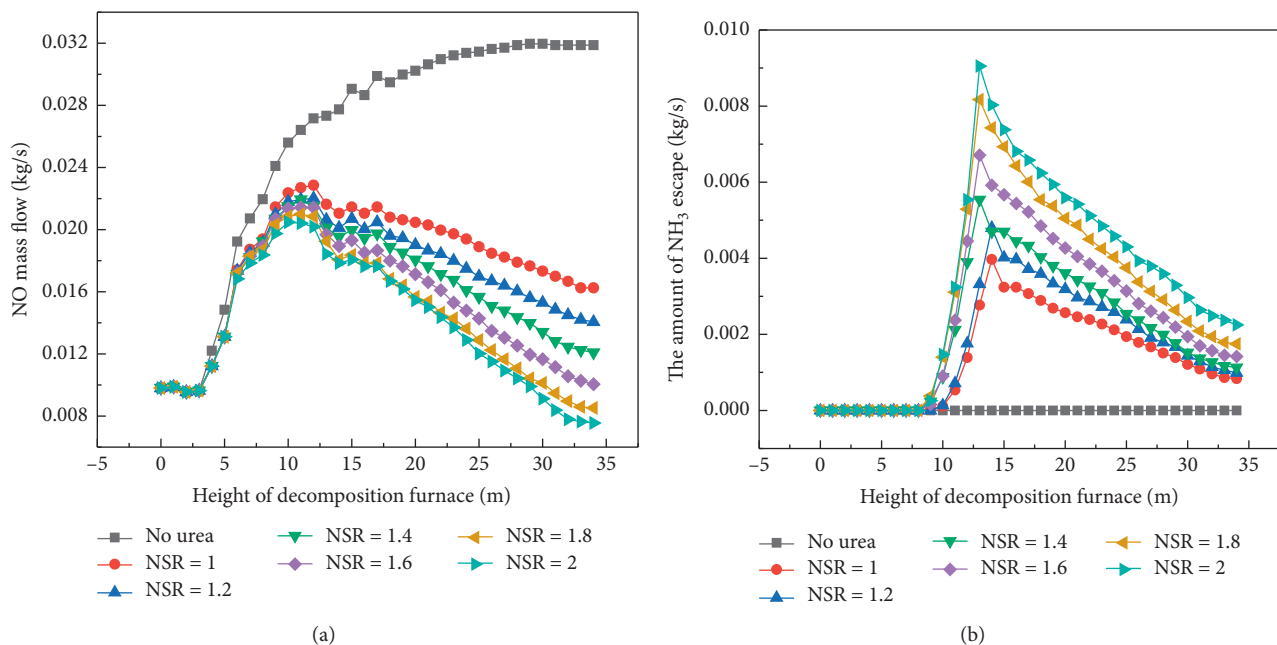


FIGURE 8: Flow curves of NO (a) and NH₃ (b) in the decomposing furnace with different NSR.

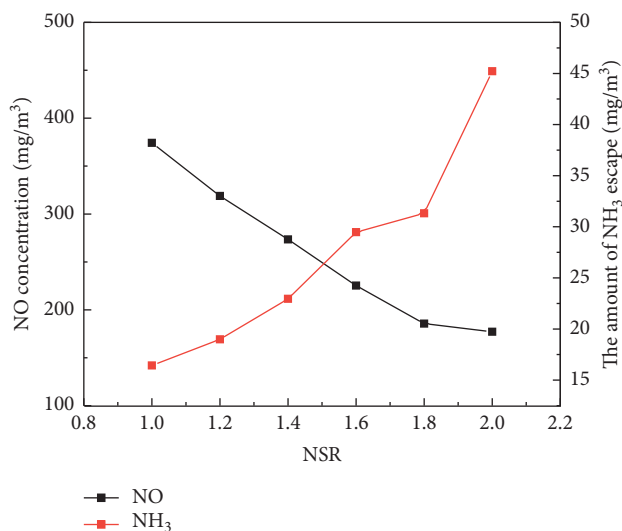


FIGURE 9: Variation of NO concentration and NH₃ escape concentration at the outlet of the decomposing furnace with NSR.

efficiency curves at different NSR are shown in Figure 10. It can be seen from Figure 10 that the denitrification efficiency increases with increasing NSR. Comprehensive analysis of SNCR simulation results under different NSR shows that when the NSR is increased from 1.0 to 1.8, the denitrification efficiency is relatively evenly improved. This is because the NO concentration in the furnace is higher at this time, and the SNCR reaction is stronger. Increasing NSR will allow more NO to be reduced. But when the NSR is greater than 1.8, the denitrification efficiency rise velocity begins to decrease, and the amount of NH₃ escape will increase much, so the optimal NSR is 1.8. Under this condition, the NO concentration of the decomposing furnace is 187.60 mg/m³,

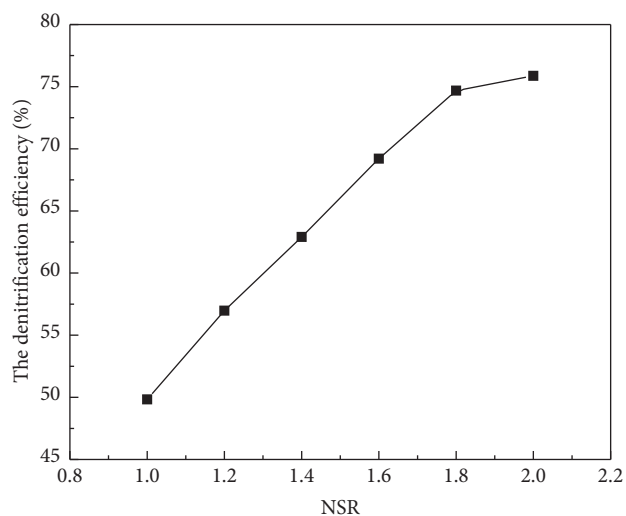


FIGURE 10: Variation of denitrification efficiency with NSR.

the NH₃ escape concentration is 32.40 mg/m³, and the denitrification efficiency is 74.75%.

4.3. Analysis of Urea Spray Velocity Results. The influence of the spraying velocity of the urea solution on the denitrification effect is mainly manifested in two aspects: the mixing degree of the urea solution with the mainstream smoke and the evaporation speed of the urea solution. Based on the above research, when the injection height of the reducing agent is 12 m and the molar ratio of ammonia and nitrogen is 1.8, simulations of different reducing agent injection velocity are performed. The jet velocity is from 20, 40, 60, and 80 m/s in order from low to high.

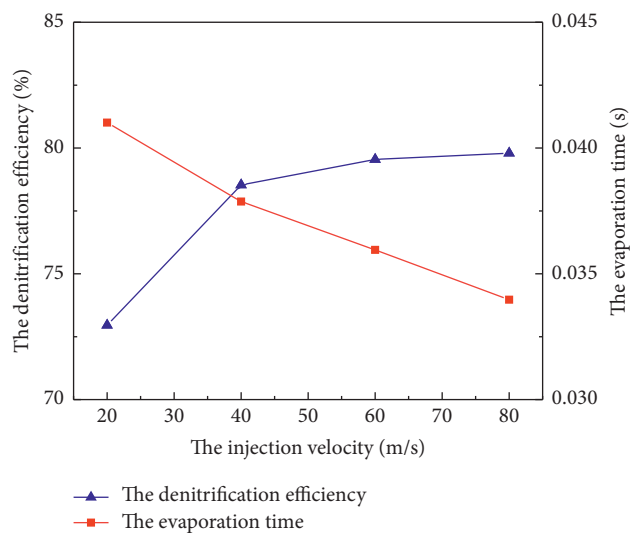


FIGURE 11: Evaporation time of urea solution and denitrification efficiency at different injection velocities.

The variations of evaporation time and denitrification efficiency of urea solution in the decomposing furnace with the spray velocity are shown in Figure 11. The variation of NO concentration and NH_3 escape concentration at the outlet of the decomposing furnace with the spray velocity of urea solution is shown in Figure 12. It can be seen from Figure 11 that the denitrification efficiency gradually increases with the increase in spraying velocity. Increasing the spray velocity and increasing the mixing speed of the urea solution and the flue gas in the decomposing furnace strengthen the heat transfer between the main flue gas stream and the urea solution, which accelerates the evaporation process of the urea solution and makes the urea decompose in advance in a suitable temperature window. At the same time, the increase of the spray velocity is conducive to extending the range of the urea solution in the depth direction of the decomposing furnace, thereby enhancing the degree of mixing of urea and the main flue gas stream and improving the denitrification efficiency. It can be seen from Figure 12 that the urea solution spray velocity increases, and the NH_3 concentration at the outlet of the decomposing furnace decreases first and then increases. This indicates that there is an optimal value for the injection velocity, and beyond this optimal value, the denitrification effect is not significantly improved, and at the same time, the NH_3 escape concentration at the outlet of the decomposing furnace is increased.

Based on the analysis in Figures 11 and 12, it can be seen that it is reasonable to choose a urea solution spray velocity of 40 m/s. At this time, the urea solution evaporation time is 0.038 s, and the NO concentration and NH_3 escape concentration at the outlet of the decomposing furnace are 350 mg/m^3 and 9.02 mg/m^3 , and the denitrification efficiency is 63.54%.

5. SNCR Simulation Test Verification

The simulation results were verified by the test results of a decomposing furnace of a cement plant in Hunan Province. The NH_3 escape concentration and NO concentration at the

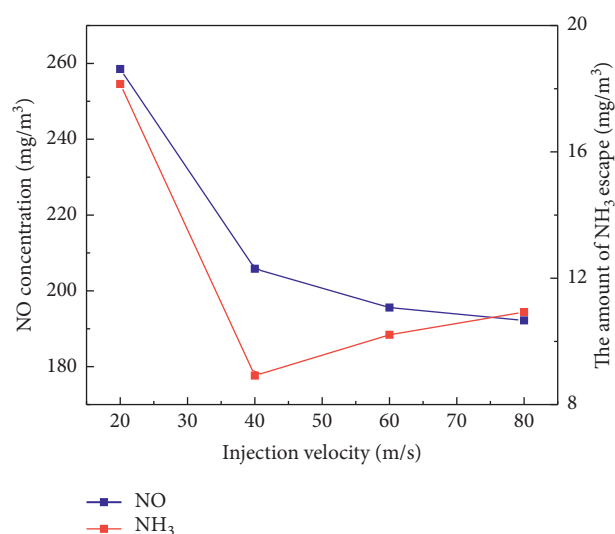


FIGURE 12: The variations of NO and NH_3 concentrations at the outlet of the decomposing furnace with spray velocity.

outlet of the decomposing furnace were measured for verification. The layout of the measurement points of the test is exactly the same with that of the simulation. Combined with verifying the actual operation of SNCR denitrification in the decomposing furnace, the SNCR denitrification parameter settings of the decomposing furnace are summarized in Table 5, and the comparison between the SNCR simulation results and the test results is summarized in Table 6. The simulation data used to support the findings of this study are included within the article, and the experimental data used to support the findings of this study are available from the corresponding author upon request.

After verification, the relative error between the test results and the simulation results is within 10%, which is within the allowable range. Therefore, the SNCR simulation calculation model has good reliability, and the simulation result can be used for production guidance.

TABLE 5: Parameter settings of SNCR.

The injection location (x, y, z) (m)				NSR	Velocity (m/s)	Grain diameter (m)
1	2	3	4			
(1.9, 1.9, 12)	(1.9, -1.9, 12)	(-1.9, -1.9, 12)	(-1.9, 1.9, 12)	1.8	40	0.0001

TABLE 6: Comparison between SNCR simulation value and experiment value.

Data categories	NO mass flow (mg/m^3)	NH_3 mass flow (mg/m^3)	Denitrification efficiency (%)
Experimental data	208.09	30.21	73.57
Simulation data	187.60	32.40	74.75
Relative error	9.85%	7.25%	1.60

6. Conclusion

SNCR numerical study was carried out based on a 2500 t/d new type dry cement kiln decomposing furnace in a plant of Hunan Province. The research conclusions are as follows:

- (1) The molar ratio of ammonia to nitrogen has a significant effect on the NO reduction in the decomposing furnace: as the molar ratio of ammonia to nitrogen increases, the concentration of NO at the outlet of the decomposing furnace decreases and the overall denitrification efficiency increases, but the concentration of NH_3 escaping also increases synchronously. Under the research conditions, a better ammonia-nitrogen molar ratio was 1.8.
- (2) The molar ratio of ammonia to nitrogen has a significant effect on the NO reduction in the decomposing furnace: as the molar ratio of ammonia to nitrogen increases, the concentration of NO at the outlet of the decomposing furnace decreases and the overall denitrification efficiency increases, but the concentration of NH_3 escaping also increases synchronously. Under the research conditions, a better ammonia-nitrogen molar ratio was 1.8.
- (3) With the increase of the spray velocity of urea solution, the mixture of urea solution and main flue gas is more uniform. Meanwhile, the evaporation process of urea solution is shorter and the denitrification efficiency is further improved. Under the study conditions, the better urea solution injection velocity was 40 m/s.
- (4) Under the study conditions, the optimal process parameters are as follows: the injection height of urea solution is 12 m, the NSR is 1.8, and the spray velocity of urea solution is 40 m/s. The simulation results under the optimal process parameters are as follows: the NO outlet concentration at the outlet of the decomposing furnace is $187.60 \text{ mg}/\text{m}^3$, the NH_3 escape concentration is $32.40 \text{ mg}/\text{m}^3$, and the denitrification efficiency is 74.75%.

In this paper, the inlet layout and particle size distribution of the urea solution are set as the same parameters in the simulation. However, according to the practical operation experience of cement plants, the particle size and

particle size distribution of urea solution would also have a great impact on SNCR denitrification.

Abbreviation

SNCR: Selective noncatalytic reduction
 SCR: Selective catalytic reduction
 CRF: Combustion research facility
 CFB: Circulating fluidized bed
 NSR: Ammonia-nitrogen molar ratio
 EDC: Eddy dissipation conceptual model

Nomenclature

ρ : Density of the gas
 k : Turbulent kinetic energy
 ε : Turbulent dissipation velocity
 μ : Molecular viscosity coefficient
 μ_t : Turbulent viscosity coefficient
 C : Constant term coefficient.

Data Availability

The experimental data used to support the findings of this study are available from the corresponding author upon request.

Conflicts of Interest

The authors declare that they have no conflicts of interest.

Acknowledgments

This work was financially supported by the National Natural Science Foundation of China (51590891), Youth Fund of National Natural Science Foundation of China (51806184), and the Science and Technology Key Project of Chenzhou Municipal (CZ2013163).

References

- [1] China Cement Association, "The 13th five-year development plan of cement industry," *Chinese Cement*, vol. 27, no. 7, pp. 7–17, 2017.
- [2] J. Wu, G. Liang, D. Hui et al., "Prolonged acid rain facilitates soil organic carbon accumulation in a mature forest in Southern China," *Science of The Total Environment*, vol. 544, pp. 94–102, 2016.

- [3] Y. Zou, X. J. Deng, D. Zhu et al., "Characteristics of 1 year of observational data of VOCs, NO_x and O₃ at a suburban site in Guangzhou, China," *Atmospheric Chemistry and Physics*, vol. 15, no. 12, pp. 6625–6636, 2015.
- [4] H. C. Lv, W. J. Yang, Z. J. Zhou et al., "Application of selective non-catalytic reduction on a power plant boiler," *Proceedings of The Chinese Society for Electrical Engineering*, vol. 28, no. 23, pp. 14–19, 2008.
- [5] F. Q. Liu, D. X. Yu, J. Q. Wu et al., "Effect of SCR on particulate matter emissions from a coal-fired boiler," *Journal of Chemical Industry and Engineering (China)*, vol. 69, no. 9, pp. 4051–4057, 2018.
- [6] S. Zandaryaa, R. Gavasci, F. Lombardi et al., "Nitrogen oxides from waste incineration: control by selective non-catalytic reduction," *Chemosphere*, vol. 42, no. 5-7, pp. 0–497, 2001.
- [7] W. Sang, S. Bae, R. Ah, and K. Done, "NO removal by reducing agents and additives in the selective non-catalytic reduction (SNCR) process," *Chemosphere*, vol. 65, no. 1, pp. 170–175, 2006.
- [8] M. Shiva, B. Jan, and P. K. Jonathan, "NO_x formation and selective non-catalytic reduction (SNCR) in a fluidized bed combustor of biomass," *Biomass and Bioenergy*, vol. 34, no. 9, pp. 1393–1409, 2010.
- [9] P. Gao, C. M. Lu, K. H. Han et al., "NO removal by adding additives in the selective non-catalytic reduction process," *Journal of Combustion Science and Technology*, vol. 14, no. 4, pp. 333–337, 2008.
- [10] D. H. Wang and N. Dong, "A review of urea pyrolysis to produce NH₃ used for NO_x removal," *Journal of Chemistry*, vol. 2019, Article ID 6853638, 11 pages, 2019.
- [11] K. H. Han, C. M. Lu, Y. Z. Wang et al., "Experimental study on de-NO_x characteristics of selective non-catalytic reduction," *Proceedings of The Chinese Society for Electrical Engineering*, vol. 28, no. 14, pp. 80–85, 2008.
- [12] F. F. Li and S. H. Wu, "Numerical simulation of selective non-catalytic reduction process with turbulence mixing influence," *Proceedings of The Chinese Society for Electrical Engineering*, vol. 23, pp. 46–52, 2008.
- [13] Q. Li, Y. X. Wu, H. R. Yang et al., "Simulation and optimization of SNCR process," *Journal of Chemical Industry and Engineering (China)*, vol. 64, no. 5, pp. 1789–1796, 2013.
- [14] S. S. Xu and L. N. Zhang, "Simulation study on the better flue gas velocity of high efficiency and low NO_x combustion of coal blends in the calciner," *Bulletin of The Chinese Ceramic Society*, vol. 33, no. 3, pp. 547–552, 2014.
- [15] D. H. Wang, X. T. Wang, Y. H. Guo et al., "Influence of OFA nozzle position on NO_x Emission," *Chinese Journal of Power Engineering*, vol. 32, no. 7, pp. 523–527, 2012.
- [16] G. S. Du, D. C. Wang, L. Li et al., "Simulation of 3-d flow around a van-body truck with RNG *k-ε* turbulence model," *Journal of Hydrodynamics*, vol. 13, no. 4, pp. 98–101, 2004.
- [17] M.-L. Zhang and Y.-M. Shen, "Three-dimensional simulation of meandering river based on 3-D RNG *k-ε* turbulence model," *Journal of Hydrodynamics*, vol. 20, no. 4, pp. 448–455, 2008.
- [18] S. X. Mei and J. L. Xie, "Numerical simulation of co-combustion of coal and RDF in coupling with decomposing of calcium carbonate in a precalciner with swirl," *Journal of Chemical Industry and Engineering (China)*, vol. 2, no. 24, pp. 1–9, 2017.
- [19] S. X. Mei, J. L. Xie, F. He et al., "Numerical simulations in double-sprayed precalciner by changing the location of raw meal inlets," *Journal of Wuhan University of Technology*, vol. 34, no. 9, pp. 26–30, 2012.
- [20] S. S. Xu, H. Wu, F. H. Liu et al., "Simulation study on the optimum bottom cone inlet diameter of coal blends combustion in the precalciner," *Bulletin of The Chinese Ceramic Society*, vol. 35, no. 8, pp. 2383–2388, 2016.

Research Article

Kinetic Modeling Study of the Industrial Sulfur Recovery Process for Operating Condition Optimization

Shan Huang ¹, Zhaohui Teng,¹ Lisheng Zhang,² Qulan Zhou ¹ and Na Li¹

¹State Key Laboratory of Multiphase Flow in Power Engineering, Xi'an Jiaotong University, Xi'an 710049, China

²Natural Gas Purification Plant of Puguang Gasfield, Dazhou 636150, China

Correspondence should be addressed to Qulan Zhou; qlzhou@mail.xjtu.edu.cn

Received 20 March 2020; Accepted 12 May 2020; Published 25 May 2020

Guest Editor: Norbert Miskolczi

Copyright © 2020 Shan Huang et al. This is an open access article distributed under the Creative Commons Attribution License, which permits unrestricted use, distribution, and reproduction in any medium, provided the original work is properly cited.

Sulfur recovery from acid gas (H_2S and CO_2), which is contained in fresh natural gas, can bring many economic and environmental benefits, and this topic has been studied for years. Finding an optimal operating condition for the factory is of much importance. In this paper, we built a reactor network analysis model with a detailed mechanism to describe and calculate the process in the sulfur recovery unit. This detailed mechanism included 94 species and 615 elementary reactions. Our model has a more accurate residence time than other existing models. This simulation model was verified with industrial data, and the calculation result was highly consistent with the industrial data and more accurate than other approaches. Then, we used this reactor network analysis model to study the effect of the excess air coefficient, the thermal reactor temperature, and the temperature of cooling water on the sulfur recovery efficiency of a real device in the Puguang gas field. The result showed the excess air coefficient and thermal reactor temperature had a clear impact on sulfur recovery efficiency. After analysis, we got the optimum condition parameters for this device. At last, these parameters were tested in the real sulfur recovery device, and the result was reasonable. Our research provides a way to improve the sulfur recovery process in the industry, and it can be helpful to reduce pollution emissions and improve economic performance.

1. Introduction

Sulfur recovery in natural gas extraction has been the subject of much research in the recent years. The Claus process is widely used to recover elementary sulfur from acid gas contained in fresh natural gas. [1] And, the gas from the sour water stripper (SWS) is also a common fuel used in Claus process. It involves thermal oxidation of hydrogen sulfide and its reaction with sulfur dioxide to form sulfur and water vapor.

The basic scheme of a sulfur recovery unit (SRU) is shown in Figure 1. [2] There are five main kinds of devices in the scheme: a burner, a thermal reactor (TR), a waste heat boiler (WHB), two Claus reactors (CR), and a series of sulfur condensers. The acid gas (containing H_2S , CO_2 , H_2O , CO , NH_3 , and so on) is mixed with air at the burner [3], and then the gas burns and flows into the thermal reactor, which

provides necessary residence time to form the Claus gas ($H_2S:SO_2=2$). Next, Claus gas goes into the waste heat boiler and the first condenser to cool down, and after that the Claus gas is sent into the Claus reactors.

The two steps of the overall process may be represented as follows. Equation (1) is the overall reaction occurring in the TR. In this process, a third of the total H_2S reacts with oxygen at the best stoichiometric ratio to form Claus gas. The main component of Claus gas is the residual H_2S and the generated SO_2 (the molar concentration ratio of H_2S and SO_2 is about 2, which meets the best stoichiometric ratio of equation (2)). Equation (2) takes place in the downstream Claus reactor, and the residual H_2S is oxidized by the generated SO_2 to form S_x . The elemental sulfur is removed by condensation in the three-level condensers:

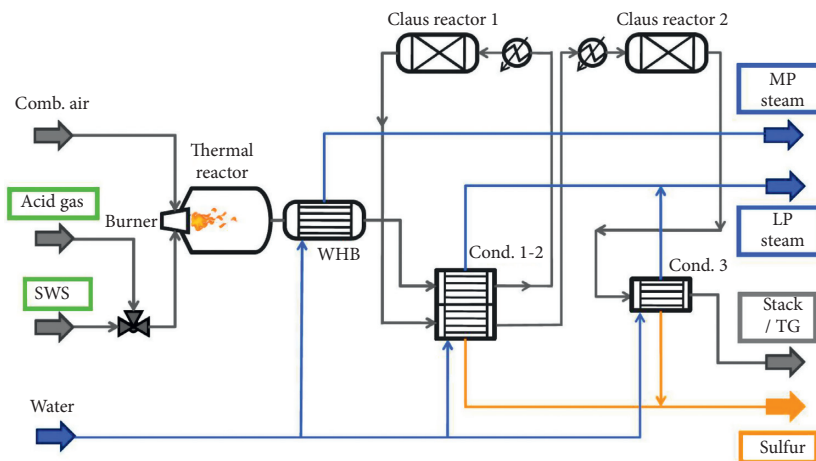
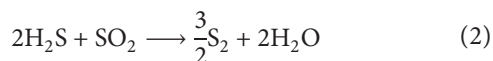
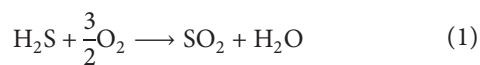


FIGURE 1: Basic scheme of a sulfur recovery unit.



The most efficient and economical way to find the best-operating conditions for an industrial sulfur recovery process is simulation calculation. In 2015, Nabikandi and Fatemi [4] performed a simulation of an industrial Claus SRU process with equilibrium and kinetic methods comparatively. Their research revealed that both kinetic and equilibrium models present reliable results, but the kinetic model which has the ability of prediction compositions, temperature, and pressure along the furnace showed higher potential to cover the industrial results. But, the reaction mechanism in this process is rather complex and has not been completely understood. With the development of the reaction mechanism and the tuning of the kinetic parameters, the kinetic simulation methods can get closer to the real results. After reviewing the kinetic models of H_2S combustion and evaluating the effect of the acid gas impurities, Gupta et al. [5] indicated that a comprehensive kinetic model that can capture the combustion chemistry of H_2S along with the presence of impurities in Claus reactors can improve the efficiency of sulfur recovery processes and sulfur quality. And, the effect of impurities such as aromatics and mercaptans on the Claus process was studied by Ibrahim [6] and Mahdipoor [7], respectively.

Though many industrial simulation studies have been conducted, there is still room for improvement. The authors in [8, 9] built a detailed reaction mechanism of the acid gas, and they used this mechanism to do a CFD simulation of the reactor furnace of the sulfur recovery units which focused on the flow fields of the process. Then, the authors in [3, 10] also did a kinetic simulation of acid gas destruction with a detailed mechanism for simultaneous syngas and sulfur recovery, and their work investigated the optimal operating conditions for H_2 production other than sulfur recovery. Manenti et al. [11–15] did much work on the modeling

simulation of the sulfur recovery process, and their work covered not only the revision of the combustion mechanism but also the optimization of the operating conditions for sulfur recovery. Though their work was valuable, the mechanism and model used in their work did not update with the recent research findings. Most of all, their optimization results were not verified by the industrial data.

To find a practical way to improve the efficiency of the industrial sulfur recovery process, this paper was trying to find the optimum operating condition for the sulfur recovery unit, especially for the burner, TR, and WHB. To achieve this, we built a new reactor network analysis (RNA) model with a revised detailed mechanism for the first step. Then, the new analysis model with the revised mechanism was verified with industrial data and other simulation results. After verification, this analysis scheme was used to do the condition optimization research of a real sulfur recovery unit in the Puguang Gas Field in China, and then the calculation result was tested in the factory to see if the optimum parameters work well.

The organization of the paper is as follows. In Section 2, we discuss the development of the reaction mechanism. In Section 3, the settings of the RNA model and the verification of this model are displayed. The operating condition optimization research is provided in Section 4. At last, we made a conclusion of this research in Section 5. The results of this research will provide further data to improve the process of elementary sulfur recovery in the industry, which can be helpful to reduce pollution emissions and improve economic performance.

2. Reaction Mechanism

In our study, we summarized and discussed the recent development of elementary reaction studies at first, and then we selected appropriate reactions to fulfill the reaction mechanism. And, some parameters of certain elementary reactions have been revised according to the new academic results. The final mechanism includes 94 species and 615 elementary reactions.

2.1. H₂S Pyrolysis. H₂S pyrolysis plays a key role in the combustion process; not only because H₂S is the source of the sulfur in SRUs, but also H₂S pyrolysis provides the radical pool, especially in the lean air combustion conditions. In 2003, Binoist et al. [16] did a kinetic study of the pyrolysis of H₂S at different residence times (0.4~1.6 s) and at different temperatures (800~1100°C) by experiment and simulation. A detailed radical mechanism was written to account for the experimental results, and it was in good agreement with the experimental data. According to Binoist et al, the pyrolysis kinetic scheme was the first step and the core of a complete detailed mechanism capable of modeling the various oxidation reactions encountered in an industrial Claus furnace. In 2013, Manenti et al. [2] put forward a revised detailed kinetic scheme for the pyrolysis and oxidation of sulfur compounds. In their research, some adjustments were done to the pyrolysis of H₂S. According to Manenti et al, the kinetic model accuracy was improved by 10–20%, depending on the operating temperature. In 2017, Li et al. [17] presented a detailed kinetic mechanism for describing the chemical process during decomposition of the H₂S–CH₄ mixture under dilution condition, and the prediction of the conversion of H₂S was accurate. The kinetic parameters for the pyrolysis of H₂S are shown in Table 1.

2.2. H₂S Oxidation. In 2013, Zhou et al. [18] studied the oxidation of H₂S in an atmospheric pressure flow reactor at temperatures from 950 to 1150 K, and a comprehensive chemical kinetic model for H₂S was developed. The H₂S oxidation mechanism developed by Zhou et al has been validated versus the experimental data of the diluted H₂S oxidation process. In 2019, Li et al. [19] explored the oxidation mechanisms of H₂S by oxygen on activated carbon, and H₂S adsorbed on activated carbon is oxidized by O₂-producing elemental sulfur, which further oxidized to SO₂. This H₂S oxidation compilation included H₂ oxidation, SO and SO₂ oxidation mechanism, S/H reaction subset, and other significant updated kinetic parameters for the H/S/O system. The reaction path analysis is shown in Figure 2.

In 2016, Barba et al. [20] did an experimental and numerical analysis of the oxidative decomposition of H₂S. In this work, a comprehensive chemical kinetic model for the oxidation of H₂S in a low-oxygen atmosphere was studied, by varying the O₂/H₂S ratio (0.2~0.35), residence time (150~300 ms), and process temperatures (900–1100°C). The results showed a very good agreement with the experimental values at higher temperatures (1100°C). Relevant reactions of the kinetic scheme are shown in Table 2.

2.3. Other Mechanisms

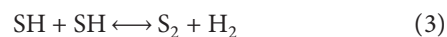
2.3.1. C/H/O Mechanism. The mechanism for C/H/O is taken from the well-known GRI-3.0. This mechanism has been validated by many researchers and experimental results. The data were cited from <http://combustion.berkeley.edu/gri-mech/>.

TABLE 1: The kinetic parameters for the pyrolysis of H₂S.

Reactions ^a	A (cm ³ ·mol ⁻¹ ·s ⁻¹)	n	E (cal·mol ⁻¹)
S + H + M = SH + M	0.62 × 10 ¹⁷	-0.6	0
S + H ₂ = SH + H	0.14 × 10 ¹⁵	0.0	19 300
S ₂ + M = S + S + M	0.48 × 10 ¹⁴	0.0	77 000
H + S ₂ + M = HS ₂ + M	0.40 × 10 ¹⁴	2.84	1 665
SH + SH = S ₂ + H ₂	0.50 × 10 ¹²	0.0	0.0
SH + S = S ₂ + H	0.30 × 10 ¹⁴	0.0	0.0
H ₂ S + M = S + H ₂ + M	0.16 × 10 ²⁵	2.613	89 100
H ₂ S + H = SH + H ₂	0.35 × 10 ⁰⁸	1.94	904
H ₂ S + S = SH + SH	0.83 × 10 ¹⁴	0.0	7400
HS ₂ + H = SH + SH	0.97 × 10 ⁰⁸	1.62	-1030
Duplicate	0.11 × 10 ¹⁴	0.353	210
HS ₂ + H = S ₂ + H ₂	0.12 × 10 ⁰⁹	1.653	-1105
HS ₂ + H = H ₂ S + S	0.44 × 10 ¹⁴	0.0	6326
HS ₂ + S = S ₂ + SH	0.42 × 10 ⁰⁷	2.2	-600
HS ₂ + SH = H ₂ S + S ₂	0.63 × 10 ⁰⁴	3.050	-1105
HS ₂ + HS ₂ = H ₂ S ₂ + S ₂	0.96 × 10 ¹	1.0	57030
H ₂ S ₂ + M = SH + SH + M	0.14 × 10 ¹⁶	0.0	15 000
H ₂ S ₂ + H = HS ₂ + H ₂	0.50 × 10 ⁰⁸	1.933	-1408
H ₂ S ₂ + H = H ₂ S + SH	0.20 × 10 ¹⁵	0.0	0.0
H ₂ S ₂ + S = HS ₂ + SH	0.29 × 10 ⁰⁷	2.31	1204
H ₂ S ₂ + SH = HS ₂ + H ₂ S	0.64 × 10 ⁰⁴	2.98	-1480

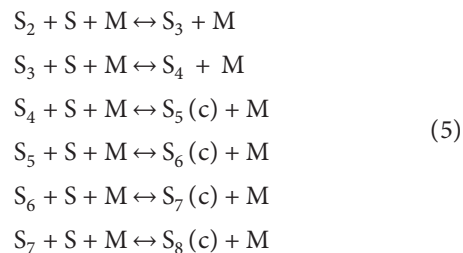
^aDeclared duplicate reaction.

2.3.2. Formation of Sulfur Vapor (S₂). Thanks to the pyrolysis and oxidation of H₂S, there will be an abundance of S radicals and HS radicals in the thermal reactor. And, elemental sulfur vapor (S₂) can be formed via the following chemical reactions [21]:



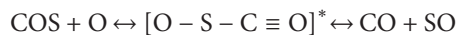
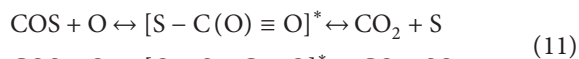
And, equation (3) leads to the production of H₂, and hydrogen is a species which deserved consideration in the Claus process. As seen in the literature, Cong et al. [8], Ravikumar et al. [10], Savelieva et al. [22], and Li et al. [23] have studied the way to increase hydrogen production via the thermolysis and oxidation of hydrogen sulfide (H₂S).

2.3.3. Molecular Growth of Sulfur. When the concentrations of S, HS, S₂, H₂S₂, and HS₂ are relatively high, the chance of growth from S to S₈ increases. The major steps can be presented as follows [24]:

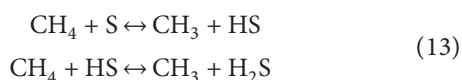


for thermodynamic reasons, the ring or the cyclic structure of S₅(c) would be formed. Depending on the temperature, an equilibrium would be formed between the open linear

Dagaut et al. [30] showed that the inhibition effect is progressively reduced with higher temperatures for the cases of stoichiometric and lean inlet oxygen. In the thermal reactor, CS₂ and COS can react with O radicals which were provided by the thermal decomposition of SO₂. The chemical paths are as follows:



2.3.6. The Oxidation of Methane. In some industrial thermal reactors, CH₄ is used for ignition and to maintain the temperature. The overall scheme for the combustion of methane is well known, and it involves, depending on the conditions, species such as CH₃, CH₂O, CHO, CO, CO₂, C₂H₆, C₂H₄, C₂H₂, CH₂, CH, C₃H₃, and C₆H₆. [31] The two-carbon molecules become more important under fuel-rich conditions. The research by Westbrook and Dryer [32] was meaningful, and they showed that the methane combustion in the atmosphere with hydrogen sulfide under fuel-rich conditions was initiated by



Through the above reactions, sulfur species can affect the main chemical paths for methane oxidation.

3. Reactor Network Analysis Model

3.1. Settings of the RNA Model. We used Chemkin Pro to do the analysis, and the scheme of the RNA model is shown in Figure 3. According to Pierucci et al. [33], a perfectly mixed reactor was adopted to describe the mix of acid gas and air. In the model, H₂S was oxidized to SO₂ as soon as it met O₂, while the other species were assumed inert because of the fast ignition of H₂S concerning the other species.

We used a plug flow reactor (PFR) to simulate the thermal reactor by defining the diameter along with the distance. A smaller diameter was used to represent the transition section between the burner and the reactor. Residence time is a key factor influencing the chemical process, and the residence time in this process is more precise in this way.

The acid gas starts to burn at the thermal burner and continues to react in the thermal reactor. Chemical equilibrium is supposed to reach before the outlet of the thermal reactor because of sufficient residence time, so the gas concentration at the end of the thermal reactor is even. The tubes in the waste boiler are the same and independent, so the chemical process and products in different tubes are the same. As a result, a PFR was used to represent one tube in the waste boiler. In the work by Manenti et al. [11, 13], the whole waste boiler was also considered as one tube, so the inlet flow rate and the structure size were not appropriate. In our simulation model, a gas flow splitter (GFS) was used. A

certain part of the gas of the thermal reactor was injected into the waste boiler, while the other part of the tail gas was directly transported to the first outlet. The product at this outlet is the same as the product of the thermal reactor. The inlet flow rate of this PFR was calculated according to the number of the tubes in the waste boiler, and the structure size of this PFR was set as the same as the real tube. Through the settings mentioned above, the residence time in the waste boiler was precisely controlled.

For the thermal reactor, the heat transfer can be assumed to be zero because of the adiabatic layer at the outside. For the waste heat boiler, the heat exchange is fierce because of the condensation effect. The tubes in the waste boiler were assumed to be clean, and the heat transfer coefficient was determined only by the heat convection between the gas and the tubes.

3.2. Verification of the RNA Model. A new RNA model with a revised mechanism has been set up according to the introduction above, and before applying this approach, verification was done. The industrial data were adopted from the research by Manenti et al. [15]. The structure parameters and inlet operating conditions are listed in Table 3.

The temperature profile is shown in Figure 4. The value of the temperature at the outlet of WHB is consistent with the industrial data. The temperature in the TR is stable because the layer was adiabatic, and the reaction heat can maintain the temperature. The temperature at the beginning of the WHB has a sharp drop because of the cooling water. The speed of temperature falling decreases with the increase of the reactor length and the residence time because of the decrease in the temperature gradient between the gas and the cooling water.

The gas-phase species composition along the thermal reactor and the waste heat boiler is shown in Figures 5 and 6. Results show that the mole fraction at the beginning of TR changes fiercely and gets to equilibrium long before the exit of the TR. Then in the WHB, the equilibrium and kinetics shift because of the rapid change of temperature. As we can see, the simulation result matches the experimental data very well. The mole fraction of H₂S decreases in the TR because of its oxidation and pyrolysis, while it increases in TR because of the change of chemical equilibrium. The formation of S₂ leads to a sharp rise in mole fraction at the beginning of TR, and then the mole fraction of S₂ decreases sharply in WHB caused by the formation of the sulfur isomers.

Due to the oxidation and pyrolysis of H₂S, the mole fractions of SO₂ and H₂ have a huge increase at the inlet. And, in the WHB, the mole fractions of H₂ and S₂ have a sharp drop, while the mole fraction of H₂S has an equivalent increase because of the shift of the chemical equilibrium. With the continuing falling of temperature in WHB, the mole fractions of most species remain the same except for S₂.

In Manenti et al's work, gas quenching was set at position 7.5 m (corresponding at temperature 950°C) and industrial S₂ data were collected at this position. The mole fraction of S₂ at 7.5 m is 0.0587 which is in accordance with the industrial data (5.9%). After this position, S₂ transforms

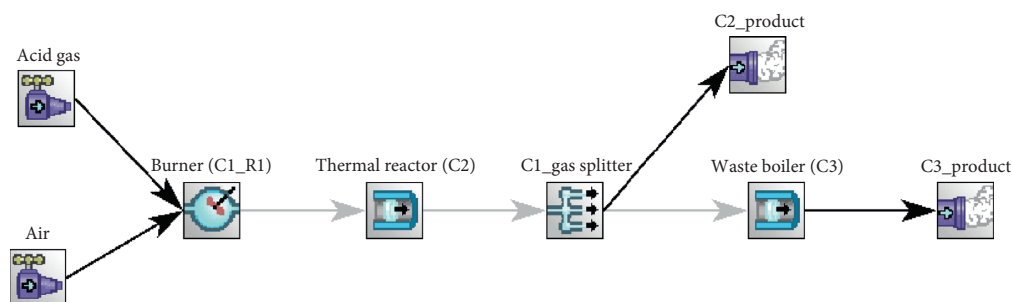


FIGURE 3: The scheme of the RNA.

TABLE 3: The structure parameters and inlet operating condition.

Parameters	Value
Acid gas composition (vol %)	C ₂ H ₆ (1.40), CH ₄ (2.1), CO ₂ (6.62), H ₂ O (6.40), H ₂ S (79.55), H ₂ (3.7), NH ₃ (0.48), C ₃ H ₈ (1.98), CO (0.32), H ₂ O (6.4)
Acid gas flow rate	4230.5 kg/h
Acid gas temperature	125°C
Combustion air composition (vol %)	H ₂ O (9.70), N ₂ (71.38), O ₂ (18.92)
Combustion air flow rate	8907.1 kg/h
Combustion air temperature	45°C
Operating pressure	159 kPa
Reactor length	6.5 m
Reactor diameter	1.55 m
WHB tube length	6.00 m
WHB tube number	470
WHB tube diameter	0.050 m

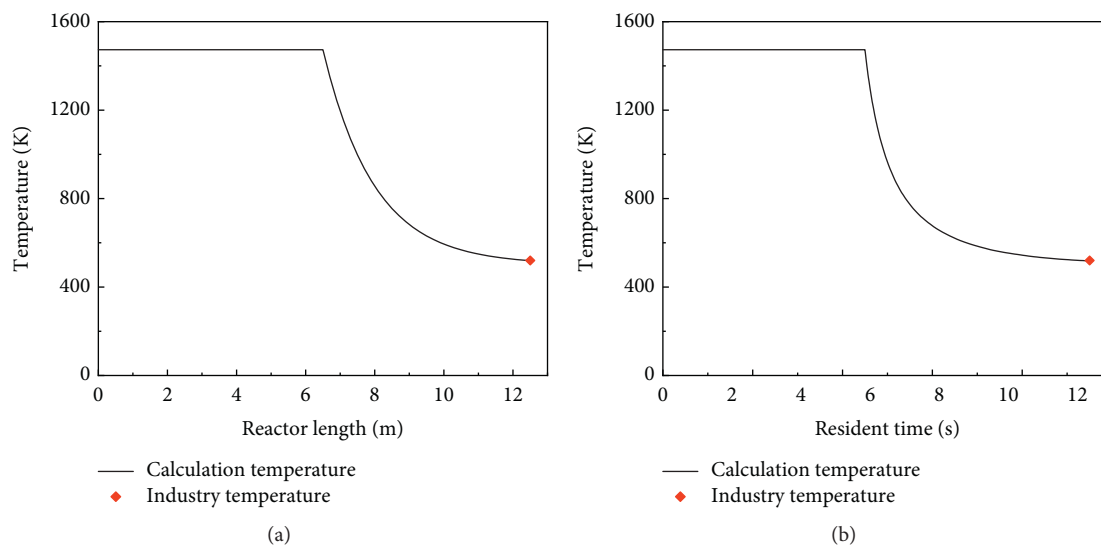


FIGURE 4: Temperature (K) profile in the TR and WHB.

into other sulfur isomers (shown in Figure 7). There are 8 allotropes (S_1 – S_8) of sulfur, and their transition is highly temperature dependent. Among all the isomers, S_2 and S_8 are the most stable ones. S_2 remains stable above 600 K, while S_8 is dominant when the temperature is below this value. As we can conclude from Figure 7, all of the S_2 have converted to

other types of sulfur allotropes due to the temperature drop, and the dominant products are S_6 , S_7 , and S_8 .

Based on the calculation result above, we did an error analysis to compare the results between our work and Manenti et al's work (shown in Figure 8). In Figure 8, different colors are used to represent different species and

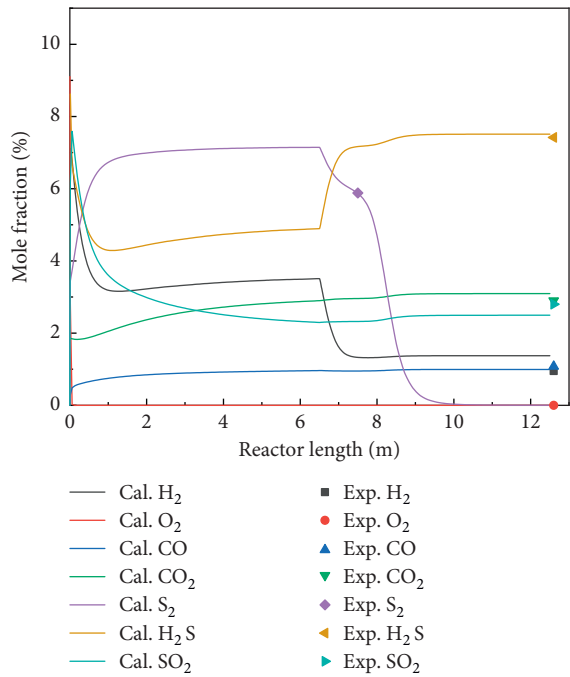


FIGURE 5: Gas-phase species composition along with the TR and WHB of industrial data and the calculation result.

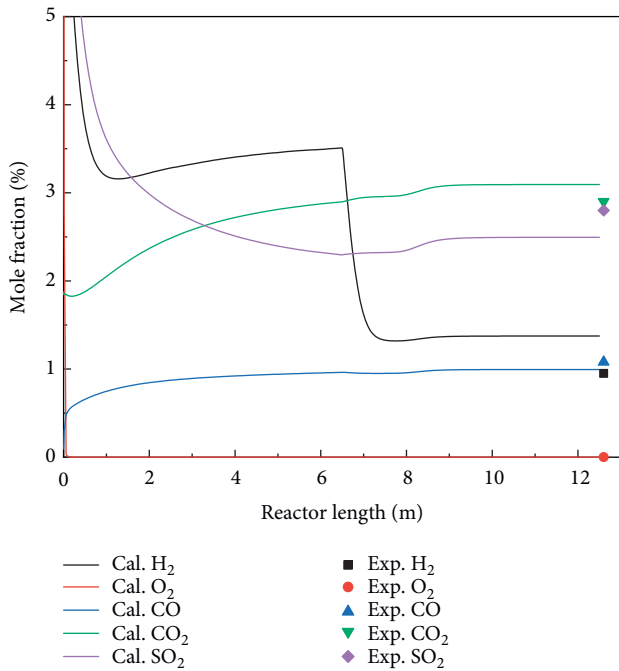


FIGURE 6: Gas-phase species composition along with the TR and WHB of industrial data and the calculation result (magnified).

squares represent Manenti et al's results while dots represent our results. As we can see, our calculation results have a better prediction in the concentration of all these species except for CO, and the deviations of the CO concentration is acceptable.

Through the analysis above, we can see that the new RNA model with a revised mechanism can not only describe the

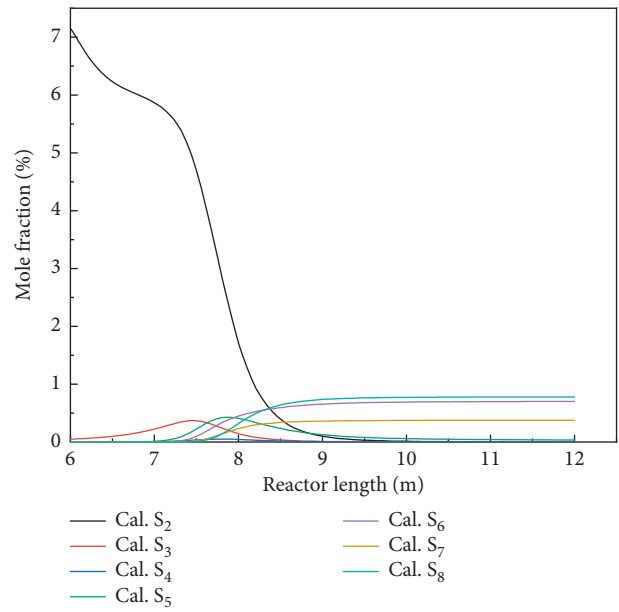


FIGURE 7: The formation of the sulfur isomers.

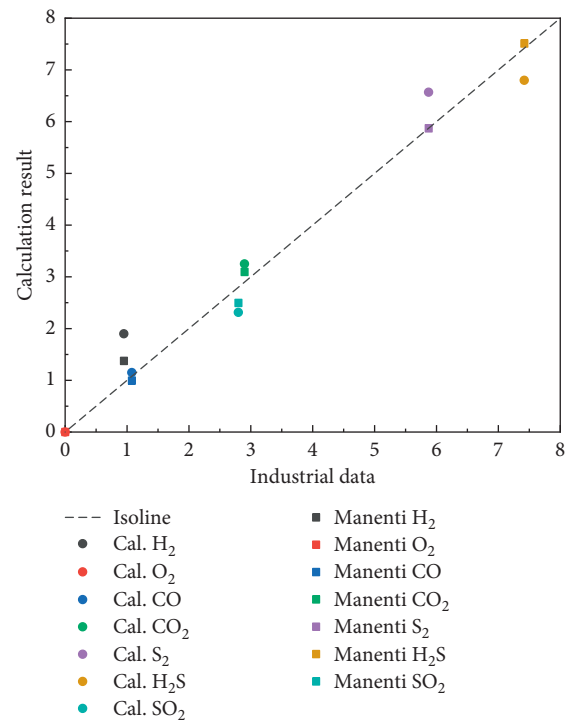


FIGURE 8: The residuals of the calculated concentration.

key features in SRUs but also predict the concentration with good accuracy.

4. Optimization Research

4.1. Sulfur Recovery Efficiency. After the verification, we did the parameter optimization study of the burner used in a real factory. This optimization research aimed to obtain the highest sulfur recovery efficiency and in this way will H₂S do

the least harm to the environment. To estimate the H₂S conversion, sulfur recovery efficiency was defined as follows:

$$E_s = \frac{S_{\text{at the exit of SRUs}}}{S_{\text{at the inlet of SRUs}}} = \frac{S_{\text{at the exit of WHB}} + S_{\text{at the exit of CR}}}{S_{\text{at the inlet of SRUs}}}, \quad (14)$$

where E_s stands for the sulfur recovery efficiency and S stands for the total amount of all the allotropes of sulfur, and its unit is g/s. The reaction of H₂S and SO₂ in real CR is always complete, so $S_{\text{at the exit of CR}}$ can be calculated by equation (2) as follows:

$$S_{\text{at the exit of CR}} = \begin{cases} \frac{3}{2} \times S_{\text{SO}_2 \text{ at the inlet of CR}}, & \left(\text{if } \frac{C_{\text{H}_2\text{S}} \text{ at the inlet of CR}}{C_{\text{SO}_2} \text{ at the inlet of CR}} \geq 2 \right), \\ \frac{3}{4} \times S_{\text{H}_2\text{S}} \text{ at the inlet of CR}, & \left(\text{if } \frac{C_{\text{H}_2\text{S}} \text{ at the inlet of CR}}{C_{\text{SO}_2} \text{ at the inlet of CR}} \leq 2 \right), \end{cases} \quad (15)$$

where the mass flow rates of SO₂ and H₂S at the inlet of CR are equal to those at the exit of WHB.

4.2. Parameter Optimization Study. In our work, the excess air coefficient, temperature in TR (T_{TR}), and temperature of the cooling water (T_{CW}) were studied. These three parameters can be adjusted easily in the factory. The excess air coefficient and T_{TR} are decided by the amount of fuel and air. The SRUs studied in our paper are located at the Puguang gas field, China. The relating structure parameters and inlet operating conditions are listed in Table 4.

4.2.1. Excess Air Coefficient. The excess air coefficient is controlled by the ratio of acid air to gas. And, from equations (1) and (2), we can see that the best stoichiometric ratio for the complete reaction of H₂S and O₂ is 2. The excess air coefficient is defined as the ratio of the actual amount of air to the amount required for complete combustion of fuel (stoichiometric amount). In a real factory, the excess air coefficient is not always 1 because there are other species in acid gas other than H₂S, taking parting in the subsequent reactions. So, it is useful to find out the best excess air coefficient to gain the highest sulfur recovery efficiency. In this paper, the excess air coefficient varied from 0.7 to 1.4, which means the ratio of the actual amount of air to the stoichiometric amount was from 0.7 to 1.4.

The results are shown in Figure 9. The sulfur recovery efficiency first has an increase and then a decrease with the excess air coefficient varying from 0.7 to 1.4. There is a maximum that lies between 0.9 and 1 where the sulfur recovery efficiency is beyond 95%. This result is reasonable because both too much and too little air will affect the conversion of H₂S. From Figure 9, we can see that the peak point is located near 0.93 and the corresponding sulfur recovery efficiency is beyond 98%.

4.2.2. Temperature in TR. From the verification result, we can see that the concentration of many species changed fiercely near the inlet of the TR. And, after the reactions take place in TR, the gas should contain appropriate H₂S and

SO₂. We have reason to believe the temperature in TR is important to the conversion of H₂S. The TR temperature was decided by the amount of fuel. The more the fuel, the higher the TR temperature. The research result of temperature is shown in Figure 10. The sulfur recovery efficiency is not a monotone function of temperature in TR. As the temperature varied from 1073 K to 1473 K, the sulfur recovery efficiency increased clearly at first and then increased with a much slower speed. And at last, it had a significant drop with the increase in temperature. This curve had a peak near 1273 K. This result indicates that the temperature did have a clear influence on the whole sulfur recovery process. Higher temperature means more fuel, and more fuel means more sulfur recovery speed. So, 1273 K was chosen to be the optimum TR temperature in the sulfur recovery process.

4.2.3. Temperature of Cooling Water. From the verification result above, the equilibrium and kinetics in WHB were different from those in TR because of the rapid change of the temperature. So, the change speed of the temperature which is decided by the temperature of the cooling water is important to this process. Different temperatures of the cooling water will result in different WHB outlet temperatures (shown in Figure 11). With the increase of the cooling water temperature, the gas temperature at WHB outlet increased. The lower the cooling water temperature, the more the gas temperature at the WHB outlet dropped with the same residence time and the faster the decrease in the gas temperature in WHB. This result was reasonable. The greater the temperature gradient was, the more powerful the heat transfer was.

The sulfur recovery efficiency as a function of the cooling water temperature is shown in Figure 12. Although the gas temperature at the WHB outlet was influenced by the cooling water temperature obviously, the sulfur recovery efficiency had little reaction to the change of this temperature. With the increase of the cooling water temperature, the sulfur recovery efficiency only had a very slight increase which can be ignored. So, the temperature of the cooling water is always set to the temperature which can help to obtain the highest heat efficiency of the WHB.

TABLE 4: The structure parameters and inlet operating condition in the Puguang gas field.

Parameters	Value
Acid gas composition (mole %)	CH ₄ (0.21), CO ₂ (32.28), H ₂ O (6.97), H ₂ S (60.52), COS (0.01)
Acid gas flow rate	46827 kg/h
Acid gas temperature	50°C
Combustion air composition (mole %)	H ₂ O (6.5), N ₂ (73.91), O ₂ (19.59)
Combustion air flow rate	53530 kg/h
Combustion air temperature	108°C
Operating pressure	159 kPa
Reactor length	6 m
Reactor diameter	2.5 m
WHB tube length	6.00 m
WHB tube number	500
WHB tube diameter	0.074 m

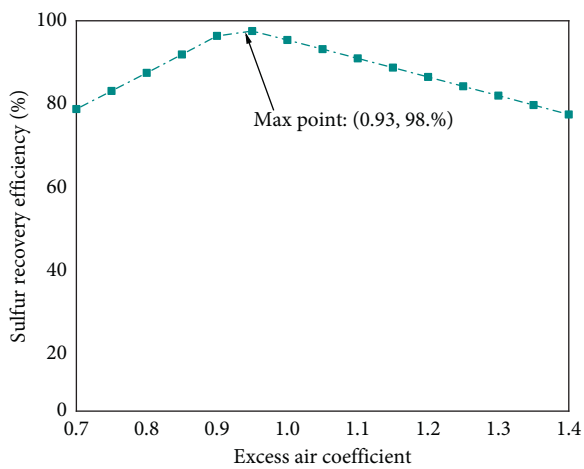


FIGURE 9: Sulfur recovery efficiency as a function of the excess air coefficient.

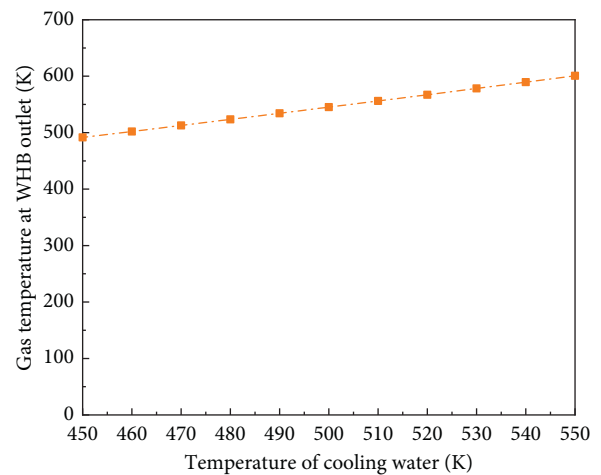


FIGURE 11: The gas temperature at the WHB outlet as a function of the temperature of cooling water.

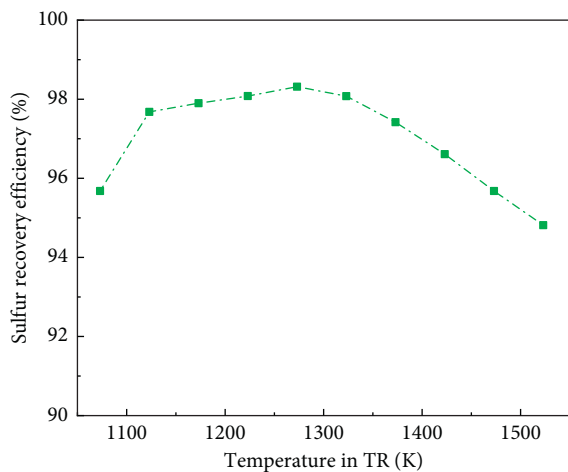


FIGURE 10: Sulfur recovery efficiency as a function of temperature in TR.

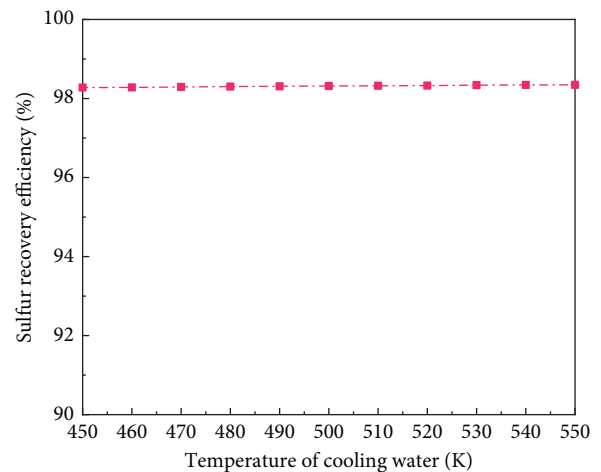


FIGURE 12: Sulfur recovery efficiency as a function of the temperature of cooling water.

4.3. *Test in Factory.* Before we tested the calculation result, we recorded an original copy of the industrial data in the Puguang gas field in China. The original operating parameters of SRUs are as follows:

$$\begin{aligned}
 Q_{\text{acid gas},1} &= 46827 \text{ kg/h}, Q_{\text{air},1} = 53530 \text{ kg/h}, \\
 T_{\text{TR},1} &= 1270 \text{ K}, \text{ and } T_{\text{CW},1} = 500 \text{ K}.
 \end{aligned}
 \tag{16}$$

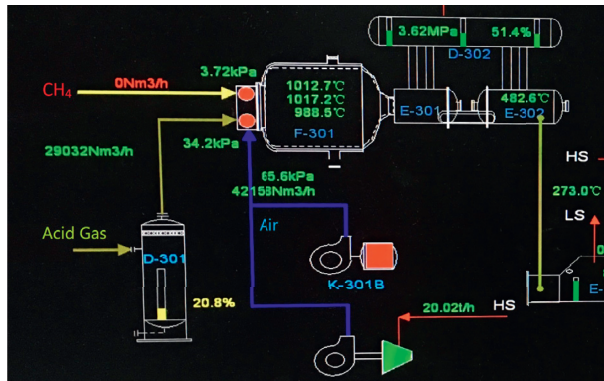


FIGURE 13: The display screen of the central controller in the Puguang gas field (test situation).

TABLE 5: Original industrial data and the optimization result.

	Original situation	Optimization situation
Acid gas (kg/s)	13.007	13.007
Air (kg/s)	14.869	14.711
Excess air coefficient	0.955	0.945
Temperature in TR (K)	1270	1280
Temperature of cooling water (K)	500	500
Sulfur production (kg/s)	6.698	6.801
Sulfur recovery efficiency (%)	96.07%	97.54%

The sulfur recovery process is a complex industrial process, and it involves so many devices and operations in a real factory that we cannot just simply change the operating parameters as we want. So, after the discussion with the engineers in the factory and considering the optimum operating condition above, the test parameters were as follows:

$$Q_{\text{acid gas},2} = 46827 \text{ kg/h}, Q_{\text{air},2} = 52961 \text{ kg/h},$$

$$T_{\text{TR},2} = 1280 \text{ K}, \text{ and } T_{\text{CW},2} = 500 \text{ K}. \quad (17)$$

The flow rate acid gas and the temperature of cooling water in these two situations stayed the same. Figure 13 shows the display screen of the central controller in the Puguang gas field when we tested the optimization parameters. We can see the flow rate of acid gas and air in Figure 13: $Q_{\text{acid gas},1} = Q_{\text{acid gas},2} = 46827 \text{ kg/h} = (46827/36.13) \times 22.4 \text{ Nm}^3/\text{h} = 29032 \text{ Nm}^3/\text{h}$ and $Q_{\text{acid gas},2} = 52961 \text{ kg/h} = (52961/28.14) \times 22.4 \text{ Nm}^3/\text{h} = 42158 \text{ Nm}^3/\text{h}$. And, after calculation, the corresponding excess air coefficient was 0.945.

The comparison of the original situation and test situation is shown in Table 5. The main difference between these two situations was the flow rate of air, which decided the excess air coefficient. The sulfur recovery efficiency in the test situation was higher than that in the original situation, which was consistent with the rules of the effect of the excess air coefficient. In the optimization research, the sulfur recovery efficiency decreased with the excess air coefficient changing from 0.93 to 1.

The test result proved our RNA model was reliable, and it can be a useful tool in the industry. But due to the complexity of the SRUs, we cannot test every possible situation. In our following work, we will improve our RNA model and try to

make it capable of investigating the effect of all other parameters. Then, a detailed optimization result will be obtained and tested in the factory.

5. Conclusions

This paper has focused on the optimization of the operating parameters that affect the sulfur recovery efficiency of the SRUs. To get the optimum operating condition, we built a combustion mechanism and a reactor network analysis model to predict the concentration in the Claus process. The calculation results were verified with the industrial data and compared with the work of other researchers. After the verification, the optimization research of real SRUs located in the Puguang gas field was done. Then, the optimum excess air coefficient, temperature in TR, and temperature of the cooling water were obtained. At last, the obtained parameters were tested in the Puguang gas field. Based on the results mentioned above, the following conclusions may be drawn:

- (1) The RNA model with the revised mechanism which includes 94 species and 615 elementary reactions had a good prediction of the TR and WHB. Because of the more accurate residence time in our model, the calculation results were highly consistent with the industrial data and even more accurate than other researcher's results.
- (2) Through the optimization research, we find that the excess air coefficient and the temperature in TR had a clear influence on the sulfur recovery efficiency, while different temperatures of the cooling water

made little difference to the results. After the analysis, the optimum condition parameters were set as follows: excess air coefficient = 0.93, $T_{TR} = 1273^{\circ}\text{K}$, and $T_{CW} = 500^{\circ}\text{K}$. The corresponding sulfur recovery efficiency was about 98.3%.

- (3) The above parameters were tested in real SRUs, and the sulfur recovery efficiency had a clear increase after our optimization research. The whole result had a positive attitude towards the RNA model with the revised mechanism, and it proved that our new approach was a useful tool in the industry.

Data Availability

All data, models, and code generated or used during the study are included within the article.

Conflicts of Interest

The authors declare that they have no conflicts of interest.

Acknowledgments

This study was funded by the National Major Science and Technology Projects of China (2016ZX05017-006), Program for New Century Excellent Talents in University (NCET-13-0468), and Fundamental Research Funds for the Central Universities.

References

- [1] R. N. Maddox, *Gas Conditioning and Processing: Gas and Liquid Sweetening*, Campbell Petroleum Series, Oklahoma, OK, USA, 1982.
- [2] F. Manenti, D. Papasidero, and E. Ranzi, "Revised kinetic scheme for thermal furnace of sulfur recovery units," *AIDIC Conference Series*, vol. 32, pp. 1185–1290, 2013.
- [3] S. Ibrahim and A. Raj, "Kinetic simulation of acid gas (H_2S and CO_2) destruction for simultaneous syngas and sulfur recovery," *Industrial & Engineering Chemistry Research*, vol. 55, no. 24, pp. 132–145, 2016.
- [4] N. J. Nabikandi and S. Fatemi, "Kinetic modelling of a commercial sulfur recovery unit based on Claus straight through process: comparison with equilibrium model," *Journal of Industrial & Engineering Chemistry*, vol. 30, pp. 1570–1586, 2015.
- [5] A. K. Gupta, S. Ibrahim, and A. Al Shoaibi, "Advances in sulfur chemistry for treatment of acid gases," *Progress in Energy and Combustion Science*, vol. 54, pp. 65–92, 2016.
- [6] S. Ibrahim, R. K. Rahman, and A. Raj, "Roles of hydrogen sulfide concentration and fuel gas injection on aromatics emission from claus furnace," *Chemical Engineering Science*, vol. 172, pp. 513–527, 2017.
- [7] H. R. Mahdipoor and A. Dehghani Ashkezari, "Feasibility study of a sulfur recovery unit containing mercaptans in lean acid gas feed," *Journal of Natural Gas Science and Engineering*, vol. 31, pp. 585–588, 2016.
- [8] T. Y. Cong, A. Raj, J. Chanaphet, S. Mohammed, S. Ibrahim, and A. Al Shoaibi, "A detailed reaction mechanism for hydrogen production via hydrogen sulphide (H_2S) thermolysis and oxidation," *International Journal of Hydrogen Energy*, vol. 41, no. 16, pp. 6662–6675, 2016.
- [9] B. Mahmoodi, S. H. Hosseini, G. Ahmadi, and A. Raj, "CFD simulation of reactor furnace of sulfur recovery units by considering kinetics of acid gas (H_2S and CO_2) destruction," *Applied Thermal Engineering*, vol. 123, pp. 699–710, 2017.
- [10] A. Ravikumar, A. Raj, S. Ibrahim et al., "Kinetic simulations of H_2 production from H_2S pyrolysis in sulfur recovery units using a detailed reaction mechanism," *Energy & Fuels*, vol. 30, no. 12, 2016.
- [11] F. Manenti, D. Papasidero, G. Bozzano, and E. Ranzi, "Model-based optimization of sulfur recovery units," *Computers & Chemical Engineering*, vol. 66, pp. 244–251, 2014.
- [12] F. Manenti, D. Papasidero, A. Cuoci et al., "Reactor network analysis of Claus furnace with detailed kinetics," *Computer Aided Chemical Engineering*, vol. 30, pp. 1007–1012, 2012.
- [13] F. Manenti, D. Papasidero, A. Frassoldati, G. Bozzano, S. Pierucci, and E. Ranzi, "Multi-scale modeling of Claus thermal furnace and waste heat boiler using detailed kinetics," *Computers & Chemical Engineering*, vol. 59, pp. 219–225, 2013.
- [14] F. Manenti, D. Papasidero, and E. Ranzi, "Revised kinetic scheme for thermal furnace of sulfur recovery units," *Chemical Engineering Transactions*, vol. 32, pp. 1285–1290, 2013.
- [15] G. Manenti, D. Papasidero, F. Manenti, G. Bozzano, and S. Pierucci, "Design of SRU thermal reactor and waste heat boiler considering recombination reactions," *Procedia Engineering*, vol. 42, pp. 376–383, 2012.
- [16] M. Binoist, B. Labégorre, F. Monnet et al., "Kinetic study of the pyrolysis of H_2S ," *Industrial & Engineering Chemistry Research*, vol. 42, no. 17, pp. 3943–3951, 2003.
- [17] Y. Li, X. Yu, Q. Guo, Z. Dai, G. Yu, and F. Wang, "Kinetic study of decomposition of H_2S and CH_4 for H_2 production using detailed mechanism," *Energy Procedia*, vol. 142, pp. 1065–1070, 2017.
- [18] C. Zhou, K. Sendt, and B. S. Haynes, "Experimental and kinetic modelling study of H_2S oxidation," *Proceedings of the Combustion Institute*, vol. 34, no. 1, pp. 625–632, 2013.
- [19] Y. Li, Y. Lin, Z. Xu, B. Wang, and T. Zhu, "Oxidation mechanisms of H_2S by oxygen and oxygen-containing functional groups on activated carbon," *Fuel Processing Technology*, vol. 189, pp. 110–119, 2019.
- [20] D. Barba, F. Cammarota, V. Vaiano et al., "Experimental and numerical analysis of the oxidative decomposition of H_2S ," *Fuel*, vol. 198, pp. 68–75, 2016.
- [21] I. A. Gargurevich, "Hydrogen sulfide combustion: relevant issues under claus furnace conditions," *Industrial & Engineering Chemistry Research*, vol. 44, no. 20, pp. 7706–7729, 2005.
- [22] V. A. Savelieva, N. S. Titova, and A. M. Starik, "Modeling study of hydrogen production via partial oxidation of H_2S - H_2O blend," *International Journal of Hydrogen Energy*, vol. 42, no. 16, pp. 10854–10866, 2017.
- [23] Y. Li, X. Yu, H. Li et al., "Detailed kinetic modeling of homogeneous H_2S - CH_4 oxidation under ultra-rich condition for H_2 production," *Applied Energy*, vol. 208, pp. 905–919, 2017.
- [24] A. J. Hynes and P. H. Wine, *Gas-phase Combustion Chemistry: Kinetics and Mechanisms of the Oxidation of Gaseous Sulfur Compounds*, Springer-Verlag, New York, NY, USA, 2000.
- [25] M. Abián, M. Cebrián, Á. Millera, R. Bilbao, and M. U. Alzueta, " CS_2 and COS conversion under different combustion conditions," *Combustion and Flame*, vol. 162, no. 5, pp. 2119–2127, 2015.
- [26] K. Karan, A. K. Mehrotra, and L. A. Behie, "A high-temperature experimental and modeling study of homogeneous

- gas-phase COS reactions applied to claus plants,” *Chemical Engineering Science*, vol. 54, no. 15-16, pp. 2999–3006, 1999.
- [27] W. D. Monnery, W. Y. Svrcek, and L. A. Behie, “Modelling the modified claus process reaction furnace and the implications on plant design and recovery,” *The Canadian Journal of Chemical Engineering*, vol. 71, no. 5, pp. 711–724, 1993.
- [28] J. R. Petherbridge, P. W. May, D. E. Shallcross et al., “Simulation of HCS containing gas mixtures relevant to diamond chemical vapour deposition,” *Diamond and Related Materials*, vol. 12, no. 12, pp. 2178–2185, 2003.
- [29] M. A. Mueller, R. A. Yetter, and F. L. Dryer, “Kinetic modeling of the CO/H₂O/O₂/NO/SO₂ system: implications for high-pressure fall-off in the SO₂ + O (+M) = SO₃ (+M) reaction,” *International Journal of Chemical Kinetics*, vol. 32, no. 6, pp. 317–339, 2000.
- [30] P. Dagaut, F. Lecomte, J. Mieritz, and P. Glarborg, “Experimental and kinetic modeling study of the effect of NO and SO₂ on the oxidation of CO H₂ mixtures,” *International Journal of Chemical Kinetics*, vol. 35, no. 11, pp. 564–575, 2003.
- [31] J. Warnatz, “Hydrocarbon oxidation high-temperature chemistry,” *Pure and Applied Chemistry*, vol. 72, no. 11, pp. 2101–2110, 2000.
- [32] C. K. Westbrook and F. L. Dryer, “Chemical kinetic modeling of hydrocarbon combustion,” *Progress in Energy and Combustion Science*, vol. 10, no. 1, pp. 1–57, 1984.
- [33] S. Pierucci, E. Ranzi, and L. Molinari, “Modeling a claus process reaction furnace via a radical kinetic scheme,” *Computer Aided Chemical Engineering*, vol. 18, no. 04, pp. 463–468, 2004.

Research Article

Research on the Impact of Carbon Tax on CO₂ Emissions of China's Power Industry

Yue Yu ¹, Zhi-xin Jin,² Ji-zu Li ¹ and Li Jia³

¹College of Economics and Management, Taiyuan University of Technology, Taiyuan 030024, China

²College of Safety and Emergency Management Engineering, Taiyuan University of Technology, Taiyuan 030024, China

³College of Electrical and Power Engineering, Taiyuan University of Technology, Taiyuan 030024, China

Correspondence should be addressed to Ji-zu Li; lijizu@tyut.edu.cn

Received 25 February 2020; Revised 17 April 2020; Accepted 22 April 2020; Published 7 May 2020

Guest Editor: Yanqing Niu

Copyright © 2020 Yue Yu et al. This is an open access article distributed under the Creative Commons Attribution License, which permits unrestricted use, distribution, and reproduction in any medium, provided the original work is properly cited.

Based on the TIMES model, a system for CO₂ emission reduction in China's power industry is built in this paper. Four scenarios including different carbon tax levels are set up, simulating the CO₂ emissions of China's power industry in 2020–2050 by using scenario analysis method. The power consumption demand, primary energy consumption structure, CO₂ emission characteristics, emission reduction potential, and cost of different carbon tax levels are quantitatively studied. In combination with the impact on China's macroeconomy, the carbon tax level corresponding to the best CO₂ emission reduction effect of China's power industry is obtained, aiming to provide key data and a theoretical basis for China's low-carbon development as well as the optimization and adjustment of global power production system. The results show that with the development of economy and society in the future, China's power consumption demand will increase year by year, while the primary energy consumption of the power industry will maintain a rapid growth. The power industry still relies heavily on fossil energy, which will cause great pressure on China's economic development and ecological environment. Carbon tax will have an important impact on the primary energy supply structure of China's power industry, and renewable energy can be developed in different degrees. CO₂ emissions will be significantly reduced, reaching the peak value during 2030–2040 in China's power industry. The medium carbon tax level (TAX-2) set in this paper can meet the requirements of both CO₂ emission reduction effect and cost in the power industry, with the most elastic impact on the national economy and the smallest GDP loss, which can be used as an effective environmental economic policy tool.

1. Introduction

The issue of climate change is receiving widespread attention worldwide, making all sectors of society realize the importance of developing low-carbon economy and achieving sustainable development of society. The peak of greenhouse gas emissions is not only the critical point in the Fifth Assessment Report (AR5) of the Intergovernmental Panel on Climate Change (IPCC) but also the focus of international climate negotiations in recent years. According to statistics, 40% of global CO₂ emissions come from power industry, 23% from transportation department, and 22% from cement plants, oil refineries, steel mills, etc. [1]. As a secondary energy, electric power plays an important role in economic development and industrial production, with a huge demand. With the development of economy, in order to

ensure sufficient power supply, a large amount of primary energy needs to be consumed [2]. In China, fossil energy accounts for 89% of the total primary energy demand in 2015 [3]. The relationship between resource reserve and consumption in China is seriously imbalanced, and how to realize the coordinated development of environment and economy has become an urgent issue to be solved for the country. According to statistics from China's National Development and Reform Commission, in July 2017, 79.8% of China's total power generation came from coal-fired power plants [4]. This coal-based energy consumption and production structure lead to excessive dependence on coal in China's power production process and has a huge impact on the ecological environment. Therefore, it is very important to adjust the energy structure of China's power industry, whether from the perspective of solving the

problem of increasing energy shortages or controlling CO₂ emissions. Reducing greenhouse gas emissions will become an urgent task for China's power industry and an inevitable direction for the energy structure adjustment of the global power production system [5].

Carbon tax is a kind of tax levied on fossil energy based on its carbon content or CO₂ emissions, so as to reduce CO₂ emissions and control the excessive use of fossil fuels [6]. In recent years, carbon tax has become an important mean of CO₂ prevention and control. Through the government's "invisible hand" to correct the externality of market economy, CO₂ emissions can be effectively reduced. In the process of levying carbon tax, on the one hand, the increase of cost will urge enterprises to actively eliminate backward production capacity and use renewable clean energy; on the other hand, the carbon tax will stimulate enterprises to invest a large amount of capital in research and development of emission reduction technologies. Under the mixed effect of multiple factors, the industrial structure will be adjusted and upgraded, with the domestic economic development mode changed from a traditional extensive model to a low-carbon economy [7]. This kind of "inverse effect" on microeconomic individuals can promote the transformation of the resource consumption structure while pushing the macroeconomy to a path of sustainable development, which ultimately leads to a "win-win" situation of economic development and environmental protection. As the second largest economic body in the world, China is not only the largest developing country, but also one of the countries with the largest CO₂ emissions. In order to alleviate the issue of greenhouse gas emissions, the Chinese government has put forward the 2030 CO₂ emission reduction independent action goal. For this task of energy conservation and emission reduction that China is going to accomplish, the power industry will be an important breakthrough point [8]. Therefore, it is urgent to study the low-carbon green development path of China's power industry in the future under the existing CO₂ emission constraints.

At present, the relevant research focuses on three aspects: CO₂ emission influencing factors, carbon tax impact, and analysis models.

Some scholars pay attention to the influencing factors of CO₂ emissions. Shipkovs et al. found that adjusting the energy consumption structure can effectively reduce greenhouse gas emissions [9]. Chen et al. found that the large-scale use of renewable energy can guarantee effective greenhouse gas control by studying China's future control strategies for major greenhouse gas emissions [10]. Using the ARDL model, Zhao et al. studied the effects of three factors, namely, industrial added value, average utilization hours of thermal power equipment, and standard coal consumption rate, on CO₂ emissions of power industry [11]. Zhang et al. found that the economic activity effect is the main reason for the increase of CO₂ emissions, while the production efficiency of electric power plays a key role in controlling CO₂ emissions [12]. However, these studies are mainly from the macrolevel, and there are obvious deficiencies in the energy system, especially in the power system.

Carbon tax policy is widely advocated and adopted as the most effective mean of emission reduction among the climate protection policies, which has been applied in different forms in many countries. Scholars have conducted a lot of research on carbon tax and its impact. Nordhaus used the DICE (Dynamic Integrated Climate-Economy) model to study the impact of different carbon tax levels on the ecological environment [13]. Peace studied that a reasonable carbon tax level can partially eliminate the negative impact on the economy. It can not only promote enterprises to adjust their production and operation activities to reduce emissions, but also use the revenue for other ecological construction [14]. Floros studied the impact of carbon tax on the CO₂ emissions of energy manufacturing industry in Greece and found that reasonable carbon tax policies can further reduce the accumulated CO₂ stock in the atmosphere and then mitigate the phenomenon of climate degradation [15]. Although carbon tax has not been included in the environmental tax currently levied in China, in view of its positive and systematic effect on the ecological environment, the research on carbon tax has attracted widespread attention from Chinese scholars. He et al. studied the data of 55 countries in the past 20 years and found that the implementation of carbon tax can help reduce CO₂ emissions and significantly improve the local environmental quality [16]. Zhu et al. analyzed the necessity and feasibility of carbon tax in China, put forward the basic objectives and principles of carbon tax, preliminarily designed the basic content, and specifically proposed the implementation framework of carbon tax system [17]. However, there are few reports on the carbon tax research of China's power industry; the low-carbon path for China's power industry to promote emission reduction through carbon tax has not been clear.

In the current research based on 3E (energy-economy-environment) systems, the widely used models mainly include the MARKAL (Market Allocation of Technologies Model) [18], the LEAP (Long-Range Energy Alternatives Planning) model [19], the CGE (Computable General Equilibrium) model [20], the Input-Output model [21], the System Dynamics model [22], and the Logistic Regression model [23]. These analytical models used in low-carbon research can be divided into "top-down" energy economic models and "bottom-up" energy technology models according to the research methods and model frameworks [24]. Of these, the energy economic model mainly simulates the real economic system, and the model subject is the various factor providers and consumers who seek to maximize utility. It is widely used in the study of energy environmental economic policies. The energy technology model is a large dynamic energy optimization model developed by international research institutions that is widely used in research on energy system optimization and emission reduction at the national, regional, and industry levels [25]. Compared with the energy technology model, the energy economy model focuses on the connection between the energy sector and other sectors but does not analyze the technical factors of the internal energy system. The energy technology model is more suitable for low-carbon research

in the power industry because it offers comprehensive analysis, calculation, and optimization from the perspective of energy supply, conversion, and demand. Researchers mainly use MARKAL and TIMES (The Integrated MARKAL-EFOM System) for modeling research. Van et al. established a MARKAL model for the Dutch power system and set up a large number of scenarios, repeatedly verifying to obtain the optimal power planning, including the selection of environmental policies, the establishment plan of power plants, and the amount of capital invested in carbon capture technology [26]. Jegarl et al. established a MARKAL model for the Korean power system, simulated different policy options and technology combinations, and evaluated these policies based on the obtained results [27]. Jia and Liu used the TIMES model to analyze the impact of energy conservation and emission reduction policies and measures on energy supply and demand as well as air pollutant emissions in Beijing for 2010–2020 [28]. Daly et al. used the TIMES model to study the impact of Iranian residents' travel cost on the CO₂ emissions of the transport department [29]. The above studies have shown that the energy technology model has better applicability in the energy-environment field, and it is more suitable for low-carbon research in the power industry.

In summary, this paper constructs a theoretical analysis model of CO₂ emission characteristics of China's power industry and studies the corresponding temporal evolution characteristics by integrating technology optimization, energy structure adjustment, CO₂ emissions, and carbon tax impact into the traditional economic growth analysis framework.

2. Materials and Methods

2.1. TIMES Model. As a "bottom-up" energy technology model, the TIMES model is a new generation of a comprehensive climate change evaluation model developed by the ETSAP (Energy Technology Systems Analysis Program) model based on the MARKAL model, and it integrates the advantages of EFOM (Energy Flow Optimization Model). The TIMES model is generally used to simulate the entire energy system, and it is also used to study individual specific industries, such as transportation industry or steel industry. It has a wide research scope, such as the impact of technological progress on energy demand, production and conversion, the mutual substitution of various energy sources, energy investment and system cost, and the impact of reducing greenhouse gas emissions on energy system and economy. The model can describe the various links of exploitation, processing, conversion, distribution, and terminal energy consumption in the energy system in detail. For each link, existing technologies and various advanced technologies and related alternatives that may appear in the future can be considered. It is a dynamic linear programming model which assumes that the energy system is in a state of complete competition; it seeks to maximize the total net surplus and simulates the market equilibrium. In the model, the maximum total net surplus of the energy system is converted into the minimum total net cost of the energy system. On this basis, the model not only meets the demand

of terminal energy services but also selects the technology combination with the lowest cost. In recent years, the model has been used in the economic analysis of climate and energy policies in approximately 70 countries. Numerous studies have shown that the TIMES model has good applicability in the energy-environment field [30, 31].

Based on the powerful technical features and the characteristics that can be used to study a single sector of the TIMES model, this paper constructs an energy technology model for CO₂ emission reduction in the power industry based on predictions of future economic and social development in China, coupled with modules of demand forecasting and emission analysis. Combined with the power industry's development attributes and characteristics of CO₂ emission control technologies, various simulation prediction and scenario analysis methods are integrated to systematically study the path of China's power industry to achieve CO₂ emission reduction through carbon tax policy.

2.2. Model Structure. The TIMES model of CO₂ emission reduction in the power industry constructed in this paper is shown in Figure 1, and the flowchart of this model is shown in Figure 2. The model mainly includes four parts: energy supply module, energy system module, energy demand module, and CO₂ emission module. The energy supply module mainly includes the supply of fossil energy (such as coal, oil, and natural gas) and nonfossil energy (such as biomass, nuclear energy, water, wind, and solar energy). The energy system module mainly includes traditional power generation technologies such as supercritical, ultrasupercritical, and IGCC (Integrated Gasification Combined Cycle), as well as new energy power generation technologies such as nuclear power, hydropower, wind power, and solar power. The energy demand module divides the terminal department into four parts: agriculture, industry, construction, and transportation. The CO₂ emission module includes two parts: CO₂ emission characteristics and potential analysis, as well as CO₂ emission reduction cost analysis.

The optimization goal of the model is to minimize the total cost of energy system in the planning period (2020–2050) under the given requirements and constraints. The objective function is shown in

$$\text{OBJ}(z) = \sum_{t \in \text{Years}} (1 + \alpha)^{R-t} \times \text{ANNC}(t) - \text{SALV}(z), \quad (1)$$

where OBJ(z) is the total system cost (yuan); α is the discount rate (%), which is 5% in this model; Years is the time period; R is the target year of discount; ANNC(t) is the technical cost of year t (yuan); and SALV is the salvage value of the assets (yuan).

The calculation of technical cost ANNC(t) is shown in formula (2).

$$\begin{aligned} \text{ANNCY}(t) = & \text{INVC}(t) + \text{INVT}(t) + \text{INVD}(t) + \text{FIXC}(t) + \text{FIXT}(t) \\ & + \text{VARC}(t) + \text{ELASTC}(t) - \text{LATER}(t), \end{aligned} \quad (2)$$

where INVC is the investment cost (yuan); INVT is the tax and subsidy (yuan); INRD is the demolition cost (yuan); FIXC is the fixed operation and maintenance (O&M) cost

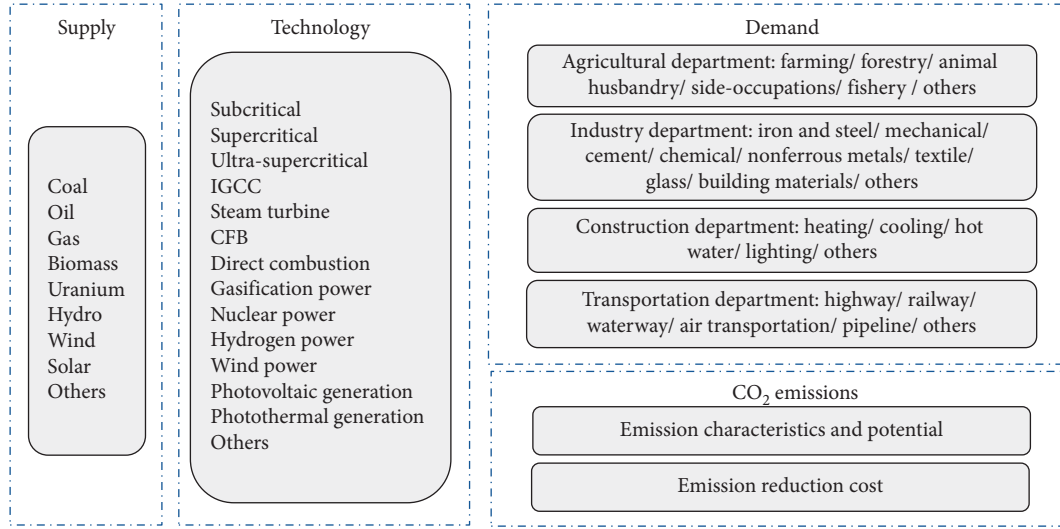


FIGURE 1: TIMES model of CO₂ emission reduction in China's power industry.

(yuan); FIXT is the tax and subsidy related to the fixed O&M (yuan); VARC is the variable annual O&M cost (yuan); ELASTC is the cost of demand change caused by price elasticity (yuan); and LATER is the cost of recycling (yuan).

According to the IPCC report, the CO₂ emissions of the power industry are the sum of the CO₂ emissions generated by the consumption of various fossil energy sources, as shown in formula (3) [32].

$$O_t = \sum_{m=1}^3 O_{mt} = \sum_{m=1}^3 E_{mt} \cdot \text{NCV}_m \cdot \text{CEF}_m \cdot \text{COF}_m \cdot \frac{44}{12}, \quad (3)$$

where O_{mt} is the total CO₂ emissions of China's power system (10^4 t); m is the different types of primary energy (including coal, oil, natural gas, biomass, hydro, nuclear, wind, and solar); E_{mt} is the energy consumption volume (10^4 t or 10^8 m³); NCV_m is the net calorific value of the corresponding energy type—this article uses the average low calorific value of each energy type provided in the China Energy Statistical Yearbook (kJ/kg); CEF_m is the carbon emissions coefficient of different kinds of energy provided by IPCC; and COF_m is the carbon oxidation factor, of which coal is 0.99 and the remaining energy types are 1.

The emission reduction cost analysis process studies the corresponding unit emission reduction cost according to the obtained CO₂ emission reduction results in different scenarios, the corresponding energy consumption structure, and the advanced level of emission reduction technology. The total cost consists of three parts: average annual fixed investment cost, operating cost, and fuel cost, as shown in

$$\text{TC} = \sum_{(l,p)} \left[C_{l,p} \cdot r_{l,p} + g_{l,p}^0 \cdot X_{l,p} + \sum_k (g_k E_{k,l,p}') \cdot X_{l,p} \right],$$

$$C_{l,p} = B_{l,p} \frac{\alpha(1+\alpha)^{T_{l,p}}}{(1+\alpha)^{T_{l,p}}}, \quad (4)$$

where TC is the total cost (10^8 yuan); $C_{l,p}$, $r_{l,p}$, $g_{l,p}^0$, $X_{l,p}$, $B_{l,p}$, $T_{l,p}$ are the average annual fixed investment cost (yuan/kW), installed capacity (10^8 kW), operating cost [yuan/(kW·a)], operating capacity (10^8 kW), initial investment cost (yuan/kW), and life (years) of facilities using l -type power generation technology and equipped with p -type control technology, respectively; α is the discount rate (%); g_k is the price of k fuel (calculated by standard coal) (yuan/t); $E_{k,l,p}'$ is the amount of fuel k consumed by facilities using l -type power generation technology and equipped with p -type control technology (calculated by standard coal) (10^8 t).

2.3. Assumptions. The model constructed in this paper takes 2015 as the research base year, and the planning period is 2020–2050. Since 2020, every 5 years is a period, that is, 2020, 2025, 2030, . . . , 2050 are the milestone years. Combined with the existing planning and future prediction [33, 34], scenario simulation is made for the development of power industry in the future. The driving factors of economic development mainly include population, urbanization rate, GDP growth rate, and industrial structure (the ratio of the primary, secondary, and tertiary industries). Therefore, the basic assumption results of the model are shown in Table 1.

It is found that during the period of 2015–2050, the total population shows a trend of increasing firstly, reaching a peak value in 2035 (1459 million), and then slowly decreasing to 1415 million in 2050. The urbanization rate continues to increase, reaching 75.9% by 2050, and the corresponding urban population will be 1074 million. While the GDP growth rate is slowly decreasing, the industrial structure has changed significantly. Compared with the base year, in 2050, the ratio of the secondary industry will decrease by 12.1%, and the ratio of the tertiary industry will increase by 17.6%. This change shows that as China's industrialization process gradually enters a stable period, the focus of energy consumption will gradually shift from industry to service industries including construction and

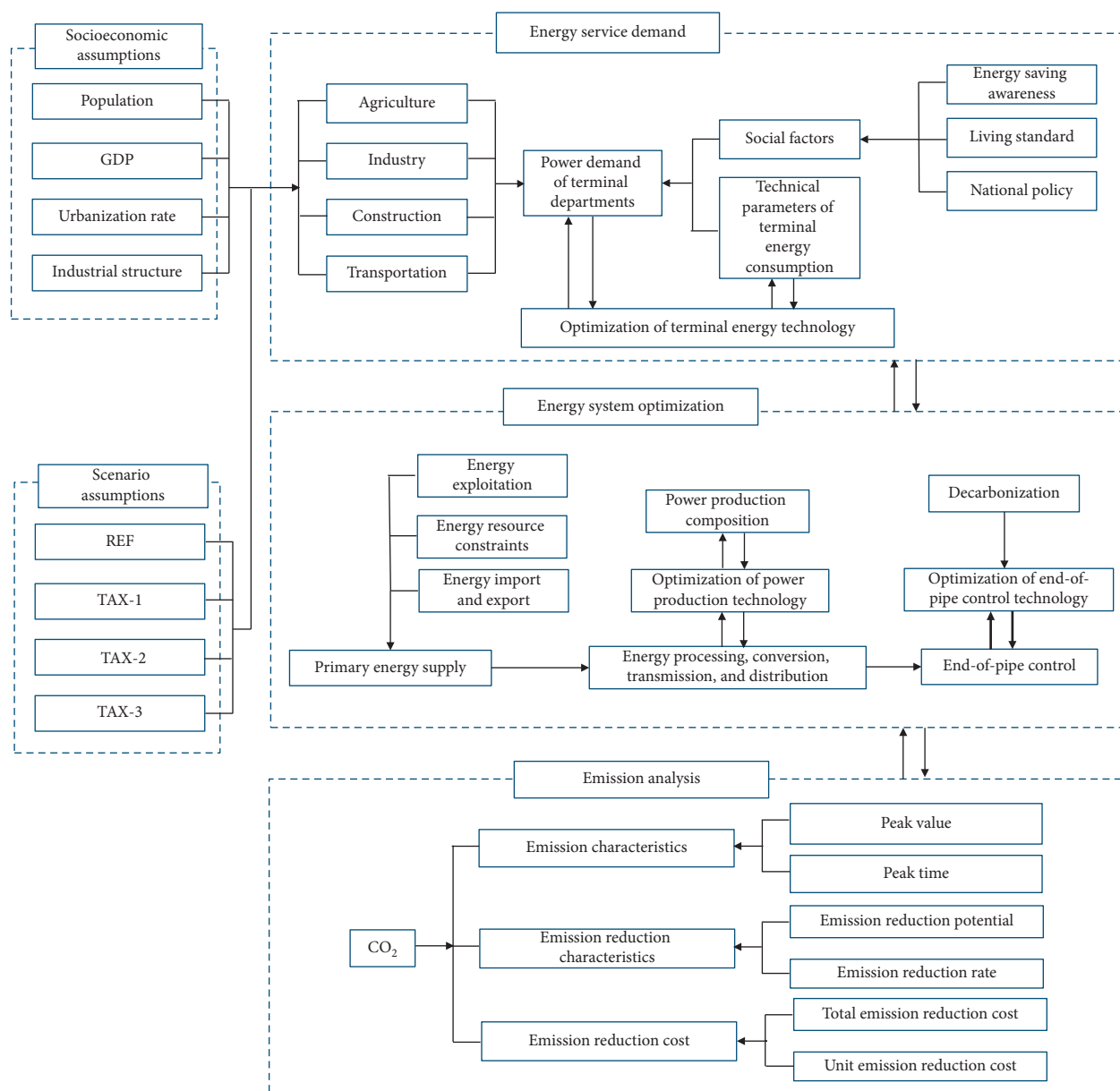


FIGURE 2: Flowchart of the proposed method.

TABLE 1: Basic assumptions of the model.

Year	Total population (million)	Urban population (million)	Rural population (million)	Urbanization rate (%)	GDP growth rate (%)	Ratio of primary industry (%)	Ratio of secondary industry (%)	Ratio of tertiary industry (%)
2015	1400	774	626	55.3	7.0	9.8	42.3	47.9
2020	1421	838	583	59.0	6.2	6.9	40.7	47.9
2025	1442	898	544	62.3	5.6	6.3	38.1	55.6
2030	1455	963	492	66.2	4.5	5.9	36.7	57.4
2035	1459	1014	445	69.5	4.5	5.6	35.0	59.4
2040	1452	1037	415	71.4	4.5	5.2	33.4	61.4
2045	1432	1048	384	73.2	4.0	4.9	31.9	63.2
2050	1415	1074	341	75.9	3.5	4.3	30.2	65.5

transportation. This adjustment of industrial structure can not only reduce the energy consumption per unit of GDP, but also lead to the improvement of technological energy-saving level,

further illustrating that the adjustment of the energy structure and technological upgrading can play important roles in the process of CO₂ emission reduction.

2.4. Scenarios. In order to obtain the optimal carbon tax level, as well as the corresponding optimal policy measures and technology combinations, four scenarios are set up in this paper, including the reference scenario and three carbon tax scenarios with different carbon tax levels.

2.4.1. Reference (REF) Scenario. The impact of CO₂ on the development of power industry is not considered. No new technology is introduced and improved. The power system develops at the original level without any change in the energy structure and emission reduction technology, which still relies on traditional coal power generation.

2.4.2. Carbon Tax Scenarios. It is divided into three scenarios, the low-carbon tax scenario (TAX-1 scenario), the medium carbon tax scenario (TAX-2 scenario), and the high-carbon tax scenario (TAX-3 scenario). As can be seen from the foregoing, the CO₂ emissions from fossil fuel combustion account for the majority of China's total greenhouse gas emissions, and the emissions are relatively centralized and easy to calculate, so it is more in line with China's current national conditions to adopt the estimated CO₂ emissions as the basis of tax calculation and levy in the way of quantity-based collection [35]. Therefore, this paper assumes the carbon tax collecting on CO₂ emissions from fossil fuel combustion. Based on the REF scenario, it is assumed that carbon tax will be levied on the power industry from 2020. The carbon tax rates set in this paper refer to the Asian Energy Model Forum and related literature [36–38], as shown in Table 2. Among them, the carbon tax set in TAX-1, TAX-2, and TAX-3 scenarios has different change rules. The unit of carbon tax rate infer to CNY per tons of CO₂. In 2020, the carbon tax is set at 70 yuan/t, 210 yuan/t, and 350 yuan/t, respectively; then it will increase at different growth rates in different periods, finally reaching 301 yuan/t, 910 yuan/t, and 1512 yuan/t, respectively, in 2050.

3. Results and Discussion

3.1. Power Consumption Demand. Parameters such as population, GDP growth rate, urbanization rate, and industrial structure are important factors to determine the national power consumption demand. Therefore, according to the basic assumptions of China's future economic and social development obtained above, China's power demand during 2015–2050 can be obtained, as shown in Table 3.

It is found that during this period, China's national power demand shows an overall upward trend and develops at a high level. In 2050, the demand (17075 billion kW·h) is 2.81 times that in 2015 (6080 billion kW·h). The annual average growth rate is 16%, far higher than the GDP growth rate in the same period, but the growth rate is decreasing year by year. This is because there is a close correlation between the process of national economic development and the intensity of power demand. It can be seen from the above that with the continuous promotion of urbanization, obvious industrial structure and rigid energy demand are the most important development characteristics, thus

TABLE 2: Carbon tax rates set under different scenarios (yuan/t).

Carbon tax scenarios	Year						
	2020	2025	2030	2035	2040	2045	2050
TAX-1	70	91	112	151	189	245	301
TAX-2	210	277	343	452	560	735	910
TAX-3	350	459	567	749	931	1222	1512

maintaining a high demand for power consumption. As a result, the growth rate of national and per capita power demand will remain above 10% in 2020–2040. With the completion of China's industrialization, the economic structure has been transformed; the proportion of the tertiary industry has increased, and the heavy industry, especially the high-energy-consuming industry, has gradually withdrawn. The intensity of power consumption has also declined, leading to a slowdown in the growth of power demand. At the same time, with the development of productivity and the improvement of living standards, the overall demand for electricity is gradually increasing. However, the promotion of energy-saving technology and the popularization of energy-saving awareness lead to the gradual slowdown in the growth rate of per capita power demand. Therefore, in 2050, the corresponding growth rate of China's overall and per capita power demand will be significantly reduced to 6% and 7%, respectively.

The power demand of each terminal department is shown in Figure 3. With the development of economy, the overall power consumption of the terminal departments will be improved to some extent in the future. The focus of power demand will gradually shift from industry to transportation and construction. Among them, the proportion of power demand in the industrial department has declined significantly, from 71.90% in 2015 to 36.24% in 2050. The reason is that, on the one hand, the productivity and efficiency have been increased, and energy consumption has been greatly reduced; on the other hand, the industrial structure has changed significantly and the tertiary industry and capital-intensive and technology-intensive industries have developed rapidly. The proportion of transportation department will increase from 13.84% in 2015 to 31.81% in 2050, mainly due to the energy utilization and the extensive application of electric vehicle technology. The proportion of power demand in the construction department has increased significantly, reaching 30.58% in 2050. On the one hand, the rate of home appliance ownership and penetration has increased year by year; on the other hand, due to the increase of urbanization rate, urban population and urban scale have been increased, leading to the power demand of corresponding infrastructure greatly increased. At the same time, the growth rate of electricity demand in the construction department will reach the highest value of 50.33% from 2025 to 2030. It can be seen from the above that this is due to the largest growth rate of urbanization and the rigid demand for power during this period. In addition, the proportion and growth rate of power demand in the agricultural department have been declining. This is mainly because with the development of economy and society, the scale effect based on

TABLE 3: Characteristics of power demand in China.

Year	National power demand (billion kW·h)	Growth rate of national power demand (%)	Per capita power demand (kW·h)	Growth rate of per capita power demand (%)
2015	6080	—	4342	—
2020	7661	26	5391	24
2025	9576	25	6640	23
2030	11491	20	7897	19
2035	13560	18	9293	18
2040	14916	10	10272	11
2045	16109	8	11249	10
2050	17075	6	12067	7

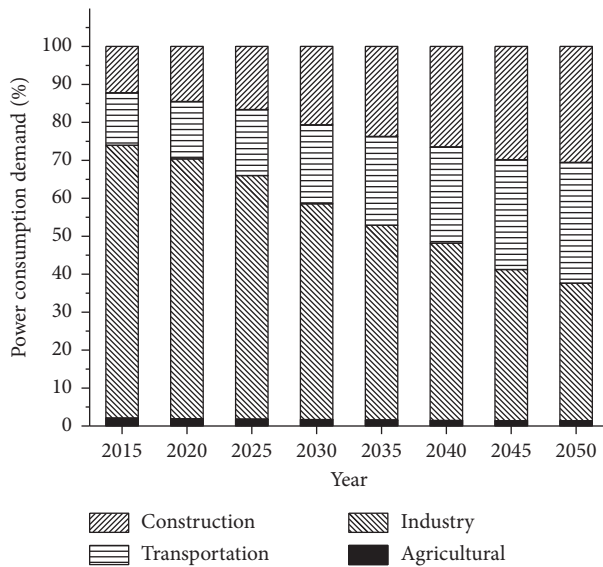


FIGURE 3: Power consumption demand of terminal departments.

the agricultural economy will show the trend of accelerating expansion. While the efficiency of electricity consumption is improving, the power demand for agricultural is greatly reduced.

3.2. Primary Energy Consumption and Composition. The simulation results of primary energy consumption and composition under the four scenarios are shown in Figure 4.

Under the REF scenario, the total primary energy consumption will increase from 53.13 EJ in the base year to 63.17 EJ, 76.61 EJ, and 87.07 EJ in 2020, 2030, and 2040, respectively. It will reach 93.24 EJ in 2050, which is a 75% increase compared with the base year, and the proportion of fossil energy will still be as high as 78.98%. This will put great pressure on the energy supply and CO₂ emission control of China's power industry, so it is necessary to reduce the total energy consumption and adjust the energy consumption structure.

Under the scenarios of TAX-1, TAX-2, and TAX-3, the primary energy consumption of China's power industry will be significantly decreased compared to the REF scenario. The total energy consumption in 2030 will reach 73.58 EJ, 71.86 EJ, and 66.34 EJ, respectively. In 2050 it will be further decreased to 88.48 EJ, 83.21 EJ, and 77.19 EJ, respectively,

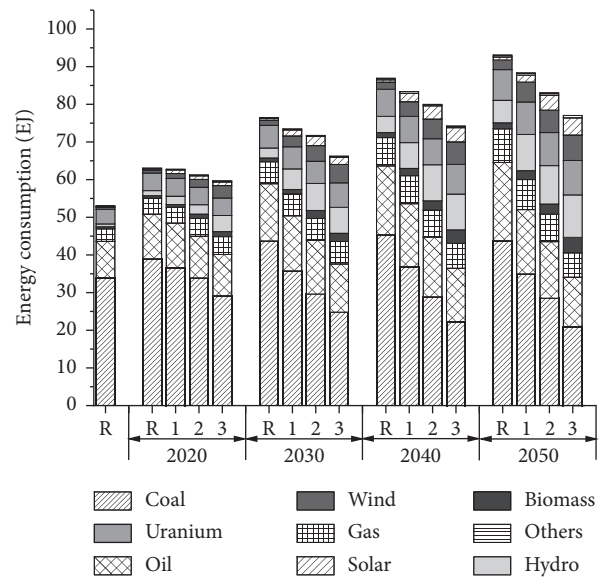


FIGURE 4: Primary energy consumption and composition.

compared with the REF scenario, the corresponding decrease is 5%, 11%, and 17%. This is mainly due to the adjustment of energy structure, as well as the use and upgrade of energy-saving technologies, such as energy-saving appliances and wall insulation technology. At the same time, the composition of primary energy consumption has a large degree of change. In 2050, under the three carbon tax scenarios, the proportion of fossil energy consumption to total consumption will be 67.97%, 61.20%, and 52.68%, respectively. Compared with the REF scenario (the corresponding proportion is 78.98%), the consumption of coal, oil, and natural gas will be greatly reduced, while the renewable energy is further developed. Among them, under the TAX-3 scenario in 2050, the proportion of hydropower, nuclear energy, wind energy, solar energy, and biomass energy will increase from 1.42% in base year to 14.66%, 7.27% to 11.87%, 1.03% to 8.71%, 0.47% to 5.97%, and 1.03% to 5.28%, respectively.

Through the price mechanism of the market, the collection of carbon tax makes power producers turn to clean energy and low-carbon products to achieve the purpose of emission reduction. It has a suppressive effect on high-energy consumption technologies and a promotion effect on

low-energy consumption technologies, resulting in a tumultuous change in the consumption of energy products. The emission reduction effect of carbon tax is positively related to the price elasticity of energy demand and the substitution of energy products. Related technologies will be promoted, with considerable benefits of the extension effect.

3.3. CO₂ Emissions and Emission Reduction Characteristics.

The CO₂ emissions, emission reduction potential, and emission reduction rate of the power industry in different scenarios are shown in Figure 5 and Table 4. The calculation of emission reduction potential and emission reduction rate is shown in formulas (5) and (6), respectively.

$$E_{qt} = E_{Rt} - E_{Tt}, \quad (5)$$

where E_{qt} is the emission reduction potential of year t under a carbon tax scenario (Gt); E_{Rt} is the CO₂ emissions of year t under the REF scenario (Gt); and E_{Tt} is the CO₂ emissions of the carbon tax scenario in the same period (Gt).

$$E_{\eta} = \frac{E_{qt}}{E_{Rt}}, \quad (6)$$

where E_{η} is the emission reduction rate (%).

Under the REF scenario, the CO₂ emissions of the power industry will be increasing year by year, reaching a peak value of 5.52 Gt in 2050, which is an increase of 44% over the base year. According to the obtained CO₂ emissions, it can be found that the power industry will not be able to achieve the CO₂ emission reduction targets in all stages if the existing structure and technology are still maintained without taking corresponding adjustment measures.

Compared with the REF scenario, under the TAX-1, TAX-2, and TAX-3 scenarios, the corresponding CO₂ emissions increase firstly and then decrease. With the increase of carbon tax level, the emissions will reach the peak values of 4.64 Gt, 4.39 Gt, and 4.12 Gt in 2040, 2035, and 2030, respectively and then decrease year by year, reaching 4.54 Gt, 4.02 Gt, and 3.79 Gt, respectively, in 2050. The corresponding emission reduction potential will be 0.98 Gt, 1.50 Gt, and 1.73 Gt, respectively. At the same time, combined with the CO₂ emission reduction rate in 2050, it will be close to 30% under the TAX-2 scenario, while under the TAX-3 scenario, although the carbon tax has increased significantly, it will only increase by 4%, which is 31.34%. The improvement degree of emission reduction effect is not obvious enough, which cannot show a high correlation with the corresponding growth degree of carbon tax.

In addition, the CO₂ emission reduction characteristics of the power industry in different scenarios are shown in Figure 6. The calculation of emission reduction is shown

$$E_{ri} = E_{oi} - E_{pi}, \quad (7)$$

where E_{ri} is the CO₂ emission reduction (Gt); E_{oi} is the CO₂ emissions under uncontrolled conditions (Gt); and E_{pi} is the actual CO₂ emissions during the same period (Mt).

Under different carbon tax scenarios, with the adjustment of energy consumption structure and level

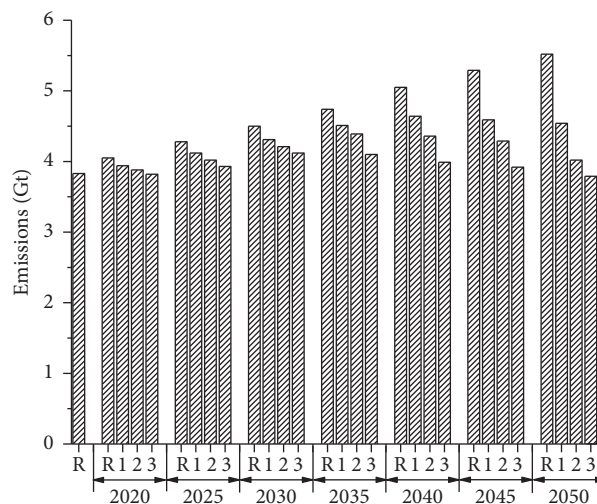


FIGURE 5: CO₂ emissions of power industry.

improvement of technology in the power industry, CO₂ emission reduction shows an increasing trend. When 2050, the emission reduction corresponding to the three scenarios will be 1.49 Gt, 2.01 Gt, and 2.24 Gt, respectively, which will increase by 0.87 Gt, 1.33 Gt, and 1.50 Gt compared to 2020. In the REF scenario, the emission reduction in 2050 will be only 0.51 Gt.

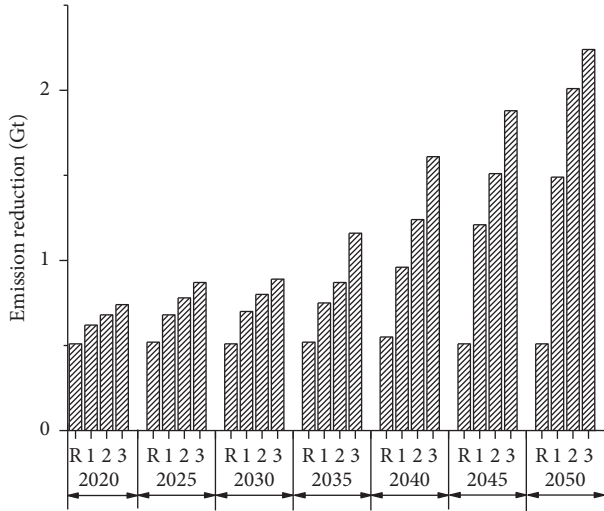
In summary, carbon tax in China's power industry can lead enterprises to actively reduce CO₂ emissions. In this process, the collection of carbon tax can increase the production cost of high-carbon emission enterprises. Therefore, it is necessary to develop the emission reduction technologies and adopt the low-carbon energy sources to achieve low-carbon production and energy structure adjustment.

3.4. CO₂ Emission Reduction Cost. In the power industry, the collection of carbon tax will have a great impact on the emission reduction cost. The transformation of production mode as well as the transformation and upgrading of power production can be guided and realized by the level of emission reduction cost [39]. Therefore, a reasonable level of carbon tax can significantly promote CO₂ emission reduction and structural optimization, while substantially reducing its impact on the economy. Combined with the above results, the cost of emission reduction under the four scenarios is further analyzed to obtain a more effective and conducive collection level for carbon tax promotion. The results are shown in Table 5, where ΔC is the cost of CO₂ emission reduction (billion yuan); ΔE is the CO₂ emission reduction (Gt); and $\Delta C/E$ is the unit emission reduction cost of CO₂ (billion yuan/Gt).

Under the REF scenario, from 2020 to 2050, as can be seen from the foregoing, the power industry's dependence on coal has not changed significantly, and the emission reduction technology has not been introduced and upgraded. Therefore, the unit emission reduction cost of CO₂ fluctuates slightly, maintaining between 6.04×10^3 and 6.63×10^3 billion yuan/Gt. Since the lifecycle of equipment

TABLE 4: Emission reduction potential and emission reduction rate of power industry.

Carbon tax scenarios	2020		2025		2030		2035		2040		2045		2050	
	E_q	E_η												
TAX-1	0.11	2.72	0.16	3.74	0.19	4.22	0.23	4.85	0.41	8.12	0.70	13.23	0.98	17.75
TAX-2	0.17	4.20	0.26	6.07	0.29	6.44	0.35	7.38	0.69	13.66	1.00	18.90	1.50	27.17
TAX-3	0.23	5.68	0.35	8.18	0.38	8.44	0.64	13.50	1.06	20.99	1.37	25.90	1.73	31.34

FIGURE 6: CO₂ emission reduction characteristics of power industry.TABLE 5: CO₂ emission reduction cost of power industry.

Year	Item	REF	TAX-1	TAX-2	TAX-3
2020	ΔC	3.28E+03	7.14E+03	1.11E+04	2.26E+04
	ΔE	0.51	0.62	0.68	0.74
	$\Delta C/E$	6.44E+03	1.15E+04	1.63E+04	3.06E+04
2025	ΔC	3.44E+03	9.13E+03	1.53E+04	3.37E+04
	ΔE	0.52	0.68	0.78	0.87
	$\Delta C/E$	6.61E+03	1.34E+04	1.96E+04	3.88E+04
2030	ΔC	3.33E+03	1.03E+04	1.94E+04	4.22E+04
	ΔE	5.10E-01	7.00E-01	8.00E-01	8.90E-01
	$\Delta C/E$	6.52E+03	1.48E+04	2.42E+04	4.74E+04
2035	ΔC	3.45E+03	1.29E+04	2.60E+04	4.17E+04
	ΔE	5.20E-01	7.50E-01	8.70E-01	1.16E+00
	$\Delta C/E$	6.63E+03	1.72E+04	2.99E+04	3.60E+04
2040	ΔC	3.49E+03	1.87E+04	2.61E+04	3.53E+04
	ΔE	5.50E-01	9.60E-01	1.24E+00	1.61E+00
	$\Delta C/E$	6.34E+03	1.95E+04	2.11E+04	2.19E+04
2045	ΔC	3.19E+03	2.64E+04	2.56E+04	2.84E+04
	ΔE	5.10E-01	1.21E+00	1.51E+00	1.88E+00
	$\Delta C/E$	6.26E+03	2.18E+04	1.70E+04	1.51E+04
2050	ΔC	3.08E+03	2.62E+04	2.02E+04	1.81E+04
	ΔE	5.10E-01	1.49E+00	2.01E+00	2.24E+00
	$\Delta C/E$	6.04E+03	1.76E+04	1.01E+04	8.10E+03

and process is basically around 20 years, the unit emission reduction cost will increase slightly during 2030 and 2035.

Under the TAX-1, TAX-2, and TAX-3 scenarios, the unit emission reduction cost of CO₂ increases firstly and then decreases. Due to different levels of carbon tax, in the short

term, in order to reduce carbon emissions and avoid the pressure of carbon tax, the emission reduction technology and production mode of power industry will be greatly changed, resulting in different degrees of increase in the cost of emission reduction. Therefore, in 2020, the unit emission reduction cost of the three scenarios will be 1.15×10^4 billion yuan/Gt, 1.63×10^4 billion yuan/Gt, and 3.06×10^4 billion yuan/Gt, respectively, among which the lower carbon tax scenarios (TAX-1, TAX-2) have lower initial unit emission reduction cost than the higher carbon tax collection scenario (TAX-3). The unit emission reduction cost corresponding to the three carbon tax scenarios will peak in 2045, 2035, and 2030, respectively, with the values of 2.18×10^4 billion yuan/Gt, 2.99×10^4 billion yuan/Gt, 4.74×10^4 billion yuan/Gt, respectively. After that, it will continue to decline, decreasing to 1.76×10^4 billion yuan/Gt, 1.01×10^4 billion yuan/Gt, and 8.10×10^3 billion yuan/Gt, respectively, in 2050. At this time, compared with the TAX-1 scenario, the unit emission reduction costs of the TAX-2 and TAX-3 scenarios are lower. From a long-term perspective (after 2050), a higher carbon tax level benefits the reduction of unit emission reduction cost. This is mainly because under the pressure of high-carbon tax level, enterprises passively accept the substantial increase of emission reduction cost in the initial period. The optimal solution with lower cost will be actively sought. The production mode gradually changes based on maintaining power production, such as using new energy power generation technology with lower CO₂ emissions and optimizing emission reduction technologies. CO₂ emissions can be reduced to offset the loss caused by carbon tax, with the energy consumption structure improved. In addition, the average unit emission reduction cost under the TAX-1, TAX-2, and TAX-3 scenarios during 2020–2050 will be 1.65×10^4 billion yuan/Gt, 1.97×10^4 billion yuan/Gt, and 2.83×10^4 billion yuan/Gt, respectively, which is 4 times, 5 times, and 9 times that of the REF scenario, respectively.

3.5. Impact of Carbon Tax on the Macroeconomy of the Power Industry. It can be seen from the above that carbon tax can force the green transformation of the power industry, but as a “double-edged sword,” it has a wide-ranging and far-reaching impact, involving many aspects of society, economy, and people’s life. Therefore, the carbon tax should consider not only the impact on the environment, but also its economic effect. Like other types of taxes, carbon tax will also change the price signal, making resources deviate from the optimal allocation under the reference scheme, resulting in the loss of GDP [40].

The impact of different carbon tax levels on the macroeconomy of the power industry is shown in Table 6. In

TABLE 6: Impact of different carbon tax levels on the macro-economy of the power industry.

Carbon tax scenarios	GDP _η				TAX _η			
	2020	2030	2040	2050	2020	2030	2040	2050
TAX-1	0.08	0.07	0.12	0.19	34.8	61.2	69.7	95.5
TAX-2	0.05	0.10	0.18	0.28	89.3	61.8	74.3	97.1
TAX-3	0.13	0.27	0.60	0.72	44.9	31.7	35.2	43.8

order to quantify the additional effect of carbon tax on GDP, based on the CO₂ emission reduction characteristics obtained previously, this paper proposes the “carbon tax elasticity coefficient” index TAX_η, which is shown in formula (8). While ensuring the emission reduction effect, the larger the value, the greater the elasticity of the corresponding carbon tax to national economy and the smaller the GDP loss. The optimal carbon tax can be obtained through the calculation of this index. It can effectively promote the decoupling between the emission reduction of CO₂ and the growth of national economy and then provide more space for emission reduction, while producing additional effects such as reducing production energy consumption and preventing greenhouse effect.

$$\text{TAX}_{\eta} = \frac{E_{\eta}}{\text{GDP}_{\eta}}, \quad (8)$$

where TAX_η is the carbon tax elasticity coefficient and GDP_η is the GDP loss rate in the same period (%).

It is found that the GDP loss rate in 2040 will be as high as 0.60% in TAX-3 scenario, which is much higher than the other scenarios. If the tail effect of the model is considered, the GDP loss rate in 2050 should exceed the calculated value of 0.72%. In the other scenarios, the peak of GDP loss rate in each year is only 0.28%. It can be seen from the above that under the TAX-3 scenario, although the carbon tax level has increased significantly, the emission reduction rate has only increased by 4% compared with the TAX-2 scenario. Its emission reduction effect has not improved significantly, with the dramatically increased resulting GDP loss. In the TAX-2 scenario, TAX_η is the highest, indicating that it has the most elastic impact on the national economy and the smallest GDP loss while ensuring the emission reduction effect. In addition, comprehensively considering the cost of CO₂ emission reduction obtained above, the CO₂ emission reduction cost in the TAX-3 scenario is as high as 9 times of that in the REF scenario. Therefore, in the long run, TAX-2 can better meet the requirements of emission reduction effect and cost in the power industry at the same time, which performs best in the four scenarios. The carbon tax set in this scenario can be used as an effective environmental economic policy tool to reduce energy consumption and CO₂ emissions, as well as changing the energy consumption structure. Although the economic growth will be restrained in the short term, it is beneficial to the healthy development of the whole economy in the medium and long term.

From the perspective of eliminating backward production capacity, carbon tax will increase the development cost of power generation enterprises; but on the contrary, these

increased production costs can prevent some power plants from blindly expanding production capacity, which promotes the technological innovation and upgrading of the power industry. As a good policy signal, carbon tax can effectively control the development of high-energy consumption technologies in power industry. In the whole world, carbon tax can promote the sustainable development of the power industry and enhance the international competitiveness of the country to a certain extent.

4. Conclusions

With the development of economy and society in the future, China’s power consumption demand and the primary energy consumption of the power industry will all show rapid growth. Power production still heavily depends on fossil energy, which will far exceed the supply capacity of coal production, causing great pressure on China’s economic development and ecological environment. Under the REF scenario, the CO₂ emissions of the power industry will be increasing year by year, reaching a peak value in 2050.

Carbon tax will have an important impact on the primary energy supply structure of China’s power industry. Under the three TAX scenarios, in 2050, when comparing with the REF scenario, the primary energy consumption of the power industry will decrease, and its composition will change to a large extent. The proportion of fossil energy consumption in total consumption will be reduced, while renewable energy has developed to different degrees. With the gradual increase of carbon tax level, the CO₂ emissions in 2050 will be reduced to varying degrees under the TAX scenarios. The corresponding emission reduction potential proves the effectiveness of carbon tax on reducing CO₂ emissions.

The medium carbon tax level (TAX-2) set in this paper can better meet the requirements of CO₂ emission reduction effect and cost in the power industry. It has the most elastic impact on the national economy and the smallest GDP loss while ensuring the emission reduction effect, which can be used as an effective environmental economic policy tool.

Combined with the research results obtained above, a low-carbon development policy is proposed to realize the CO₂ emission reduction of China’s power industry: (1) save primary energy and improve energy efficiency; (2) make full use of renewable energy and optimize energy structure; (3) integrate CO₂ control and economic transformation; and (4) improve carbon tax system and pollution management mechanism.

To further enhance the practical application value of the research, the fiscal immunity and transfer payment will be studied based on carbon tax in the future, in combination with “top-down” energy economic models such as CGE model.

Data Availability

The data used to support the findings of this study are available from the corresponding author upon request.

Conflicts of Interest

The authors declare that there are no conflicts of interest regarding the publication of this paper.

Acknowledgments

The authors acknowledge the financial support for this work provided by The National Science Fund for Distinguished Young Scholars (no. 51925402); Shanxi Province High Education Humanities and Social Sciences Key Research Base Project (no. [2018]33); and Shanxi Province Doctoral Education Innovation Project (no. 2019BY061).

References

- [1] L. Dong, Z. Wang, Y. Zhang et al., "Study on pyrolysis characteristics of coal and combustion gas release in inert environment," *Journal of Chemistry*, vol. 2019, Article ID 1032529, 9 pages, 2019.
- [2] G. Feuyit, S. Nzali, J. N. Lambi, and S. Laminsi, "Air quality and human health risk assessment in the residential areas at the proximity of the Nkolfoulou landfill in Yaoundé metropolis, Cameroon," *Journal of Chemistry*, vol. 2019, Article ID 3021894, 9 pages, 2019.
- [3] Z.-J. Zhou, X.-W. Liu, B. Zhao et al., "Effects of existing energy saving and air pollution control devices on mercury removal in coal-fired power plants," *Fuel Processing Technology*, vol. 131, pp. 99–108, 2015.
- [4] L. Jia, B.-g. Fan, Y.-x. Yao et al., "Study on the elemental mercury adsorption characteristics and mechanism of iron-based modified biochar materials," *Energy & Fuels*, vol. 32, no. 12, pp. 12554–12566, 2018.
- [5] Y. Niu, Y. Lv, Y. Lei et al., "Biomass torrefaction: properties, applications, challenges, and economy," *Renewable and Sustainable Energy Reviews*, vol. 115, Article ID 109395, 2019.
- [6] L. Jia, B.-g. Fan, R.-p. Huo et al., "Study on quenching hydration reaction kinetics and desulfurization characteristics of magnesium slag," *Journal of Cleaner Production*, vol. 190, pp. 12–23, 2018.
- [7] Y. Niu, S. Liu, Y. Gong et al., "Effects of FGR and changeable combustion parameters and coal/char properties on the formation of ultrafine PMs during pulverized coal char combustion under various O₂/N₂ and O₂/CO₂ atmospheres," *Combustion Science and Technology*, vol. 191, no. 10, pp. 1898–1915, 2019.
- [8] S. Saint Akadiri, A. Adewale Alola, G. Olasehinde-Williams, and M. Udom Etokakpan, "The role of electricity consumption, globalization and economic growth in carbon dioxide emissions and its implications for environmental sustainability targets," *Science of The Total Environment*, vol. 708, Article ID 134653, 2020.
- [9] P. Shipkovs, G. Kashkarova, and M. Shipkovs, "Renewable energy utilization in Latvia," *Renewable Energy*, vol. 16, no. 1–4, pp. 1241–1244, 1999.
- [10] W. Chen, "The costs of mitigating carbon emissions in China: findings from China MARKAL-MACRO modeling," *Energy Policy*, vol. 33, no. 7, pp. 885–896, 2005.
- [11] X. Zhao, Q. Ma, and R. Yang, "Factors influencing CO₂ emissions in China's power industry: co-integration analysis," *Energy Policy*, vol. 57, pp. 89–98, 2013.
- [12] M. Zhang, X. Liu, W. Wang, and M. Zhou, "Decomposition analysis of CO₂ emissions from electricity generation in China," *Energy Policy*, vol. 52, pp. 159–165, 2013.
- [13] W. Nordhaus, "Optimal greenhouse-gas reductions and tax policy in the "DICE" model," *The American Economic Review*, vol. 83, pp. 313–317, 1993.
- [14] D. Pearce, "The role of carbon taxes in adjusting to global warming," *The Economic Journal*, vol. 101, no. 407, pp. 938–948, 1991.
- [15] N. Floros and A. Vlachou, "Energy demand and energy-related CO₂ emissions in Greek manufacturing: assessing the impact of a carbon tax," *Energy Economics*, vol. 27, no. 3, pp. 387–413, 2005.
- [16] P. He, L. Chen, X. Zou, S. Li, H. Shen, and J. Jian, "Energy taxes, carbon dioxide emissions, energy consumption and economic consequences: a comparative study of nordic and G7 countries," *Sustainability*, vol. 11, no. 21, p. 6100, 2019.
- [17] N. Zhu, L. Qian, D. Jiang, and N. Mbroh, "A simulation study of China's imposing carbon tax against American carbon tariffs," *Journal of Cleaner Production*, vol. 243, Article ID 118467, 2020.
- [18] M. Jaskólski, "Modelling long-term technological transition of Polish power system using MARKAL: emission trade impact," *Energy Policy*, vol. 97, pp. 365–377, 2016.
- [19] L. Rivera-González, D. Bolonio, L. F. Mazadiego, and R. Valencia-Chapi, "Long-term electricity supply and demand forecast (2018–2040): a LEAP model application towards a sustainable power generation system in Ecuador," *Sustainability*, vol. 11, no. 19, p. 5316, 2019.
- [20] P. G. Machado, M. Cunha, A. Walter, A. Faaij, and J. J. M. Guilhoto, "The potential of a bioeconomy to reduce Brazilian GHG emissions towards 2030: a CGE-based life cycle analysis," *Biofuels, Bioproducts and Biorefining*, vol. 14, no. 2, pp. 265–285, 2020.
- [21] S. Wu and H. Han, "Sectoral changing patterns of China's green GDP considering climate change: an investigation based on the economic input-output life cycle assessment model," *Journal of Cleaner Production*, vol. 251, Article ID 119764, 2020.
- [22] M. A. Morshedi and H. Kashani, "A system dynamics model to evaluate the housing market response to vulnerability reduction promotion policies," *International Journal of Disaster Risk Reduction*, vol. 44, Article ID 101438, 2020.
- [23] Y. Asar and J. Wu, "An improved and efficient biased estimation technique in logistic regression model," *Communications in Statistics-Theory and Methods*, vol. 49, no. 9, pp. 2237–2252, 2020.
- [24] J. L. Campos, D. Valenzuela-Heredia, A. Pedrouso, A. Val del Río, M. Belmonte, and A. Mosquera-Corral, "Greenhouse gases emissions from wastewater treatment plants: minimization, treatment, and prevention," *Journal of Chemistry*, vol. 2016, pp. 1–12, 2016.
- [25] J. Yang, Q. Li, M. Li et al., "In situ decoration of selenide on copper foam for the efficient immobilization of gaseous elemental mercury," *Environmental Science & Technology*, vol. 54, no. 3, pp. 2022–2030, 2020.
- [26] M. van den Broek, P. Veenendaal, P. Koutstaal, W. Turkenburg, and A. Faaij, "Impact of international climate policies on CO₂ capture and storage deployment," *Energy Policy*, vol. 39, no. 4, pp. 2000–2019, 2011.
- [27] S. Jegarl, J.-I. Baek, D.-S. Jang, and C.-K. Ryu, "Impact assessment of CO₂ mitigation options in Korea using energy system analysis model," *Energy Procedia*, vol. 1, no. 1, pp. 3747–3754, 2009.

- [28] Y. Jia and R. Liu, "Analysis of Beijing energy saving and emission reduction strategy based on TIMES model," *Journal of Basic Science and Engineering*, vol. 21, pp. 857–865, 2013.
- [29] H. E. Daly and B. P. Ó Gallachóir, "Modelling future private car energy demand in Ireland," *Energy Policy*, vol. 39, no. 12, pp. 7815–7824, 2011.
- [30] J. Shi, W. Chen, and X. Yin, "Modelling building's decarbonization with application of China TIMES model," *Applied Energy*, vol. 162, pp. 1303–1312, 2016.
- [31] H. Zhang, W. Chen, and W. Huang, "TIMES modelling of transport sector in China and USA: comparisons from a decarbonization perspective," *Applied Energy*, vol. 162, pp. 1505–1514, 2016.
- [32] J. Yang, W. Zhu, W. Qu et al., "Selenium functionalized metal-organic framework MIL-101 for efficient and permanent sequestration of mercury," *Environmental Science & Technology*, vol. 53, no. 4, pp. 2260–2268, 2019.
- [33] Z. Zhou, T. Cao, X. Liu, S. Xu, Z. Xu, and M. Xu, "Vanadium silicate (EVS)-supported silver nanoparticles: a novel catalytic sorbent for elemental mercury removal from flue gas," *Journal of Hazardous Materials*, vol. 375, pp. 1–8, 2019.
- [34] Y. Niu, Y. Gong, X. Zhang, Y. Liang, D. Wang, and S. e. Hui, "Effects of leaching and additives on the ash fusion characteristics of high-Na/Ca Zhundong coal," *Journal of the Energy Institute*, vol. 92, no. 4, pp. 1115–1122, 2019.
- [35] J. Yang, W. Zhu, S. Zhang et al., "Role of flue gas components in Hg⁰ oxidation over La_{0.8}Ce_{0.2}MnO₃ perovskite catalyst in coal combustion flue gas," *Chemical Engineering Journal*, vol. 360, pp. 1656–1666, 2019.
- [36] L. Wen and Y. Cao, "Influencing factors analysis and forecasting of residential energy-related CO₂ emissions utilizing optimized support vector machine," *Journal of Cleaner Production*, vol. 250, Article ID 119492, 2020.
- [37] Z. Zhou, E. Leng, C. Li, X. Zhu, and B. Zhao, "Insights into the inhibitory effect of H₂O on Hg-catalytic oxidation over the MnO_x-based catalysts," *ChemistrySelect*, vol. 4, no. 11, pp. 3259–3265, 2019.
- [38] L. Jia, B. Fan, B. Li et al., "Effects of pyrolysis mode and particle size on the microscopic characteristics and mercury adsorption characteristics of biomass char," *Bioresources*, vol. 13, pp. 5450–5471, 2018.
- [39] Y. Wang, J. Liu, L. He, J. Dou, and H. Zhao, "Responses of carbon dynamics to nitrogen deposition in typical freshwater wetland of sanjiang plain," *Journal of Chemistry*, vol. 2014, Article ID 603948, 9 pages, 2014.
- [40] Y. Niu, X. Zhang, H. Zhang et al., "Performance of low-temperature SCR of NO with NH₃ over MnO_x/Ti-based catalysts," *The Canadian Journal of Chemical Engineering*, vol. 97, no. S1, pp. 1407–1417, 2019.

Research Article

Reaction Kinetics of Chlorine Corrosion to Heating Surfaces during Coal and Biomass Cofiring

Yongzheng Wang , Yu Sun, Maozhen Yue, and Yungang Li

School of Energy and Power Engineering, Shandong University, Jinan 250061, China

Correspondence should be addressed to Yongzheng Wang; sddxwyz@163.com

Received 1 November 2019; Revised 30 December 2019; Accepted 16 January 2020; Published 12 February 2020

Guest Editor: Ningbo Gao

Copyright © 2020 Yongzheng Wang et al. This is an open access article distributed under the Creative Commons Attribution License, which permits unrestricted use, distribution, and reproduction in any medium, provided the original work is properly cited.

The high content of chlorine in biomass will cause serious ash deposition and corrosion problems on the heating surface in boiler, reduce heat transfer efficiency, and endanger the boiler operation safety. On the basis of discussing the mechanism of chlorine corrosion to heating surface in the boiler, the temperature, atmosphere, and fouling in the boiler are simulated by high-temperature reaction device. Reaction kinetics of chlorine corrosion to heating surfaces during coal and biomass cofiring was studied by the weight gain method, which provides a theoretical basis for solving the problem of corrosion and improving the safety of boiler operation. The results show that the weight gain caused by corrosion increases with time, and its curve is in accordance with the parabola. In the early stage, the corrosion rate is very fast, and the corrosion gradually slows down after the protective layer is formed. The mixing ratio of straw biomass increases, and the corrosion rate increases proportionally. With the increase in temperature, the rate of corrosion reaction increases continuously. When the temperature exceeds 600°C, the corrosion reaction rate increases greatly. The concentration of HCl in the gas phase increases and the rate of corrosion reaction increases rapidly. Under the constant temperature, the reaction kinetics characteristics of chlorine corrosion were analyzed by model function matching. The best kinetic model function for calculating the kinetic parameters was determined, and the kinetic equation of corrosion reaction was established to quantitatively characterize the corrosion reaction.

1. Introduction

Fossil fuels such as coal continue to be consumed and result in the environmental problems that are becoming increasingly prominent. Biomass, a kind of green renewable energy source, has drawn more attention all over the world [1]. Biomass resource in China, especially crop straw, is abundant. Besides, cofiring technology applied in coal-fired boilers is a promising biomass utilization approach [2]. If biomass is used in large power plants and directly blended with coal to combust in coal-fired boiler, existing facilities of the power plant can be utilized without a large amount of investment; therefore, it is a low-cost and low-risk way to utilize renewable energy at current stage [3, 4].

During cofiring of biomass and coal, especially large amounts of straw biomass and coal blended to combustion, owing to high contents of alkali metal and chlorine in straw biomass, it would lead to deposition, slagging, and corrosion

problems of metal heating surfaces which could seriously harm the safety and economy of boiler equipment and consequently limit large-scale use of biomass in power plants [5–7]. The corrosion of heating surface metal is divided into gas phase corrosion and ash corrosion. Gases such as HCl and Cl₂ cause gas phase corrosion. In an oxidizing atmosphere, the metal surface is oxidized to an oxide film, which prevents corrosion from proceeding further [8]. However, the gas chloride also reacts with the metal to form a metal chloride. The metal chloride is oxidized and releases Cl₂ again, and Cl₂ diffuses into the gas for a new round of reaction, which is named active oxidative corrosion [9]. In a reducing atmosphere, the metal oxide film is absent, and the Cl₂ can directly react with the metal. Ash deposition is the main cause of high-temperature corrosion [10], due to the large amount of KCl in the ash. The sedimentary layer of ash is divided into three layers, wherein the innermost main component is KCl, the middle layer is K₂SO₄, and the

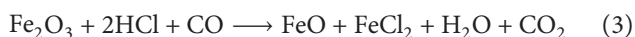
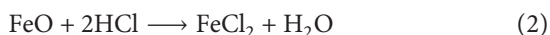
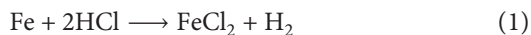
outermost layer is mainly SiO₂ [11]. It was found that the precipitation of K in wheat straw, rice straw, and rice husk was higher, and the precipitation of Cl in corn stalk and cotton stalk was higher [12]. KCl can directly react with the oxide film on the metal surface to form Cl₂, metal oxides, and potassium compounds [13, 14].

The current related research mainly focusing on characteristics of combustion, pollutant emission, and ash fusion during cofiring of biomass and coal [15–18] seldom involves in corrosion problem of metal heating surfaces. Hence, the problems of chlorine corrosion to metal heating surfaces will be studied in this paper to explore the process mechanism and reaction kinetics characteristics of chloride corrosion to metal heat delivery surface in large coal-fired power plant boiler during biomass and coal cofiring. It can quantitatively analyze the corrosion process under constant temperature conditions, provide a reference for the optimization of boiler operating parameters, and provide the theoretical foundation for extensive and efficient use of biomass resources.

2. Chlorine Corrosion Mechanism

During cofiring of biomass and coal, the corrosion to metal heating surfaces in boiler was mainly related to chlorine and sulfur in fuels [19]. The precondition that influences the corrosion most is the molar ratio between sulfur and chlorine in the fuel [20]. When the amount of biomass blended to coal was large, corrosion effect was given priority to chloride corrosion to metal. Studies found that chlorine in biomass fuel played an important role in high-temperature corrosion to metal heat delivery surface in boiler. When the content of chlorine in biomass fuel reached a certain value, the corrosion effect of chlorine would be greater than that of sulfur in biomass fuel. Some studies indicated that high-temperature corrosion involving chlorine tended to be serious when the content of chlorine in the fuel was more than 0.3% [21]. Chlorine mainly presented in the form of HCl, Cl₂, KCl, and NaCl during cofiring of biomass and coal, and corrosion effect of HCl in flue gas was principal. Experiment results showed that 95% of chlorine in fuel released with converting into HCl during flue combusting [22].

HCl releasing from fuel combustion is gaseous corrosion medium with high activity. It can directly react with metal heat delivery surfaces and actively involves in corrosion to Fe, FeO, Fe₂O₃, Fe₃O₄, and Cr₂O₃ under high-temperature condition:



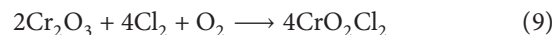
Owing to the presence of HCl, the protective oxide film on the surface of the metal can be destroyed. It makes the

transmission rate of gaseous corrosion medium toward metal interface increase and consequently leads to corrosion to metal base.

When the surface temperature on the pipe wall exceeds the melting point temperature of FeCl₂, FeCl₂ will evaporate into gas phase. When FeCl₂ escapes into flue gas, due to oxygen pressure increasing along the way, FeCl₂ is oxidized by O₂ to form Cl₂:



The formed Cl₂ permeates into the metal surface and reacts with Fe, FeCl₂, and Cr₂O₃ as follows:



FeCl₃ formed in the above reaction, which is of low melting point (303°C) and high vapor pressure (1670 Pa), is very easy to volatilize under the surface temperature of the metal. It causes gaps in the protective film and the film becomes loose and significantly reduces the transmission resistance of active gaseous corrosion medium to metal base interface. In addition, corrosion products are more likely to spall off, thereby promoting the reaction process of corrosion to metal.

Then formed FeCl₃ will be transformed into Cl₂ under certain conditions:



In the above cyclic reaction process, Cl₂ with strong oxidization constantly erodes iron and its compounds. Hence, the reaction process of chlorine corrosion is of repetitive features.

Furthermore, chloride and sulfur oxides will coexist during cofiring of biomass and coal, by means of O₂ and H₂O, and it not only accelerates the formation of sulfate but also contributes to produce HCl and Cl₂, which greatly increases the extent of high-temperature corrosion [23]:



The above analysis shows that chloride and its reaction products HCl and Cl₂ are the main causes of the high-temperature corrosion to metal heating surfaces in boilers. The main factor leading to corrosion to metal heating surfaces is that HCl reacts directly with the heating surface metal, consequently accelerates the oxidization of metal alloys, and then results in corrosion which is active oxidation corrosion [24]. Cl₂, which is similar to the catalyst, has almost no consumption in the corrosion process [25]. If HCl and Cl₂ are supplied constantly, the recurrent corrosion will

be always going on to damage the iron and its compounds and seriously endangers the operation safety of boiler equipment.

3. Experimental System and Experimental Method

3.1. Experimental System. The experimental system of chlorine corrosion on heating surfaces is illustrated in Figure 1, which consists of gas distribution device, high-temperature tube reactor, temperature control unit, and absorption apparatus for tail gas. The gas distribution device provides the simulated flue gas for experiment requirement. The proportion of the components of simulated flue gas is controlled by regulating the gas flow from 3 gas cylinders. The gases flowing out of gas cylinders are mixed in the gas mixing device sufficiently and then feed into the high-temperature tube reactor to simulate flue gas atmosphere in the area of superheater. In the high-temperature tube reactor, the silicon-carbon tube acts as a heating element with built-in corundum tube forming experimental closed flat-temperature zone. Metal specimens in porcelain combustion boat are put into the closed flat-temperature zone through a sample delivery device. The reaction region in the high-temperature tube reactor keeps the temperature constant with a temperature controller to simulate the temperature in the area of superheater. In the temperature controller, the temperature ranging from indoor to 1600°C is measured by platinum-rhodium platinum thermocouples, and automatic temperature accommodator is used for data display and temperature control. A large amount of HCl gas containing in simulated flue gas after the reaction is completely absorbed by absorber bottle with NaOH solution in case of personnel poisoning and environment polluted.

3.2. Experimental Samples. The biomass samples are straw biomass including corn stalks and wheat stalks in Shandong Province, and coal sample is lean coal. Before the experiment, the biomass and coal samples were ground into powder of 200 mesh by using a small coal mill and an electric vibrating screen and dried in the drying oven under the temperature of 105°C. The preparation of coal ash is accorded with the method in the coal quality analysis standard GB/T212-2001, and the standard ASTM E1755-01 should be used for the preparation of biomass ash. The proximate analysis and ultimate analysis of biomass samples and coal sample, and ultimate analysis of ash samples are shown in Tables 1 and 2, respectively. The cofiring ash samples in the experiment are made of mixtures of biomass ash and coal ash obtained with the above methods. The metal specimen is made of T91 steel which is commonly used on heat delivery surface of superheater in boilers and has high allowable stress, endurance strength, fatigue strength, thermal conductivity, and well corrosion resistance [26]. The chemical contents of T91 steel are listed in Table 3.

3.3. Experimental Conditions. The cofiring ash samples of coal and biomass are made of mixture of biomass ash and

coal ash based on the weight percentage of fuel before burning. The blending proportions of biomass are 0%, 20%, 50%, and 100%, and under normal conditions that is 50%. In the course of experiments, O₂ concentration is 6%, CO₂ concentration is 12%, HCl concentration is 500 μL·L⁻¹, and N₂ is used as balance gas to keep stable flow of mixing gas which is 50 ml·min⁻¹. When the experimental conditions changed, the HCl concentration ranges are 0, 200, 300, and 500 μL·L⁻¹. The ranges of temperature are 450, 500, 550, 600, and 650°C, and normal condition is 600°C.

3.4. Experimental Methods. Before the experiment, the metal pipe used on the heat delivery surface of superheater in boilers was made into specimens of 30 mm × 8 mm × 4 mm. The specimens were successively polished smoothly by sandpaper of 200 mesh and 1000 mesh, and the size of specimens was measured accurately with vernier calipers in order to calculate the surface area. First, the specimens were put into absolute ethyl alcohol to clean and degrease, and their surfaces were blotted up with filter paper. Then, the specimens were put into the drying oven under the temperature of 105°C. After 30 minutes, the specimens were taken out and their weights were measured. Then, the specimens were coated with cofiring ash samples fasten with absolute ethyl alcohol on the surface and put into the drying oven again to dry for 20 minutes under the temperature of 105°C, and finally taken out to be used for experiments.

The coated metal specimens along with porcelain combustion boats were put into the flat-temperature zone of the high-temperature tube reactor. The experiments on static oxidation were carried out, and method of corrosion mass gain was used to determine the extent of corrosion to metal. According to the results of previous experimental studies, the extent of corrosion to metal specimens had great growth in the early 20 hours and tended to stable after 30 hours, and hence, the total experimental time of corrosion to metal specimens was determined to be 30 hours, metal specimens were weighed for every 6 hours, and weighing time is controlled within 20 minutes to ensure that each weighing interval is equal.

4. Results and Discussion

4.1. Characteristics of Chlorine Corrosion

4.1.1. Analysis of Reaction Characteristics of Corrosion Chloride. The corrosion mechanism of the metal heating surface shows that a large amount of chloride in the ash deposition on the superheater and gaseous chlorine released during the combustion are the main reasons for the corrosion to the heating surface in boiler. Gaseous chlorine can directly react with the heated surface metal, and there are two ways for alkali metal chloride corrosion: first, it will react with SO₂ in flue gas to form sulfate near the metal surface, and the reaction products HCl and Cl₂ cause active oxidative corrosion which can exacerbate the metal corrosion; the second is to form a low-temperature eutectic with other corrosion products, resulting in the oxide layer on metal surface melting and exacerbating the corrosion. The high-

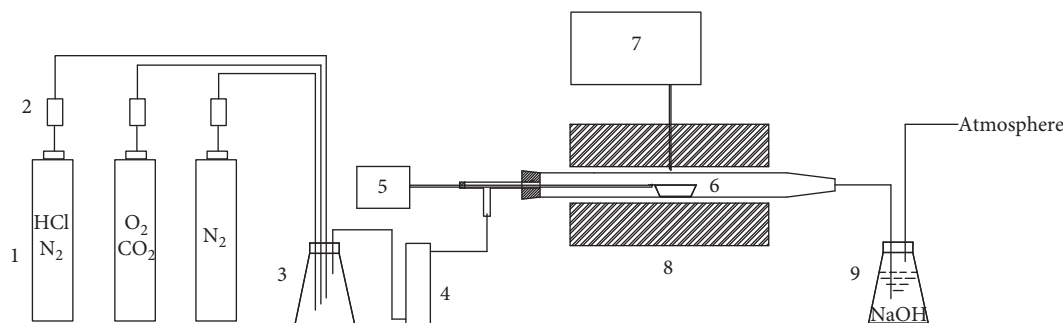


FIGURE 1: Experimental system for chlorine corrosion to metal heat delivery surfaces. (1) gas cylinders; (2) gas flowmeters; (3) gas mixing device; (4) dryer; (5) sample delivery device; (6) porcelain combustion boat; (7) temperature controller; (8) high-temperature tube reactor; (9) absorber bottle.

TABLE 1: Proximate analysis and ultimate analysis of biomass samples and coal sample (air-dried basis)/wt.%.

Sample	Symbol	Proximate analysis					Ultimate analysis			
		M_{ad}	A_{ad}	V_{ad}	FC_{ad}	C_{ad}	H_{ad}	N_{ad}	S_{ad}	
Corn stalks	CS	6.35	5.08	68.33	20.24	42.95	6.65	0.87	1.11	
Wheat stalks	WS	5.44	10.82	64.03	19.71	40.27	6.34	0.68	1.07	
Lean coal	LC	1.43	33.74	12.99	51.84	55.41	2.97	0.96	3.24	

*M: moisture; A: ash; V: volatile matter; FC: fixed carbon.

TABLE 2: Ultimate analysis of ash samples/wt.%.

Sample	Na	Mg	Al	Si	P	S	Cl	K	Ca	Fe
Corn stalk ash	0.84	6.88	0.21	5.53	1.73	1.15	34.90	45.62	2.79	0.35
Wheat stalk ash	1.16	4.22	1.03	31.38	1.98	4.06	15.39	32.70	8.08	0.00
Lean coal ash	1.21	2.66	27.15	56.32	0.49	0.33	0.71	1.45	2.22	7.46

TABLE 3: Chemical contents of T91 steel/wt.%.

C	S	P	Si	Mn	Cr	Mo	V	Nb	N	Al	Ni
0.08~0.12	≤0.01	≤0.02	0.20~0.50	0.30~0.60	8.00~9.50	0.85~1.05	0.18~0.25	0.06~0.10	0.03~0.07	≤0.04	≤0.40

temperature tube reactor was used to simulate high-temperature environment in the area of superheater. Cofiring ash of coal and biomass served as ash deposition was coated on the surface of metal specimens in order to simulate the effect of ash deposition on corrosion to metal heating surfaces, and mixing gas consisting of HCl, O₂, CO₂, and N₂ was used to simulate flue gas atmosphere in boilers. The issues of chlorine corrosion to metal heating surfaces of superheater in boilers were experimentally studied in this paper, with simulating the operating condition of metal heating surfaces of superheater in boilers.

Figures 2 and 3 illustrate the mass gain curves of corrosion to T91 steel specimens coated with cofiring ash of coal and biomass blended to coal with different percentages. It can be found from the above figures that the mass gains of corrosion to metal specimens increase along with the lapse of time. The mass gains of corrosion to metal specimens increased rapidly at the initial stage, which was a rapid corrosion stage, and then gradually slowed down and tend to be flat at the later stage. The curves of corrosion mass gains accorded with parabola.

The corrosion process of the samples is analyzed as follows: when iron or iron alloy is exposed to a high-temperature oxidation environment, the outer layer of the metal will gradually oxidize into a stable and dense oxide film. But the alkali metal chloride in the ash reacts with the oxide film on the metal surface, and releasing Cl₂, resulting in the destruction of the metal oxide film. The Cl₂ can penetrate the protective oxide film, diffuse to the interface between oxide film and metal, and react with the metal to form a metal chloride. The metal chloride has a lower melting point. When the temperature of the metal tube is high, metal chloride will evaporate and diffuse to the surface of the oxide film, react with the oxygen in flue gas, and gradually form a loose oxide layer. The oxide layer cannot protect the metal from further corrosion. This reaction generates Cl₂ again, and Cl₂ returns to the metal surface through the loose oxide layer, so that the corrosion process continues. In the initial stage, there are more alkali metal chlorides in ash, and the corrosion rate is fast; as the reaction continues, the alkali metal chloride content gradually depletes, and the corrosion reaction rate also gradually decreases.

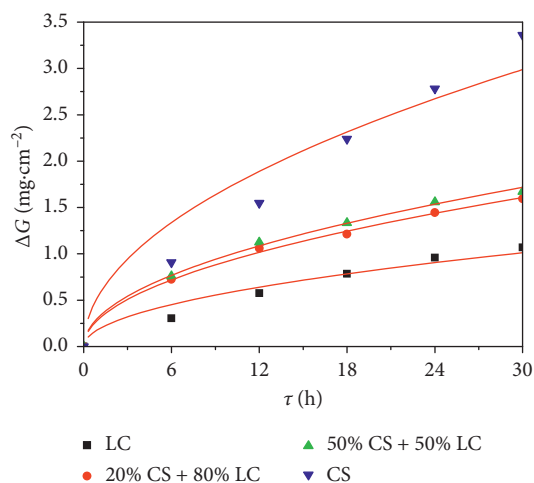


FIGURE 2: Mass gain curves of corrosion to metal specimens coated with cofiring ash of coal and biomass (corn stalks) blended to coal with different percentages.

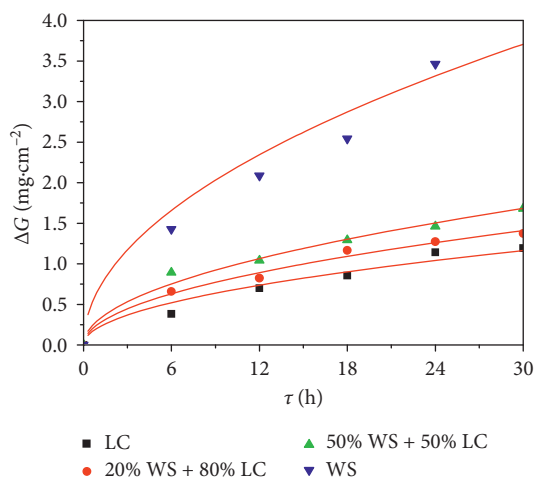


FIGURE 3: Mass gain curves of corrosion to metal specimens coated with cofiring ash of coal and biomass (wheat stalks) blended to coal with different percentages.

It can be also found from the above figures that with increasing the percentage of straw biomass blended to coal, the rate of corrosion to metal specimens increases proportionately, and corrosion to metal specimens was most serious when all was straw biomass. The reason can be explained as follows. During cofiring of coal and straw biomass, the content of residual chloride in ash deposition increased with the straw biomass blended to coal. Chloride in ash deposition will participate in salinization to form aluminosilicate and release HCl from the metal surface, thus accelerating the process of corrosion reaction and increasing the rate of chlorine corrosion.

4.1.2. Effects of Temperature on Chlorine Corrosion Characteristics. Temperature had a significant influence on corrosion to metal. The operating experiences from foreign biomass power plant showed that when the temperature of

steam in superheater was high, the serious corrosion would occur generally on the pipe wall of superheater [27], but when the temperature of steam in superheater was low (such as 450°C), the serious corrosion was not found [28]. Figure 4 illustrates the mass gain curves of corrosion to ash-coated metal specimens under different temperatures. It can be found that the rate of corrosion to metal specimens increases constantly with temperature increasing. When the temperature was below 600°C, it had a little influence on corrosion to metal specimens and the rate of corrosion to metal specimens increased slowly. But when the temperature exceeded 600°C, the rate of corrosion to metal specimens increased significantly. The reason is mainly due to the different corrosion mechanism.

In the initial stage of the corrosion, all elements in the metal are jointly participated in the reaction. As a crucial element of the alloy, Cr can preferentially react with oxygen and form a dense and adhesive oxide film, so that the corrosion resistance of metal can be enhanced. However, when the temperature increases, the diffusion velocity of C in the interior of the metal grain is greater than Cr. The formation and precipitation of carbides in the metal base cause local chromium deficiency near the grain boundary. Alkali metal chloride such as NaCl from deposits easily reacts with metal carbides to generate Cl₂, which causes severe intergranular corrosion. Intergranular corrosion spreads inward along the interface between metal grains, which greatly reduces the mechanical strength of the metal. The higher the grain boundary carbon content, the more severe this effect. It is observed from the corrosion layer on the metal surface that with the increase in temperature, the corrosion layer became thicker and serious pitting corrosion occurred gradually on the surface.

In addition, when the temperature is low, the metal corrosion is mainly common oxidative corrosion. Once the temperature increases, the alkali metal sulfate in the ash deposit becomes a molten liquid phase on the surface of the oxide layer, which rapidly exacerbates the corrosion. During the cofiring of biomass and coal, due to the sulfation reaction, there is a large amount of sulfate in the ash deposition, and it also contains some alkali metal chloride. Alkali metal chlorides in ash deposition may cause the melting point of low-temperature comelts to decrease further. The metal base is easier to be corroded by the HCl and SO₂/SO₃ in the surrounding gas phase due to the melting and destruction of the protective oxide layer, which makes the corrosion exacerbate.

4.1.3. Effects of HCl Concentration on Chlorine Corrosion Characteristics. The views on the effect of HCl on chloride corrosion to metal were different. Montgomery and Larsen considered that the corrosiveness of HCl was lower than the corrosiveness of KCl in depositing on the surface of the oxidation layer [29]. Lith et al. found from experiments that when there was the element chlorine in ash deposition, the presence of HCl was not a necessary condition for the chlorine corrosion, but it can accelerate chlorine corrosion [30]. Yin and Wu found by the study on corrosion of

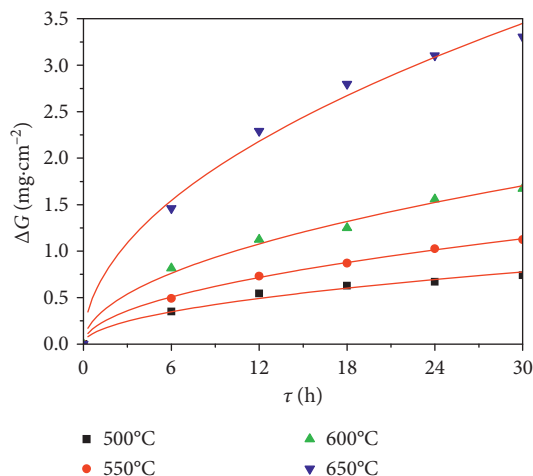


FIGURE 4: Mass gain curves of corrosion to ash-coated metal specimens under different temperatures.

chlorine in biomass that the rate of corrosion to metal increased proportionally with the increase in the concentration of HCl [31]. Figure 5 illustrates the mass gain curves of corrosion to ash-coated metal specimens under different concentrations of HCl. It can be found that if there is no HCl in the gas phase, mass gains of metal specimens vary a little and the rate of corrosion is very low. With the increase in the concentration of HCl, mass gains of metal specimens vary a lot and the rate of corrosion increases rapidly. Because the oxide layer on the metal surface cannot block the penetration of HCl, HCl can penetrate the cracks or pores on the metal surface and contact and react with metal alloy elements (Fe, Cr, and Ni). With the increase of HCl, the chlorine pressure difference between atmosphere/oxide film interface and oxide film/metal interface increases, which enhances the kinetic force of HCl diffusion to the metal surface, so HCl can easily pass through the oxide film and accelerate corrosion. In addition, the higher the concentration of HCl, the stronger the active oxidation. As the HCl concentration increases, the mass gain of the metal sample changes greatly, and the corrosion rate increases rapidly.

4.2. Reaction Kinetics of Chlorine Corrosion

4.2.1. The Basic Equation of Corrosion Reaction Kinetics.

The main task in the study of chemical reaction kinetics is how to determine the process mechanism of chemical reaction and relevant reaction kinetics parameters [32]. In experimental study on characteristics of chlorine corrosion to metal heating surfaces, every experiment of chlorine corrosion to metal specimens was carried out under constant temperature condition. Hence, the reaction rates of corrosion to metal specimens were described by constant temperature and heterogeneous reaction kinetics equation [33]:

$$\frac{d\alpha}{d\tau} = k \cdot f(\alpha). \quad (14)$$

In (14), τ is the reaction time, k is the reaction rate constant, and α is the conversion rate from reactants to

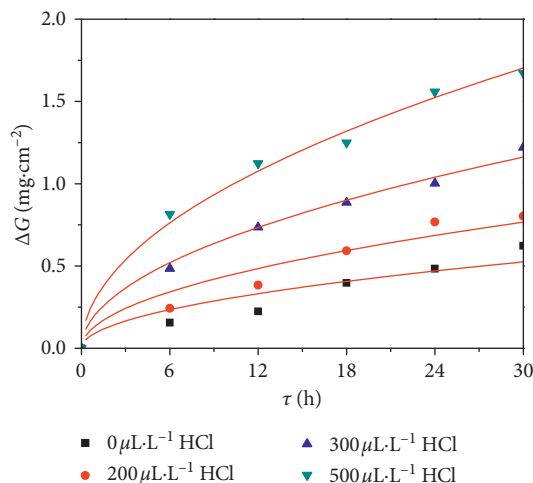


FIGURE 5: Mass gain curves of corrosion to ash-coated metal specimens under different concentrations of HCl in the gas phase.

resultants in the time of τ . $\alpha = w - w_0/w_\infty - w_0$, w_0 and w_∞ are the initial and final weight of specimens, respectively, w is the weight of specimens in the time of τ . $f(\alpha)$ is the reaction kinetics model function which reveals the mechanism of chemical reaction.

The relationship between reaction rate constant k and temperature T is expressed by Arrhenius law [34]:

$$k = A \exp\left(-\frac{E}{R_m T}\right). \quad (15)$$

In the (15), A is the frequency factor, E is the activation energy, T is the reaction temperature, and R_m is the universal gas constant and its value is $8.3145 \text{ J}\cdot\text{mol}^{-1}\cdot\text{K}^{-1}$.

The basic equation of reaction kinetics of corrosion to metal is obtained through substituting (15) into (14):

$$\frac{d\alpha}{d\tau} = A \exp\left(-\frac{E}{R_m T}\right) f(\alpha). \quad (16)$$

4.2.2. Determination of the Optimal Dynamic Model Function.

The reaction kinetics model function $f(\alpha)$ expresses a certain functional relationship to follow between the rate of chemical reaction and conversion rate α and represents the chemical reaction mechanism. Its corresponding integral form is defined as follows:

$$G(\alpha) = \int_0^\alpha \frac{d\alpha}{f(\alpha)}. \quad (17)$$

The correctness of reaction kinetics model function had great effects on kinetics parameters of reaction. The characteristics of chemical reaction kinetics can be analyzed by various methods to determine the correct reaction kinetics model, such as isothermal method, nonisothermal single-scan method, kinetic compensation effect method, and nonisothermal multiple scan method [35]. The isothermal method will be used to solve the following problems because experiments of chlorine corrosion to metal specimens are carried out under constant temperature condition.

TABLE 4: The conversion rate of metal specimens at different times.

$t(^{\circ}\text{C})$	α					
	0	6 h	12 h	16 h	24 h	30 h
500	0	0.472	0.735	0.849	0.906	1.000
550	0	0.438	0.650	0.775	0.913	1.000
600	0	0.454	0.672	0.798	0.932	1.000
650	0	0.442	0.693	0.847	0.939	1.000

TABLE 5: Model functions of reaction kinetics.

Model functions	Symbol	$f(\alpha)$	$G(\alpha)$
One-dimensional diffusion model	D1	$(1/2)\alpha^{-1}$	α^2
Two-dimensional diffusion model	D2	$[-\ln(1-\alpha)]^{-1}$	$\alpha + (1-\alpha)\ln(1-\alpha)$
Three-dimensional diffusion model (Jander)	D3	$(3/2)(1-\alpha)^{2/3}[1-(1-\alpha)^{1/3}]^{-1}$	$[1-(1-\alpha)^{1/3}]^2$
Three-dimensional diffusion model (Ginstling-Brounstein)	D4	$(3/2)[(1-\alpha)^{-1/3}-1]^{-1}$	$1-(2/3)\alpha-(1-\alpha)^{2/3}$
Secondary nucleation and growth reaction	A2	$2(1-\alpha)[- \ln(1-\alpha)]^{1/2}$	$[-\ln(1-\alpha)]^{1/2}$
Secondary phase interface reaction	R2	$2(1-\alpha)^{1/2}$	$1-(1-\alpha)^{1/2}$

The isothermal method is relatively simple, and the model fitting method is generally used to fit experimental data with reaction kinetics model functions. At a certain constant temperature, the reaction rate constant k is constant, so it can be separated with $f(\alpha)$ or $G(\alpha)$ by substituting (16) into (17):

$$G(\alpha) = \int_0^{\tau} A \exp\left(-\frac{E}{R_m T}\right) \cdot d\tau = k(T)\tau. \quad (18)$$

From (18), it can be seen that $G(\alpha)$ has a linear relationship with time τ , and the slope of the line is the reaction rate constant k . A set of data of α and τ under constant temperature condition is selected to substitute into tentative $G(\alpha)$ and draw the relationship curve of $G(\alpha)$ versus time τ . If $f(\alpha)$ corresponded to $G(\alpha)$ has a optimal linear relationship with time τ , it is deemed to be the optimal reaction kinetics model function.

4.2.3. Establishment of Reaction Kinetics Equations of Chlorine Corrosion. The purpose of the study on reaction kinetics of chlorine corrosion to metal is to determine the optimal kinetics model function $f(\alpha)$, calculate the reaction kinetics parameters A , E , and the reaction rate constant k , then put forward reaction rate function, and finally obtain reaction kinetics equations to quantitatively represent the process of chlorine corrosion reaction. Hence, the characteristics of reaction kinetics of chlorine corrosion to metal were studied in this paper with isothermal method basing on experimental data listed in Figure 4. Table 4 getting from Figure 4 shows the conversion rate of metal specimens at different times under certain temperature.

The reaction kinetics model functions listed in Table 5 were chosen to use for tentative model function to fit model. The data in Figure 4 were, respectively, substituted into $G(\alpha)$ corresponding to six reaction kinetics model functions selected in common use, to obtain the value of $G(\alpha)$ at different times τ under certain temperature. The relationship curves of $G(\alpha)$ versus τ were drawn respectively and fitted linearly, and then $f(\alpha)$ corresponded to $G(\alpha)$, which has optimal

linear relationship with time τ , was deemed to be the optimal reaction kinetics model function.

By means of drawing respectively and fitting linearly the relationship curves of $G(\alpha)$ versus τ , the optimal reaction kinetics model function was obtained to be $G(\alpha)$ and $f(\alpha)$ corresponding with one-dimensional diffusion model. Only the relationship curves of $G(\alpha)$ versus τ fitted linearly with one-dimensional diffusion model are given in Figure 6.

(15) was taken logarithm on both sides:

$$\ln k = \ln A - \frac{E}{R_m T}. \quad (19)$$

From (19), it can be seen that the relationship between $\ln k$ and T^{-1} was linear and the parameters A and E were calculated through the intercept $\ln A$ and slope $-E/R_m$.

The values of k under certain temperature were obtained from fitting curves in Figure 6 and corresponding values of T^{-1} and $\ln k$ are calculated in Table 6. Basing on the data in the above table, the relationship curve of $\ln k$ versus T^{-1} was drawn and fitted linear and is shown in Figure 7. The fitting relationship equation was finally obtained as follows: $\ln k = -3.1386 - 205.5553 T^{-1}$, and the correlation coefficient of fitting linear was $R^2 = 0.9814$.

By means of the above fitted linear relationship equation, the reaction kinetics parameters A and E were calculated. The results of $A = 0.04334$ and $E = 1709.08954 \text{ J}\cdot\text{mol}^{-1}$ were, respectively, derived from $\ln A = -3.1386$ and $E/R_m = 205.5553$.

The value of A and E and the optimal model function $f(\alpha) = (1/2)\alpha^{-1}$ were substituted into (16) to obtain following reaction kinetics equations of chlorine corrosion to metal specimens:

$$\frac{d\alpha}{d\tau} = 0.02167 \exp\left(\frac{-205.5553}{T}\right) \cdot \alpha^{-1}. \quad (20)$$

The time integral of (20) was taken. Because the experiments were carried out under constant temperature, temperature was not a function of time and therefore considered as constant. At the time of $\tau = 0$, the experiments have not started, and the conversion rate was zero. In other

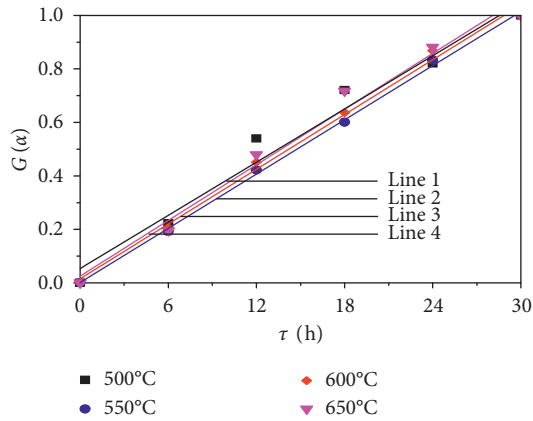


FIGURE 6: Fitting curves of $G(\alpha)$ versus τ with one-dimensional diffusion model. Line 1—500°C: $G(\alpha) = 0.05258 + 0.03321\tau$ and $R^2 = 0.9655$; Line 2—550°C: $G(\alpha) = 0.00071 + 0.03383\tau$ and $R^2 = 0.9980$; Line 3—600°C: $G(\alpha) = 0.01485 + 0.03416\tau$ and $R^2 = 0.9934$; Line 4—650°C: $G(\alpha) = 0.02463 + 0.03474\tau$ and $R^2 = 0.9789$.

TABLE 6: Reaction rate constants k under certain temperature.

$t(^{\circ}\text{C})$	$T(\text{K})$	$T^{-1}(\text{K}^{-1})$	Reaction rate constant k	$\ln k$
500	773	0.001294	0.03321	-3.4049
550	823	0.001215	0.03383	-3.3864
600	873	0.001145	0.03416	-3.3767
650	923	0.001083	0.03474	-3.3599

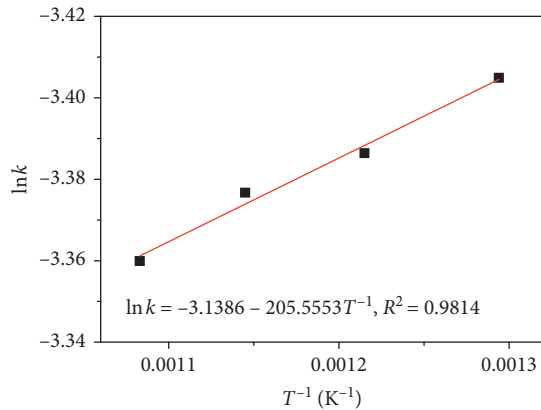


FIGURE 7: Fitting curve of $\ln k$ versus T^{-1} . Fitting line: $\ln k = -3.1386 - 205.5553T^{-1}$, $R^2 = 0.98114$.

words, if $\tau = 0$, then $\alpha = 0$. The equation of the conversion rate α through integral is obtained as follows:

$$\alpha = 0.2082 \exp\left(\frac{-102.7777}{T}\right) \cdot \tau^{-(1/2)}. \quad (21)$$

5. Conclusions

During cofiring of coal and biomass, alkali metal chlorides, HCl and Cl_2 , cause high-temperature corrosion to metal heating surfaces in boilers. HCl is the main factor leading to corrosion to metal heating surfaces, which can directly react with metal heating surfaces and accelerate

oxidization of alloy. Cl_2 has almost no consumption in the process of corrosion, which was similar to the catalyst. If HCl and Cl_2 were supplied constantly, the recurrent reaction process of corrosion will be always going on, and thus, it is of repetitive features. If chlorides coexist with sulfur oxides, the process of high-temperature corrosion will greatly be accelerated.

The mass gain curves of metal accorded with parabola, and the degree of corrosion is greatly affected by the blending ratio of biomass. At the initial stage, there was a rapid corrosion stage, the corrosion reaction rate was high, and the protective oxidation layer was soon formed on the surface of metal specimens. As the oxidation layer gradually becomes thicker, the corrosion reaction rate gradually slowed down and tends to be flat at the later stage. With the percentage of straw biomass blended to coal increasing, due to the increasing the content of residual chloride in ash deposition, the rate of corrosion to metal specimens increases proportionately, and corrosion to metal specimens was most serious when all was straw biomass.

Temperature and concentration of HCl in the gas phase also had a significant influence on corrosion to metal. With the increase in temperature, the rate of corrosion to metal increased constantly. When the temperature was below 600°C, the rate of corrosion to metal specimens increased slowly. But when the temperature exceeded 600°C, the rate of corrosion to metal specimens increased significantly. The rate of corrosion to metal specimens rapidly increased with the increase in the concentration of HCl in the gas phase.

Using model fitting methods, the analyses on reaction kinetics of chlorine corrosion to metal heating surfaces were carried out under constant temperature condition. It is found that the experimental data were fitted well with one-dimensional diffusion model, and therefore, optimal kinetic model function and corresponding kinetics parameters of chlorine corrosion reaction were obtained, and finally, the reaction kinetics equation of chlorine corrosion to metal was established:

$$\frac{d\alpha}{d\tau} = 0.02167 \exp\left(\frac{-205.5553}{T}\right) \cdot \alpha^{-1}. \quad (22)$$

Notations

Explanation of symbols

- A: Frequency factor, s^{-1}
- E: Activation energy, $\text{J}\cdot\text{mol}^{-1}$
- $f(\alpha)$: Reaction kinetics model function
- $G(\alpha)$: Integral form of reaction kinetics model function
- k : Reaction rate constant
- R_m : Universal gas constant, $8.3145 \text{ J}\cdot\text{mol}^{-1}\cdot\text{K}^{-1}$
- T: Reaction temperature, K
- w : Weight of specimens in the time of τ , mg
- w_0, w_{∞} : Initial and final weight of specimens, respectively, mg
- α : Conversion rate from reactants to resultants in the time of τ
- ΔG : Mass gain of corrosion to metal specimens, $\text{mg}\cdot\text{cm}^{-2}$
- τ : Reaction time, h

Subscript

0: Initial time

∞ : Final time.

Data Availability

The data used to support the findings of this study are available from the corresponding author upon request.

Conflicts of Interest

The authors declare that there are no conflicts of interest regarding the publication of this paper.

Acknowledgments

This work was supported by Shandong Provincial Natural Science Foundation, China (ZR2017MEE009).

References

- [1] S. Xiong, J. Burvall, H. Orberg et al., "Slagging characteristics during combustion of corn stovers with and without kaolin and calcite," *Energy & Fuels*, vol. 22, no. 5, pp. 3465–3470, 2008.
- [2] J. B. Królczuk, A. Rezwiakow, and M. Tukiendorf, "Mixing of biomass and coal in a static mixer as an example of technological solutions involving implementation of renewable energy sources," *Ecological Chemistry and Engineering S*, vol. 21, no. 4, pp. 685–696, 2015.
- [3] J. Mao, "Coal fired coupling biomass power generation," *Distributed Energy Resources*, vol. 2, no. 5, pp. 47–54, 2017.
- [4] P. Basu, J. Butler, and M. A. Leon, "Biomass co-firing options on the emission reduction and electricity generation costs in coal-fired power plants," *Renewable Energy*, vol. 36, no. 1, pp. 282–288, 2011.
- [5] L. L. Baxter, "Ash deposition during biomass and coal combustion: a mechanistic approach," *Biomass and Bioenergy*, vol. 4, no. 2, pp. 85–102, 1993.
- [6] A. L. Robinson, H. Junker, and L. L. Baxter, "Pilot-scale investigation of the influence of coal–biomass cofiring on ash deposition," *Energy & Fuels*, vol. 16, no. 2, pp. 343–355, 2002.
- [7] T. Nussbaumer, "Combustion and Co-combustion of biomass: fundamentals, technologies, and primary measures for emission reduction," *Energy & Fuels*, vol. 17, no. 6, pp. 1510–1521, 2003.
- [8] M. Srivastava, J. N. Balaraju, B. Ravisankar, C. Anandan, and V. K. William Grips, "High temperature oxidation and corrosion behaviour of Ni/Ni-Co-Al composite coatings," *Applied Surface Science*, vol. 263, no. 24, pp. 597–607, 2012.
- [9] C. Berlanga and J. A. Ruiz, "Study of corrosion in a biomass boiler," *Journal of Chemistry*, vol. 2013, Article ID 272090, 8 pages, 2013.
- [10] J. Song, J. Song, and J. Li, "Study on influence of high temperature corrosion and pollutants emission of co-combustion of coal in biomass boiler," *Power System Engineering*, vol. 31, no. 2, pp. 37–43, 2015.
- [11] L. Li, C. Yu, F. Huang, J. Bai, M. Fang, and Z. Luo, "Study on the deposits derived from a biomass circulating fluidized-bed boiler," *Energy & Fuels*, vol. 26, no. 9, pp. 6008–6014, 2012.
- [12] X. Song, S. Zhu, B. Huang et al., "Study of emission characteristics of chlorine and potassium in biomass combustion," *Acta Energetica Solaris Sinica*, vol. 36, no. 10, pp. 2543–2547, 2015.
- [13] C. Yu, Z. Wang, B. Gong et al., "Corrosion characteristics of biomass boiler steel in KCl contact condition," *Journal of Zhejiang University*, vol. 48, no. 11, pp. 2046–2052, 2014.
- [14] Y. He, Y. Li, H. Zhang et al., "High temperature corrosion behavior of T91 in alkali metal chloride medium," *Corrosion and Protection*, vol. 36, no. 11, pp. 1021–1025, 2015.
- [15] X. Wang, Z. Xu, B. Wei et al., "The ash deposition mechanism in boilers burning Zhundong coal with high contents of sodium and calcium: a study from ash evaporating to condensing," *Applied Thermal Engineering*, vol. 80, pp. 150–159, 2015.
- [16] P. Molcan, G. Lu, T. L. Bris, Y. Yan, B. Taupin, and S. Caillat, "Characterisation of biomass and coal co-firing on a 3MWth combustion test facility using flame imaging and gas/ash sampling techniques," *Fuel*, vol. 88, no. 12, pp. 2328–2334, 2009.
- [17] X. Wang, Z. Hu, S. Deng, Y. Xiong, and H. Tan, "Effect of biomass/coal co-firing and air staging on NO_x emission and combustion efficiency in a drop tube furnace," *Energy Procedia*, vol. 61, pp. 2331–2334, 2014.
- [18] K. Qiu, H. Zhang, H. Zhou, B. Zhou, L. Li, and K. Cen, "Experimental investigation of ash deposits characteristics of co-combustion of coal and rice hull using a digital image technique," *Applied Thermal Engineering*, vol. 70, no. 1, pp. 77–89, 2014.
- [19] Y. Wang, K. Zhang, L. Jiang et al., "Study on sulfur-chlorine synergistic corrosion in biomass and coal co-firing," *Journal of Chemical Engineering of Chinese Universities*, vol. 29, no. 6, pp. 1422–1429, 2015.
- [20] A. Miltner, G. Beckmann, and A. Friedl, "Preventing the chlorine-induced high temperature corrosion in power boilers without loss of electrical efficiency in steam cycles," *Applied Thermal Engineering*, vol. 26, no. 16, pp. 2005–2011, 2006.
- [21] G. Li, S. Guo, and X. Zhao, "High temperature chloridization corrosion on the bio-fuel boiler," *Total Corrosion Control*, vol. 23, no. 11, pp. 44–45, 2009.
- [22] S. Li, W. Yan, and L. Fang, "The mechanism of the high temperature chloridization corrosion on the heat transfer surface of utility boiler," *Boiler Manufacturing*, vol. 1999, no. 4, pp. 19–23, 1999.
- [23] H. Song and H. Zhen, "Study on mechanism of high temperature superheater corrosion of biomass fired boiler," *Boiler Manufacturing*, vol. 2010, no. 5, pp. 14–18, 2010.
- [24] A. Zahs, M. Spiegel, and H. Grabke, "The influence of alloying elements on the chlorine-induced high temperature corrosion of Fe-Cr alloys in oxidizing atmospheres," *Materials and Corrosion*, vol. 50, no. 10, pp. 561–578, 1999.
- [25] N. S. Harding and D. C. O'Connor, "Ash deposition impacts in the power industry," *Fuel Processing Technology*, vol. 88, no. 11–12, pp. 1082–1093, 2007.
- [26] R. Wang, Y. Xu, W. Chen et al., "Performance and application of heat resistant steel T/P91 for supercritical boilers," *Modern Metallurgy*, vol. 37, no. 3, pp. 1–3, 2009.
- [27] M. Montgomery, T. Vilhelmsen, and S. A. Jensen, "Potential high temperature corrosion problems due to co-firing of biomass and fossil fuels firing of biomass and fossil fuels," *Materials and Corrosion*, vol. 59, no. 10, pp. 783–793, 2008.
- [28] H. P. Nielsen, F. J. Frandsen, K. Dam-Johansen, and L. L. Baxter, "The implications of chlorine-associated corrosion on the operation of biomass-fired boilers," *Progress in*

- Energy and Combustion Science*, vol. 26, no. 3, pp. 283–298, 2000.
- [29] M. Montgomery and O. H. Larsen, “Field test corrosion experiments in Denmark with biomass fuels. Part 2: co-firing of straw and coal,” *Materials and Corrosion*, vol. 53, no. 3, pp. 185–194, 2002.
- [30] S. C. V. Lith, F. J. Frandsen, M. Montgomery, T. Vilhelmsen, and S. A. Jensen, “Lab-scale investigation of deposit-induced chlorine corrosion of superheater materials under simulated biomass-firing conditions. Part 1: exposure at 560°C,” *Energy & Fuels*, vol. 23, no. 7, pp. 3457–3468, 2009.
- [31] J. Yin and Z. Wu, “Corrosive characters of TP347H steel in superheater’s atmosphere of biomass-burned boiler,” *Thermal Power Generation*, vol. 38, no. 7, pp. 27–31, 2009.
- [32] H. Guo, *Applied Chemical Engineering Kinetics*, Chemical Industry Press, Shanghai, China, 2003.
- [33] N. Ren and J. J. Zhang, “Progress in datum treatment methods of thermal analysis kinetics,” *Progress in Chemistry*, vol. 18, no. 4, pp. 410–416, 2006.
- [34] C. Lu and Y. Wang, *The Theory and Techniques of Coal Combustion*, Seismological Press, Beijing, China, 2001.
- [35] R. Hu, S. Gao, and F. Zhao, *Thermal Analysis Kinetics*, Science Press, Beijing, China, 2008.

Research Article

Characteristics of Corrosion Related to Ash Deposition on Boiler Heating Surface during Cofiring of Coal and Biomass

Yongzheng Wang , Yu Sun, Lei Jiang, Lu Liu, and Yungang Li

School of Energy and Power Engineering, Shandong University, Jinan 250061, China

Correspondence should be addressed to Yongzheng Wang; sddxwyz@163.com

Received 1 November 2019; Accepted 30 December 2019; Published 24 January 2020

Guest Editor: Yanqing Niu

Copyright © 2020 Yongzheng Wang et al. This is an open access article distributed under the Creative Commons Attribution License, which permits unrestricted use, distribution, and reproduction in any medium, provided the original work is properly cited.

In order to investigate the regularity and mechanism of corrosion related to ash deposition on the boiler heating surface during cofiring of coal and biomass, the influence of fuel property, type of metal tubes (heating surface), proportion of blended biomass, and atmosphere in the furnace was studied by using the static corrosion mass gain method with the high-temperature tube furnace system. The results indicated that the effect of biomass property on ash corrosion is greater than that of coal, which was mainly due to high content of alkali metals and chlorine in biomass fuels. The corrosion resistance of metal pipes is $T91 > 12CrMoVG > 20G$. T91 is the most appropriate one, and it can effectively inhibit chlorine corrosion and can be used as the ideal material for the biomass-fired boiler and the biomass and coal cofired boiler. In addition, ash deposition can significantly aggravate the corrosion of metal tubes, and the degree of corrosion tends to become significant with increasing proportion of blended biomass fuels. HCl can aggravate metal corrosion, which can be inhibited by SO_2 .

1. Introduction

Because of the depletion of fossil fuels and their environmental pollution all over the world, the development and utilization of clean renewable energy has gradually drawn more attention, in which biomass energy receives much attention for its characteristics, including easy to burn and low emission of CO_2 , SO_x , NO_x , and other pollutants [1]. However, biomass fuels are generally low in heat value and also difficult to collect, transport, and store. There are problems in utilization of biomass such as high investment costs and low utilization efficiency. These problems can be solved by the biomass and coal co-combustion technology. The volatile content in biomass fuels is generally higher, typically more than 60%. With a small amount of blended biomass fuels, the ignition temperature of coal can be greatly reduced and ignition performance can be improved. Meanwhile, the equipment of cofiring of biomass and coal can be transformed from the original coal-fired equipment, which is more economical [2, 3].

Biomass fuels usually contain more alkali metals, alkali-earth metals, chlorine, and other elements. During biomass combustion, chlorine is released in the form of HCl and Cl_2 , reacting with the metal heating surface, causing severe active oxidation corrosion [4, 5]. Also, it can promote the gasification of the alkali metal elements in the fuel and react with alkali metals to form volatile alkali chloride in the gas phase [6]. The vast majority of gaseous alkali metals are deposited and condensed on the low-temperature metal heating surface. Furthermore, they trap solid particles in flue gas, which leads to serious slagging, fouling, and corrosion. The boiler parameters of an advanced coal-fired power plant are in the supercritical and ultra-supercritical states, and the parameters of a biomass boiler are still limited to high temperature and high pressure, which greatly restrains the improvement of boiler efficiency. High-temperature corrosion has always been a major obstacle to improve the boiler steam parameters. The temperature of a high-temperature superheater in a Danish biomass boiler must always be in control within $580^\circ C$. Main steam parameters of a Chinese biomass boiler

also tend to control within 450°C to avoid high-temperature corrosion, which is a serious disorder in massive scale utilization of the biomass energy [7, 8].

High-temperature chloride corrosion of biomass can be eased by cofiring with coal or additives. A biomass and coal cofiring boiler can reach the same steam parameters as the coal-fired boiler; at the same time, it can ensure the low emission of pollutants [9]. In biomass and coal cofiring boilers, due to the high content of Si and Al in coal, most of the alkali metals exist in the form of aluminosilicate with lower reactivity and higher melting point, thus decreasing the content of chlorine and viscosity of the ash deposition, which means the corrosion related to ash deposition is slowed down [10]. Due to the high content of sulfur in coal, the SO₂ content in the atmosphere increases, which leads to sulfur oxide corrosion. Meanwhile, the composition of the deposition becomes complicated. If the content of alkali in the fuel is high, sulfur oxide will conduct complex reactions with the alkali to form low-melting point compound sulfate, focal sulfate, and other complex low-temperature comelts, which lead to local liquid phase appearance. The protective oxide film on the surface of the tube wall is damaged, thus resulting in more corrosion [11].

Due to the reaction of multiphase gases, liquids, and solids, the combustion mechanism of biomass cofiring with coal is more complicated. The high content of chlorine in the biomass and sulfur in the coal will cause serious ash deposition and corrosion problems on the heat exchange surface of the boiler, which reduce the heat transfer efficiency of the heating surface and even harm the boiler operation safety. It has become one of the most serious problems restricting the application of biomass combustion. Therefore, this research focuses on the corrosion related to ash deposition during biomass and coal cofiring. By simulating the cofiring environment of biomass and coal, the regularity and mechanism of corrosion related to ash deposition during cofiring of biomass and coal under different fuel properties, type of metal tubes (heating surface), proportion of blended biomass, and atmosphere in the furnace were explored. It provides a theoretical basis for the effective utilization of biomass fuels and the optimization of boiler operating parameters.

2. Materials and Methods

2.1. Experimental Samples. Common crops in Shandong province are used as biomass fuels: straw, corn stalk, and cotton stalk. Lean coal and bitumite are used as blended coal. Proximate and ultimate analysis of fuels is shown in Table 1. Table 2 shows the elemental analysis of ashes. The data in the tables are the weight percentage. Before the experiment, fuels are separately ground to 20 mesh. and dried in the drying oven at a constant temperature of 100°C and then stored under seal. Experimental ash samples are fired according to the standard material (coal ash) using a mixture of biomass fuels and coal by weight ratio [12]. The proportion of blended biomass is 0%, 20%, 50%, 70%, and 100%. The metal samples 12CrMoVG, 20G, and T91 are taken from power plants in Shandong. Through wire

cutting and other metal processing methods, the samples are made into 20 mm × 3 mm × 3 mm standard size. The metal samples are polished before experiment using 200, 500, and 1000 grit sand paper sequentially in order to remove the last traces and get a unified standard sample surface. Their size is measured by a vernier caliper to calculate the surface area, followed by washing in acetone to remove the fouling on the metal surface. After drying with a filter paper, they are placed in the drying oven at a constant temperature 100°C for 20 min. The chemical composition of the metal materials is shown in Table 3.

2.2. Experimental System. The experimental system is shown in Figure 1. Due to the higher content of chlorine in biomass fuels, it mainly exists in the form of HCl in the combustion process, and sulfur in the coal is almost completely oxidized to SO₂. Therefore, this experiment mainly investigates corrosion characteristics of ash deposits under the coexistence atmosphere of sulfur chlorine in the gas phase. In the mixed gas, N₂ is the balance gas. The concentration of O₂ is kept at 6%, while CO₂ is maintained at 12%. The content of HCl and SO₂ is adjusted through a flow meter. They are mixed well in the gas mixing device in order to simulate the flue gas atmosphere in the boiler superheater [13]. The high-temperature reaction part adopts a horizontal tube furnace electric heating system. The temperature is under precise control by using an intelligent PDI temperature controller and solid state relay (SSR). The temperature difference between the constant temperature section in the reaction zone is less than 5°C. Exhaust gas treatment adopts NaOH solution to absorb excess SO₂ and HCl to avoid polluting the environment.

2.3. Experimental Procedure. The metal samples are coated with the synthetic deposits: first, the deposited sample are prepared in a suspension liquid with anhydrous ethanol, smeared evenly it on the surface of metal samples, and the amount of plaster is controlled at 15 mg/cm². Then, the samples are placed into the oven at a constant temperature of 100°C for 20 min to remove the residual ethanol solution. The metal samples covered with synthetic deposits are placed into the constant temperature section of the horizontal tube furnace to carry out the corrosion experiment. The concentration of HCl and SO₂ is changed to investigate the effect of different atmospheres on corrosion. The total air flow is controlled at 120 mL/min, and the temperature is controlled at 600°C. Preliminary experiments show that the corrosion weight gain of samples increases rapidly in the early stage (within 15–20h), but tends to be stable in the later stage. [9]. The whole process presents the regularity of a similar parabola curve. For the convenience of quantitative analysis, the parabola fitting for the corroded weight curve is carried out. The equation is as follows:

$$\Delta G = k\tau^{1/2} + C, \quad (1)$$

where k is a rate constant of the parabolic curve, characterizing the reaction rate of corrosion, and C is the

TABLE 1: Proximate and ultimate analysis of fuels (air-dried) (%).

Fuel	Sample number	Proximate analysis			Ultimate analysis						
		M _{ad}	A _{ad}	V _{ad}	FC _{ad}	C _{ad}	O _{ad}	H _{ad}	N _{ad}	S _{ad}	Cl _{ad}
Straw	B1	8.22	7.05	65.62	19.11	40.87	37.22	5.71	0.78	0.15	0.31
Corn stalk	B2	7.96	8.32	65.46	18.26	40.51	36.58	5.83	0.67	0.13	0.065
Cotton stalk	B3	5.67	4.23	69.74	21.38	44.26	38.94	6.32	0.50	0.08	0.074
Bitumite	C1	4.35	20.69	35.18	39.79	61.02	7.54	4.01	1.18	1.21	–
Lean coal	C2	1.30	34.94	10.15	53.62	55.27	3.27	2.96	0.61	1.65	–

TABLE 2: Major ash constituents in fuels (%).

Fuel	K	Na	Ca	Mg	Al	Si	Fe
Straw	1.96	0.78	0.84	0.072	1.69	1.83	0.17
Corn stalk	1.88	0.64	1.20	0.069	3.16	2.24	0.16
Cotton stalk	0.86	0.35	0.84	—	1.65	0.51	0.25
Bitumite	0.081	0.11	1.05	0.50	15.87	21.71	3.99
Lean coal	0.098	0.16	1.61	0.86	15.38	24.36	5.66

integration constant, indicating the deviation of the parabola curve on the initial corrosion reaction caused by kinds of factors. The following experimental cycle is selected: 30 h, weighed every 6 h, in order to obtain a corrosion mass gain curve. For analyzing the cross section of the corrosion layer, the metal sample is first fixed with the epoxy resin and cured at normal temperature for 24 hours. It is cut transversely with a small cutter, and then the cross section is polished with a polisher. The SEM is used to observe the morphological characteristics of the corrosion layer on the cross section of the metal sample; the energy dispersive spectrometer (EDS) is used to detect the elemental composition of several regions in the corrosion layer.

3. Results and Discussion

3.1. Effect of Fuel Property on Deposit Corrosion. Deposit corrosion properties are quite different because of the difference in characteristics of biomass fuels. In this paper, common biomass fuels (wheat straw, corn stalk and cotton stalk) and different types of coals (lean coal and bituminous coal) are blended to combust in the weight ratio of 1:1 to study the effect on deposit corrosion caused by different fuel characteristics under the coexistence atmosphere of sulfur and chlorine. Figure 2 shows the fitting curve of the increased weight for 12CrMoVG metal samples under the coexistence atmosphere of sulfur and chlorine using different synthetic deposits at 600°C. The fitted correlations are shown in Table 4. R^2 in Table 4 represents a coefficient of determination or a goodness of fit, which refers to the degree to which the regression line fits the observed value. The value of R^2 in the table is close to 1, indicating that the regression line fits the observations well.

It can be seen from Figure 2 that the weight of metal samples increases with time. It increases faster in the initial stage and gradually decreases in the later stage. The corrosion weight curve is approximately parabola. This is because, in the initial stage, the oxidative corrosion reaction rate is high and a thin oxide layer is quickly formed on the metal surface. As the corrosion reaction continues, the oxide

layer gradually becomes thicker, preventing the metal from direct contact with the reactants and slowing down the corrosion reaction. The corrosion weight of the metal samples increases with time, and its variation curve is parabola: $\Delta G = k\tau^{1/2}$. The corrosion is intensified when the samples are covered by deposits. And it shows significant difference in the degree of corrosion with the changes in fuel properties. The corrosion performance of biomass fuels from strong to weak is as follows: wheat straw, corn stalk, and cotton stalk. The corrosion of lean coal is more intense than bituminous coal when the same biomass fuel blends with different coals.

From analysis of rate constant k of the parabolic curve in Table 4, it can be seen that the effect of biomass fuels is significantly greater than the effect of coal. The component of deposits varies widely as the fuel characteristics, combustion conditions, and other factors. Lith et al. [13] suggest that the corrosion in the process of cofiring of biomass and coal is mainly based on the alkali metals existed in deposits. They react directly with the wall metal of the heat exchanger, causing the corrosion of the metal matrix. Also, they generate low-temperature eutectic with other compounds. Sometimes, it can even cause serious electrochemical corrosion. So, the damage of deposit corrosion is larger.

Ash deposition mainly exacerbates corrosion through two effects. First, the corrosive salts such as KCl and NaCl directly chemically react with the metal, resulting in intensified active oxidative corrosion at the heating surface; second, the formation of complex low-temperature eutectic melts destroys the oxide film on the metal surface and causes electrochemical corrosion. From the content of major ash constituents in Table 2, it can be seen that the content of alkali metals and chlorine is the highest in wheat straw. The alkali metal content in corn stalk is slightly lower than that in straw. However, the chlorine content is significantly lower than that of wheat straw. The cotton stalk and corn stalk have a similar chlorine content. However, it is lowest for alkali metal content in cotton stalk, even less than half of the two former. So, it is visible that the component of alkali metals and chloride in biomass fuels are the main cause of ash deposit corrosion. The component of alkali metals and chlorine in biomass fuels is obviously higher than that in the coal. Also, there is a large difference. So the effect of the difference between biomass fuels on corrosion is larger than the effect of the coal.

During cofiring of coal and biomass, due to the fixing effect of Al and Si in the ash on the alkali metals, most of the chlorine released in the form of gas phase HCl or Cl₂, the

TABLE 3: Elemental composition of the heating surface metal (%).

Steel	C	S	P	Si	Mn	Cr	Mo	V	Cu	Ni
12CrMoVG	0.08~0.15	≤0.03	≤0.03	0.17~0.37	0.40~0.70	0.90~1.20	0.25~0.35	0.15~0.30	≤0.20	≤0.25
20G	0.17~0.24	≤0.03	≤0.03	0.17~0.37	0.35~0.65	–	–	–	–	–
T91	0.08~0.12	≤0.02	≤0.02	0.02~0.50	0.30~0.60	8.00~9.50	0.85~1.05	0.18~0.25	–	≤0.40

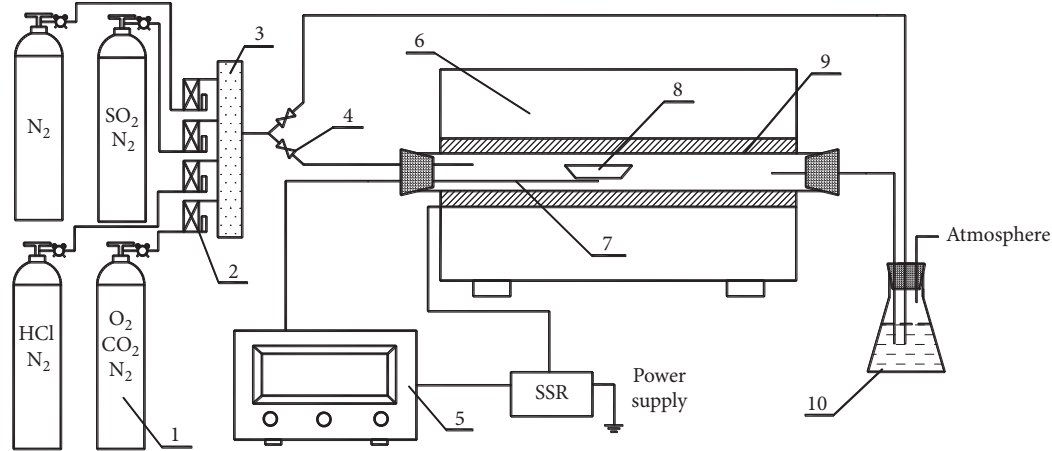


FIGURE 1: The schematic diagram of the experimental system. 1, gas cylinder; 2, gas flowmeter; 3, mixing equipment; 4, gas valve; 5, PID temperature controller; 6, tube furnace; 7, thermocouple; 8, porcelain boat; 9, corundum tube; 10, absorber bottle.

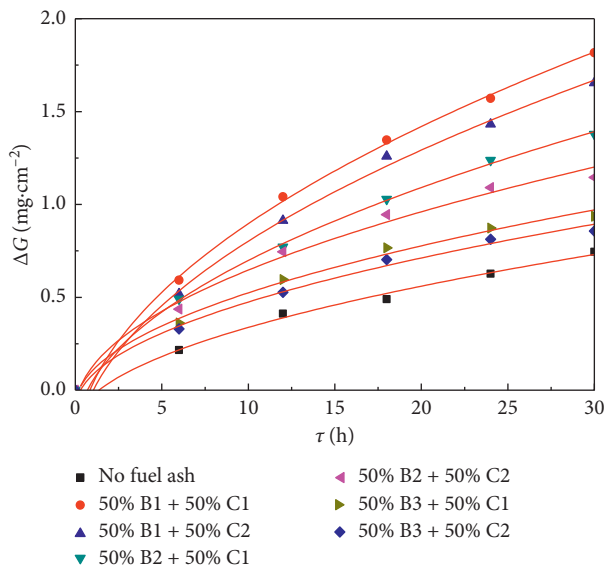
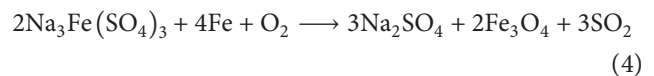
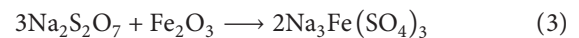
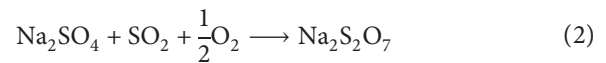


FIGURE 2: Curves of corrosion mass gain of different metal samples coated with different fuel ash.

alkali metal was mostly in the form of silicate, aluminosilicate, and sulfate, and only a very small amount of Cl remained in the ash, and the chemical activity of the ash was relatively stable. Generally, Ca and Mg in fuels do not exist in the form of chlorides during combustion, but they still affect the content of active corrosion components in the ash by complex reactions. When the content of Ca or Mg in fuels is high, most of the Al will react with it to form compounds such as $MgAl_2O_4$, $CaAl_2O_4$, etc., so that the fixation of Al to the alkali metal is weakened, and the content of alkali metal chloride in the ash is correspondingly increased.

There is a high content of ash in lean coal and bitumite. The composition of the oxide in ash is based on SiO_2 and Al_2O_3 [14] and is mostly considered to be inert. Through the study, Li et al. [15] find that the oxide from ash can be divided into basic oxide and acidic oxide, where the basic oxide has lower ionic energy as important composition of low-melting eutectic mostly. Alkali metals and alkali-earth metals content such as Na, K, Ca, Mg, and others in the ash of lean coals is higher than that of bitumite coals. The alkaline component in ash generated by cofiring of the same biomass fuels and lean coals is certainly higher than bitumite coals. So, it results in increase in the content of low-melting point eutectic in deposits, which can accelerate the corrosion. Meanwhile, sulfur content of lean coal is high. It can be also easy to cause the molten salt corrosion of alkali metal sulfate in deposits [11]:



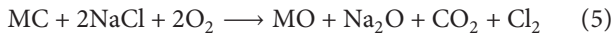
3.2. *Effect of Pipe Components on Deposit Corrosion.* The deposit corrosion of the superheater varies while the pipe components are different. Under simulated condition, the contents of HCl and SO_2 in the flue gas are both 500 $\mu L/L$, and blended percent of straw and lean coal is, respectively, 50%. The fitting curve and fitting correlation of the corrosion weight gains of the tube metal materials including 12CrMoVG, 20G and T91 are shown in Figure 3. It can be

TABLE 4: Fitting correlations of corrosion mass gain of different metal samples coated with different fuel ash.

Fuels	Fitting correlations ($\Delta G = k\tau^{1/2} + C$)	k	R^2
No fuel ash	$\Delta G = 0.1695\tau^{1/2} - 0.19802$	0.1695	0.98618
50%B1 + 50%C1	$\Delta G = 0.39923\tau^{1/2} - 0.36598$	0.3992	0.99751
50%B1 + 50%C2	$\Delta G = 0.37439\tau^{1/2} - 0.38188$	0.3744	0.99388
50%B2 + 50%C1	$\Delta G = 0.29955\tau^{1/2} - 0.24879$	0.2996	0.99752
50%B2 + 50%C2	$\Delta G = 0.23953\tau^{1/2} - 0.11091$	0.2395	0.96897
50%B3 + 50%C1	$\Delta G = 0.19297\tau^{1/2} - 0.08606$	0.1930	0.97963
50%B3 + 50%C2	$\Delta G = 0.18106\tau^{1/2} - 0.09793$	0.1811	0.97704

seen that the corrosion resistance of three kinds of metal materials from strong to weak is T91, 12CrMoVG, and 20G. The corrosion resistance of T91 is much higher than that of the latter two. From the beginning of the reaction to about 10 h, the increase in corrosion mass gain appears to be not obvious. The corrosion resistance of 12CrMoVG is slightly better than that of 20G. Nevertheless, from the corrosion reaction rate k , it can be seen that the difference between the two is nonobvious.

In the initial corrosion reactions, each of elements in metals participates in the corrosion reaction. Cr can react preferentially with oxygen in the atmosphere as a crucial element in alloy, form the oxide film with dense and adhesive properties, and produce the passivation phenomenon, so that the corrosion resistance of metals can be enhanced. However, when the temperature rises, the diffusion velocity of C in the interior of the metal grain is greater than that of Cr. The formation and precipitation of carbides make the chrome poor locally near the grain boundary. NaCl from deposits is easy to react with metal carbide generated Cl_2 , which can increase the susceptibility to intergranular corrosion and cause serious intergranular corrosion. The reaction equation is as follows (M represents the metal of the heat transfer surface) [16]:



The sectional micromorphology of 20G after the deposit corrosion experiment is shown in Figure 4. The corrosion resistance performance of 20G is the worst as plain carbon steel without any addition of other alloying elements. The surface of the corrosion layer is loose and porous, and there is a large gap in the surface of the metal substrate. The adhesion of the corrosion layer is poor and cannot effectively prevent the corrosive medium HCl/SO_2 in the gas phase from further erosion of the metal. Because of the major Cl element in the biomass fuel, the content of gaseous HCl and Cl^- of deposits increases while cofiring of biomass and coal. As very small atom radius, Cl atom tends to agglomerate to the location of the defects on the metal heating surface, even directly pass through the oxide film on metal surface, and lead to pitting corrosion. When deposits contain alkali metal chlorides, they will directly react with the metal oxide film and continue to cause corrosion. The reaction equations are as follows:

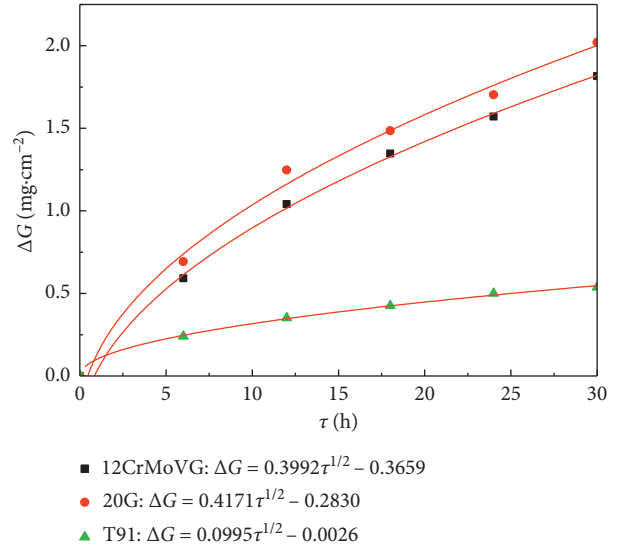
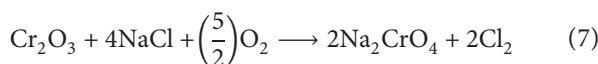
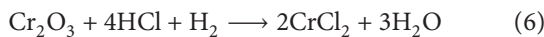


FIGURE 3: Curves and fitting correlations of corrosion mass gain of metal samples coated with ash.

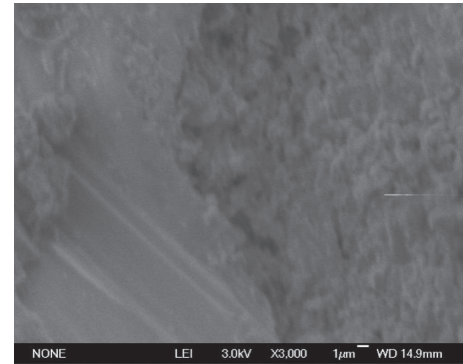


FIGURE 4: Sectional topography of 20G after deposition corrosion.

12CrMoVG is superior to use as stainless steel in terms of corrosion resistance than 20G. But it is not very perfect in corrosion resistance to use for biomass-fired boiler due to the high Cl content in biomass fuel. Wang et al. [17] found that adding Mo and Ni elements into alloy can improve the microeutectic structure of metals, suppress the intergranular corrosion and pitting corrosion effectively, and improve the adhesion of protective oxide film, thereby improving the corrosion resistance of metals. When the Mo content is more than 3% in steel, it can significantly inhibit the penetration of Cl into metallic matrix.

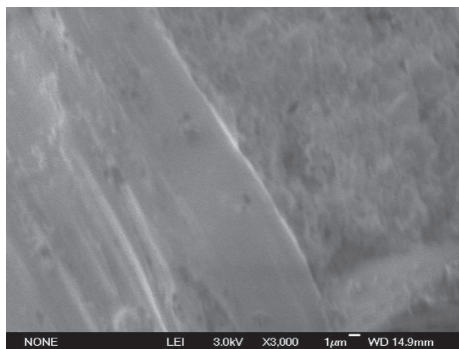


FIGURE 5: Sectional topography of T91 after deposition corrosion.

The sectional micromorphology of T91 is shown in Figure 5. For T91, Cr content is more than that of 12CrMoVG by an order of magnitude. The content of trace elements such as Mo and Ni in T91 is also higher than that in 12CrMoVG. A dense protective film is formed between the metal matrix and the deposit corrosion layer. The corrosion film is thin and has a good combination with the metal matrix. It can isolate the metal matrix from the surrounding corrosive environment. So, the corrosion resistance is the strongest. In addition, it can be used as the ideal material for the cofiring boiler of biomass and coal.

3.3. Effect of Proportion of Blended Fuel on Deposit Corrosion.

Figure 6 shows the fitting curve of the increased weight for 12CrMoVG under the coexistence atmosphere of sulfur and chlorine, using synthetic deposits with different blending ratios of wheat straw. The fitted correlations are shown in Table 5. The relation curve between the coefficient indicating corrosion rate k and the proportion of blended biomass λ is shown in Figure 7. From Figure 6, final corrosion weight of metal samples increases with the proportion of blended biomass. However, this increase does not show regularity of weighted average according to the proportion of blended biomass and coal.

When the proportion of blended wheat straw is more than 20%, the ash deposit shows the obvious accelerated corrosion phenomenon on the metal samples. From 50% to 70%, it changes little for the increased corrosion weight. When the proportion of blended biomass is more than 70%, the value of k increases obviously. When the proportion of blended wheat straw is 100%, the corrosion degree is most serious. Compared with the sample with no ash added, the weight of the metal sample with ash added increases slightly, but not significantly, while the ash is pure lean coal ash. Therefore, each composition of the ash generated by combustion of pure coal works little for the metal corrosion. In addition, the addition of lean coal in the combustion effectively inhibits the corrosion caused by wheat straw.

As shown in Table 6, from the analysis of EDS elements of different gray samples, it was found that there were significant differences in the content of the corrosive key elements in ash when different proportion of blended biomass was burning. When the proportion of blended wheat straw is 100%, the content of alkali metals and chlorine in deposits is high. In addition, it is mainly in the

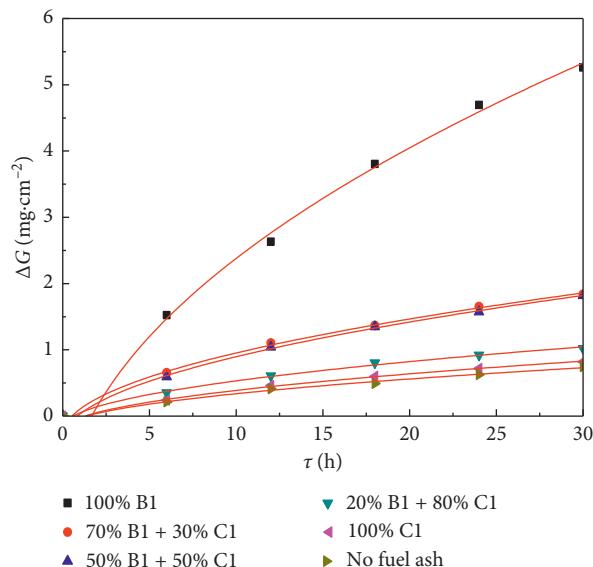


FIGURE 6: Curves of corrosion mass gain of metal samples coated with ash under different proportion of straw biomass blended to coal.

form of chlorides and other substances with a strong chemical reaction activity. The corrosion is the most severe: on the one hand, it can directly cause severe active oxidation corrosion; on the other hand, as the reaction is prolonged, alkali metal chloride such as KCl can react with the corrosion products FeCl_2 and CrCl_2 and produce the eutectic with a melting point of 355°C and 470°C , respectively. Also, the melting point of the eutectic formed with FeCl_3 is even as low as $202\text{--}220^\circ\text{C}$ [18], thereby enabling ash deposition to appear liquid phase and resulting in more severe corrosion. The deposit corrosion activity declines significantly with the adding of the lean coal. The Cl content has decreased obviously while blending 50% lean coal into wheat straw. There is a high content of sulfur in lean coal. While cofiring of wheat straw and lean coal, the partial pressure of SO_2 increases in the atmosphere, and the activity of alkali metal chloride decreases because of the sulfate reaction in deposits [19]. The corrosion was obviously reduced. Meanwhile, Si and Al elements in the coal can react with alkali metal chloride and form aluminosilicate [20], so that the corrosion of deposits has a further reduction.

When the proportion of blended wheat straw reduced from 70% to 50%, the deposition corrosion degree decreased slightly, but not obvious. With the increase in lean coal blending ratio, alkali metal compounds will form low-melting eutectics with SiO_2 , aluminosilicate, sulfate, etc. For example, the melting temperature of $\text{K}_2\text{O}\cdot 4\text{SiO}_4$ is 764°C , and $\text{KCl}\text{--}\text{K}_2\text{SO}_4\text{--}\text{Fe}_x\text{O}_y$ will melt at 557°C . The appearance of some trace elements such as Pb, Zn, and Ni will also lead to the increase of low-temperature eutectic materials in the ash, and the local liquid phase will appear and lead to serious electrochemical corrosion [19, 21]. With increasing proportion of blended wheat, the corrosion rate has an unobvious change when the proportion of blended wheat straw is lower than 20%. Montgomery et al. [22] find

TABLE 5: Fitting correlations of corrosion mass gain under different proportion of straw biomass blended to coal for metal samples coated with ash.

Proportion of straw biomass blended to coal (%)	Fitting correlations ($\Delta G = k\tau^{1/2} + C$)	k	R^2
100	$\Delta G = 1.2737\tau^{1/2} - 1.6477$	1.2737	0.9945
70	$\Delta G = 0.3913\tau^{1/2} - 0.2843$	0.3913	0.9967
50	$\Delta G = 0.3992\tau^{1/2} - 0.3659$	0.3992	0.9975
20	$\Delta G = 0.2221\tau^{1/2} - 0.1707$	0.2221	0.9894
0	$\Delta G = 0.1906\tau^{1/2} - 0.2145$	0.1906	0.9969
No fuel ash	$\Delta G = 0.1695\tau^{1/2} - 0.1980$	0.1695	0.9862

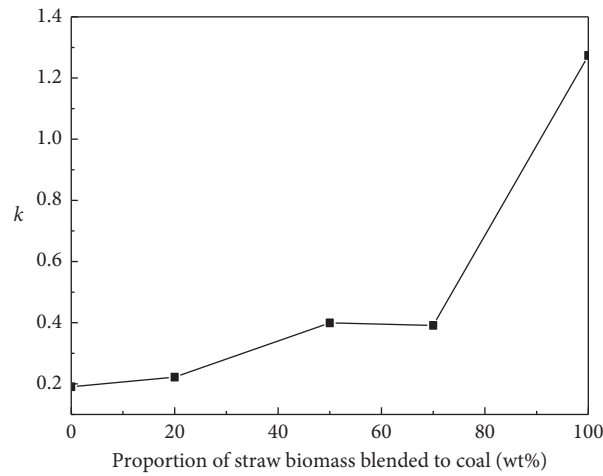
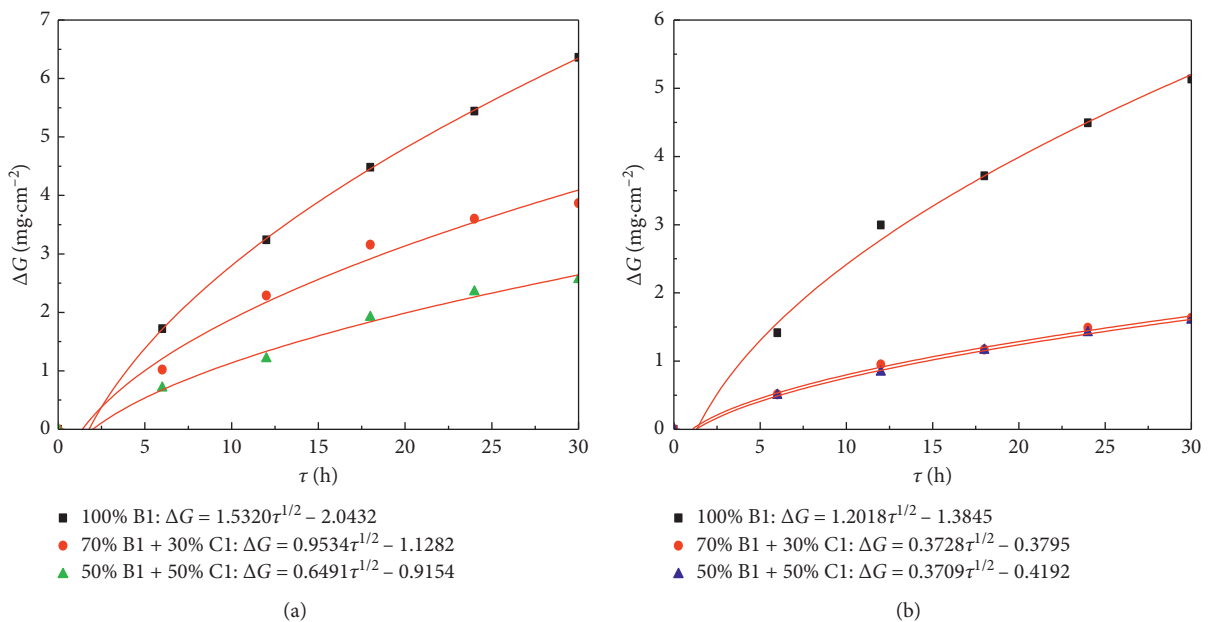


FIGURE 7: Curves of coefficient indicating corrosion rate versus proportion of straw biomass blended to coal.

TABLE 6: Content of elements in different ash.

Element	Na	Al	Si	S	Cl	K
Straw ash	0.433	7.602	10.855	2.54	13.521	21.529
Lean coal	0.612	28.169	33.481	0.837	0.412	0.262
50% straw and 50% lean coal ash	0.498	17.635	25.282	3.911	0.649	7.076

FIGURE 8: Curves and fitting correlations of corrosion weight gain of the metal samples coated with ash under different atmospheres. (a) HCl: 500 $\mu\text{L/L}$, not containing SO_2 . (b) SO_2 : 500 $\mu\text{L/L}$, not containing HCl.

that all KCl transform into noncorrosive alkali aluminosilicate while cofiring blended with 20% biomass. Then, sulfate corrosion plays a main role, but the corrosion is weakened dramatically. It is also consistent with the experimental results of this paper.

3.4. Effect of Atmosphere in Furnace on Deposit Corrosion.

The effect of the change of the atmosphere in the furnace on deposit corrosion is shown in Figure 8. The increased weight curves and the fitting correlations when the blended proportion of wheat straw is 50%, 70%, and 100% under the simulating flue atmosphere containing 500 $\mu\text{L/L}$ HCl only are shown in Figure 8(a) while the simulating flue only contains 500 $\mu\text{L/L}$ SO_2 in Figure 8(b). With the increase of wheat straw ratio, it tends to be severe for the corrosion of samples when the flue gas only contains HCl. Comparing with the situation under the coexistence atmosphere of sulfur and chlorine (Figure 6), it can be found that the degree of corrosion is intensified significantly when the proportion of blended wheat straw increases from 50% to 70% under the atmosphere of HCl merely. Once the SO_2 is mixed, the corrosion will be inhibited obviously. Also, the increased weight of the metal samples covered with combustion ash by 70% wheat straw and lean coal is even less than 1/2 of that under the HCl atmosphere. The corrosion rules of samples under the atmosphere containing only 500 $\mu\text{L/L}$ SO_2 are similar with the rules under the coexistence atmosphere of sulfur and chlorine. There is a further reduction in the increased corrosion weight. However, the reduction is not obvious, and the corrosion rate does not appear to be significant. So, when the SO_2 content in the atmosphere is certain, the corrosion effect of HCl on samples is obviously weakened.

The analysis of the above test results shows that the corrosion of the metal samples caused by the change of the atmosphere is affected by the characteristics of the deposits in the metal wall. The corrosion degree of the samples under different atmospheres tends to be severe with the increase of the blending ratio of biomass. When the simulated flue gas contains only HCl, both KCl from the deposits and HCl from the gas can cause metal corrosion. The corrosion of the metal by SO_2 is mainly reflected in the early rapid corrosion stage. As the reaction proceeds, SO_2 reacts with the alkali metal salts in the ash to form products with lower activity, such as sulfate, chromate, and oxide, which can evenly cover the metal surface, and a similar passivation state appears between the metal and the gas phase interface, which inhibits further corrosion.

However, under different atmospheres, it can be seen that the corrosion of the metal samples covered with wheat straw burning ash is still very serious and is not under the control obviously with the adding of SO_2 . Broström et al. found that sulfation of alkali chlorides is mainly based on SO_3 content in the atmosphere [23, 24]. When the KCl content in deposits is high enough, the inhibitory effect of SO_2 on corrosion is weakened, and the corrosion is mainly based on KCl from deposits. When SO_2 forms a metal protective layer on the metal surface, it will undergo a sulfation reaction with KCl in the ash deposit, which will increase the partial pressure of HCl at the wall, and the active

oxidative corrosion reaction of chlorine will intensify. KCl will also destroy the protective layer of the metal surface and intensifies the corrosion reaction.

4. Conclusions

- (1) During cofiring of different biomass fuels with coals, characteristics of corrosion show obvious differences. Effect of corrosion from strong to weak is as follows: wheat straw, corn stalk, and cotton stalk, because the content of alkali metals and chlorine in wheat straw is significantly higher. During cofiring of the same biomass fuels with different coals, the corrosiveness of lean coal is stronger than that of bituminous coal. The content of alkaline metal oxides and sulfides in coal ash is relatively high, and it will also cause ash melt corrosion.
- (2) The corrosion resistance on three kinds of common boiler metal materials is as follows: T91, 12CrMoVG, and 20G. This is because T91 contains more Cr, which can form a dense oxide film to slow down corrosion. The content of Mo and Ni is more than that in the other two metals, which improves the microeutectic structure of the metal. The corrosion resistance of 12CrMoVG is not much better than that of 20G. T91 can effectively inhibit the rate of corrosion, and it can be used as the ideal metal materials of the heat transfer surface in biomass and coal cofired boilers.
- (3) The degree of ash deposit corrosion enhances with the increase in the proportion of blended wheat straw. Under the atmosphere with coexistence of sulfur and chlorine, when the proportion of blended wheat straw is greater than 70%, the corrosion rate decreases significantly with the addition of coal. When the proportion decreases from 70% to 50%, the metal corrosion weight reduces slightly. When the proportion is as low as 20%, it can be regarded that alkali metal chlorides in deposits are all converted into aluminosilicate and sulfate, and the corrosion rate shows no obvious change with the increase in the proportion of blended biomass.
- (4) The metal corrosion caused with the atmosphere change is influenced by the ash property. HCl in atmosphere can aggravate the metal corrosion. The presence of SO_2 significantly inhibits HCl corrosion through the sulfate reaction. Especially when the proportion of blended wheat straw is below 70%, the inhibitory effect of SO_2 on deposit corrosion is more significant. When the proportion of blended wheat straw is 100%, the presence of SO_2 does not significantly inhibit corrosion due to the high KCl content in deposits.

Data Availability

The data used to support the findings of this study are available from the corresponding author upon request.

Conflicts of Interest

The authors declare that there are no conflicts of interest regarding the publication of this paper.

Acknowledgments

This work was supported by Shandong Provincial Natural Science Foundation, China (ZR2017MEE009).

References

- [1] H. Raclavska, D. Juchelkova, V. Roubicek, and D. Matysek, "Energy utilisation of biowaste-sunflower-seed hulls for co-firing with coal," *Fuel Processing Technology*, vol. 92, no. 1, pp. 13–20, 2011.
- [2] Z. Ma, S. Wu, and Y. Bai, "Technical analysis on cofiring of coal and biomass," *Power System Engineering*, vol. 25, no. 6, pp. 1–4, 2009.
- [3] T. Wang, T. Kuang, Q. Fang et al., "Experimental study of coal/biomass mixture combustion in O₂/CO₂ atmosphere," *Thermal Power Generation*, vol. 46, no. 4, pp. 16–21, 2017.
- [4] Y. Wang, K. Zhang, L. Jiang et al., "Research on the co-corrosion characteristics of sulfur chloride in the combustion process of biomass mixed coal," *Journal of University Chemical Engineering*, vol. 6, pp. 1422–1429, 2015.
- [5] H. J. Grabke, E. Reese, and M. Spiegel, "The effects of chlorides, hydrogen chloride, and sulfur dioxide in the oxidation of steels below deposits," *Corrosion Science*, vol. 37, no. 7, pp. 1023–1043, 1995.
- [6] P. A. Jensen, F. J. Frandsen, K. Dam-Johansen, and B. Sander, "Experimental investigation of the transformation and release to gas phase of potassium and chlorine during straw pyrolysis," *Energy & Fuels*, vol. 14, no. 6, pp. 1280–1285, 2000.
- [7] Z. Wang, Y. Cao, and Z. Zhang, "Analysis and countermeasures of corrosion of high temperature superheater of biomass boiler," *Zhejiang Power*, vol. 35, no. 9, pp. 53–56, 2016.
- [8] W. Wei, F. Huang, C. Yu et al., "Primary investigation of high-temperature corrosion problems in biomass combustion equipment," *Energy Engineering*, vol. 2, pp. 23–28, 2011.
- [9] Y. Wang, L. Jiang, M. Yue et al., "Study on sulfur-chlorine synergistic corrosion in biomass and coal co-firing," *Proceedings of the CSEE*, vol. 29, no. 26, pp. 118–124, 2009.
- [10] A. L. Robinson, H. Junker, and L. L. Baxter, "Pilot-scale investigation of the influence of coal–biomass cofiring on ash deposition," *Energy & Fuels*, vol. 16, no. 2, pp. 343–355, 2002.
- [11] Y. Zhang, L. Shi, X. Li et al., "Alkali sulfate deposits induced hot corrosion of iron based alloys at intermediate temperatures," *Corrosion Science and Protection Technology*, vol. 4, no. 4, pp. 250–257, 1992.
- [12] X. Dong, R. Li, Z. Liu et al., "Investigation on the ash characteristic during co-firing of coal and biomass," *Proceedings of the CSEE*, vol. 29, no. 26, pp. 118–124, 2009.
- [13] S. C. V. Lith, F. J. Frandsen, M. Montgomery, T. Vilhelmsen, and S. A. Jensen, "Lab-scale investigation of deposit-induced chlorine corrosion of superheater materials under simulated biomass-firing conditions. Part 1: exposure at 560°C," *Energy & Fuels*, vol. 23, no. 7, pp. 3457–3468, 2009.
- [14] X. Li, Y. Wang, M. Yue et al., "Study on corrosion and influencing factors during co-combustion of coal and biomass," *Power Station System Engineering*, vol. 27, no. 6, pp. 13–15, 2011.
- [15] R. Li, Y. Nie, A. Li et al., "Study on physical chemical characteristics of fly ash from municipal solid waste incinerator," *Journal of Fuel Chemistry and Technology*, vol. 32, no. 2, pp. 175–179, 2004.
- [16] M. Mobin and A. U. Malik, "Studies on the interactions of transition metal carbides and sodium chloride in the temperature range 900–1200 K in oxygen," *Journal of Alloys and Compounds*, vol. 186, no. 1, pp. 1–14, 1992.
- [17] J. Wang, G. Zhang, and S. Li, "Investigation of microstructure and corrosive behavior of NiAl-31Cr-3Mo alloy at high temperature," *Mining and Metallurgical Engineering*, vol. 30, no. 6, pp. 93–96, 2012.
- [18] Y. Shinata, "Accelerated oxidation rate of chromium induced by sodium chloride," *Oxidation of Metals*, vol. 27, no. 5–6, pp. 315–332, 1987.
- [19] H. P. Nielsen, F. J. Frandsen, and K. Dam-Johansen, "Lab-scale investigations of high-temperature corrosion phenomena in straw-fired boilers," *Energy & Fuels*, vol. 13, no. 6, pp. 1114–1121, 1999.
- [20] M. Montgomery and O. H. Larsen, "Field test corrosion experiments in Denmark with biomass fuels. Part 2: co-firing of straw and coal," *Materials and Corrosion*, vol. 53, no. 3, pp. 185–194, 2002.
- [21] L. Jiang, Y. Wang, T. Yu et al., "Study on synergy corrosion mechanism of sulfur-chlorine during biomass and coal co-firing," *Power System Engineering*, vol. 29, no. 3, pp. 1–4, 2013.
- [22] M. Montgomery, T. Vilhelmsen, and S. A. Jensen, "Potential high temperature corrosion problems due to co-firing of biomass and fossil fuels," *Materials and Corrosion*, vol. 59, no. 10, pp. 783–793, 2008.
- [23] M. Broström, H. Kassman, A. Helgesson et al., "Sulfation of corrosive alkali chlorides by ammonium sulfate in a biomass fired CFB boiler," *Fuel Processing Technology*, vol. 88, no. 11–12, pp. 1171–1177, 2007.
- [24] K. Lisa, Y. Lu, and K. Salmenoja, "Sulfation of potassium chloride at combustion conditions," *Energy & Fuels*, vol. 13, no. 6, pp. 1184–1190, 1999.

Review Article

A Review of Urea Pyrolysis to Produce NH₃ Used for NO_x Removal

Denghui Wang , Ning Dong , Yanqing Niu , and Shien Hui 

State Key Laboratory of Multiphase Flow in Power Engineering, School of Energy and Power Engineering, Xi'an Jiaotong University, Xi'an 710049, China

Correspondence should be addressed to Denghui Wang; denghuiwang@163.com and Yanqing Niu; yqniu85@mail.xjtu.edu.cn

Received 6 August 2019; Revised 11 November 2019; Accepted 18 November 2019; Published 9 December 2019

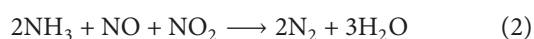
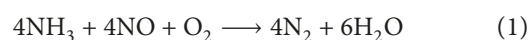
Academic Editor: Leonardo Palmisano

Copyright © 2019 Denghui Wang et al. This is an open access article distributed under the Creative Commons Attribution License, which permits unrestricted use, distribution, and reproduction in any medium, provided the original work is properly cited.

Urea pyrolysis, from which the denitration reactant ammonia is produced, plays an important role in the urea-based NO_x removal process. Research into urea pyrolysis is mostly focused on three parts: urea pyrolysis pathway, catalytic hydrolysis of HNCO, and catalytic pyrolysis of aqueous urea solution. In this paper, detailed overview on research progress of urea pyrolysis was conducted. From the review, it could be concluded that although much research has been carried out, concentration was mainly in analysis of urea pyrolysis products and exploration of catalysts used to improve ammonia yields. Little work has been done on mechanism study and development of a kinetic model with high accuracy, which are still in great need nowadays.

1. Introduction

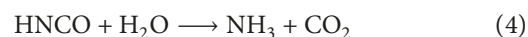
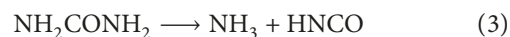
With the sustained combustion of fossil fuels in boilers and diesel vehicles, massive harmful emissions of nitrogen oxides (NO_x), mainly including NO and NO₂, have been discharged into the atmosphere [1–5]. In recent decades, widespread serious environmental problems, such as urban smog, acid rain, and ozone depletion, have been caused from it [5–7]. To reduce the severe NO_x emission, a number of techniques have been developed and utilized up to now, and the selective catalytic reduction (SCR) and the selective non-catalytic reduction (SNCR) stand out on account of the high denitration efficiency [8–10]. In SCR and SNCR processes, reducing agents are injected into the flue gas to reduce NO_x into harmless nitrogen (N₂). At present, the most popular reducing agent is ammonia (NH₃), principally in forms of aqueous ammonia and liquid ammonia [11–13]. Related NO_x reduction reactions are as follows:



However, as a hazardous chemical, NH₃ implies potential risk to safety operation. Its production, transportation, storage, application, and handling require strict

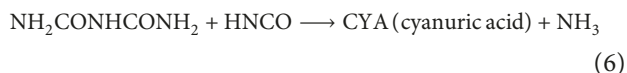
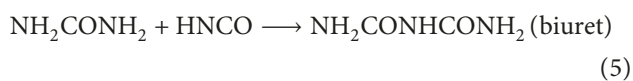
safety and environmental regulations, which immensely restricts the convenience of its utilization [14, 15]. On this account, as a substitution, urea (NH₂CONH₂) has been suggested as the reducing agent nowadays because of its nontoxicity, innocuousness, impossibility of explosion, and capacity to be carried on board [16–18].

In service, urea is firstly pyrolyzed to NH₃, and then the generated NH₃ reduced NO_x as reactions (1) and (2). Therefore, the pyrolysis of urea significantly influences the following NO_x removal. Ideally, 1 mole of urea experiences two-step reactions to form 2 moles of NH₃: the direct thermal decomposition of urea into NH₃ and isocyanic acid (HNCO) (3) and the hydrolysis of HNCO into NH₃ and CO₂ (4) [19, 20]:



Unfortunately, in the actual urea-based NO_x removal process, 1 mole of urea can hardly generate 2 moles of NH₃. It is mainly due to the following two factors: (i) ignored side reactions in parallel with reactions (3) and (4) and (ii) the rather low reaction rate of (4) [21, 22]. These side reactions include the generation of macromolecular by-products such as biuret and cyanuric acid, which leads to

reduction of NH_3 production. The product of urea decomposition HNCO reacts with intact urea to produce biuret (5), and a small amount of HNCO can react with biuret to produce cyanuric acid (6) [23]:



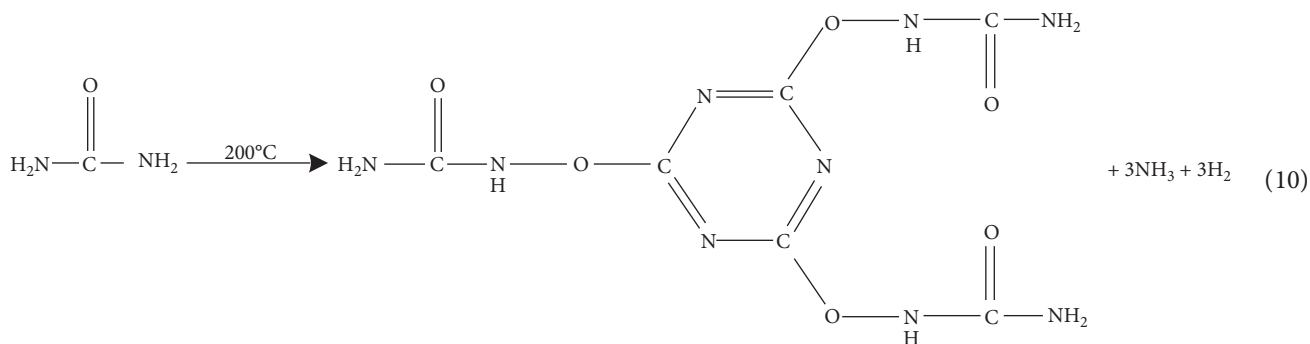
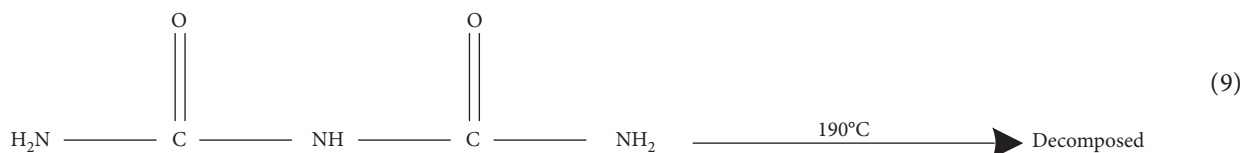
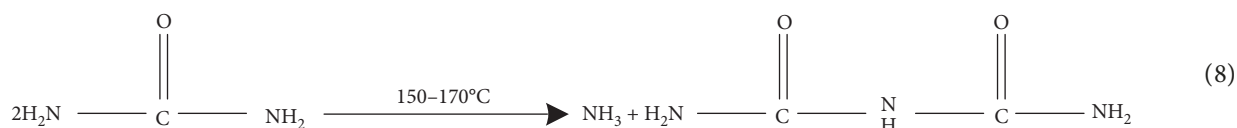
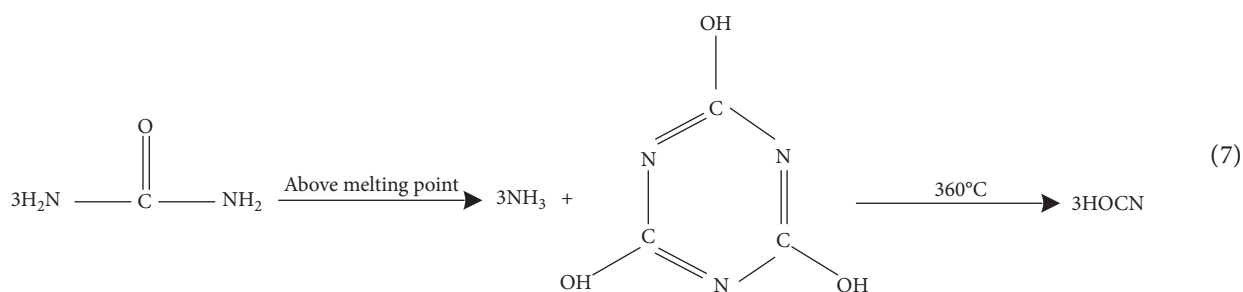
Therefore, the systematic study on urea pyrolysis mechanism and the methods to improve the reaction rate of (4) have been deeply focused on, in order to promote the NH_3 production efficiency for NO_x removal [17, 24–26]. In this paper, a review of urea pyrolysis is presented to summarize related studies.

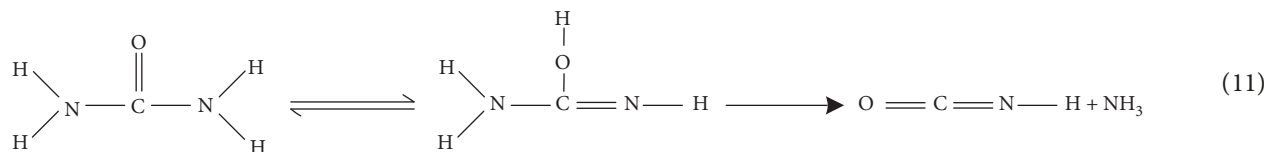
2. Discussion

2.1. Urea Pyrolysis Pathway. To make the complex urea pyrolysis pathway clear, abundant experimental research

was carried out, and possible conversion pathways were proposed based on the experimental results.

Chen and Isa firstly used simultaneous thermogravimetry/differential thermal analysis/mass spectrometry (TG/DTA/MS) to measure the gaseous products during urea pyrolysis [27]. They used TG-DTA technology to heat and decompose urea at a heating rate of $4^\circ\text{C}\cdot\text{min}^{-1}$ in $25\text{--}500^\circ\text{C}$. The urea melting point was measured to be 132.5°C , and no gaseous urea was detected during the whole pyrolysis process, indicating that the decomposition reaction of urea completed after melting and before gasification. The whole pyrolysis process was divided into four stages, corresponding to 66%, 13%, 18%, and 3% weight loss, respectively. This was the first time that the pyrolysis process of urea was artificially divided into four stages in open literature. Simultaneously, the synthesis pathways of biuret and other macromolecular products as well as the decomposition route of biuret at high temperature were also proposed in this research. In addition, related reaction formulas (7)–(12) were hypothesized to explain the whole urea pyrolysis process.





In order to accurately determine the formation and decomposition of relevant macromolecular products during urea pyrolysis, Schaber et al. adopted thermogravimetric analysis (TGA), liquid chromatography analysis (HPLC), ammonium ion electrode analysis (ISE), and Fourier transform infrared spectroscopy (FTIR) to analyze the substance types and corresponding quality of the residues in the reactor where 100.0 g urea was heated to different temperature under sand bath in an open reaction vessel [23]. Through their measurement and analysis, the whole process of urea pyrolysis was also divided into four weight loss stages (room temperature to 190°C, 190–250°C, 250–360°C, and above 360°C), corresponding to different typical reactions via which different macromolecular products formed and decomposed, as shown in Figure 1. Similar to the experimental results of Chen and Isa [27], Schaber et al. also divided the urea weight loss process into four stages, and the weight loss ratio in each stage was approximately equal to that proposed by Chen and Isa. However, Schaber et al. adopted more abundant measurement methods to determine the types of reaction products and the mass values of related products in each stage. Meanwhile, Schaber et al. carried out a detailed analysis process and proposed hypothetical representative reactions in each stage, so the completeness of the theoretical system was initially achieved. Although these hypothetical reactions still need further meticulous verification, their experimental results could help to provide essential literature support for later researchers.

Lundström et al. used differential scanning calorimetry (DSC) for the first time to measure the value of heat exchange during the thermal decomposition of solid urea in quartz crucible at the heating rates of 10°C·min⁻¹ and 20°C·min⁻¹, respectively [28]. Chemical analysis methods were mainly used to focus on the measurement and analysis of products in the pyrolysis process as reported in the literature [23, 27], while Lundström et al. applied thermal analysis methods to research urea pyrolysis [28]. In addition, in order to determine the specific reactions ascribed to corresponding caloric values as accurately as possible, they measured and analyzed the DSC curves of biuret and cyanic acid. The production of HNCO in urea pyrolysis was also measured by FTIR, but the measurement accuracy was not too high. The experimental results of Lundström et al. indicated that, during pyrolysis of solid urea in quartz cup at a heating rate of 20°C·min⁻¹, the production of NH₃ peaked only at around 250°C, while the production of HNCO peaked at around 250°C and 400°C. The experimental results were consistent with the results of the above literature [23, 27]: biuret began to decompose at 190°C and consumed

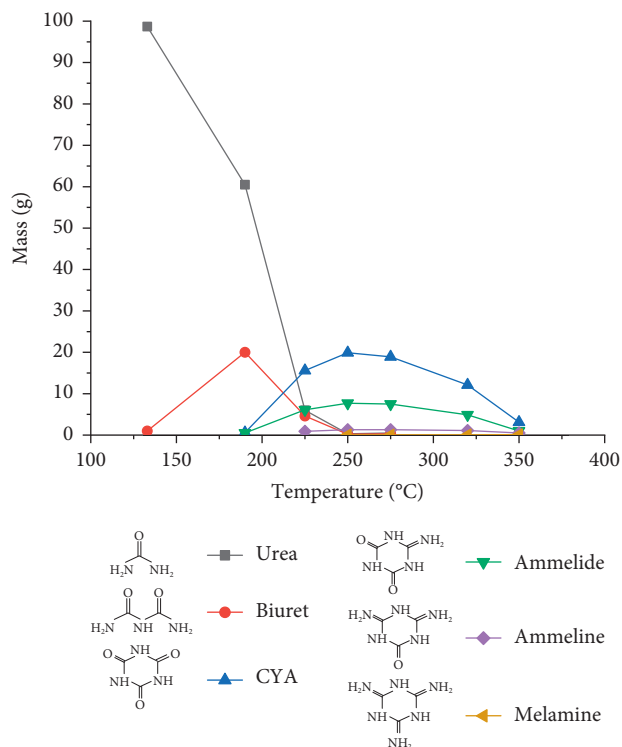


FIGURE 1: HPLC Mass Plot: urea pyrolysis reaction.

a lot in the range of 190–250°C, which indicated that the decomposition reaction of biuret (9) produced NH₃, resulting in that the production of NH₃ peaked at 250°C. The production of HNCO that peaked at 250°C was due to the decomposition reaction of urea, while the production of HNCO that peaked at 400°C may be due to the decomposition reaction of cyanic acid (7).

Bernhard et al. studied the effect of temperature increase rate and heating time on the urea gasification process under normal pressure by a temperature-programmed desorption method, and the pyrolysis products were analyzed by using HPLC and FTIR techniques qualitatively and quantitatively [29]. The experimental results showed that the urea solution could be successfully heated and converted into gaseous state under normal pressure. Gaseous urea molecules could be obtained up to 97% under the experimental conditions of high evaporation area and high carrier gas flow rate, and the massive production of other byproducts could be effectively avoided. This discovery verified the fact that a considerable amount of urea did not decompose after the urea solution was completely vaporized, and it proved that urea still

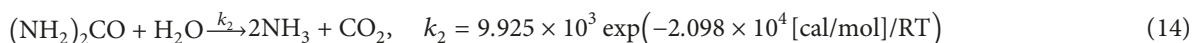
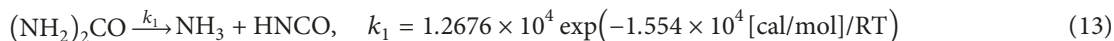
existed in the reactor in the form of fixed gaseous urea molecule. At present, there are few experimental and simulation studies on urea gasification. Considering the gasification of urea, the degree of urea pyrolysis reaction (3)–(12) could be determined more accurately, which is beneficial to improve the computational modeling of urea-based NO_x removal systems.

The contribution of urea solution to denitration was the generation of NH₃, and the yield of NH₃ was very important for the efficient denitration. Mahalik et al. studied the yield of NH₃ generated by aqueous urea solution heated by a stable heat source at standard atmospheric pressure in a self-made semicontinuous reactor [30]. The effects of reaction temperature, reaction time, stirring rate, and initial urea concentration on ammonia generation rate in the reactor were systematically researched. In their experiments, the urea concentration in the reactor, rather than the reaction product NH₃, was measured to reflect the depth of the reaction and the urea conversion rate. The experimental results showed that the increase of reaction temperature, the extension of reaction time, and the increase of stirring rate effectively increased the urea conversion rate. The increase of the initial concentration of urea solution also led to the increase of urea conversion rate. According to the experimental results, they simulated the reaction process by Fluent and obtained the temperature field distribution and concentration field distribution in the reaction process [31]. The simulation results were compared with experimental data and analyzed in detail, based on which the specific expressions of the reaction rate and reaction activation energy in the pyrolysis of aqueous urea solution were calculated. The activation energy was determined to be 59.85 kJ·mol⁻¹, and the pre-exponential factor was determined to be 3.9 × 10⁶·min⁻¹.

Our group focused on the effect of different oxygen concentration and heating rates on the mass loss and the formation of gaseous products (NH₃, N₂O, and CO) during solid urea pyrolysis [21]. Experimental results showed that there were two sharp endothermic peaks in the process,

reflecting urea melting and its decomposition, respectively. Little NH₃ was detected below 140°C, confirming that little urea decomposed before urea melting. This was consistent with the results of the literature by Chen and Isa [27]. Above the urea melting point, NH₃ production dramatically increased. The presence of O₂ lowered the highest NH₃ yield, possibly as a result of the oxidation of partial generated NH₃, but O₂ accelerated the formation of N₂O and CO. At the same condition, the formation amount of N₂O was approximately twice that of CO.

Although some progress was made in urea pyrolysis, and some important experimental results were obtained by diverse measurement and analysis methods, these studies mainly focused on analysis of urea pyrolysis products. Too many experimental data were acquired on urea pyrolysis, but too few literatures were published on the reaction kinetics analysis. Through specific experiments, Brack et al. calculated the reaction order, reaction pre-exponential factor, and reaction activation energy of urea pyrolysis [32]. They focused their research on the formation pathways of ammonia, isocyanic acid, urea, biuret, cyanic acid, and ammeline in the pyrolysis process of solid urea, and a simplified reaction mechanism including 15-step elementary reactions (shown in Table 1) was proposed through the combined use of FTIR-TGA and HPLC analysis. Besides, Ebrahimian et al. proposed a condensed-phase kinetic scheme containing 12 reactions for urea thermal decomposition, as shown in Table 2 [33]. The mechanisms were validated by thermogravimetric experiments including gaseous data as well as solid-phase concentration profiles. Compared with the corresponding experimental data, it was confirmed that both the two models had good qualitative consistency and certain application reference value, but the errors of quantitative calculation were debatable. Aoki et al. performed urea thermal decomposition experiments using a laminar flow reactor and the urea decomposition and NH₃ and HNCO formation rates were presented [34]. They assumed the following decomposition pathways, which have been widely adopted up to now.



For urea pyrolysis pathways, Eichelbaum et al. drew the whole diagram, as shown in Figure 2 [35]. It clearly showed the generation and decomposition of macromolecular products in detail.

Much work has been done on urea pyrolysis mechanism, and valuable research results have been achieved. The urea pyrolysis network has been accomplished already, which includes not only the direct thermal decomposition reaction of urea and the hydrolysis reaction of HNCO, but also the generation path and decomposition path of macromolecular products such as biuret and cyanuric acid during urea

pyrolysis. Even so, the detailed mechanism with accurate prediction ability still needs more study.

2.2. Catalytic Hydrolysis of HNCO. During urea pyrolysis, HNCO was an important intermediate product, as its hydrolysis reaction (12) played an important role in NH₃ production [16–18]. The HNCO formed from urea decomposition is quite stable in the gas phase, so its hydrolysis reaction does not proceed as a homogeneous reaction. To accelerate it, various oxides have been applied as catalysts.

TABLE 1: Kinetic reaction scheme of urea decomposition.

	Reaction	γ_j	A	E_A (kJ/mol)
I	$CYA_{(s)} \rightarrow 3HNCO_{(g)}$	0	1.001×10^3 mol/s	118.42
II	$Biuret_{(m)} \rightarrow urea_{(m)} + HNCO_{(l)}$	1	1.107×10^{20} 1/s	208.23
III	$Urea_{(m)} + HNCO_{(l)} \rightarrow biuret_{(m)}$	1/1	3.517×10^{11} ml/mol s	75.45
IV	$Urea_{(m)} \rightarrow HNCO_{(l)} + NH_{3(g)}$	0.3	2.000×10^4 mol ^{0.7} /ml ^{0.7} s	74.00
V	$2 biuret_{(m)} \rightarrow ammeline_{(s)} + HNCO_{(l)} + NH_{3(g)} + H_2O_{(g)}$	2	3.637×10^{26} 1/s	257.76
VI	$Biuret_{(m)} + HNCO_{(g)} \rightarrow CYA_{(s)} + NH_{3(g)}$	1/1	9.397×10^{20} ml/mol s	158.68
VII	$Biuret_{(m)} + HNCO_{(g)} \rightarrow triuret_{(s)}$	1/1	1.091×10^{15} ml/mol s	116.97
VIII	$Triuret_{(s)} \rightarrow CYA_{(s)} + NH_{3(g)}$	1	1.238×10^{18} 1/s	194.94
IX	$Urea_{(m)} + 2HNCO_{(l)} \rightarrow ammeline_{(s)} + H_2O_{(g)}$	1/2	1.274×10^{20} ml ² /mol ² s ²	110.40
X	$Biuret_{(m)} \rightarrow biuret_{(matrix)}$	1	8.193×10^{26} 1/s	271.50
XI	$Biuret_{(matrix)} \rightarrow biuret_{(m)}$	1	3.162×10^{09} 1/s	122.00
XII	$Biuret_{(matrix)} \rightarrow 2HNCO_{(g)} + NH_{3(g)}$	1	5.626×10^{24} 1/s	266.38
XIII	$Urea_{(s)} \rightarrow urea_{(m)}$	1	$1.000 \times 10^{15} \cdot T^{1.5}$ 1/s	160.00
XIV	$Ammeline_{(s)} \rightarrow ammeline_{(g)}$	1	1.000×10^{14} ml/mol s	201.67
XV	$HNCO_{(l)} \rightarrow HNCO_{(g)}$		Herz-Knudsen equation	

Note. States of aggregation: (s): solid, (m): molten, (g): gaseous, (l): liquid/dissolved, (matrix): solid matrix. Triuret: $NH_2-CO-NH-CO-NH-CO-NH_2$. For reactions with two educts the reaction order γ_j of the second educt is specified as second value.

TABLE 2: Condensed-phase kinetic scheme for urea thermal decomposition.

Reaction	A_i (s ⁻¹)	E_i (kJ mol ⁻¹)
(1) $Urea \rightarrow NH_4^+ + NCO^-$	8.50×10^6	84
(2) $NH_4^+ \rightarrow NH_{3(g)} + H^+$	1.50×10^2	40
(3) $NCO^- + H^+ \rightarrow HNCO_{(g)}$	6.57×10^2	10
(4) $Urea + NCO^- + H^+ \rightarrow biuret$	7.87×10^{14}	115
(5) $Biuret \rightarrow urea + NCO^- + H^+$	1.50×10^{24}	250
(6) $Biuret + NCO^- + H^+ \rightarrow CYA + NH_{3(g)}$	2.81×10^{18}	150
(7) $CYA \rightarrow 3NCO^- + 3 H^+$	1.50×10^{19}	260
(8) $CYA + NCO^- + H^+ \rightarrow ammeline + CO_2$	3.48×10^5	35
(9) $Ammeline \rightarrow 2NCO^- + 2H^+ + HCN_{(g)} + NH_{(g)}$	6.00×10^{14}	220
(10) $Urea_{(aq)} \rightarrow NH_4^+ + NCO^-$	1.20×10^8	84
(11) $NCO^- + H^+ + H_2O_{(aq)} \rightarrow NH_3 + CO_{2(g)}$	5.62×10^9	59
(12) $Urea_{(aq)} + NCO^- + H^+ \rightarrow biuret$	3.93×10^{14}	115

(g): gaseous; (aq): aqueous.

Kleemann et al. studied the reaction rate and ammonia yield of the HNCO hydrolysis reaction under the catalysis of commonly used SCR catalysts (TiO_2 , V_2O_5/TiO_2 , $V_2O_5-WO_3/TiO_2$) [36]. And the catalytic effects of catalysts with different vanadium and tungsten contents on ammonia production from HNCO hydrolysis were compared in 140–475°C. The experimental results showed that HNCO had a higher hydrolysis reaction rate under the catalysis of pure TiO_2 than under V_2O_5/TiO_2 and $V_2O_5-WO_3/TiO_2$, while the addition of V_2O_5 or WO_3 reduced the reaction rate to some extent. The activation energy of the HNCO hydrolysis reaction was determined to be about 13 kJ·mol⁻¹, indicating that the overall reaction rate was mainly affected by the mass transfer rate.

Piazzesi et al. carried out experimental research on the catalytic effect of Fe-ZSM5 and $V_2O_5-WO_3/TiO_2$ catalysts on the HNCO hydrolysis reaction and also compared the influence of different V_2O_5 contents on the catalytic effect of $V_2O_5-WO_3/TiO_2$ catalysts [37]. Experimental results showed that Fe-ZSM5 had a very high catalytic effect on the hydrolysis process of HNCO. The conversion efficiency of HNCO increased to 100% at about 260°C, and the perfect

conversion rate was stably maintained until 450°C. The $V_2O_5-WO_3/TiO_2$ catalyst also exhibited a high catalytic effect on HNCO hydrolysis, and the catalytic effect of 1% V_2O_5 content was more significant than that of 3% V_2O_5 content. It indicated that, for the $V_2O_5-WO_3/TiO_2$ catalyst, the increase of V_2O_5 content resulted in the decrease of catalytic efficiency, which was consistent with the experimental results of Kleemann et al. [36].

Czekaj and Kröcher studied the catalytic effect of TiO_2 and $\gamma-Al_2O_3$ on HNCO hydrolysis by Diffuse Reflectance Infrared Fourier Transform Spectra (DRIFTS) [38]. The experimental results proved that both TiO_2 and $\gamma-Al_2O_3$ had significant catalytic effects on HNCO hydrolysis under the same reaction conditions and TiO_2 had better catalytic performance than $\gamma-Al_2O_3$. Additionally, Czekaj and Kröcher used density functional theory to calculate the adsorption energy required for HNCO adsorbed on the catalyst surface during the reaction. The calculation results showed that the adsorption energy required for HNCO adsorption on TiO_2 was lower than that on $\gamma-Al_2O_3$, which scientifically explained why the two catalysts differed in catalytic performance from the perspective of energy.

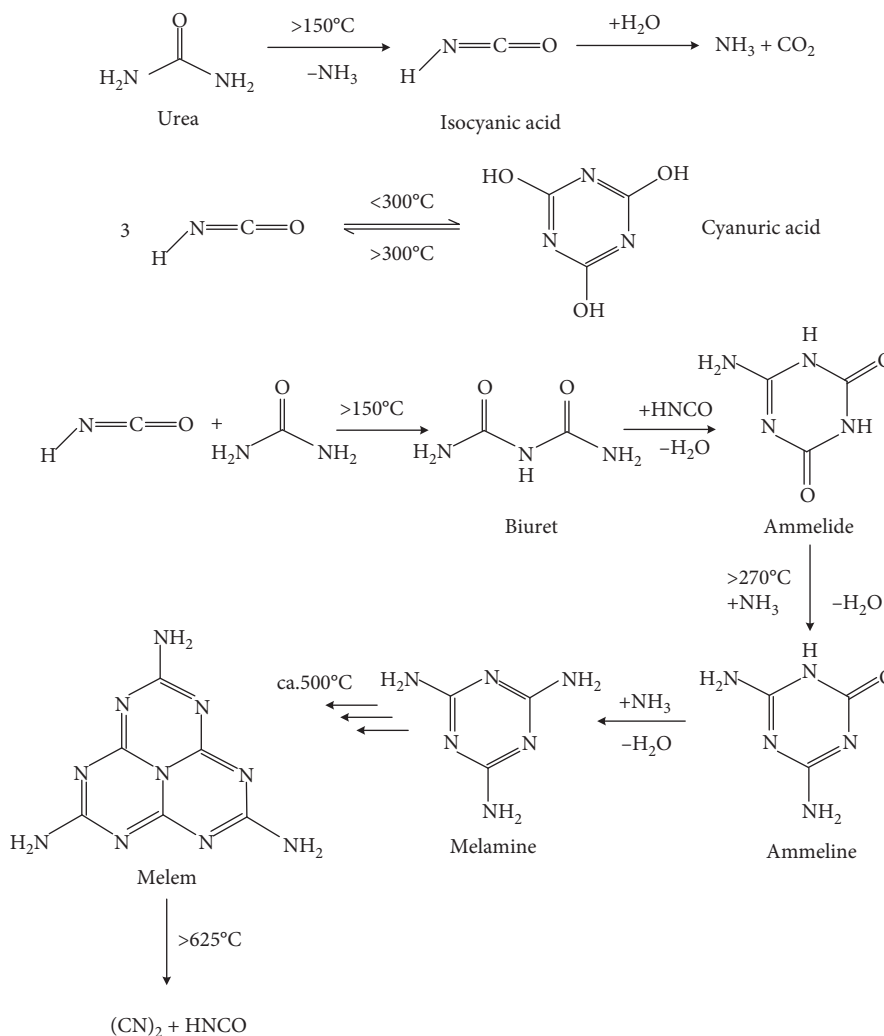


FIGURE 2: Schematic of all major reactions, intermediate and final products for the pyrolysis and hydrolysis of neat urea in the temperature range between 20 and 750°C.

Hauck et al. specifically carried out experimental research on the catalytic effect of TiO_2 on HNCO hydrolysis, as well as the thermodynamic catalytic mechanism [39, 40]. In the self-made experimental system, mass spectrometry was used to determine the production of different atomic groups, and the reaction rate of the elemental reactions that might occur on the TiO_2 surface was calculated by quantitative analysis. After calculation and analysis, they obtained the conclusion that HNCO hydrolysis was affected by mass transfer rate, which was consistent with the research conclusion of Kleemann et al. [36]. Moreover, Hauck et al. found that HNCO catalytic hydrolysis over TiO_2 was restricted by the external mass transfer rate. However, the calculation by Hauck et al. rested on the reaction rate constant, but further activation energy calculation was not involved. It was worth mentioning that NO , NH_3 , and NO_2 were added to the carrier gas stream, and the influence of the presence or absence of these gases on HNCO hydrolysis was investigated. Through the comparison and analysis of the experimental results, it was found that the existence of NO ,

NH_3 , and NO_2 all inhibited HNCO hydrolysis to different degree, following the order of $\text{NO} < \text{NH}_3 < \text{NO}_2$. The main reason for the inhibitory effect was that the gases could be adsorbed on the surface of TiO_2 , thus reducing the adsorption of HNCO .

Chen et al. measured and compared the similarities and differences of catalytic effects of $\gamma\text{-Al}_2\text{O}_3$ and $\text{CuO}/\gamma\text{-Al}_2\text{O}_3$ on HNCO hydrolysis and calculated the activation energy of HNCO hydrolysis over the two catalysts, respectively [41]. They found that the catalytic effect of $\gamma\text{-Al}_2\text{O}_3$ was slightly higher than that of $\text{CuO}/\gamma\text{-Al}_2\text{O}_3$. According to their experimental data and calculation results, the activation energy of the HNCO hydrolysis over the two catalysts changed with the temperature range. When the temperature was higher than 200°C , the activation energy of HNCO hydrolysis over $\gamma\text{-Al}_2\text{O}_3$ was $13 \text{ kJ}\cdot\text{mol}^{-1}$, while over $\text{CuO}/\gamma\text{-Al}_2\text{O}_3$ it was $16 \text{ kJ}\cdot\text{mol}^{-1}$. The activation energy of HNCO hydrolysis measured by Chen was close to that measured by Kleemann et al. [36]. Such low activation energy reflected that the HNCO hydrolysis over $\gamma\text{-Al}_2\text{O}_3$ and $\text{CuO}/\gamma\text{-Al}_2\text{O}_3$ was

mainly controlled by external mass transfer. When the temperature was lower than 200°C, the calculated activation energy obviously increased. The activation energy over $\gamma\text{-Al}_2\text{O}_3$ was calculated to be $25\text{ kJ}\cdot\text{mol}^{-1}$, while over $\text{CuO}/\gamma\text{-Al}_2\text{O}_3$ it was calculated as $26\text{ kJ}\cdot\text{mol}^{-1}$. It indicated that the reaction below 200°C was mainly dominated by mass transfer inside the catalyst pores. In addition, no matter what the temperature range was, the value of reaction activation energy over $\gamma\text{-Al}_2\text{O}_3$ was lower than that over $\text{CuO}/\gamma\text{-Al}_2\text{O}_3$, consistent with the phenomenon that $\gamma\text{-Al}_2\text{O}_3$ showed stronger catalytic effect than $\text{CuO}/\gamma\text{-Al}_2\text{O}_3$.

It could be concluded from the analysis of the above literature [33–38] that the HNCO hydrolysis over metal oxides catalysts could be basically determined as a reaction process under mass transfer control. However, the determination of whether external or internal mass transfer is still controversial now. It is also a recognized fact that the hydrolysis reaction is slow without the assistance of relevant catalysts. All the catalysts used in the study were metal oxides, and they were mainly concentrated on the catalysts commonly used in SCR technology. Among them, TiO_2 performed prominent catalytic effect, while the addition of vanadium and tungsten could hardly improve the catalytic efficiency.

2.3. Catalytic Pyrolysis of Aqueous Urea Solution. The aforementioned studies on urea pyrolysis mechanism and on catalytic hydrolysis of HNCO were conducted for the production of NH_3 , and effectively converting urea to NH_3 with low energy consumption was decidedly pursued in actual operation. As aqueous urea solution is the most widely used agent in the urea DeNO_x process, many researchers have focused their research on the catalytic pyrolysis of aqueous urea solution.

Koebel and Struts conducted an experimental study on the synergistic process of urea pyrolysis and hydrolysis in SCR system of automotive internal combustion engines [42]. They focused their research on how to reasonably select the heating source for urea pyrolysis. In the paper, Koebel and Strutz listed the heat source selection of different ways in the urea pyrolysis process in detail and carried out specific energy consumption calculation, heat calculation, and experimental research for these selections, respectively. By analyzing and comparing, the following most energy-saving technical scheme was put forward: selecting part of the hot exhaust gas of the internal combustion engine to provide heat supply for urea pyrolysis, and improving the ammonia production efficiency of urea pyrolysis by rationally using the integral-type catalyst. This technical scheme could not only improve the ammonia yield, but also effectively utilize the exhaust heat of the internal combustion engine, which was in line with the principle of economy and practicability.

Yim et al. carried out experimental research and theoretical calculation on NH_3 production from urea pyrolysis in SCR system in 150–450°C [43]. The atomized urea solution particles were heated and decomposed in a self-made aluminum reaction system, and the effects of residence time and reaction temperature on the pyrolysis of urea solution were

mainly investigated. Their experimental results demonstrated that the hydrolysis of HNCO occurred without catalysts when the reaction temperature was high enough ($\geq 400^\circ\text{C}$). The prolongation of residence time was beneficial to urea pyrolysis and effectively promoted ammonia yield. In order to improve the ammonia generation rate, they also studied the catalytic effect of the high efficiency denitration catalyst CuZSM5 on pyrolysis of aqueous urea solution. The reaction rate and reaction activation energy of the two-step pyrolysis reactions of aqueous urea solution were calculated based on the obtained experimental results. However, an aluminum reactor was used in their experimental system, and it was likely that Al_2O_3 attached on the inner surface of the reactor might catalyze the reaction, so their conclusion results needed further verification.

In order to compare the effects of different oxide catalysts on the pyrolysis reaction of aqueous urea solution and obtain detailed catalytic efficiency values, Kröcher and Elsener tested the catalytic effects of twenty potential catalyst materials on the pyrolysis of aqueous urea solution in a self-made fluidized bed reactor [44]. The results are listed in Table 3. By comparison, $\gamma\text{-Al}_2\text{O}_3$ was identified as the most suitable catalyst material in fluidized bed reactor. Although TiO_2 showed the highest catalytic efficiency during the experiments, its wear resistance was far lower than that of $\gamma\text{-Al}_2\text{O}_3$. The catalytic efficiency of the catalysts was tested under the fluidized state, which was usually higher than that in fixed bed reactor, so it limited the application reference value to some extent.

In the above literature [42–44], the solvent of urea solution was water, which might affect the catalytic effect of catalysts. Perhaps being aware of it, Bernhard et al. carried out experimental tests and kinetic analysis on the catalytic efficiency of stationary catalysts soon afterwards [45]. In their experimental system, the catalytic effects of different characteristic sizes of TiO_2 , ZrO_2 , Al_2O_3 , H-ZSM-5, and SiO_2 on urea pyrolysis and HNCO hydrolysis were tested, respectively. Particularly, the catalytic effect of the above materials on urea pyrolysis under anhydrous conditions was a conspicuous highlight. In previous studies, catalytic efficiency was tested in experiments with water. Differently, Bernhard et al. used methanol and ethanol as solvents to avoid the presence of water in the experiments, which provided convincing experimental data for the catalytic research of oxides on urea pyrolysis without water. The experimental results showed that the presence or absence of water had a great influence on the catalytic effect of the catalysts. When the urea solvent was water, the order of catalytic effect of different catalysts was $\text{ZrO}_2 > \text{TiO}_2 > \text{Al}_2\text{O}_3 > \text{H-ZSM-5} > \text{SiO}_2$. Under anhydrous conditions, the order changed to $\text{TiO}_2 > \text{H-ZSM-5} \approx \text{Al}_2\text{O}_3 > \text{ZrO}_2 > \text{SiO}_2$. Additionally, the ammonia production efficiency over these catalysts under anhydrous conditions was significantly lower than that under hydrous conditions.

Lundström et al. adopted differential scanning calorimetry and mass spectrometry to study the effects of TiO_2 , Al_2O_3 , and Fe-Beta catalysts on the production of ammonia, isocyanic acid, and carbon dioxide from urea pyrolysis under anhydrous and hydrous conditions [46]. The

TABLE 3: Test of fluidized bed materials for the thermohydrolysis of 50% urea solution.

Bed material	Particle diameter (mm)	Reactor diameter (mm)	Volume of bed material (ml)	Air flow (L _N /h)	Urea dosage type	Urea solution dosage (g/h)	Bed loading (g/(h·ml))	Fluidized bed temperature (°C)	Y _{NH₃} (%)	Y _{H₂NCO} (%)	Urea slip (%)
γ-Al ₂ O ₃ "Uetikon1"	0.2–0.315	20	15	150	From top	185	6.2	300	99	1	0.4
								275	99	1	0.4
								250	100	0	0.4
								225	102	0	0.5
								200	96	1	1.2
γ-Al ₂ O ₃ "Uetikon1"	0.50–0.63	25	15	520	From top	185	6.2	300	97	4	1.2
								275	96	5	1.3
								250	84	12	2.6
								225	73	16	3.9
γ-Al ₂ O ₃ "compalox"	0.50–0.63	25	15	520	From top	185	6.2	300	96	0	1
								275	95	0	0.7
								250	96	1	0.9
								225	93	2	2.3
γ-Al ₂ O ₃ "puralox"	0.2–0.315	20	15	150	From top	185	6.2	300	96	5	0.4
								275	99	5	0.3
								250	96	4	0.4
								225	98	4	0.4
								200	99	4	0.9
γ-Al ₂ O ₃ "CAT 250"	0.50–0.63	50	60	1860	From top	340	2.9	300	97	2	0.7
								275	98	3	0.6
								250	96	2	0.6
								225	97	3	0.6
								200	95	3	1.2
γ-Al ₂ O ₃ "CAT 250"	1.0–1.25	50	60	3900	From top	350	2.9	300	96	0	1.9
								275	95	0	1.8
								250	94	1	1.6
								225	83	5	2.4
								200	66	15	5
γ-Al ₂ O ₃ "CAT 250"	1.0–1.25	50	60	3900	From top	350	2.9	300	94	0	1.1
								275	94	1	1.2
								250	93	1	1.3
								225	89	6	2.3
γ-Al ₂ O ₃ "CAT 250"	1.0–1.25	25	15	1109	From top	186	6.2	300	101	0	1.9
								275	100	2	1.7
								250	99	3	1.8
								225	84	12	3.2
γ-Al ₂ O ₃ "condea"	1.0–1.25	20	15	554	From top	185	6.2	300	89	5	5.8
								275	78	16	6.1
								250	69	23	6.3
γ-Al ₂ O ₃ "seralite 537"	1.0–1.25	50	60	3900	Into bed	350	2.9	300	94	3	1.9
								275	91	5	2.2
								250	85	7	3
								225	72	13	5
α-Al ₂ O ₃ "seralite 512 S"	1.6–2.0	50	60	4700	Into bed	290	2.4	300	47	31	9.1
α-ALOOH (boehmite)	0.2–0.315	20	15	150	From top	185	6.2	300	99	3	0.8
								275	94	4	0.5
								250	96	3	0.8
								225	95	5	0.6
								200	96	5	0.7
SiO ₂ "aerosil"	0.50–0.63	25	15	410	From top	185	6.2	300	70	25	4.2

TABLE 3: Continued.

Bed material	Particle diameter (mm)	Reactor diameter (mm)	Volume of bed material (ml)	Air flow (L _N /h)	Urea dosage type	Urea solution dosage (g/h)	Bed loading (g/(h·ml))	Fluidized bed temperature (°C)	Y _{NH₃} (%)	Y _{HNCO} (%)	Urea slip (%)
AlSiO _x (moločite)	0.22–0.50	20	15	150	From top	4.5	0.02	400	61	25	n.d.
								350	55	34	n.d.
								300	38	33	n.d.
								250	24	20	n.d.
MgSiO _x “florisil”	0.50–0.63	25	15	400	From top	185	6.2	300	90	8	2.3
								275	86	7	2.1
								250	83	9	3
TiO ₂ “macrosorb T”	0.2–0.315	20	15	150	From top	185	6.2	300	104	1	0.7
								275	102	1	0.8
								250	95	4	2.7
								225	62	8	5.9
TiO ₂ “7702”	0.50–0.63	25	15	520	From top	185	6.2	300	98	0	1.5
								275	99	0	1.2
								250	99	0	1
								225	99	1	1
V ₂ O ₅ /WO ₃ - TiO ₂	0.315–0.50	25	15	356	From top	185	6.2	200	98	2	1.6
								300	96	1	0.6
								275	96	1	0.6
								250	90	6	1.1
Molsieve 5 Å	0.2–0.315	20	15	150	From top	94	3.1	225	87	6	1.5
								200	82	6	2.9
								300	93	7	0.9
								275	58	21	7.2
Molsieve “13X”	0.50–0.63	25	15	410	From top	185	6.2	300	93	2	0.7
								275	76	13	1.2
								250	43	20	5.5
H-MOR	ca.2.(2–4)	50	60	3900	From top	350	2.9	300	85	4	2.6
								275	83	6	2.8
H-ZSM-5	ca.2.(2–4)	50	60	3900	From top	350	2.9	300	72	19	3.1
								275	66	25	3.6
Dealuminated Y	ca.2.(2–4)	50	60	3900	From top	350	2.9	300	52	35	5
								275	51	36	5.6

differences of ammonia production between anhydrous and hydrous conditions were also detected. However, different from the reference [45], in this paper, researchers did not recognize that TiO₂, Al₂O₃, and Fe-Beta catalysts could catalyze urea pyrolysis under anhydrous conditions. They attributed the difference to the absence of HNCO hydrolysis under anhydrous conditions. This conclusion contradicted the results of Yim and Bernhard et al. [43, 45] but lacks scientific basis.

In the literature mentioned above, urea was pyrolyzed on the catalyst which was put into the reactor in the form of solution with water, methanol, or ethanol as solvent. In the experiment of Bernhard et al., N₂ at 100°C was passed through honeycomb-like TiO₂ cordierite filled with aqueous urea solution [47]. The formed mixed gas stream was determined by HPLC and FTIR. In this paper, Bernhard et al. first clearly analyzed and obtained the adsorption form of urea on the surface of TiO₂ and calculated the energy value consumed during the adsorption process.

The effect of oxygen concentration and different additives (Na₂CO₃ and NaNO₃) on NH₃ yields and N₂O and CO production from pyrolysis of aqueous urea solution was studied by our group [22]. Without additives, the presence of oxygen made the NH₃ yields drop rapidly in 550–800°C. The addition of Na₂CO₃ or NaNO₃ not only increased the NH₃ yields but also reduced the N₂O and CO production via a series of chain reactions of sodium species, but it did not restrain the NH₃ oxidation at high temperatures. The addition of sodium species probably provided plenty of NaO and NaO₂, which might catalyze the HNCO hydrolysis to dramatically increase the NH₃ yields. Moreover, the harmful gaseous by-products (N₂O and CO) might participate in the chain reactions of sodium species, so most N₂O and nearly all CO could be consumed.

Various catalysts were selected for hydrolysis of aqueous urea solution, and some outstanding ones stood out for the excellent efficiency. Many studies have been carried out on the exploration and development of catalysts, while little attention has been paid to the catalytic mechanism

investigation. Further work, especially the dynamic mechanism, was still needed to help to make better use of these catalysts.

3. Conclusion

Urea pyrolysis plays an important role in urea-based NO_x removal technology. Research into urea pyrolysis mostly focused on three parts: urea pyrolysis pathway, catalytic hydrolysis of HNCO, and catalytic pyrolysis of aqueous urea solution. The network of urea pyrolysis has been basically established, which includes not only the direct thermal decomposition reaction of urea and the hydrolysis reaction of HNCO, but also the generation path and decomposition path of macromolecular products such as biuret and cyanuric acid during urea pyrolysis. The HNCO hydrolysis over metal oxides catalysts could be basically determined as a reaction process under mass transfer control. And it is also a recognized fact that the HNCO hydrolysis reaction is slow without the assistance of relevant catalysts. No matter whether in the presence or absence of water, TiO₂ has relatively higher catalytic effect on urea pyrolysis and HNCO hydrolysis.

Although much work has been done, concentration was mainly on analysis of urea pyrolysis products and exploration of catalysts used to improve ammonia yields. In future work, it is necessary to determine the detailed reaction mechanism and catalytic mechanism in the urea pyrolysis process more clearly and to establish a high-precision kinetic model.

Conflicts of Interest

The authors declare that they have no conflicts of interest.

Acknowledgments

This work was supported by the National Natural Science Foundation of China (51906193), the Fundamental Research Funds for the Central Universities (xjh012019013), and the China Postdoctoral Science Foundation (2019M653624). The authors specially thank the support from the Young Talent Support Program of Xi'an Association for Science and Technology.

References

- [1] Z. Zhou, X. Liu, Y. Hu et al., "Investigation on synergistic oxidation behavior of NO and HgO during the newly designed fast SCR process," *Fuel*, vol. 225, pp. 134–139, 2018.
- [2] S. Li, Y. Ge, and X. Wei, "Experiment on NO_x reduction by advanced reburning in cement precalciner," *Fuel*, vol. 224, pp. 235–240, 2018.
- [3] P. Glarborg, J. A. Miller, B. Ruscic, and S. J. Klippenstein, "Modeling nitrogen chemistry in combustion," *Progress in Energy and Combustion Science*, vol. 67, pp. 31–68, 2018.
- [4] Y. Hu, W. Liu, Y. Yang, X. Tong, Q. Chen, and Z. Zhou, "Synthesis of highly efficient, structurally improved Li₄SiO₄ sorbents for high-temperature CO₂ capture," *Ceramics International*, vol. 44, no. 14, pp. 16668–16677, 2018.
- [5] Y. Zhao, D. Feng, B. Li, S. Sun, and S. Zhang, "Combustion characteristics of char from pyrolysis of Zhundong sub-bituminous coal under O₂/steam atmosphere: effects of mineral matter," *International Journal of Greenhouse Gas Control*, vol. 80, pp. 54–60, 2019.
- [6] Z. Zi, B. Zhu, Y. Sun, Q. Fang, and T. Ge, "Promotional effect of Mn modification on DeNO_x performance of Fe/nickel foam catalyst at low temperature," *Environmental Science and Pollution Research*, vol. 26, no. 10, pp. 10117–10126, 2019.
- [7] C. Zhou, Y. Wang, Q. Jin, Q. Chen, and Y. Zhou, "Mechanism analysis on the pulverized coal combustion flame stability and NO_x emission in a swirl burner with deep air staging," *Journal of the Energy Institute*, vol. 92, no. 2, pp. 298–310, 2019.
- [8] D. Fang, F. He, and J. Xie, "Characterization and performance of common alkali metals and alkaline earth metals loaded Mn/TiO₂ catalysts for NO_x removal with NH₃," *Journal of the Energy Institute*, vol. 92, no. 2, pp. 319–331, 2019.
- [9] A. S. Ayodhya, V. T. Lamani, M. Thirumoorthy, and G. N. Kumar, "NO_x reduction studies on a diesel engine operating on waste plastic oil blend using selective catalytic reduction technique," *Journal of the Energy Institute*, vol. 92, no. 2, pp. 341–350, 2019.
- [10] M. Zhu, J.-K. Lai, and I. E. Wachs, "Formation of N₂O greenhouse gas during SCR of NO with NH₃ by supported vanadium oxide catalysts," *Applied Catalysis B: Environmental*, vol. 224, pp. 836–840, 2018.
- [11] B. Zhu, G. Li, Y. Sun et al., "De-NO_x performance and mechanism of Mn-based low-temperature SCR catalysts supported on foamed metal nickel," *Journal of the Brazilian Chemical Society*, vol. 29, no. 8, pp. 1680–1689, 2018.
- [12] B. Zhu, Q. Fang, Y. Sun et al., "Adsorption properties of NO, NH₃, and O₂ over β-MnO₂(110) surface," *Journal of Materials Science*, vol. 53, no. 16, pp. 11500–11511, 2018.
- [13] H. Zhou, X. Guo, M. Zhou, W. Ma, M. W. Dahri, and K. Cen, "Optimization of ammonia injection grid in hybrid selective non-catalyst reduction and selective catalyst reduction system to achieve ultra-low NO_x emissions," *Journal of the Energy Institute*, vol. 91, no. 6, pp. 984–996, 2018.
- [14] D. Wang, Q. Yao, S. Hui, and Y. Niu, "Source of N and O in N₂O formation during selective catalytic reduction of NO with NH₃ over MnO/TiO₂," *Fuel*, vol. 251, pp. 23–29, 2019.
- [15] D. Wang, N. Dong, S. Hui, and Y. Niu, "Analysis of urea pyrolysis in 132.5–190°C," *Fuel*, vol. 242, pp. 62–67, 2019.
- [16] D. Yin, J. Li, J. Wang, L. Ling, and W. Qiao, "Low-temperature selective catalytic reduction of NO_x with urea supported on carbon xerogels," *Industrial & Engineering Chemistry Research*, vol. 57, no. 20, pp. 6842–6852, 2018.
- [17] L. Tan, P. Feng, S. Yang, Y. Guo, S. Liu, and Z. Li, "CFD studies on effects of SCR mixers on the performance of urea conversion and mixing of the reducing agent," *Chemical Engineering and Processing—Process Intensification*, vol. 123, pp. 82–88, 2018.
- [18] M. Stein, V. Bykov, A. Bertótiné Abai et al., "A reduced model for the evaporation and decomposition of urea-water solution droplets," *International Journal of Heat and Fluid Flow*, vol. 70, pp. 216–225, 2018.
- [19] X. Fan, J. Li, D. Qiu, and T. Zhu, "Production of ammonia from plasma-catalytic decomposition of urea: effects of carrier gas composition," *Journal of Environmental Sciences*, vol. 66, pp. 94–103, 2018.
- [20] X. Zhang, B. Zhang, X. Lu, N. Gao, X. Xiang, and H. Xu, "Experimental study on urea hydrolysis to ammonia for gas denitration in a continuous tank reactor," *Energy*, vol. 126, pp. 677–688, 2017.

- [21] D. Wang, S. Hui, and C. Liu, "Mass loss and evolved gas analysis in thermal decomposition of solid urea," *Fuel*, vol. 207, pp. 268–273, 2017.
- [22] D. Wang, S. Hui, C. Liu, and H. Zhuang, "Effect of oxygen and additives on thermal decomposition of aqueous urea solution," *Fuel*, vol. 180, pp. 34–40, 2016.
- [23] P. M. Schaber, J. Colson, S. Higgins, D. Thielen, B. Anspach, and J. Brauer, "Thermal decomposition (pyrolysis) of urea in an open reaction vessel," *Thermochimica Acta*, vol. 424, no. 1–2, pp. 131–142, 2004.
- [24] Y. Ma, X. Wu, J. Zhang, R. Ran, and D. Weng, "Urea-related reactions and their active sites over Cu-SAPO-34: formation of NH_3 and conversion of HNCO," *Applied Catalysis B: Environmental*, vol. 227, pp. 198–208, 2018.
- [25] F. Lu and G. G. Botte, "Understanding the electrochemically induced conversion of urea to ammonia using nickel based catalysts," *Electrochimica Acta*, vol. 246, pp. 564–571, 2017.
- [26] Y. Liao, P. Dimopoulos Eggenschwiler, D. Rentsch, F. Curto, and K. Boulouchos, "Characterization of the urea-water spray impingement in diesel selective catalytic reduction systems," *Applied Energy*, vol. 205, pp. 964–975, 2017.
- [27] J. P. Chen and K. Isa, "Thermal decomposition of urea and urea derivatives by simultaneous TG/(DTA)/MS," *Journal of the Mass Spectrometry Society of Japan*, vol. 46, no. 4, pp. 299–303, 1998.
- [28] A. Lundström, B. Andersson, and L. Olsson, "Urea thermolysis studied under flow reactor conditions using DSC and FT-IR," *Chemical Engineering Journal*, vol. 150, no. 2–3, pp. 544–550, 2009.
- [29] A. M. Bernhard, I. Czekaj, M. Elsener, A. Wokaun, and O. Kröcher, "Evaporation of urea at atmospheric pressure," *The Journal of Physical Chemistry A*, vol. 115, no. 12, pp. 2581–2589, 2011.
- [30] K. Mahalik, J. N. Sahu, A. V. Patwardhan, and B. C. Meikap, "Kinetic studies on hydrolysis of urea in a semi-batch reactor at atmospheric pressure for safe use of ammonia in a power plant for flue gas conditioning," *Journal of Hazardous Materials*, vol. 175, no. 1–3, pp. 629–637, 2010.
- [31] J. N. Sahu, S. Hussain, and B. C. Meikap, "Studies on the hydrolysis of urea for production of ammonia and modeling for flow characterization in presence of stirring in a batch reactor using computational fluid dynamics," *Korean Journal of Chemical Engineering*, vol. 28, no. 6, pp. 1380–1385, 2011.
- [32] W. Brack, B. Heine, F. Birkhold et al., "Kinetic modeling of urea decomposition based on systematic thermogravimetric analyses of urea and its most important by-products," *Chemical Engineering Science*, vol. 106, pp. 1–8, 2014.
- [33] V. Ebrahimian, A. Nicolle, and C. Habchi, "Detailed modeling of the evaporation and thermal decomposition of urea-water solution in SCR systems," *AIChE Journal*, vol. 58, no. 7, pp. 1998–2009, 2012.
- [34] H. Aoki, T. Fujiwara, Y. Morozumi, and M. Takatoshi, "Measurement of urea thermal decomposition reaction rate for NO selective non-catalytic reduction," in *Proceedings of the Fifth International Conference on Technologies and Combustion for a Clean Environment*, pp. 115–118, Lisbon, Portugal, 1999.
- [35] M. Eichelbaum, R. J. Farrauto, and M. J. Castaldi, "The impact of urea on the performance of metal exchanged zeolites for the selective catalytic reduction of NO_x part I. Pyrolysis and hydrolysis of urea over zeolite catalysts," *Applied Catalysis B: Environmental*, vol. 97, no. 1–2, pp. 90–97, 2010.
- [36] M. Kleemann, M. Elsener, M. Koebel, and A. Wokaun, "Hydrolysis of isocyanic acid on SCR catalysts," *Industrial & Engineering Chemistry Research*, vol. 39, no. 11, pp. 4120–4126, 2000.
- [37] G. Piazzesi, M. Devadas, O. Kröcher, M. Elsener, and A. Wokaun, "Isocyanic acid hydrolysis over Fe-ZSM5 in urea-SCR," *Catalysis Communications*, vol. 7, no. 8, pp. 600–603, 2006.
- [38] I. Czekaj and O. Kröcher, "Decomposition of urea in the SCR process: combination of DFT calculations and experimental results on the catalytic hydrolysis of isocyanic acid on TiO_2 and Al_2O_3 ," *Topics in Catalysis*, vol. 52, no. 13–20, pp. 1740–1745, 2009.
- [39] P. Hauck, A. Jentys, and J. A. Lercher, "Surface chemistry and kinetics of the hydrolysis of isocyanic acid on anatase," *Applied Catalysis B: Environmental*, vol. 70, no. 1–4, pp. 91–99, 2007.
- [40] P. Hauck, A. Jentys, and J. A. Lercher, "On the quantitative aspects of hydrolysis of isocyanic acid on TiO_2 ," *Catalysis Today*, vol. 127, no. 1–4, pp. 165–175, 2007.
- [41] Z.-C. Chen, W.-J. Yang, J.-H. Zhou, H.-K. Lv, J.-Z. Liu, and K.-F. Cen, "HNCO hydrolysis performance in urea-water solution thermohydrolysis process with and without catalysts," *Journal of Zhejiang University-Science A*, vol. 11, no. 11, pp. 849–856, 2010.
- [42] M. Koebel and E. O. Strutz, "Thermal and hydrolytic decomposition of urea for automotive selective catalytic reduction systems: thermochemical and practical aspects," *Industrial & Engineering Chemistry Research*, vol. 42, no. 10, pp. 2093–2100, 2003.
- [43] S. D. Yim, S. J. Kim, J. H. Baik et al., "Decomposition of urea into NH_3 for the SCR process," *Industrial & Engineering Chemistry Research*, vol. 43, no. 16, pp. 4856–4863, 2004.
- [44] O. Kröcher and M. Elsener, "Materials for thermohydrolysis of urea in a fluidized bed," *Chemical Engineering Journal*, vol. 152, no. 1, pp. 167–176, 2009.
- [45] A. M. Bernhard, D. Peitz, M. Elsener, T. Schildhauer, and O. Kröcher, "Catalytic urea hydrolysis in the selective catalytic reduction of NO_x : catalyst screening and kinetics on anatase TiO_2 and ZrO_2 ," *Catalysis Science & Technology*, vol. 3, no. 4, pp. 942–951, 2013.
- [46] A. Lundström, T. Snelling, P. Morsing, P. Gabrielsson, E. Senar, and L. Olsson, "Urea decomposition and HNCO hydrolysis studied over titanium dioxide, Fe-Beta and γ -Alumina," *Applied Catalysis B: Environmental*, vol. 106, no. 3–4, pp. 273–279, 2011.
- [47] A. M. Bernhard, I. Czekaj, M. Elsener, and O. Kröcher, "Adsorption and catalytic thermolysis of gaseous urea on anatase TiO_2 studied by HPLC analysis, DRIFT spectroscopy and DFT calculations," *Applied Catalysis B: Environmental*, vol. 134–135, pp. 316–323, 2013.

Research Article

The Online Research of B_2O_3 on Crystal Behavior of High Ti-Bearing Blast Furnace Slag

Yin-he Lin ¹, Bin Zheng,² Lin-gen Luo ³, Yu-long Jia ¹ and Li-qiang Zhang ⁴

¹Institute of Chemical Engineering, Yangtze Normal University, Chongqing 408100, China

²Institute of Transportation and Automobile Engineering, Panzhihua University, Panzhihua 617000, China

³China Iron & Steel Research Institute Group, Beijing 100081, China

⁴School of Metallurgical Engineering, Anhui University of Technology, Maanshan 243000, China

Correspondence should be addressed to Yin-he Lin; linyinhe2009@163.com and Yu-long Jia; yljia2017@126.com

Received 22 July 2019; Revised 11 September 2019; Accepted 18 September 2019; Published 13 October 2019

Guest Editor: Yanqing Niu

Copyright © 2019 Yin-he Lin et al. This is an open access article distributed under the Creative Commons Attribution License, which permits unrestricted use, distribution, and reproduction in any medium, provided the original work is properly cited.

The existence and phase structures of high Ti-bearing blast furnace slag at a high temperature are the key issue to flow performance and reaction temperature. It is essential to evaluate the physical-chemical properties, such as viscosity and melting point. In this work, a new method of online research of B_2O_3 on crystal behavior of high Ti-bearing blast furnace slag is proposed. By ultrahigh-temperature confocal laser scanning microscope and area scanning analysis, it can be concluded that the effect of B_2O_3 additives on the viscosity has a more obvious effect among the low-temperature region of the slag. Compared to the samples without B_2O_3 additives, the liquid phase of Ti-bearing slag with B_2O_3 additives appears earlier at the same experimental temperature, and the solid particles floating on the surface of liquid slag become less. Moreover, the B_2O_3 additives can promote the migration of titanium elements from the high melting point phase to the low melting point phase, and the transferring quantity increases with the addition of the amount of B_2O_3 additives. These results demonstrate that B_2O_3 additives can restrain the appearance of the perovskite phase, decrease the apparent viscosity, and promote the metallurgical properties of Ti-bearing blast furnace slag.

1. Introduction

The lower production cost for iron and steel enterprise becomes one of the most important objectives in the present situation under the premise of ensuring quality. The use of local vanadium titanomagnetite replacing ordinary iron ore could save expensive freight and reduce material cost due to geographical location of Panzhihua Iron and Steel. But the TiO_2 content in slag increased with the improving proportion of vanadium titanomagnetite in blast furnace. The TiO_2 content in blast furnace (BF) slag has a significant effect on the fluidity of slag. The influence degree increases with the fluctuation of TiO_2 proportion in blast furnace, thus affecting the slag iron reaction and performance of BF.

At the condition of current technology of BF coal powder injection, the TiO_2 in slag will react with the unburned pulverized coal and produce high melting point phase, such as TiC. The high melting point phase will further increase the slag viscosity and make the slag iron more

difficult to separate. Meanwhile, the quality of raw material and fuel into the furnace deteriorates with the continuous exploitation of mineral resources, which results in larger fluctuations of furnace burden composition and makes metallurgical properties of slag deterioration. Therefore, it is essential to improve the flow performance and decrease the effect of component fluctuation [1, 2].

Lin et al. [3] studied the influence of CaF_2 additives on the apparent viscosity of Ti-bearing blast furnace slag and concluded that the CaF_2 additives could reduce the apparent viscosity to a certain extent. Li et al. [4] investigated the variation regularity of B_2O_3 additives replacing SiO_2 for CaO - BaO - SiO_2 - Al_2O_3 - CaF_2 system and obtained the quantitative relationship between alkalinity and desulfurization rate. Nakamoto et al. [5] studied the evolution regularity of the surface tension of molten silicate with B_2O_3 , CaF_2 , and Na_2O surfactants. Zhang et al. [6] analyzed the change rules of B_2O_3 and Na_2O in the fluorine-free slag from 1300°C to 1400°C by using a thermogravimetric analyzer.

Tasuku and Fumitaka [7] studied the effect of B_2O_3 additives on desulfurization capacity in FeO_x - CaO - MgO_{satd} - SiO_2 slag at the temperature of $1300^\circ C$. Shi et al. [8] studied the phase equilibrium law of CaO - SiO_2 -5wt.% MgO -20wt.% Al_2O_3 - TiO_2 system at $1300^\circ C$ and $1400^\circ C$ by SEM-EDS, XRD, and XRF. Li et al. [9] performed some studies about the effect of Al_2O_3 additives on precipitated phase transformation, and the results showed that Al_2O_3 additives could prompt phase change from perovskite to low melting point phase. Bian and Gao [10] investigated the influence of basicity and B_2O_3 on apparent viscosity and microstructure using high-temperature viscosity meter, XRD, etc., and the results showed that the apparent viscosity decreased with the increasing number of B_2O_3 additives and CaO/SiO_2 ratio. Qiu et al. [11] studied the influence of Cr_2O_3 additives on apparent viscosity and microstructure. Above all the researches [12–19], the physical-chemical properties and phase structures of metallurgical slag at high temperature are characterized based on the cooled samples by different cooling rates such as air cooling, water cooling, or nitrogen cooling. However, the actual phase structures of slag melt at high temperature are different from that of solidified slag. The influence mechanism and evolution of the actual structure of Ti-bearing blast furnace slag on the smelting process need to be characterized precisely. Compared with the traditional offline research, the online research can clearly observe the continuous change process of slag melting at high temperature. At the same time, the online research can provide some references for the smelt slag change in the “black box” of blast furnace.

In this work, a new method of online research of B_2O_3 on crystal behavior of high Ti-bearing blast furnace slag is proposed. The viscosity variation below melting temperature with B_2O_3 additives was detected. The variation law with time of perovskite formation was analyzed by ultrahigh-temperature confocal laser scanning microscope. The crystal behavior of perovskite with B_2O_3 additives was investigated by SEM-EDS. This work provides an exploratory research on the evolution rule of online high-temperature state.

2. Experimental

2.1. Materials, Apparatus, and Equipment. These materials were synthesized with various analytical grade chemicals according to chemical components of high Ti-bearing blast furnace slag of Panzhihua Steel and Iron Group Corporation, which are listed in Table 1. The synthesized high Ti-bearing blast furnace slag was heated to $1500^\circ C$ and then kept for 30 minutes to ensure the melt homogenized under Ar atmosphere. After that process, the melt quenched into the water. The quenched samples were ground into powder and sieved with different particle sizes. The grain size of experimental slags was in the range of 50 to 74 micrometer. The B_2O_3 additives were all analytical reagents, which was used in apparent viscosity and confocal laser scanning experiments.

The basic schematic diagram of apparent viscosity experimental apparatus by the rotating cylinder method in the literature [3] and ultrahigh-temperature confocal laser

TABLE 1: The chemical compositions of samples (%).

	CaO	SiO ₂	MgO	Al ₂ O ₃	TiO ₂	V ₂ O ₅	C	B ₂ O ₃	R
0#	27.55	26.20	9.19	14.89	21.85	0.10	0.22	0	1.05
1#	27.02	25.73	9.19	14.89	21.85	0.10	0.22	1.0	1.05
2#	26.51	25.24	9.19	14.89	21.85	0.10	0.22	2.0	1.05
3#	26.00	24.75	9.19	14.89	21.85	0.10	0.22	3.0	1.05

scanning microscope’s (VL2000DX-SVF17SP, LASERTEC, Japan) principle is shown in Figure 1. The light beam emitted by the light source was focused on the surface of the experimental sample, and the reflected light to the experimental sample went back along original paths. The reflected light passed through lens, focused again, and imaged onto photoreceptors. Only the reflected light which shined on the surface of experimental samples could be received by the original paths in the confocal laser scan microscope system, and other reflected lights were shielded by pinhole. The maximum temperature of ultrahigh-temperature confocal laser scanning microscope could reach $1700^\circ C$, and the error was less than $\pm 2^\circ C$. The platinum crucibles instead of graphite crucibles were used in experiment to prevent the TiO_2 reacting with carbon. The chemical components are listed in Table 1. The 0# sample without B_2O_3 was set as a reference slag; the B_2O_3 additives were 1% in 1# sample and 2% in 2# sample.

2.2. Experimental Procedure. The apparent viscosity of high Ti-bearing blast furnace slag was measured by Brookfield digital viscometer (RTW-10, Northeastern University) by the rotating cylinder method. The molten slag was cooled down by the temperature-controlling program until the viscosity-temperature curve became stationary. The viscosity curves that changed with temperature were recorded by software on computer. Then, the morphologies of samples were analyzed by ultrahigh-temperature confocal laser scanning microscope (VL2000DX-SVF17SP, LASERTEC, Japan).

The platinum crucible which was filled with high Ti-bearing blast furnace slag was put on Al_2O_3 sheets above the sample bracket, and the content of slags was between 50% and 75%. The experimental sample moved slowly until the fixed position by the particular hydraulic system. At this point, high-purity argon was injected into the furnace body, and gas flow rate was kept at about 30 ml/min. The experimental samples were heated up at a rate of $300^\circ C/min$. After reaching the set value ($1485^\circ C$), the experimental samples were kept at a constant temperature for 120 min by adjusting the temperature control system. Then, high-purity argon was switched to helium gas, and the helium flow rate was set to 400 ml/min for cooling the experimental samples down. The huge cooling rate could make the morphologies of products closer to high-temperature state of slags than other cooling methods. After cooling the hot products to room temperature using helium gas, shut the air transporting pipe and collect completely the experimental products for fine-grinding, polishing, composition, and micrograph analysis.

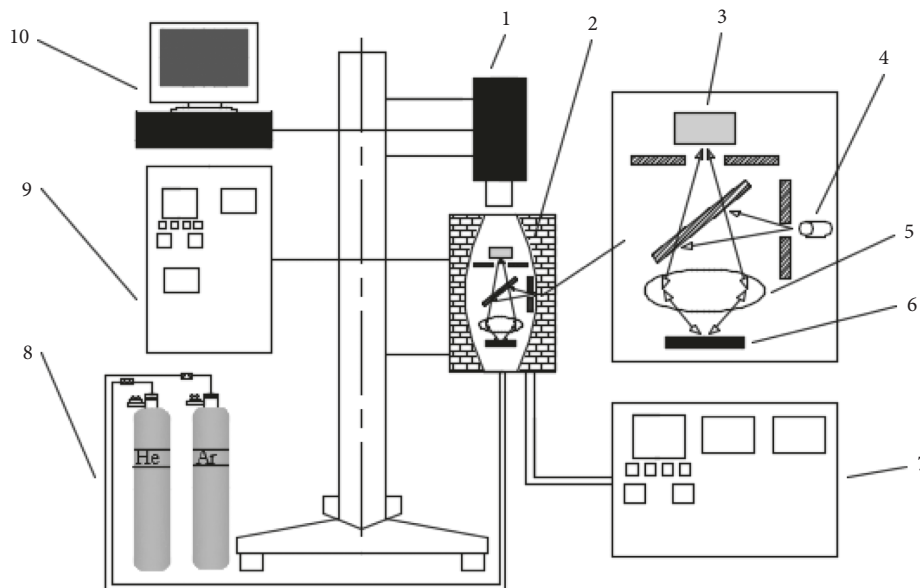


FIGURE 1: The schematic diagram of the experimental apparatus (1, optical system; 2, furnace; 3, thermal insulation; 4, light source; 5, lens; 6, Al_2O_3 sheets; 7, temperature control system; 8, gas; 9, water cooling system; 10, computer).

3. Results and Discussion

3.1. Effect of B_2O_3 Additives on the Viscosity of Slag. The effect of B_2O_3 additives on the apparent viscosity of slag with temperature variation is shown in Figure 2, the vertical coordinate is the apparent viscosity of high Ti-bearing blast furnace slag, and the horizontal axis is the experimental temperature. The viscosity-temperature curve is a graph drawn by the computer connected with the viscosimeter in the process of measuring viscosity by cooling slag. The 0# sample is the benchmark specimen without B_2O_3 , and the B_2O_3 amount of 1#, 2#, and 3# samples is, respectively, 1%, 2%, and 3%.

According to Figure 2, the B_2O_3 additives improve the fluidity and reduce the apparent viscosity of high Ti-bearing blast furnace slag. With increase in the B_2O_3 additives, there are lower apparent viscosity at the same experimental temperature. When the temperature of high Ti-bearing blast furnace slag is above the melting temperature, the apparent viscosity of slag with B_2O_3 additives is lower than that of 0# sample, the difference between the content of B_2O_3 additives is not obvious, and the curves are almost completely coinciding. Compared with the benchmark specimen, the apparent viscosity with B_2O_3 additives is slightly lower than the slag without B_2O_3 . Therefore, the B_2O_3 additives can slightly reduce the apparent viscosity of high Ti-bearing blast furnace slag for the temperature above the melting temperature.

When the experimental temperature is lower than the melting temperature, the apparent viscosity of high Ti-bearing blast furnace slag decreases with the addition of B_2O_3 . Compared to the benchmark curve, the drop of apparent viscosity is more obvious with the increasing B_2O_3 additives shown in Figure 2. According to Figure 2, making a straight line perpendicular to the ordinate to intersect at four points with four curves, the lower temperature is essential as increasing the amount of B_2O_3 additives to maintain the

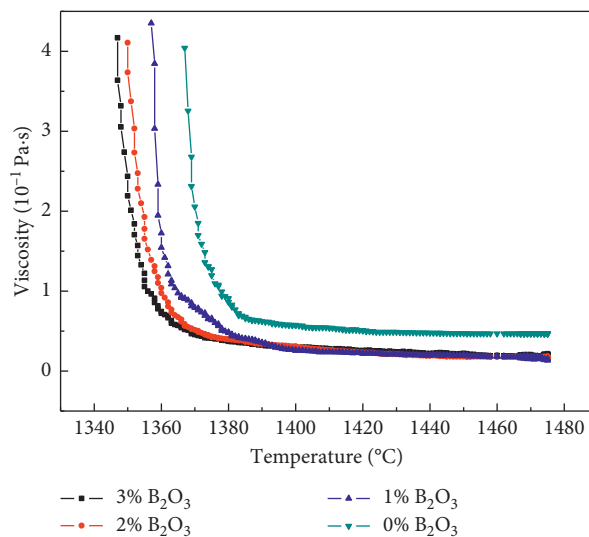


FIGURE 2: The relationship between apparent viscosity and the amount of B_2O_3 additives.

same apparent viscosity of high Ti-bearing blast furnace slag; that is, the slag has lower apparent viscosity at the same experimental temperature as the amount of B_2O_3 additives increases. When the experimental temperature is equal to the melting temperature, it decreases with the increasing amount of B_2O_3 additives. Therefore, the B_2O_3 additive has an obvious effect on low temperature area of high Ti-bearing blast furnace slag, influences the area above the hearth of BF, and promotes the stability of blast furnace.

3.2. The Evolution of Perovskite Phase at Different Temperatures. Figures 3–5 show the evolution morphologies of high Ti-bearing blast furnace slags within B_2O_3 additives with the variation of the temperature. The temperature of slag

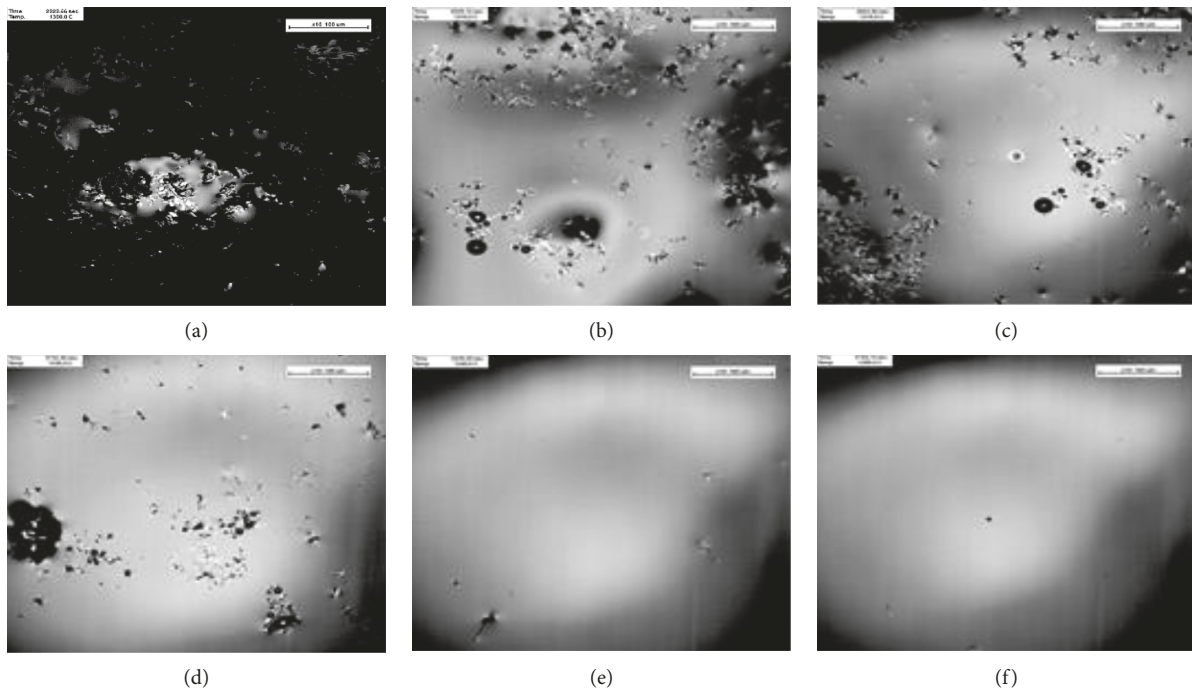


FIGURE 3: The evolution rules of morphology without B_2O_3 : (a) 1300°C; (b) 1310°C; (c) 1320°C; (d) 1340°C; (e) 1350°C; (f) 1360°C.

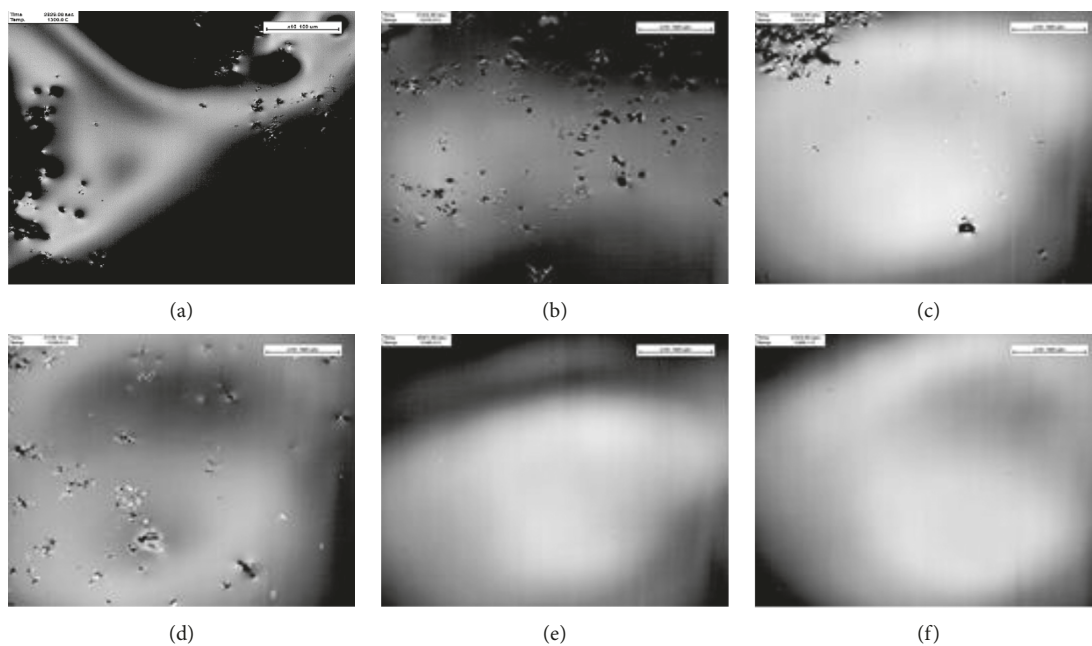


FIGURE 4: The evolution rules of morphology with 1% B_2O_3 : (a) 1300°C; (b) 1310°C; (c) 1320°C; (d) 1340°C; (e) 1350°C; (f) 1360°C.

in the picture is 1300°C (Figures 3(a), 4(a), and 5(a)) and 1360°C (Figures 3(f), 4(f), and 5(f)), and the temperature interval of two adjoining pictures is 10°C. Compared with the traditional offline research, the online research can clearly observe the continuous change process of slag melting at high temperature. At the same time, the online research can provide some references for the smelt slag change in the “black box” of blast furnace.

According to Figure 3(a), the liquid phase of high Ti-bearing blast furnace slag starts to appear at the temperature of 1300°C, as shown in the white area, and the black area is the solid materials. As the temperature of high Ti-bearing blast furnace slag continuously increases, the liquid slag steadily becomes more as shown in the white area of Figure 3(b), and the other solid materials floats on the surface of the liquid slag. When the temperature of slag

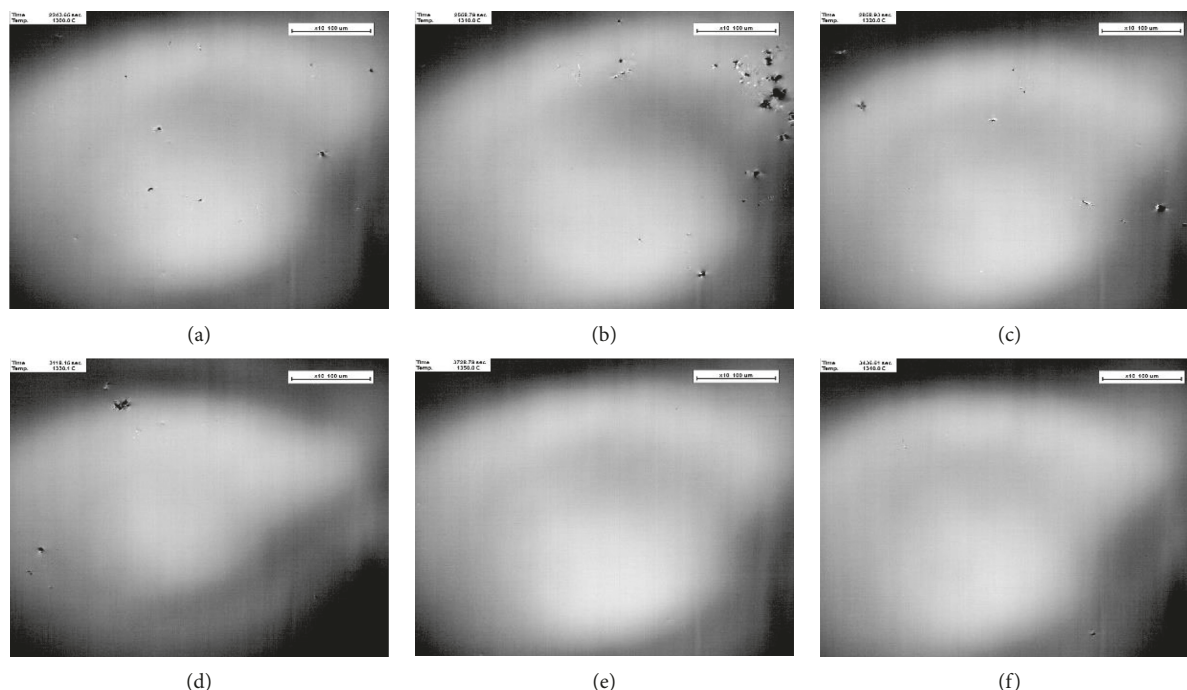


FIGURE 5: The evolution rules of morphology with 2% B_2O_3 : (a) 1300°C; (b) 1310°C; (c) 1320°C; (d) 1340°C; (e) 1350°C; (f) 1360°C.

continues to rise (Figures 3(c) and 3(d)), the suspended phase on the surface of liquid slag gradually disappears, and the suspended phase is hardly visible in Figures 3(e) and 3(f). This phenomenon is inconsistent with the ultrahigh melting point of perovskite phase. Therefore, it can be concluded that the perovskite phase is distributed in liquid slag with fine dispersion particles and influences the viscosity of slag.

According to Figures 3–5, the amount of suspended phase appears smaller at the same temperature with addition of the B_2O_3 , the degrees of decline increase with the increasing amount of B_2O_3 additives. When the amounts of B_2O_3 additives are added to 2%, there have no obvious suspended phase on the surface of the slag at the temperature of 1300°C. The phenomenon shows that the B_2O_3 addition can decrease the melting temperature of Ti-bearing slag and lead to downward movement of viscosity-temperature curves. Compared with offline research [3], the online research of Ti-bearing blast furnace slag could reflect the constant changes in “black box” rather than a frozen moment.

Therefore, the B_2O_3 addition can not only make the slag become the liquid phase earlier but also can translate the high melting point of Ti-bearing slag into other low melting point phase, showing better flowing properties.

3.3. The Crystal Behavior of Perovskite on Adding B_2O_3 . In order to investigate the effect of B_2O_3 additives on the Ti-bearing phase below high-temperature condition, the samples in ultrahigh-temperature confocal laser scanning microscope were cooled by helium at the temperature of 1485°C, in which the B_2O_3 amount was 0%, 1%, and 2%, respectively. The quench products kept the morphology of

slag in a great degree below high-temperature condition. Figures 6–8 represent the results of area scanning mapping of Ca, Si, Mg, Al, O, and Ti in different additions of B_2O_3 .

Lots of cruciform phases disperse in blast furnace slag without B_2O_3 addition at the temperature of 1485°C, as shown in Figure 6. It can be concluded that the crossed phase is perovskite by the analysis of the area scanning mapping and energy spectrum. The perovskite phase still exists in liquid slag in the form of solid particles and forms solid-liquid mixtures at the temperature of 1485°C.

When the amount of B_2O_3 additives is equal to 1%, the existential state of slag is shown in Figure 7 at the temperature of 1485°C. According to Figure 7, the crossed phase is perovskite which exists in the form of solid particles under the experimental temperature. Compared with the samples without B_2O_3 additives, a certain amount of perovskite phase disappears in liquid slag.

When the amount of B_2O_3 additives further increases to 2%, there is a significant area of nonperovskite phase in samples, as shown in Figure 8(a). Compared with 0# sample and 1# sample, the amounts of perovskite phase decrease significantly. The product is cooled to room temperature from 1485°C by helium, and the scanning mapping and energy spectrum analysis results are shown in Figure 8(b). According to Figure 8(b), the titanium element not only concentrates in the perovskite phase but also distributes largely in the nonperovskite area. Finally, based on the results, it can be concluded that the B_2O_3 addition can translate perovskite phase of high melting point into the other Ti-bearing materials of low melting point. It is one of the important reasons that B_2O_3 additives cause the decrease of slag's viscosity.

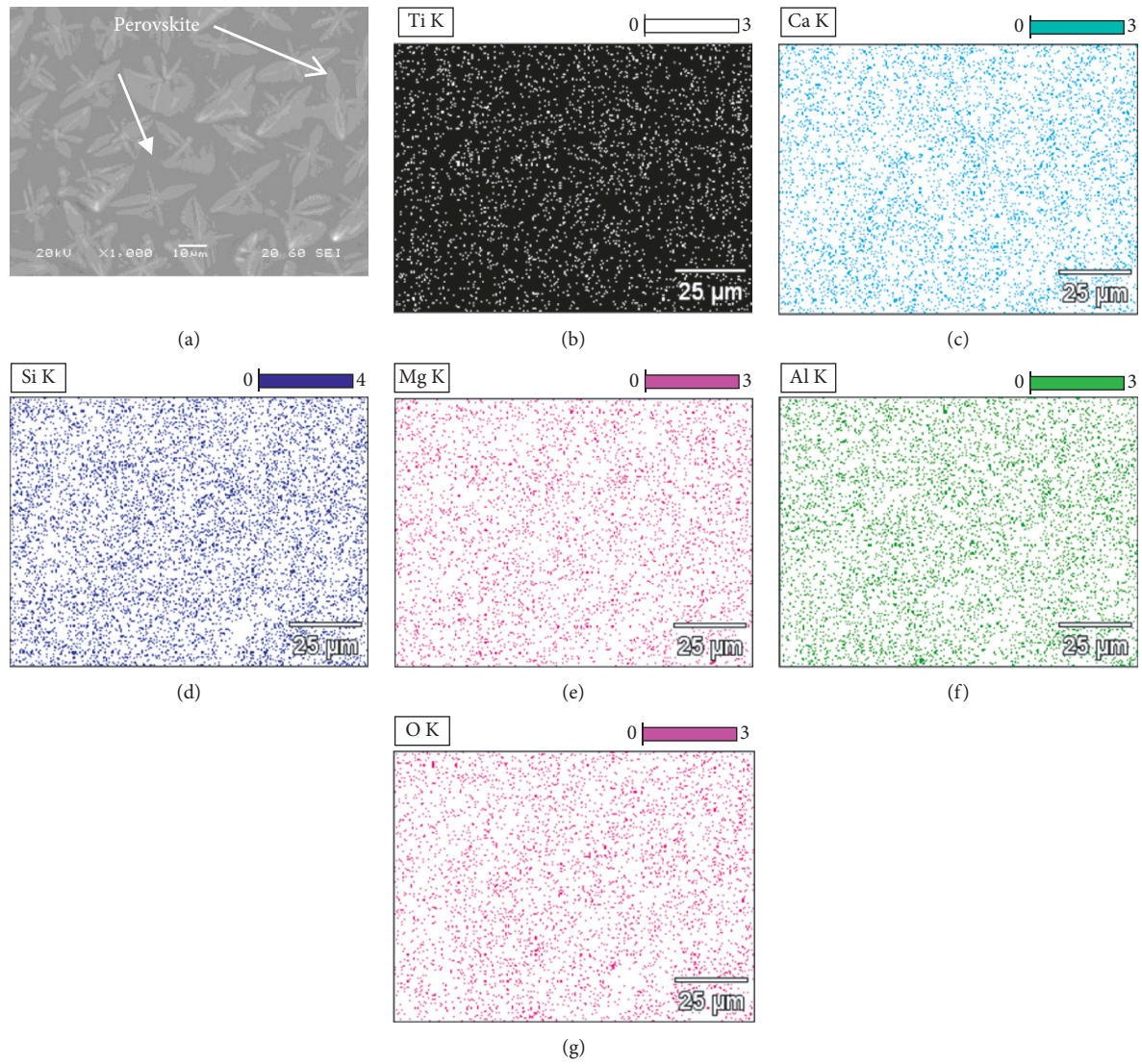


FIGURE 6: Area scanning mapping of Ti, Ca, Si, Mg, Al, O, and EDS in 0# sample without B_2O_3 at $1485^\circ C$.

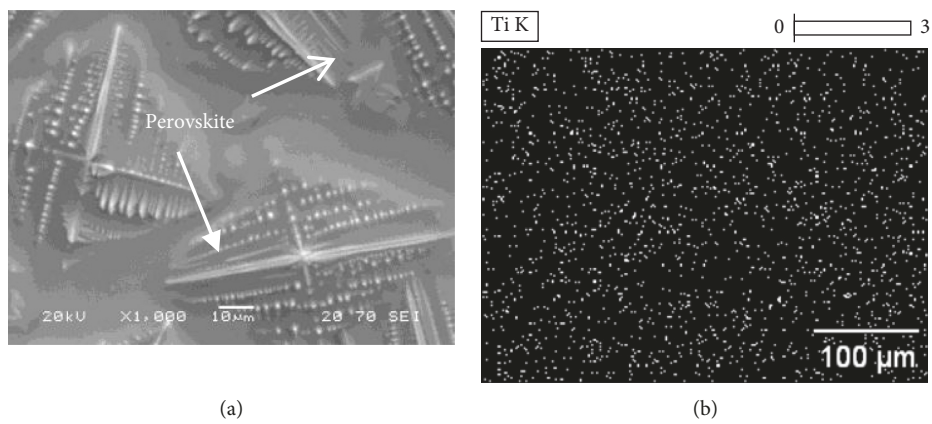


FIGURE 7: Area scanning mapping of Ti and EDS in 1# sample with 1% B_2O_3 .

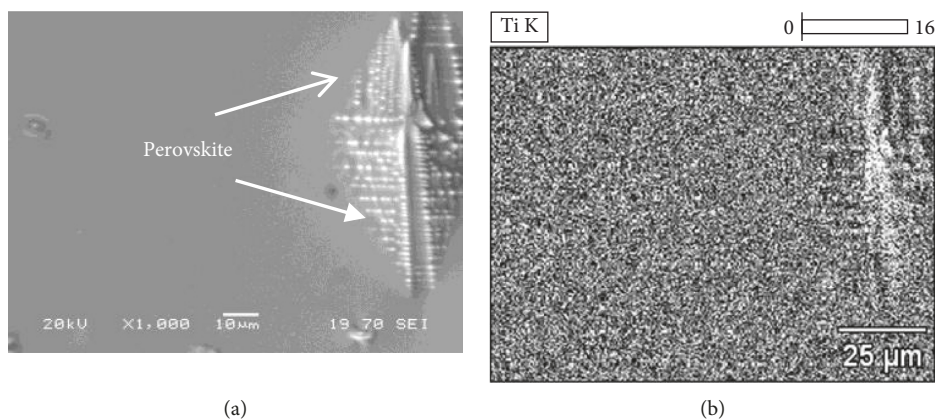


FIGURE 8: Area scanning mapping of Ti and EDS in 2# sample with 2% B_2O_3 .

4. Conclusions

The effect of B_2O_3 additives on the crystallization behavior of high Ti-bearing blast furnace slag was investigated online by ultrahigh-temperature confocal laser scanning microscope under inert atmosphere. The results show that the B_2O_3 additives can have a significant impact on the melting temperature and Ti element distribution of slag, and some important conclusions are as follows:

When the temperature of high Ti-bearing blast furnace slag is higher than the melting temperature, the apparent viscosity of slag slightly decreases with the increasing amount of B_2O_3 additives. However, the apparent viscosity of slag appears largely to change with the increasing amount of B_2O_3 additives as the temperature of slag is lower than the melting temperature. Therefore, the B_2O_3 additives have more obvious influence on the low temperature region of slag.

The B_2O_3 additives can induce the earlier appearance of liquid phase and decrease the amounts of solid particles which float on the surface of liquid slag at the same experimental temperature by online observation. Combined with the area scanning analysis, the B_2O_3 additives can make the titanium elements migrate from the high melting point phase to the low melting point phase, which result in a loss of the perovskite phase and titanium distribution more diffuse. The B_2O_3 additives could not only restrain the appearance of perovskite production but also provide the higher metallurgical properties of Ti-bearing blast furnace slag. Therefore, the rational content of B_2O_3 additives provides a feasible and convenient method to reduce the melting temperature and increase the liquidity of Ti-bearing blast furnace slag.

Data Availability

The raw/processed data required to reproduce these findings cannot be shared at this time as the data also form part of an ongoing study.

Conflicts of Interest

The authors declare that they have no conflicts of interest.

Acknowledgments

The present work was supported by the National Natural Science Foundation of China (U1960101, U1760108, and 51874001), Science and Technology Major Project of Sichuan Province (2019YFSY0029), and Science Foundation of Yangtze Normal University (no. 2017KYQD103).

References

- [1] Y.-L. Zhen, G.-H. Zhang, X.-L. Tang, and K.-C. Chou, "Influences of Al_2O_3/CaO and Na_2O/CaO ratios on viscosities of $CaO-Al_2O_3-SiO_2-Na_2O$ melts," *Metallurgical and Materials Transactions B*, vol. 45, no. 1, pp. 123–130, 2014.
- [2] G.-H. Zhang, K.-C. Chou, and K. Mills, "A structurally based viscosity model for oxide melts," *Metallurgical and Materials Transactions B*, vol. 45, no. 2, pp. 698–706, 2014.
- [3] Y.-H. Lin, L.-Q. Zhang, and X.-L. Huang, "Influence of CaF_2 on the apparent viscosity of $CaO-SiO_2-MgO-Al_2O_3-TiO_2$ slags," *Metallurgical Research & Technology*, vol. 114, no. 6, pp. 606–611, 2017.
- [4] G.-R. Li, H.-M. Wang, C.-B. Huang et al., "Action of B_2O_3 in $CaO-BaO-SiO_2-Al_2O_3-CaF_2$ refining slag," *Steelmaking*, vol. 23, no. 1, pp. 24–26, 2007.
- [5] M. Nakamoto, T. Tanaka, L. Holappa, and M. Hämäläinen, "Surface tension evaluation of molten silicates containing surface-active components (B_2O_3 , CaF_2 or Na_2O)," *ISIJ International*, vol. 47, no. 2, pp. 211–216, 2007.
- [6] Z. T. Zhang, S. Sridhar, and J. W. Cho, "An investigation of the evaporation of B_2O_3 and Na_2O in F-free mold slags," *ISIJ International*, vol. 51, no. 1, pp. 80–87, 2011.
- [7] H. Tasuku and T. Fumitaka, "The effect of B_2O_3 on dephosphorization of molten steel by $FeOx-CaO-MgO_{satd.}-SiO_2$ slags at 1873 K," *ISIJ International*, vol. 45, no. 2, pp. 159–165, 2006.
- [8] J. J. Shi, L. F. Sun, J. Y. Qiu, and M. Jiang, "Phase equilibrium investigation for $CaO-SiO_2-5wt. \%MgO-20wt. \%Al_2O_3-TiO_2$ system relevant to Ti-bearing slag system," *ISIJ International*, vol. 58, no. 3, pp. 431–438, 2018.
- [9] Z. Li, J. Li, Y. Sun et al., "Effect of Al_2O_3 addition on the precipitated phase transformation in Ti-bearing blast furnace slags," *Metallurgical and Materials Transactions B*, vol. 47, no. 2, pp. 1390–1399, 2016.
- [10] L. Bian and Y. Gao, "Influence of B_2O_3 and basicity on viscosity and structure of medium titanium bearing blast furnace

- slag,” *Journal of Chemistry*, vol. 2016, Article ID 6754593, 8 pages, 2016.
- [11] G. Qiu, L. Chen, J. Zhu, X. Lv, and C. Bai, “Effect of Cr_2O_3 addition on viscosity and structure of Ti-bearing blast furnace slag,” *ISIJ International*, vol. 55, no. 7, pp. 1367–1376, 2015.
- [12] H. M. Wang, G. R. Li, Q. X. Dai, B. Li, X.-J. Zhang, and G.-M. Shi, “CAS-OB refining: slag modification with B_2O_3 -CaO and CaF_2 -CaO,” *Ironmaking & Steelmaking*, vol. 34, no. 4, pp. 350–353, 2007.
- [13] H. M. Wang, T. W. Zhang, H. Zhu, G. Li, Y. Yan, and J. Wang, “Effect of B_2O_3 on melting temperature, viscosity and desulfurization capacity of CaO-based refining flux,” *ISIJ International*, vol. 51, no. 5, pp. 702–706, 2011.
- [14] L. Zhang, W. Zhang, J. H. Zhang, and G.-Q. Li, “Effects of additives on the phase transformation, occurrence state, and the interface of the Ti component in Ti-bearing blast furnace slag,” *International Journal of Minerals Metallurgy and Materials*, vol. 23, no. 9, pp. 1029–1040, 2016.
- [15] C. Wang, J. L. Zhang, H. S. Zhang, K. X. Jiao, J. Q. Yang, and K. C. Chou, “Effect of chlorine on the viscosities and structures of blast furnace slags,” *Ironmaking & Steelmaking*, vol. 43, no. 10, pp. 769–774, 2016.
- [16] J. Han, Y. Lai, X. Yao et al., “Structure and crystallization behavior of Al containing glasses in the CaO- B_2O_3 - SiO_2 system,” *RSC Advances*, vol. 7, no. 24, pp. 14709–14715, 2017.
- [17] L. Wang, J. Zhang, Y. Sasaki, O. Ostrovski, C. Zhang, and D. Cai, “Stability of fluorine-free CaO- SiO_2 - Al_2O_3 - B_2O_3 - Na_2O mold fluxed,” *Metallurgical and Materials Transactions B: Process Metallurgy and Materials Processing Science*, vol. 48, no. 2, pp. 1055–1063, 2017.
- [18] L. Zhang, W. Wang, and I. Sohn, “Crystallization behavior and structure analysis for molten CaO- SiO_2 - B_2O_3 based fluorine-free mold fluxes,” *Journal of Non-crystalline Solids*, vol. 511, pp. 41–49, 2019.
- [19] G. H. Kim and I. Sohn, “Effect of CaF_2 , B_2O_3 and the CaO/ SiO_2 mass ratio on the viscosity and structure of B_2O_3 -containing calcium-silicate-based melts,” *Journal of the American Ceramic Society*, vol. 102, no. 11, pp. 6575–6590, 2019.